ENGINEERING CHARACTERISATION OF SINGLE-USE BIOREACTOR TECHNOLOGY FOR MAMMALIAN CELL CULTURE APPLICATIONS

Akinlolu Oyekunle Oluseun Odeleye

A thesis submitted for the degree of Doctor of Philosophy to the University College London

University College London

Department of Biochemical Engineering

2015

I, Akinlolu Oyekunle Oluseun Odeleye confirm that the work presented in this thesis is my own. Where information has been derived from other sources, I confirm that this has been indicated in the thesis.

Signed:

To my Mother, Father and Siblings

Acknowledgements

As I come to the end of my doctoral study, I will take this time to acknowledge and thank those that have contributed to my time and made it a thoroughly fulfilling and positive experience.

I would first like to sincerely thank my supervisor Dr. M. Micheletti, for all of her support and guidance throughout my research. I am truly grateful for all the time and effort she expended in helping me with my research. I am also grateful to my second supervisor Prof. G. Lye for all the support and the ability to put my mind at ease when needed. I would also like to thank both my supervisors for the empathy and understanding shown during difficult periods throughout my time at UCL.

I am thankful to the BBSRC for the financial support provided for my work.

I would like to acknowledge and thank all of my colleagues, friends and the academic staff at UCL for all of their scientific support, advice and guidance. I would like to thank my friends for having the patience to listen to my complaints as well as being there to share the good times. In particular, I would like to thank Patty, Leo, CJ and Rooni among many others. For that I am truly grateful.

Finally, I am deeply grateful to my family for all the love and affection they have provided me.

Abstract

The thesis describes an experimental investigation of the fluid dynamics within novel single-use bioreactors (SUBs), including stirred, rocked and pneumatically driven mixing systems. Biological studies to ascertain the impact of hydrodynamic conditions within these systems, on the growth and protein productivity of a mammalian cell line, are also presented.

Two-dimensional velocity measurements within different SU technology were acquired with the use of a whole flow field laser-based technique, Particle Image Velocimetry (PIV). Fluid dynamic characteristics including velocity, turbulence, turbulent kinetic energy and vorticity were determined from time-resolved and phase-resolved velocity measurements. Commercial bioreactor systems were modified, if needed, in order to perform experiments within bioreactors commonly used for cell culture experiments, in preference to using vessel mimics.

The fluid flow characteristics in both the impeller region and bulk fluid of a single-impeller stirred bioreactor were investigated, facilitating an enhanced understanding of the spatial distribution of velocity and turbulence throughout the vessel. PIV was also used to study the flow in a dual-impeller stirred bioreactor, providing a rare examination of the interaction between the flow fields generated by two impellers. The whole flow field velocity and turbulence characteristics measured within a rocked bag and pneumatically driven vessel, allow a unique insight into the flow pattern and turbulence distribution within two novel cell culture systems.

Cell viability, size, growth, protein productivity and metabolites concentration were monitored under different cell culture operating conditions. Cell culture experiments, combined with the hydrodynamic information acquired using PIV, offer an insight into the physiological response of the cells to highly disparate flow conditions. This information helped to understand how the hydrodynamics induced by novel commercially used mixing systems, can impact upon a mammalian cell line. Having implications for an augmented capacity for cross-compatibility, in addition to enhanced strategies for scale translation and optimal bioreactor design.

Contents

List of Figures

List of Tables

Nomenclature

Roman Characters

B	Baffle thickness, mm
C_1	Clearance of lower impeller from tank bottom, mm
C_2	Distance between two impellers in a dual-impeller stirred tank, mm
C_3	Submergence of uppermost impeller from liquid surface in a stirred tank, mm
C_i	Viable cell concentration on day i of cell culture, cells/mL
D	Impeller diameter, mm
T	Vessel internal diameter, mm
H	Bioreactor height, mm
H_L	Liquid height, mm
IVC_i	Integral viable cell concentration from day 0 to i of cell culture, cells.day/mL
k	Turbulent kinetic energy from time-resolved measurements, $m^2\ s^{-2}$
k_ϑ	Turbulent kinetic energy from phase-resolved measurements, $m^2\ s^{-2}$
k_La	Oxygen transfer coefficient, hr^{-1}
N	Impeller rotational speed (revolutions per second), s^{-1}
P	Power, W
Po	Power number, dimensionless
R	CellReady bioreactor internal radius, m
r	Radial direction distance, m
Re	Reynolds number $(= \rho ND^2/\mu)$, dimensionless
t_i	Elapsed time of cell culture on day i, hours
t_m	Mixing time, s
U_r, U_z, U_θ	Radial, axial and tangential components of instantaneous velocity, $m\ s^{-1}$
$\overline{U}_r, \overline{U}_z, \overline{U}_\theta$	Ensemble-averaged radial, axial and tangential velocity, $m\ s^{-1}$
U_{tip}	Impeller tip speed $(= \pi DN)$, $m\ s^{-1}$
$\overline{U}_{rz}$	Ensemble-averaged magnitude of radial and axial velocity components, $m\ s^{-1}$
$\overline{U}_{\theta,rz}$	Phase-resolved magnitude of radial and axial velocity components at phase θ, $m\ s^{-1}$

u_r, u_z, u_θ	Radial, axial and tangential fluctuating velocity components $(u_r = U_r - \overline{U}_r)$, m s^{-1}
u'_r, u'_z, u'_θ	Root-mean-square (r.m.s.) velocity $\left(u'_r = \sqrt{\overline{u_r{}^2}}\right)$, m s^{-1}
u'_{rz}	Root-mean-square (r.m.s.) velocity (in axial and radial direction) $\left(u'_{rz} = \sqrt{\frac{1}{2}\left(\overline{u_r{}^2} + \overline{u_z{}^2}\right)}\right)$, m s^{-1}
u''_r, u''_z, u''_θ	Radial, axial and tangential turbulent fluctuations $\left(u''_r = U_r - \overline{U}_{\vartheta,r}\right)$, m s^{-1}
U_{Wheel}	Wheel outer circumference speed $(= \pi DN)$, m s^{-1}
V	Volume, m^3
V_L	Bioreactor liquid volume, L
x_r, x_z, x_θ	Radial, axial and tangential distance, m
z	Axial direction distance, m

Greek Characters

ε	Rate of viscous dissipation of the turbulent kinetic energy, m^2 s^{-3}
η	Kolmogorov length scale, m
θ	Tangential direction and phase angle, ^{o}
μ	Dynamic viscosity, kg m^{-1} s^{-1}
ν	Kinematic viscosity, m^2 s^{-1}
ρ	Fluid density, kg m^{-3}
ω_θ	Phase-resolved vorticity around the tangential axis, s^{-1}

Abbreviations

1-D	One-dimensional
2-D	Two-dimensional
3-D	Three-dimensional
ATP	Adenosine Triphosphate
CFD	Computational Fluid Dynamics
CHO	Chinese Hamster Ovary
CIP	Clean-In-Place
CTA	Constant Temperature Anemometry

DE	Direct Evaluation
DOT	Dissolved Oxygen Tension
EDR	Energy Dissipation Rate
GS	Glutamine Synthetase
IA	Interrogation Area
ICH	International Conference on Harmonisation of Technical Requirements for Registration of Pharmaceuticals for Human Use
LDA	Laser Doppler Anemometry
LDH	Lactate Dehydrogenase
LDV	Laser Doppler Velocimetry
mAb	Monoclonal Antibody
mM	Millimolar
mOsm	Milliosmoles
NADH	Nicotinamide Adenine Dinucleotide
PBT	Pitch Blade Turbine
PIV	Particle Image Velocimetry
pg	Picograms
oxPPP	Oxidative Pentose Phosphate Pathway
RO	Reverse Osmosis
rpm	Revolutions Per Minute
r.m.s.	Root Mean Square
RT	Rushton Turbine
SGS	Subgrid Scale
SNR	Signal-to-Noise Ratio
SIP	Steam -In-Place
STR	Stirred Tank Reactor
SUB	Single-Use Bioreactor
TKE	Turbulent Kinetic Energy
vvm	Volume of air per volume of culture per minute
wv	Working Volume

Chapter 1 Introduction

1.1 The context of the research

Single-use bioreactors (SUBs) are systems intended for a single culture/fermentation run, to be subsequently disposed upon completion of the run. In contrast to stainless steel multi-use bioreactors, SUBs are typically manufactured from a multilayer polymer, where polypropylene is often used as the contact layer (Barbaroux and Sette, 2006). The utilisation of single-use technology for syringes, flasks and roller bottles has been widespread since the 1980s. However since the release of the first rocked bag by Wave Biotech US in 1996 (GE Healthcare Life Sciences), there has been an increase in the employment of SUBs in place of traditional stirred tanks at lab to pilot scale, in particular within the upstream processing of mammalian cell cultures (Brecht, 2009). The disposable bioreactor alternative for the culture of mammalian cells offer a number of advantages for bioprocess facilities, including an attenuated risk of cross-contamination and a reduction in the time and costs associated with cleaning, due to the pre-sterilisation procedures applied by the vendor which guarantee sterility (Lim and Sinclair, 2007). In addition, these systems offer a greater degree of flexibility as well as easier handling, and a large portion of savings can arise from a reduced shutdown penalty during the start-up phase (Foulon et al., 2008). Although SUBs offer attractive advantages, there are a number of factors that have precluded their widespread utilisation. These include the limited experience in operating such units, which leads to additional time required to train the workforce to enable the correct operation of the equipment. This difficulty increases at greater bioreactor scales. Single-use cell culture chambers also require the appropriate disposal procedures. Due to the multilayer nature of single-use bioreactor bags, the ability to recycle is limited. For this reason, incineration and landfill are the most common disposal methods for single-use technology (Sinclair et al., 2008). The availability of reliable disposable sensors to measure and control the primary process parameters is also a concern (Rao et al., 2009). The presence and detection of extractables and leachables, both of which can interact with the desired product, represent an additional issue to be acknowledged (Jenke, 2007). Of great importance is the prerequisite of shifting the traditional mind-set of multi-use stirred vessels (with established guidelines and scaling criteria), to novel single-use units

which are not as extensively characterised from an engineering point of view. This knowledge gap regarding the full engineering characterisation of SUBs has significantly limited the widespread adoption of these devices.

The SUB industry is characterised by vessels with a range of mixing mechanisms and bioreactor geometries. There are bag-based, stirred tank and hollow-fibre bioreactors (Eibl et al., 2009), mechanically (i.e. tipping, stirring or vibrating) and pneumatically driven devices such as airlift or slug bubble devices (Terrier et al., 2006). SUBs whose mixing is achieved by either rocked motion or by using a rotating impeller are currently the most employed for the growth of mammalian cells in the biopharmaceutical industry. Issues with large-scale facility fit, bag expenses, supply and the potential impact of SUBs on process and product quality have obstructed the production of larger scale SUBs (Krishnan and Chen, 2012). The reliability of supply chain management and quality management systems have, however, supported the use of single-use technology in commercial manufacturing (Cappia et al., 2014). In the last few years single-use systems have been primarily used to produce seed inoculum for high volume production in traditional industrial scale bioreactors, as well as commercial manufacturing in a development/pilot and GMP environment, of low volume products (Brecht, 2009).

The characterisation of the overall flow regime and turbulence levels for traditional stirred reactors has been well documented. Parameters such as Reynolds number, mixing time, power input and impeller tip speed have been utilised as scale-up criteria for single-use and reusable stirred tank bioreactors. However, these parameters are dependent upon the vessel geometry, including the impeller and vessel diameter. As a result, for culture systems such as orbitally shaken multiwell plates, tube flasks or bags (in which the vessel geometry may vary at different axial and radial locations), the usual parameters cannot be easily applied (Löffelholz et al., 2013).

Mammalian cells, due to their capacity for assembly, correct protein folding and post-translational modifications, have become the dominant host cell type for the production of therapeutic proteins for clinical use in humans. Monoclonal antibodies in particular represent an important class of therapeutics whose benefits to patients have been recognized in the fields of oncology and immunology (Pavlou and

Reichert, 2004; Reichert et al., 2005). Commercial production of these antibodies rely on the development of a robust large-scale cultivation process step. While SUBs represent the cost-effective choice for cell cultivation, to date the ability to optimise and translate the process to larger scales has been rather limited. Rigorous fluid dynamics studies and the definition of appropriate scaling parameters in novel SUB systems are crucial to improve understanding of the effect of the hydrodynamic environment on cellular performance and to ensure the same process and product characteristics are achieved at different scales in line with regulatory demands and Quality by Design approaches (the reader is referred to ICH guidelines Q8, Q9 and Q10 for more information).

Despite the need for detailed information on the whole flow field and localised velocity and mixing characteristics in single-use bioreactors, few studies have focused on the engineering characterisation of these novel devices (Löffelholz et al., 2013). The diversity of mixing mechanisms induced by the bioreactors currently in the market further augments the need for a greater understanding of the hydrodynamic environment experienced by mammalian cells. Fluid dynamic parameters that are both pertinent to cell culture behaviour/performance and applicable to the array of different mixing strategies available on the market is necessary, in order to improve cross-compatibility between bioreactor platforms, as well as greater efficacy in scale-up procedures.

The aim of this project is to characterise novel single-use bioreactors from a hydrodynamic engineering perspective. Subsequently, such knowledge is to be used to understand the impact of fluid dynamics upon the cell culture performance of a mammalian cell line and to inform scale translation. The project comprises fundamental engineering studies aimed at the evaluation of mixing characteristics, fluid flow patterns and shear stress quantification within these novel systems in comparison to conventional bioreactors. This information will be achieved using the non-invasive imaging technique known as Particle Image Velocimetry (PIV). PIV is a laser-based technique that acquires 1-D, 2-D or 3-D instantaneous velocity measurements of a fluid flow system. PIV will facilitate the production of 2-D instantaneous velocity vector maps of the flow within these unit operations, thus enabling much of the engineering characteristics of the fluid to be obtained. In addition, a biological study will be carried out including the development of the

culture and subsequent measurement of the product in order to ascertain the biological impact of the fluid mechanics on cellular growth and productivity. Finally, novel methods in which these technologies can be scaled and compared will be investigated.

1.2 Literature survey

1.2.1 Single-use bioreactor technology

The bioreactor stage is a key component of a whole bioprocess that marks the main starting point with which process optimisation occurs (Löffelholz et al., 2013). Traditionally, glass and stainless steel vessels have been used at the laboratory and pilot scales, including GMP manufacturing across all phases of product development to commercial products. However, the use of fixed plant equipment is costly and time-consuming due to the time required for the installation of vessels, supporting infrastructure and process validation (Oosterhuis et al., 2011). There is also a high burden that results from cleaning validation requirements and maintenance. For these reasons, the utilisation of single-use technology (originally used in the biotechnology field for the processing of blood and blood products) has spread into the biopharmaceutical production arena. Initially used for medium preparation and buffer storage, the technology was then applied to cell culture vessels. Single-use vessels can be rapidly introduced into a manufacturing facility, with reduced expense and time spent on cleaning validation, start-up, shut-down, installation and utilities. The pre-sterilised vessels remove the need for steam-in-place (SIP) or clean-in-place (CIP) operations, and the reduced piping, valve and instrumentation associated, thus allowing for a smaller footprint (Oosterhuis et al., 2011).

Although numerous bioreactor types have been developed in the past few decades, there are specific types of bioreactors that prevail in today's market. Such systems typically consist of a multilayer polymer bag mounted on a metal skid (Barbaroux and Sette, 2006), or of a rigid plastic case moulded to the desired shape and geometry. As mentioned previously, SUBs can be distinguished by their mixing mechanism and/or bioreactor geometry. Understanding the variety of SUBs currently on the market will offer a clear picture of the challenges one faces when utilising

SUBs with such disparate mixing regimes at differing scales. A sample of these bioreactors will be described in the following section.

Rigid stirred tank SUBs have become widely employed for process development and GMP manufacturing for smaller scale production, as their geometrical configuration facilitates process translation to larger scales of operation, and traditional scale-up criteria such as mixing time, power input and/or k_La can be applied. The Mobius® 3 L CellReady was one of the first rigid stirred tank SUBs to be released on the market and has been widely employed for process development. It is part of EMD Millipore's family of Mobius® CellReady SUBs, including 50 L and 200 L vessels suitable for pilot-scale and clinical-scale applications. It has a three-bladed marine scoping impeller, and arrives pre-assembled and sterilised via gamma irradiation. This unit is designed to replace traditional bench-scale glass bioreactors by reducing the assembly time, down time and maintenance time associated with traditional bioreactors. Computational Fluid Dynamic (CFD) analyses of this vessel have facilitated comparability with traditional stirred vessels. An estimated power input of up to 38.3 Wm^{-3} (at N = 250 rpm), impeller power number of 0.3 and dimensionless mixing time (the number of impeller revolutions required to achieve the desired homogeneity) of 34 have been reported by Kaiser et al. (2011a). The fluid flow regime can also be estimated using CFD, with visualisation of the upward-pumping impeller induced compartmentalisation of fluid flow and radial dominance in the impeller ejection zone (Kaiser et al., 2011a).

Single-use stirred-bag bioreactors introduced in 2006, are also commercially available (Brecht, 2009). The working principle behind these bioreactors is akin to that of stainless steel bioreactors. This facilitates the comparability of these units to conventional vessels allowing for process transfer to large-scale facilities (Brecht, 2009). The flexible bags are fixed and enclosed by a stainless steel container, that is also used for temperature control (Kaiser et al., 2011b). This technology has been used primarily for mammalian cell cultures, and has shown results with regards to viable cell density, viability profile, expression profile and analysed product quality comparable to that of conventional STRs (Brecht, 2009). Growth of CHO fed-batch cultures within a Cultibag STR 50 (50 L working volume stirred bag) and BIOSTAT D-DCU 10-3 (10 L working volume glass stirred bioreactor) resulted in peak stationary phase viable cell densities of 26 and 28 $x10^6$ cells/mL, respectively

(Weber et al., 2013). Although single-use stirred bags and rigid vessels allow for the application of known scaling relationships, the same scale-up issues remain. Conventional scale-up parameters rely on physiochemical and geometric similarity (Zlokarnik, 2006), however, given the interdependency of the various factors, one must identify the key parameters that have the strongest influence on protein productivity and cellular growth, whilst ensuring acceptable product characteristics. Pertinent operating parameters such as oxygen transfer, mixing efficiency, mechanical stress, can all (to varying degrees) be correlated to specific power input. However, the shortfall of this approach is that they represent the average condition in a bioreactor system. Therefore, when used to scale-up, localised structures of fluid flow and turbulence levels are not preserved (Kaiser et al., 2011b).

The use of pneumatically driven bioreactors provide the added benefit of combining gas transfer with the mixing mechanism. This reduces the amount of power inputted to the system, resulting in a smaller footprint. The Slug Bubble (SB, Nestle S.A., Switzerland) bioreactor consists of a vertical flexible plastic column filled with medium up to a working volume of around 80%. The agitation and aeration within the system is generated by the intermittent release of large bubbles at the bottom of the column. These bubbles rise through the bioreactor to the top of the cylinder, hence the name slug bubble. The bubbles occupy the cross-section of the pipe, and between the bubble and the cylinder wall is a thin film of liquid. As the bubble flows upward at a constant speed, the liquid flows downward as a falling film. The head of the slug bubble is a stable region, however the rear of the bubble is a region of strong mixing where transfer processes are enhanced. Thus mixing and oxygen transfer are achieved at the same time (Terrier et al., 2006). The application of this system for the cultivation of plant species has produced growth rates comparable to bench-scale (10 L) stirred tanks. Here, tobacco cell cultures were grown to a maximum dry weight of approximately 12 and 14 g/L within 10 L STR and 20 L SB bioreactors, respectively (Terrier et al., 2006).

PBS Biotech's 3 L Pneumatic Bioreactor System (PBS 3), is another system whereby mixing is induced by the buoyancy of bubbles. This mode of mixing again facilitates a smaller footprint, whilst providing the necessary mixing and oxygen transfer for CHO cell growth (Kim et al., 2013). Growth of CHO-S cultures within a 2 L PBS and 1 L STR show comparable peak viable cell densities of $10.6x10^6$ cells/mL and

$9.7x10^6$ cells/mL, respectively. Even though mixing time studies within the PBS scale well between 2 to 50 L vessels, mixing is highly dependent upon, and limited by, the air flow rate. Hence comparability with STRs is also limited given the interdependency of oxygen transfer with mixing efficacy. In addition, traditional scaling parameters such as power input, mixing time and Reynolds number cannot be easily translated from stirred-tanks, as these parameters represent the whole fluid flow environment within the vessel, which may significantly differ at a localised level.

One of the first SUBs introduced for cell culture was Wave Biotech's rocked bag bioreactor, the Wave Bioreactor™. A rocked bag bioreactor comprises of a flexible plastic bag which sits upon a rocking platform; this platform houses the thermocouple that enables temperature control of the bag contents. In operation, the rocked bag is partially filled with media and inflated with air through an inlet filter. The rocking motion produced by the platform induces mixing within the bag and facilitates oxygen transfer. The disposable contact material negates the cleaning requirements including validation, thus significantly reducing costs in cGMP operations. The rocked bag bioreactor system also facilitates rapid installation and utilisation, thus making it auspicious for process development and clinical manufacturing as well as minimising the time to market for biological products (Mikola et al., 2007). A number of sources have noted k_La values of between 10 to 30 hr^{-1} (Mikola et al., 2007), whilst mixing time studies show values of approximately 2-3 mins for scales up to 100 L. This applies particularly to lower rocking rates of below 20 rpm, whilst for culture volumes of over 100 L mixing times can increase significantly with values of up to 5 mins (Oosterhuis et al., 2011).

Many other bioreactor types which for brevity were not mentioned in this section fall into the single-use category including membrane, wave and undertow, in addition to orbitally shaken flasks and wells. These vessels were not included in the study presented, as their mixing mechanisms are not indicative of larger scale processes. So despite the fact that shaken bioreactors are widely used at the small scale for high throughput studies, and larger vessels are beginning to appear (e.g. the Sartorius BIOSTAT® ORB 200); the commercial uptake of such bioreactor types is still limited at large production scales.

Given the traditional utilisation of volume averaged parameters as scale-up criteria for mammalian cell culture, the introduction of vessels with such differing flow structures and hydrodynamic environments adds further convolution to scalability and cross-compatibility. Scaling a rocked bag from 2 L to 2000 L is not a trivial task, given the complex geometry of the vessel and its impact upon the fluid dynamics as the scale increases. Different mixing times, power inputs, k_La values and Reynolds numbers have been measured at a variety of scales (Eibl and Eibl, 2006). In addition, the nutrient and mass transfer distribution effects that any hydrodynamic change would engender and the convoluted multi-phase and boundary layer interactions that occur, will all affect the complexity of characterising these systems. The utilisation of CFD to estimate turbulence levels and fluid flow regimes can be very complicated and time-consuming. Thus, finding a technique that can experimentally quantify fluid dynamics, in addition, to validate CFD simulations is particularly important. One such technique that has been widely used to characterise flow within a mixing vessel is Particle Image Velocimetry (PIV).

1.2.2 Experimental and computational studies in mixing vessels

The accurate measurement of fluid flow characteristics in three-dimensional (3-D) turbulent flows has always been challenging. Furthermore, the presence of a gas phase enhances the system complexity and the difficulty in carrying out the experiments (Aubin et al., 2004). Laser techniques have enabled the acquisition of whole flow field instantaneous velocity vector maps. The measurement of instantaneous velocity is important as it allows for both the mean and turbulent component of velocity to be determined, thus facilitating the calculation of the mean fluid flow regime as well as parameters such as turbulent kinetic energy, energy dissipation rates and Kolmogorov length scales. There have been a number of studies that make use of laser-based techniques to obtain velocity field information within stirred tank reactors (Baldi et al., 2002; Deen and Hjertager, 2002; Gabriele et al., 2009; Hill et al., 2008; Pan et al., 2008 to name a few). However, two-dimensional (2-D) imaging techniques have inevitable resolution limitations depending on the camera field of view and lens properties, as well as dimensional restrictions, making assumptions necessary (Khan, 2005). Spatial fluctuating velocity gradients can be

used to obtain an estimate of the energy dissipation rate (Hinze, 1975), however, consideration must be given to inaccuracies that arise from calculating energy dissipation rates at integral length scales below the actual measurement resolution (Gabriele et al., 2009). It has been demonstrated that techniques such the Smagorinsky Closure Method can be useful in estimating the energy dissipation rate at such scales with a reasonable degree of accuracy (Meyers and Sagaut, 2006). This section will aim to delineate the current understanding and information of flow characteristics within mixing vessels as observed using laser-based investigations, and the attempts to estimate the flow conditions within SUBs using CFD.

A number of impellers are widely used in the biopharmaceutical industry for microbial and mammalian processes. These include Rushton turbine, pitched blade and marine impellers. Rushton turbines are flat-blade radial impellers typically used for cell lines not considered "shear-sensitive", such as yeasts and bacteria (Mirro and Voll, 2009). Both pitched blade (usually inducing both axial and radial flow) and marine impellers (normally producing an axial flow) are widely used for mammalian or other "shear-sensitive" cells. Given its unidirectional flow, k_La values of marine impellers tend to be lower than the bidirectional flow induced by pitched blade impellers (Mirro and Voll, 2009).

The flow in the discharge region of an impeller is characterised by strong velocity fields in the axial, radial and tangential direction, exhibiting periodic fluctuations in velocity and turbulence. The location of the mean active impeller zone is dependent upon the impeller clearance (C_1) from the tank bottom, as well as the fluid discharge angle and the point at which the fluid impinges upon the wall (Bittorf and Kresta, 2000). An increase in the impeller speed is only responsible for an increase in the fluid velocity magnitude, and normally does not substantially change the mean active zone size (Bittorf and Kresta, 2000).

The flow field around a Rushton turbine has been investigated in a number of works using laser-based techniques (Baldi and Yianneskis, 2004; Ducci and Yianneskis, 2005; Micheletti et al., 2004). Schaefer et al. (1997) used Laser Doppler Velocimetry (LDV) to visualise the flow within a Rushton turbine equipped stirred-tank. The 6-bladed turbine was housed by a baffled cylindrical tank with dimensions of $D = T/3$, $H = D/5$, W (blade width) $= D/4$, a clearance of $H/3$ and a tank diameter of $T = 150$

mm. Radial velocities of up to $0.85U_{tip}$ were observed in the impeller ejection zone, with values dropping to $0.15U_{tip}$ above the stirrer. Dimensionless turbulent kinetic energy (TKE) ranged from $0.08U_{tip}^2$ in the impeller zone, to below $0.002U_{tip}^2$ in the bulk fluid away from the impeller. Micheletti et al. (2004) used 1-D Laser Doppler Anemometry (LDA) to study the flow around a six bladed Rushton turbine. The impeller was in a baffled cylindrical tank with dimensions of $D = H/3$, $H = T$, a clearance $C_1 = T/3$ and a tank diameter of $T = 80.5$ mm. In this work, mean radial velocities were found to scale with the impeller speed in the impeller discharge region ($z/T = 0.33$), but did not away from it ($z/T = 0.82$). Sharp et al. (2000) employed 2-D PIV to estimate the energy dissipation rate induced by a 6-bladed symmetric Rushton turbine ($D = 50.8$ mm) within a cylindrical tank of $T = 3D$ and an impeller clearance of $C_1 = T/2$. Spatial turbulent velocity gradients were calculated from the 2-D instantaneous velocity measurements, and (along with the assumption of isotropy) used to estimate the kinetic energy viscous dissipation rate. Two isotropic estimates of dissipation were calculated, one with only the radial turbulent velocity gradient and the second with both the axial and radial turbulent velocity gradients. Disparity between the one dimensional and two dimensional estimates reached up to 70%, although it was expected that this difference would reduce at higher Reynolds numbers (Sharp et al., 2000). Gabriele et al. (2009) took the estimation of energy dissipation rate further, with the application of the Smagorinsky Closure Method to account for the limitation in spatial resolution. These works demonstrate the effectiveness of laser-based techniques to precisely characterise hydrodynamic flow properties, including turbulent kinetic energy, energy dissipation rates and velocity characteristics.

In most cases, PIV is performed in the single liquid phase, so as to avoid any laser distortion caused by the presence of the gas phase. However, in the context of the SUBs, a gas phase within the fluid is imperative to the maintenance and control of oxygen concentration during a cell culture. A few studies have conducted laser-based studies on the impact of a gas phase upon the fluid dynamics within stirred tank reactors. Aubin et al. (2004) investigated fluid flow disparities between single and two-phase systems in a stirred vessel with a 6-bladed pitched blade turbine (45^o) in both upward and downward pumping configurations. The cylindrical tank was 0.19 m in diameter ($T = 190$ mm), with a liquid height of $H_L = 190$ mm, an impeller

diameter of $D = 0.5T$, and an impeller clearance of $C_1 = 0.33T$. The presence of a gas phase did not substantially change the fluid flow pattern, but led to a slight reduction in measured velocities (although an increase in axial velocity in the impeller exit stream was observed). Maximum TKE was found to remain stable within the impeller discharge zone under both aerated and non-aerated conditions. Peak up-pumping impeller discharge TKEs of $0.020U_{tip}^2$ and $0.022U_{tip}^2$ for non-aerated and aerated conditions, respectively, were noted. A maximum TKE value of $0.028U_{tip}^2$ was measured in the down-pumping mode for both aerated and non-aerated conditions. The spatial distribution of TKE was reduced under aerated conditions, with an approximately 50% decrease in TKE occurring in the bulk of the fluid (down-pumping mode), although dimensionless TKE in the bulk fluid of the up-pumping mode were close to zero with and without gas. Furthermore, a large quantity of gas became entrained in the lower circulatory loop in the up-pumping configuration, with gas holdup determined to be approximately 36% greater for the upward pumping investigation (Aubin et al., 2004).

Zhu et al. (2009) studied the impact of aeration at varying flow rates (0.01 to 0.5 vvm) upon the fluid flow and turbulence induced by a 3-bladed 'Elephant Ear' impeller in both up and down-pumping modes of operation. The Elephant Ear impeller was housed by a cylindrical vessel with dimensions; T = 15 cm, D = 0.45T, $T = H_L$, and $C_1 = 0.25T$. In the up-pumping impeller mode, aeration did not significantly affect the peak TKE values (with maximum values of up to $0.025U_{tip}^2$ without gas and $0.0225U_{tip}^2$ with gas, observed in the impeller stream). In the down-pumping flow regime, peak TKE of about $0.0215U_{tip}^2$ is noted in the impeller discharge zone when operated in the single phase, which again is seen to remain constant upon aeration. Even though under aeration the maximum TKE remained constant, the spatial distribution of TKE changed. Below the up-pumping impeller, TKE decreased by as much as 30% at the highest aeration rate compared to the single phase, whilst bulk fluid TKE remained close to zero at all conditions (Zhu et al., 2009). These studies demonstrate the importance of the gas phase upon the fluid flow characteristics, and should be taken into consideration when analysing single-phase data. Fishwick et al. (2005) utilised Positron Emission Particle Tracking technology to show the variations in axial and radial velocity in response to aeration, where a down-pumping pitched blade (six blades at 45^o) turbine in a 100 mm

diameter vessel (with dimensions $H = T = 100$ mm, $C_1 = T/3$, $D = 0.48T$) was susceptible to input of gas, and showed a change to "almost-radial" flow as well as lower velocities upon aeration.

The type of impeller present will have a significant impact upon the bubble breakage efficacy and gas flow pattern, as well as the single-phase flow regime that is developed within a stirred tank. Martín et al. (2008) used CFD studies along with high-speed video techniques to study the hydrodynamics developed by a Rushton turbine, propeller and a concave pitched blade turbine. The flow pattern was observed to lead the gas phase through preferential paths, with bubbles being broken either by deformation due to flow or by direct impact with the blades. The lower the impeller clearance (C_1), the greater the direct effect of the impeller was upon the bubble breakage mechanism. The Rushton turbine maintained the same bubble breakage efficacy regardless of the initial bubble size, with bubbles being retained on the blade until their breakage. The pitched blade impeller caused bubble deformation and resulting breakage due to the flow pattern developed. The impact of a propeller on the gas size distribution was not significant, with the propeller observed deflecting (or redirecting) the bubbles more so than retaining them on the blade and subsequently breaking the bubbles. In this case, bubble deformation, breakage and coalescence was shown to occur during entrainment of the gas phase beneath the propeller (Martín et al., 2008).

Computational Fluid Dynamics (CFD) has been found to accurately predict laminar flow behaviour within stirred tank reactors, if the appropriate velocity boundary conditions are applied around the impeller. However, turbulent conditions may not be as accurately predicted using CFD, leading to an inaccurate description of the large-scale instabilities in the flow that are detected by PIV (Bakker et al., 1996). As well as velocity and turbulence characteristics, the flow pattern and mixing regime is of pertinence to the cells that experience them. The ability to identify poorly or well mixed regions of fluid within a vessel, allows for further optimisation of the hydrodynamic system to which the cells are exposed.

Despite the need for detailed information on velocity and mixing characteristics in single-use bioreactors, few studies have focused on the engineering characterisation of these novel devices (Löffelholz et al., 2013). Kaiser et al. (2011a) used CFD

approaches to determine engineering characteristics such as mixing time, power input and oxygen transfer within the 3 L Mobius® CellReady bioreactor. The marine impeller fitted within this bioreactor was found to produce an up-pumping circulation loop directed 25^{o} above the horizontal plane, with the fluid velocity dominated by its radial component. In addition, gas distribution was found to be significantly heterogeneous, with flooding of the impeller observed (up to an impeller rate of N = 200 rpm). A dead zone of fluid velocity (close to 0 ms^{-1}) was also noted at the drain inlet, which led to cell sedimentation and accumulation in the region (Kaiser et al., 2011a). The Euler-Euler approach was employed to simulate multiphase flow in the work of Kaiser et al. (2011a). However, as a result of assuming uniform bubble size, a variation of approximately 40% was noted when CFD-predicted and measured overall mass transfer coefficients were compared (at 200 rpm and 0.1 vvm aeration).

Löffelholz et al. (2011) used the Volume of Fluid (VOF) model to simulate the fluid dynamics within 2 L and 200 L (1 L and 100 L working volume, respectively) Sartorius Cultibag RM bioreactors. The Cultibag was noted to show a more homogenous dissipation of energy (compared to stirred vessels), with the 200 L bag dissipating energy more homogenously than its 2 L counterpart. The maximum specific power inputs in the 2 L and 200 L bags were estimated at 150 W/m^3 and 250 W/m^3, respectively, whilst the upper 10% dissipation rates were found in volume fractions of between 0.02% and 0.9% of the fluid. Given the larger surface to volume ratio, the 2 L bag was also expected to have higher oxygen transfer. Accordingly, the need to investigate the effect of bag geometry upon the traditional operational parameters (e.g. k_La) used to describe bioreactor performance is evident (Löffelholz et al., 2011).

Investigations into the fluid dynamics within SUBs is not widespread, and typically are conducted using CFD. While several fluid dynamics investigations have utilised Particle Image Velocimetry (PIV) approaches to obtain flow pattern information, velocity field and local energy dissipation rates in a stirred tank reactor geometry, in most cases results were obtained using a reactor mimic. The mimic often had a flat bottom and standard geometry configuration, as opposed to a commercially available bioreactor. Furthermore, the impact of whole flow field characteristics upon cellular behaviour has rarely been investigated.

1.2.3 Bioreactor operating parameters

The overall performance of a bioreactor is strongly dependent on the flow field generated by its mixing mechanism and geometric configuration. The geometric configuration of bioreactors will have a significant impact on the process parameters widely used when characterising and scaling bioreactors, including aeration, mass transfer, power input and Reynolds number among others (Kumaresan et al., 2005). This section will provide a brief introduction to typical operating parameters within single-use bioreactors (including stirred, rocked and pneumatically driven systems), used to describe the conditions experienced by cells. The typical operating parameters used to control the performance of a bioreactor include the volumetric oxygen transfer coefficient (k_La), power input per unit volume (P/V), volumetric gas flow rate per unit volume of liquid, superficial gas velocity, mixing time, impeller tip speed and impeller rotation rate (for stirred tanks) (Ju and Chase, 1992). Bubble size is also of importance, with the potential for cell damage (through bubble rupture) increasing as the bubble diameter decreases (Hu et al., 2011). However these parameters represent the mean flow environment, whilst the cells are responsive to their local environment (Mollet et al., 2007). Categorising the flow structures across a range of SUBs, would be a significant step in understanding the performance differences between varying mixing vessels.

Oxygen transfer is a significant parameter for cell culture applications, and is strongly linked to the mixing efficiency of a given vessel. The efficacy of oxygen transfer within a cell culture is also dependent upon the chosen method of aeration, whether it is bubble, surface membrane or external aeration. The level of aeration is characterised by the volumetric oxygen transfer coefficient (k_La). Although bubble aeration can facilitate greater oxygen transfer, the bursting of these bubbles can be damaging to the cells given the shear stress that they engender. With wave induced mixing, there is bubble-free aeration; thus eliminating a significant deleterious mechanism that the cells are exposed to. It has been demonstrated for the BioWave® and Wave Bioreactor™ that high volumetric oxygen transfer coefficients can be ensured by increasing the rocking rate, rocking angle and aeration rate. At constant parameters, a reduction in the culture volume within the bag, results in an increased specific surface area and power input, and greater k_La values (Eibl et al., 2009).

The wave-induced motion within rocked bag bioreactors is the principle factor for mass and energy transfer efficiency and thus for its aeration and mixing characteristics. Like the oxygen transfer coefficient, the power input can be adjusted manually via the rocking angle, rocking rate, bag dimensions and culture volume. The maximum possible specific power input may be typically achieved using the minimum filling level, maximum rocking angle and rocking rate. Although Eibl et al. (2009) have also shown that up to rocking rates of 20 rpm the specific power input is directly proportional to the rocking rate, when the rocking angle and culture volume are kept constant. As the rocking rate (at maximum culture volume) is increased above 20 rpm, the power input may level out and could be followed by a slight decrease. This behaviour may be explained by a phase shift from wave motion towards rocking movement. It has been observed that a subsequent increase in rocking rate both lowers hydrodynamic stress for the cells, and augments nutrient and oxygen transfer efficacy, thus promoting cell growth (Eibl et al., 2009).

Likewise, within stirred tanks the impeller rate (power input), aeration rate and working volume will all impact upon the oxygen transfer capability of the system. Typically the oxygen transfer coefficient is correlated to the power input per unit volume in the general form:

$$k_L a = c \left(\frac{P}{V}\right)^m U_s^n \qquad (1.1)$$

Where U_s is the superficial gas velocity, and c, m and n are empirical constants (Varley and Birch, 1999). k_La values upwards of 5 hr^{-1} are noted within stirred tanks, with up to 50 hr^{-1} when microsparging is used (Eibl et al., 2009).

Mixing within PBS Biotech's PBS 3 is induced by the buoyancy of bubbles, thus resulting in an overall lower power input (when compared with traditional stirred tanks). Measured k_La values range from 1.62 to 7.66 hr^{-1}, between aeration rates of 0.05 and 0.5 vvm (at the 3 L lab scale) (Kim et al., 2013). Mixing times within the 3 L PBS vessel reduce from 15 to 5 secs, when the aeration is increased from 0.01 to 0.15 vvm (Kim et al., 2013). The mixing performance is limited by the wheel speed and aeration rate allowable by the vessel, although oxygen transfer and mixing characteristics are well within the range required for typical CHO mammalian cell cultures. CFD investigations of the two-phase flow (using the Euler granular model

to determine momentum exchange between the two phases) with a working volume of 10 to 1000 L, indicate a complex flow pattern, with the fluid flow clockwise and velocities reducing to about 10% of the wheel speed at the peripheral regions of the vessel. Enhanced uniformity in regards to the fluid flow characteristics was observed, with a maximum specific energy dissipation rate of $2x10^3$ W/m^3 (10 L wv and 20 rpm) estimated (Löffelholz et al., 2011). This shows the significant variation in hydrodynamic conditions estimated in the PBS (compared with both stirred and rocked vessels), and the need for experimental verification using PIV.

When considering stirred tanks in isolation, power input is indeed a pertinent criteria used to characterise conditions in a stirred tank. With impeller type and diameter in addition to aeration, impacting on the overall power inputted to the system. However, impellers will dissipate energy with disparate levels of efficacy, resulting in a variety of spatial distributions of energy dissipation rates for various impellers. The same can be stated for the pneumatic and rocked bioreactor types described. Furthermore, the vessel/impeller geometry, location and speed have significant effects upon the power input, mass transfer and mixing characteristics. Even with constant geometry upon scale-up, power dissipation mechanisms and local turbulence levels can vary considerably (Aunins et al., 1989), indicating that care should be taken when comparing bioreactors and scaling based on parameters that reflect the mean volume conditions and which were originally designed for stirred microbial systems. Therefore, understanding the whole flow field range of energy dissipation rates inputted to the vessels and their impact upon mammalian cells, can be important for enhancing cross-compatibility between these platforms.

1.2.4 Mammalian cell cultures and hydrodynamic environment

The following section will elucidate the investigations and current knowledge on the impact of fluid dynamics upon cellular behaviour/performance. This includes both the mechanisms of cell death and damage as a result of hydrodynamic stress, in addition to the correlation of measured stress parameters to cellular response.

The importance of a well-mixed environment and the effect of operating conditions on cell growth and productivity have been widely documented (Abu-Reesh and

Kargi, 1991; Cherry, 1993; Kunas and Papoutsakis, 1990, to name a few). High agitation rates in a stirred tank bioreactor have been found to significantly impact cell viability, glucose consumption rates and mAb production of hybridoma cells grown in 15% serum medium (Abu-Reesh and Kargi, 1991). In the aforementioned study, impeller tip speeds of up to 0.4 ms^{-1} were shown to cause a significant drop in cell concentration (with increased lactate dehydrogenase released into the culture), a decrease in mAb concentration and elevated specific glucose consumption rates (Abu-Reesh and Kargi, 1991). A few studies have indicated that cells which are acclimated to high agitation rates are more resistant to the hydrodynamic stresses associated with the impeller rotation than those that are suddenly exposed to an increase in turbulence levels (Petersen et al., 1988; Schmid et al., 1992). In addition, cell physiology plays an important role as cells were found to respond differently to an increase in impeller agitation according to their growth stage (Petersen et al., 1990, 1988). The combination of air flow rate and increasing impeller rates of up to 300 rpm have been found to cause a decrease in stationary phase cell viability of TB/C3 hybridomas from over 95% to approximately 75% (Oh et al., 1989). Sorg et al. (2011) have demonstrated that the gradient of shear stress is also as important as the mean stress that cells experience. In their work, a Lobed Taylor-Couette bioreactor was used to simulate the hydrodynamic stress conditions occurring in the impeller zone of a stirred tank reactor, with mean shear stress values of up to 0.4 Pa. An increase in lactate production and a decrease in antibody titre was observed, whilst consumption of the primary nutrients remained largely unchanged. One of the major operational issues with regards to mammalian cell culture is the cellular response to shear forces (Abu-Reesh and Kargi, 1991; Cherry, 1993; Kretzmer and Schiigerl, 1991). It is generally noted that mammalian cells can physically tolerate the typical hydrodynamic stresses induced by the impeller in the liquid-phase within stirred tank bioreactors (Oh et al., 1989), while the primary cause of physical damage has been attributed to interfacial shear and therefore to air bubble breakage and coalescence during culture (Ma et al., 2002). Therefore, the aim for many of the novel mixing regimes designed into SUBs is to provide an environment that further enhances cellular productivity, whilst maintaining the mixing necessary for optimal cell growth.

Understanding the mechanisms of cell death due to high energy dissipation rates can also facilitate greater understanding of cellular responses to varying conditions. Cell death is a pertinent part of cell culture, which can result from mechanical damage, nutrient depletion, the accumulation of by-products or chemical agents (Krampe and Al-Rubeai, 2010). Two significant forms of cell death are apoptosis (programmed death) and necrosis (passive death). Necrosis results from cell exposure to severe external stress and is indicated by cellular swelling, chromatin digestions and disruption of the plasma membrane. Apoptosis is characterised by cell shrinkage, loss of surface microvilli and subsequent chromatin condensation, membrane blebbing and mitochondrial depolarisation (Krampe and Al-Rubeai, 2010).

Al-Rubeai et al. (1995) investigated the cellular death response of murine hybridoma cells in 1 L batch cultures without gas sparging, to impeller induced energy dissipation rates ranging from 1.5 Wm^{-3} to 1870 Wm^{-3}. A decrease in viable cell concentration was reported at a power input of 320 Wm^{-3}, with the dead cells demonstrating morphological features of apoptosis (whilst necrosis was also a significant observed death mechanism). Once cells were subjected to an energy dissipation rate of 1870 Wm^{-3}, a 50% reduction in cell population was observed within 2 hrs, accompanied by a subpopulation of smaller cells. Cell cycle analysis indicated greater proportions of S and G2 cells becoming apoptotic, along with preferential survival of G1 cells. The difference in flow type, be it simple uniform flows, or oscillating extensional flows, may also have a role to play in relation to cell death mechanisms. Tanzeglock et al. (2009) noted that CHO cells enter an apoptotic pathway when subjected to low levels of shear stress (approximately 2.0 Pa) in oscillating laminar extensional flow, whereas necrotic death dominates when the cells were exposed to hydrodynamic stresses of 1.0 Pa in simple shear flow or approximately 500 Pa within turbulent extensional flow.

Both the level and duration of stress exposure can affect the viability and morphology of (adherent) mammalian cells (Kretzmer and Schiigerl, 1991). Changes in the morphology (increase in spherically shaped cells) of baby kidney hamster cells (BHK 21 c13) were seen at laminar shear forces of 26 Pa, using a custom-made flow chamber. With regards to stress duration, cells exposed to 12 Pa for 3-4 hours were reported to decrease in size and became more rounded (Kretzmer and Schiigerl, 1991). The levels of hydrodynamic forces at which cells exhibit a physical and

metabolic response can vary depending on cell type, the type of flow whether it be laminar/turbulent and the presence of sparged air. Oh et al. (1989) tested the cellular viability, growth and metabolic activity of three murine hybridoma lines (TB/C3 hybridomas, EBNA and HPV grown within bench-scale stirred tanks with both marine and Rushton turbines). Their performance was noted to be independent of hydrodynamic conditions up to tip speeds of 1.4 ms^{-1} and energy dissipation rates of 0.34 Wkg^{-1} (Oh et al., 1989), when tested in the absence of sparged air. Upon the commencement of sparging, the growth of the TB/C3 and EBNA cells was reported to significantly reduce.

There are a number of studies that investigate the energy dissipation rate (EDR) at which cell damage occurs. Ma et al. (2002) noted damage detection of CHO cells flowing through a microfluidic flow channel (4 mL) at 1 x 10^4 kWm^{-3}. Mollet et al. (2007) used a contraction flow device to enable the quantification and simulation of the EDR with which CHO-K1 cells are exposed to. Cell membrane damage of approximately 5-15% was noted for CHO cells subjected to a single pass through the flow device at a power input of 10^8 Wm^{-3} (Mollet et al., 2007). A threshold EDR value of 2.3 x 10^6 Wm^{-3} was found by Godoy-Silva et al. (2009a) to cause lethal damage to CHO cells for a single exposure. In order to summarise the EDR levels determined in literature that have been shown to cause damage to mammalian cells, Ma et al. (2002) constructed a graph of EDR levels and the associated response of mammalian cell lines collated from various studies. This data is summarised in the Tables 1.1 and 1.2 below:

Cell Type	EDR (W/m^3)	Mode of Growth	Reference
CHO-K1	$1x10^3$	Anchorage	(Gregoriades et al., 2000)
Hybridoma	$7x10^6$, $2x10^7$	Suspended	(Thomas et al., 1994; Zhang et al., 1993)
MCF-7	$2x10^7$	Suspended	(Ma et al., 2002)
Mouse myeloma	$2.6x10^7$	Suspended	(McQueen and Bailey, 1989)
HeLa S3, mouse L929	$5x10^7$	Suspended	(Augenstein et al., 1971)
CHO-K1, SF-9, HB-24	$9x10^7$	Suspended	(Ma et al., 2002)

Uninfected and viral infected PERC6 cells	$2x10^8$	Suspended	(Mollet et al., 2007)

Table 1.1: Summary of reported energy dissipation rate at which cells are damaged, adapted from Ma et al. (2002).

Process	Description	EDR (W/m^3)	Reference
Agitation	Volume average in typical animal cell bioreactors.	$1x10^1$	(Varley and Birch, 1999)
Agitation	Volume average in a 10 L mixing vessel (RT 700 rpm)	$7x10^2$	(Zhou and Kresta, 1996)
Agitation	Maximum in the 10 L mixing vessel (RT 700 rpm)	$9x10^4$	
Agitation	Volume average in a 22,000 L mixing vessel (RT, 240 rpm)	$2x10^4$	(Wernersson and Tragardh, 1999)
Agitation	Maximum in the 22,000 L mixing vessel	$9x10^4$	
Agitation	Maximum in a spinner vessel (200 rpm)	$1.25x10^3$	(Venkat, 1995)
Bubble rupture	Pure water, bubble diameter: 6.32 mm	$9x10^4$	(Garcia-Briones and Chalmers, 1994)
Bubble rupture	Pure water, bubble diameter: 1.7 mm	$2x10^7$ to $4x10^8$	(Boulton-Stone and Blake, 1993; Garcia-Briones and Chalmers, 1994)
Flowthrough pipe	Pure water, 100 mL/min, 1 mm diameter	$9.5x10^3$	(Mollet et al., 2004)
Flowthrough a micropipette tip	Flowthrough a 200 µL micropipette tip in 0.2 sec	$9x10^4$	(Mollet et al., 2004)

Table 1.2: Summary of energy dissipation rate levels in various bioprocess environments, adapted from Ma et al. (2002).

The findings discussed in the previous paragraph leads on to the question of how the repetitive exposure to increased EDR may affect mammalian cells. In addition to the quantification of EDR, the broadness of EDR values throughout the bioreactor may also play an important role. The chronic exposure of CHO cells to both high and low EDR within stirred tanks versus the more uniform distribution of the EDR akin to wave induced bioreactors has been shown to engender a higher production of lactate

in the latter condition (Sorg et al., 2011). Godoy-Silva et al. (2009a) determined the EDR exposure level of $2.3x10^6$ Wm^{-3} that resulted in lactate dehydrogenase (LDH) release was the same for both single and repetitive exposure of CHO cells to a high EDR microfluidic device ("torture chamber"). Furthermore, the increase in LDH at EDR levels of up to $6.4x10^6$ Wm^{-3} did not correlate with a reduced viable cell concentration (VCC), viability or product titre, but with a reduction in the average cell diameter (Godoy-Silva et al., 2009a). Perhaps suggesting selective survival of smaller cells and death of larger ones (Godoy-Silva et al., 2009a). This finding, however, is in contrast to Godoy-Silva et al. (2009b)'s results showing that in the same torture chamber (TC), CHO-6E6 cells exhibited LDH release at $2.3x10^6$ Wm^{-3} which was accommpanied by a reduction in cell viability and VCC. This demonstrates the importance of the cell line, when considering cell culture response to hydrodynamic conditions.

The question of how fluid dynamics can be used to enhance cell culture performance is yet to be fully answered. Although there are studies aimed at investigating the sensitivity of cells to stress values, it is difficult to compare because cellular response is also dependent upon other factors that affect the flow field, including the length of stress exposure time, the presence of protective additives and the cell line (Garcia-Briones and Chalmers, 1994). Protective additives incorporated within cell culture media, have been shown to induce both an increase and decrease in the oxygen transfer coefficient, depending on the additive (in this case Pluronic F68) concentration (Sieblist et al., 2013). The fluid dynamics within most systems are characterised by parameters that are dependent upon the geometric characteristics of the system used, i.e. mean power input, impeller tip speed or Reynolds number. However these parameters represent the mean flow environment, and as mentioned, the cells are responsive to their local environment (Mollet et al., 2007). Determining a parameter that can be universally utilised within bioreactors that exhibit disparate mixing regimes will be imperative in elucidating the impact of fluid dynamics. Such a parameter could be the energy dissipation rate (EDR). EDR is intrinsic to any moving fluid; whilst being independent of the flow regime, it accounts for both shear and extensional components of 3-dimensional flow (Godoy-Silva et al., 2009b). Although the specific mechanisms by which metabolic behaviour may be affected by hydrodynamic forces is unclear, the accurate quantification of this and other

parameters for a number of mixing conditions is necessary, and will enhance the ability to compare different fluid flow conditions.

1.3 Main conclusions of the literature survey

The increase of SUB utilisation in bioprocessing for cell culture and the presence of a wide variety of new technologies has attracted attention from the scientific world, although the number of publications on SUBs still remains small in comparison to current literature on traditional bioreactors. SUBs have many advantages and represent an attractive alternative for production facilities. However, accurate characterisation of these systems is still limited. There are very few studies aimed to compare different systems, and these have rarely been linked to cell culture performance and productivity. This has been partly due to the difficulties of the hydrodynamic characterisation of SUBs, because of the variety of novel geometries and mixing mechanisms available. However, improving this knowledge base would further increase the current understanding of cellular behaviour, and hence provide improved scalability and cross-compatibility; facilitating further process optimisation and expedited translation of biopharmaceutical discoveries to market.

Numerous laser-based investigations have been undertaken to characterise the flow within stirred vessels. These reactors are typically mimics of the original tank, manufactured to improve optical accessibility of the system, and so may not fully represent the real system. Laser-based techniques have been substantially applied to the flow field generated by Rushton, propeller and pitched blade impellers, with velocity fields, turbulence and vorticity among the many parameters derivable from the instantaneous velocity datasets. The estimation of the dissipation rate of turbulent kinetic energy has been hampered by limitations in the resolution capabilities of equipment used. The resolution necessary to measure the spatial variation of turbulent velocity at the Kolmogorov scale, make assumptions such as isotropy a requirement (Khan, 2005). In addition, the variety of numerical techniques used in literature to compensate for this limitation, precludes the ability to compare this important parameter between different investigations (Gabriele et al., 2009; Micheletti et al., 2004). Studies regarding the whole flow field fluid dynamics within stirred vessels, have rarely been applied to single-use bioreactors. A limited number

of studies have been conducted using CFD to characterise single-use stirred vessels (Kaiser et al., 2011b), however even fewer have been applied to rocked bag and pneumatically driven systems. For this reason, the experimental determination of whole flow field velocity characteristics are pertinent for both enhanced process understanding, and the ability to cross-validate attempts to simulate the fluid dynamics within novel current and future single-use bioreactors.

The importance of the fluid dynamics in which cells are cultured is evident within the current literature. The physical impact of turbulence and bubble breakage/coalescence upon mammalian cells has indeed attracted interest. However these studies are restricted to determining the extreme conditions that cells are able to tolerate, with threshold values of EDR noted for a variety of cell types (Mollet et al., 2007). Very few studies have taken into account the fluid dynamics within stirred vessels, and rarely looked at flow structures with varying levels of turbulence and oxygen entrainment, and how these affect biological performance. Similarly with bioreactor operating parameters, as mentioned previously, these typically describe the average flow conditions. Given that cells are responsive to their local environment, greater understanding of the various flow structures exhibited within SUBs currently on the market, is important.

1.4 The present contribution

The fluid dynamics within traditional glass/stainless steel stirred vessels has been investigated using laser-based techniques. However, these studies have not been extensively applied to commercially available bioreactors and to the latest SUB types in particular. For this reason, Particle Image Velocimetry investigations were carried out in this work for a range of SUBs, motivated by the lack of data in literature on the flow characteristics within these novel systems. Due to the reliance upon mean parameters such as Reynolds number, power input and k_La, for scale-up procedures, whole field velocity and turbulence levels were acquired, to augment understanding of the local environment experienced by the cells. The dissipation rate of turbulent kinetic energy, vorticity and Reynolds stress were all determined, and an effort was made to compare these parameters across the multiple systems studied. In

addition to single and double-impeller stirred bioreactors, these studies were also applied to pneumatically driven and rocked bag bioreactors.

A custom-manufactured rocked bag mimic was produced by machining a digitise plaster impression of a 2 L bag into two blocks of cast acrylic (Perspex). A specially-made rocking platform for the rocked bag mimic enabled accessibility for the laser. In addition, an optically accessible version of the 2 L UniVessel® SU bioreactor was designed and sent to Sartorius Stedim for manufacture. These constructions allowed enhanced optical accessibility necessary for PIV studies. Whilst ensuring the fluid flow regime represented the conditions during cell culture as closely as possible. Phase-resolved measurements facilitated visualisation of flow development throughout the periodic rotation of impellers within the stirred bioreactors and rocking motion of the rocked vessel. Thus allowing for further decomposition of the flow structures present throughout the agitation and its effectiveness.

Operating parameters essential to the mixing characteristics, such as agitation speed and fluid working volume were investigated to analyse their impact upon flow characteristics. Mammalian cell cultures were conducted in order to correlate hydrodynamic conditions, to cell culture performance. Cell growth characteristics, protein productivity and metabolite concentrations were all investigated in order to further understand the differences in performance induced by the fluid dynamics.

1.5 Outline of the thesis

The remainder of this thesis comprises eight chapters. Chapter 2 delineates the bioreactor geometries and configurations, along with the experimental techniques used to determine the velocity and turbulence characteristics within the fluid. In addition, cell culture and protein analysis materials and methods are described.

Chapter 3 presents the results of PIV and cell culture analysis using the Mobius® CellReady bioreactor. This vessel has a total volume of 3 L and houses a single up-pumping impeller. In this chapter the impact of varying Reynolds number upon the fluid flow characteristics within the vessel is reported.

The hydrodynamic environment induced by a double-impeller configuration (Sartorius UniVessel® SU as determined using PIV is reported in Chapter 4. Similar

to the study in Chapter 3, the influence of impeller rotational rate on whole flow field characteristics is investigated. A purpose-built vessel with improved optical accessibility (Sartorius, UK) was designed and used for the investigation.

Chapter 5 introduces a pneumatically driven bioreactor, PBS Biotech® PBS 3, with a novel AirWheel™ mixing system. PIV was used to elucidate the flow regime, turbulent kinetic energy and energy dissipation rates at varying wheel rotation rates.

The Sartorius BIOSTAT® Cultibag RM was investigated using PIV in Chapter 6. Here a custom-made Perspex mimic of the bioreactor bag is manufactured to enable optical access for the PIV laser. The fluid dynamic characteristics were determined at different angles during the rocking motion. In addition, the influence of fluid working volume upon the energy dissipation rates and turbulence levels was studied.

Chapter 7 shows the impact of differing fluid dynamics upon the performance of an antibody producing mammalian cell line. Cellular growth, protein productivity and metabolite concentration were all investigated for both the CellReady and Sartorius Cultibag RM.

Chapter 8 aims to compare the fluid dynamic data obtained within the differing SUBs using PIV, to correlate flow characteristics and parameters between the different systems studied.

Finally Chapter 9 presents a summary of the main findings of this work, in addition to recommendations for future work.

Chapter 2 Materials & Methods

2.1 Bioreactor configurations

This chapter will describe the vessel configurations used in this work, the experimental techniques used to carry out the engineering investigations, as well as the cell culture methods and related analytical techniques. The fluid dynamic characterisation of the bioreactors was conducted using Particle Image Velocimetry. PIV is a laser-based method (described in further detail in Section 2.2) that enables 2-D whole flow field measurement of instantaneous velocities within a fluid. PIV measurements were as much as possible, acquired within the actual commercially available single-use bioreactors. In two cases, a custom-made mimic of the bioreactor was constructed in order to enable adequate optical access for the laser and to reduce laser refraction. Cell culture experiments were conducted within both single-use and traditional glass stirred tank bioreactors.

The Millipore Mobius® 3 L CellReady employed in the PIV measurements and cell culture experiments, is an unbaffled stirred tank made of polycarbonate, marketed by Merck Millipore for cell culture process development experimentation. Equipped with a three-blade marine scoping impeller, the vessel is available pre-assembled and sterilised via gamma irradiation. Figure 2.1 displays an image of the 3 L Mobius® CellReady (Fig. 2.1a), a schematic representation of the bioreactor with the measurement area shaded (Fig. 2.1b) and a horizontal top-down view of the laser and CellReady system (Fig. 2.1c). The CellReady has an internal tank diameter T = 137 mm and height H = 249 mm. The marine scoping impeller diameter D = 76.2 mm is located near the bottom with a clearance C_1 = 30 mm from the base. The PIV investigations were performed without dissolved oxygen (DO), pH and temperature probes, normally present within the bioreactor during operation. Whilst the probes would possibly affect the flow field, it was difficult, if not impossible to carry out PIV measurements with the probes inserted as they would considerable obstruct the field of view. Given that the actual vessel was used, it should be noted that certain areas of distortion and optical inaccessibility are inevitably present, due to the curvature of the base and the grooves by which the vessel is attached to its base support.

The Sartorius UniVessel is a double impeller stirred tank bioreactor with a working volume range of 0.6 to 2.0 L, whilst the total volume of the vessel is 2.6 L. The cylindrical vessel has a concave base and houses two down-pumping 3-bladed pitched (30^o) segment impellers. The clearance of the lowest impeller from the base is C_1 = 47.3 mm. The vessel and impeller dimensions are D = 54 mm, T = 130 mm, H = 242 mm along with an impeller shaft thickness of 15 mm. A custom-made replica of the 2 L UniVessel was designed and manufactured by Sartorius specifically for this project. The main changes made concerned the presence of a detachable lid (to allow easy cleaning and liquid transfer) and the removal of sample lines which would have obstructed considerably the optical access. A schematic diagram of the vessel along with its dimensions is given in Figure 2.2.

PBS Biotech's 3 L bioreactor is a pneumatically driven bioreactor with a rigid hard polycarbonate body. The mixing is induced through the buoyancy of bubbles, whereby gas bubbles are captured in the air-cups located around the circumference of the AirWheel^{TM}. The rotating wheel provides mixing to the fluid without any other external mixing device (Kim et al., 2013). The bioreactor has a working volume of up to 2.5 L, and its dimensions are height H = 275 mm, liquid height H_L = 176 mm, width W = 100 mm, length L = 175 mm and the AirWheel^{TM} outer diameter D = 130 mm. A schematic diagram of the vessel along with its dimensions is given in Figure 2.3. No probes or tubing were used in the vessel during PIV data acquisition in order to reduce any laser light distortion or refraction due to obstacles.

The Sartorius Cultibag RM (shown in Figure 2.4) is a rocked bag bioreactor with a stated 2 L total volume and 1 L working volume. It was necessary to construct a purposely built Perspex mimic of this vessel in order to obtain the optical access required for PIV studies. In addition, a mimic of the rocking platform was built, to enable mounting of both the Cultibag mimic and the camera. The platform needed to allow clear access for the laser light sheet. The platform was constructed with the full range of rocking capabilities as the original Sartorius platform i.e. rocking rate of 8 to 42 rpm and rocking angle of 4.5 to 10^o.

The height of an actual inflated bag is H = 75 mm, the width W = 260 mm and the length L = 310 mm. The base of the bag that was in contact with the rocking platform has a width and length of 155 and 175 mm, respectively. The bag is made

of a multilayer film with pharmaceutical grade low density polyethylene (LDPE) as the contact layer. An image of the vessel along with the control tower is displayed in Figure 2.4. The bag mimic was constructed out of Perspex, with the shape of both the top and bottom half of the bag machined into two Perspex blocks. In order to obtain an accurate description of the bag surface, an actual 2 L Cultibag was filled with plaster of Paris (approximately 3 L was added), until the shape of an inflated bag was attained. This was then allowed to set until it was hardened. Once set, the original Sartorius bag was stripped from the mould. The mould was then sent to be digitised and codified. The codified Cultibag shape was then used to machine the shape of the Cultibag into two blocks of Perspex which combined have dimensions; height H = 130 mm, width W = 350 mm and length L = 400 mm. An image of the Perspex mimic is displayed in Figure 2.5.

Cell culture experiments were also conducted using a Sartorius BIOSTAT® 5 L bioreactor. The bioreactor has a 3.5 L working volume (5 L total volume) and houses a three-blade segment pitched (45^o) impeller. The vessel and impeller dimensions are D = 76.7 mm, T = 160 mm, H = 350 mm. The dimensions of each of the stirred vessels investigated in this thesis are shown in Table 2.1.

Table 2.1: Sartorius BIOSTAT® B-DCU, Mobius® CellReady and Sartorius UniVessel® SU bioreactor and impeller dimensions

Bioreactor	Sartorius BIOSTAT® B-DCU	Mobius® CellReady	Sartorius UniVessel® SU
Vessel Height (H)	350 mm	249 mm	242 mm
Vessel Diameter (T)	160 mm	137 mm	130 mm
Impeller Diameter (D/T)	0.44	0.56	0.42
Blade clearance (C_1/T)	0.50	0.22	0.36

2.2 PIV system and data processing

2.2.1 Particle Image Velocimetry system

The experimental setup of a PIV system consists of a laser, a high speed camera and tracer particles. The tracer particles are added to the flow that is to be studied, with the assumption that these particles will faithfully follow the single-phase fluid flow regime. A laser light sheet is used to illuminate the flow on the plane of interest. The

laser sheet is produced in rapid pulses at user-specified time intervals. The light scattered by the particles is recorded in a sequence of frames using a high-speed camera, and the displacement of the particles between the image frames can be determined through a cross-correlation algorithm. A description of this process is shown in Figure 2.6. The time difference between the light pulses is typically smaller than the time-scale of the system to allow for a reasonable particle displacement to occur (within the image frame dimensions). These displacement measurements (along with the known time difference between each image pair) can then be used to produce velocity measurements for the fluid flow in the target area. Sophisticated post-processing procedures are then used to evaluate the large amount of data that can be produced from the PIV system (Raffel et al., 2007).

The analysis of the digital PIV recordings are divided into small sub-areas called "interrogation areas". Statistical methods such as auto- and cross-correlation are used to determine the local displacement vector for the images of the tracer particles from the first and second illumination. It is also assumed that all particles within an interrogation area have moved in the same direction between two laser pulses.

Both time-resolved and phase-resolved measurements were performed. Time-resolved PIV refers to the acquisition of instantaneous vector maps at a set frequency (e.g. 50 Hz), over a period of time. Phase-resolved PIV measurements involves synchronisation of the laser and camera equipment with a trigger signal, usually from the motor encoder, thus allowing the acquisition of instantaneous vector maps at a set position (i.e. at a specific angle with respect to the leading impeller blade, or to the location of the rocking platform).

2.2.2 PIV system components

A Dantec Dynamics PIV system was employed to measure velocity characteristics. Two 50mJ DualPower 50-100 (Nd:YAG) lasers were used to provide a light sheet at a wavelength of 532 nm at up to 100 Hz. A SpeedSense 1020 camera with a frame rate of 170 Hz and a full resolution of 2.3 x 1.7k was used. The camera included a Nikon F = 60 mm f2.8 lens with data storage direct to the PC hard disk. A timer box, an Allen-Bradley (Ultraware 3000) motor, encoder and trigger system along with 4 x 10 Bayonet Neill-Concelman connectors (BNC) were used to synchronise the laser

pulses and trigger the SpeedSense 1020 camera. The Allen-Bradley motor was used for the stirred systems only. Data was stored on a HP Compaq DC7800 desktop with an Intel® Core™ 2 Quad CPU, Q6600 @ 2.40 GHz. 8 GB of RAM, 64-bit operating system and 1.2 TB RAID disk array. The DynamicStudio software was used to process the raw images captured by the camera. Each velocity vector was determined from a 16x16 pixel interrogation area.

The particles used in this project are silver-coated hollow glass 10 µm spheres. The choice of particle size is a balance between particles with an adequate response to the fluid motion, and light scattering with a high signal-to-noise ratio for which larger diameters are necessary (Melling, 1997).

2.2.3 PIV acquisition & initial post processing

The acquisition and processing software used was DynamicStudio which includes, automatic device detection, distributed acquisition, camera support, image stitching and image processing library. In addition, the 2-D PIV software and validation package includes adaptive PIV correlation and vector processing capabilities such as vorticity calculation (Dantec, 2010).

Cross-correlation peak analysis of PIV images showed SNR (signal-to-noise ratio) values greater than 5 and in most whole flow field locations greater than 10. This is greater than the SNR threshold of 2 used by Aubin et al. (2004) and Zhu et al. (2009) to distinguish between valid and invalid correlation peaks. Initial time-resolved PIV experiments involved establishing the appropriate acquisition frequency rate. Laser/camera acquisition was varied from 10 Hz up to 50 Hz (in 10 Hz increments) and analysed accordingly. Slight increases in maximum fluid velocity were noted as the acquisition rate was increased. It was thus deemed appropriate to acquire data at the highest achievable acquisition rate, to maximise the number of vector maps obtained throughout an impeller revolution. Data acquired at acquisition rates greater than 50 Hz were not achievable due to the camera limitation and the resulting quality of the second frame.

The initial analysis of PIV images obtained in different bioreactor systems, was carried out according to a sequence of similar steps. Adaptive correlation was used to produce the initial instantaneous velocity vector maps from the image pairs. With

this technique, multiple cross-correlation calculations are performed, whereby each previous pass is used to improve the accuracy of the next calculation. The interrogation area (IA) of frame 2 of the second pass is offset according to the results of the first pass. This helps to improve spatial resolution and the dynamic range of measurements compared with traditional cross-correlation methods (Dantec, 2010).

In an attempt to remove areas of reflected light and obstructions during the UniVessel acquisitions, an additional peak validation step was added to the initial adaptive correlation whereby a minimum ratio criterion of peak height 1 to peak height 2 was set at 1.2. This is a value typically used during PIV investigations (Dantec, 2010).

Adaptive PIV was performed for Cultibag RM experiments. This method iteratively optimises the size and shape of each interrogation area in order to adapt to local flow gradients and seeding densities. This was chosen to optimise detection of any flow structures that develop within the fluid. A grid step size of 8x8 pixels was used, with an interrogation area (IA) size of 16x16 pixels and 50% IA overlap.

The velocity vectors measured using PIV can be prone to "outliers". These "outliers" degrade the quantitative information within the velocity field and can show misleading information with regards to the velocity derived quantities. Outliers originate from interrogation areas that contain either insufficient or noisy correlated particle images. A number of factors can play an imperative role in the production of outliers i.e. inhomogeneous seeding of particles, low signal-to-noise ratio of the images, fluctuating light pulse intensity and laser reflection. These “outliers” can be seen as comparatively large velocity vectors within the vector image. In order to detect and remove these vectors, it was necessary to validate the initial adaptive correlation vector maps. Special algorithms that work automatically were used for this task. The ‘range validation’ feature present in the Dantec Dynamic Studio suite was used for this purpose, to remove vectors that lay outside of a specified range (Dantec, 2010). A range validation criteria equal to the known tip speed during acquisition was adequate to remove clearly erroneous (too large) velocities. A subsequent moving average validation step can remove velocities that are within the specified validation range, but are not congruent with their surrounding fluid velocities (as well as the spatial location with which they occupy).

In order to produce a complete set of equally spaced vectors, any outliers removed previously need to be replaced (Raffel et al., 2007). This can be achieved by performing a moving average validation step, which calculates the average of the vectors surrounding a given vector and compares this average value to the central vector. If the difference between the given vector and the average of its surrounding vectors is greater than a certain value (the acceptance factor) then that vector is rejected. The rejected vector may be replaced by a local average of its neighbours (Dantec, 2010). This step also serves to produce a smooth flow structure. A 9x9 moving average validation was conducted, with an acceptance factor of 0.18 and 3 iterations.

MATLAB was used in this work to apply fluid dynamic calculations, and to represent the numerical information acquired using PIV in the form of contour/vector plots.

2.3 Stirred tank velocity measurements

2.3.1 PIV experimental set-up & data acquisition

3L Mobius® CellReady

A cylindrical coordinate system was used to describe the acquired data from the CellReady, with the radial, axial and azimuthal coordinates indicated in this work by r, z and θ, respectively. The systems origin is located in the centre of the bioreactor bottom and $\theta = 0^{o}$ corresponds to the vertical plane intersecting the centre of the blade. The impeller and shaft were painted with fluorescent paint FP R6G (red in colour), which has the property of absorbing green light (in particular Nd:YAG 532 nm light). This ensured a reduction in laser light scattering and reflection. The detachable base of the CellReady was attached to the base of a glass tank (with dimensions of 40x40x40 cm) using a multipurpose silicone adhesive. The CellReady bioreactor was attached to its detachable base and the glass tank filled with water, in order to minimise errors due to refraction/diffraction of the laser on the CellReady's cylindrical surface. The bioreactor was filled with RO water and seeded with 10 µm silvered hollow glass tracer particles. RO water was deemed appropriate as a model fluid because the glucose concentration of CD-CHO media and the cell density

attained during cell culture would not significantly increase the culture viscosity above that of water (Chimica et al., 1999; Clincke et al., 2013). The tank was positioned so that the light sheet was perpendicular to the surface of the tank. The camera was thus positioned to face the light sheet plane of view in order to capture the measurement area (as shown in Figure 2.1b).

Measurements were carried out for a range of impeller speeds from N = 80 to 350 rpm, corresponding to Reynolds numbers Re = 8,699 to 38,057, at constant bioreactor fill volume equal to 2.4 L. The laser light sheet was aligned so as to intersect the centre of the impeller shaft, thus illuminating one half of the CellReady in the vertical plane. Both time and phase-resolved measurements were acquired. In order to carry out phase-resolved measurements the camera and laser were synchronised to the rotation speed of the impeller, and set to collect images once per revolution at the required angular position. Angular positions from $\theta = 0^o$ to 105^o in 15^o intervals, were investigated at different rotational speeds. An angle of $\theta = 0^o$ corresponds to the vertical laser light sheet intersecting the mid-point of the leading impeller.

For each condition 250-500 image pairs were taken to produce instantaneous velocity vector maps. Root-mean-square velocity values for both 250 and 500 vector maps were compared in order to test statistical reliability, resulting in a difference of less than 1%. These were then collated and analysed using a developed MATLAB code to determine fluid dynamic characteristics.

Sartorius UniVessel® SU

The 2 L UniVessel was investigated attached to the base of a glass tank filled with water. Instantaneous images were taken in the vertical plane. A cylindrical coordinate system was used, with the radial, axial and azimuthal coordinates indicated in this work by r, z and θ, respectively. The origin of the coordinate system is located in the centre of the bioreactor bottom and $\theta = 0^o$ corresponds to the vertical plane intersecting the centre of the blade.

Measurements were carried out for impeller speeds N = 200, 250, 300, 350 and 400 rpm, which correspond to Reynolds numbers Re between 10,904 and 21,808, at a constant bioreactor fill volume of 2 L. The laser light sheet was aligned so as to

intersect the centre of the impeller shaft, thus illuminating one half of the UniVessel in the vertical plane. Both time and phase-resolved measurements were acquired. In order to carry out phase-resolved measurements the camera and laser were synchronised to the rotation rate of the impeller, and set to collect images once per revolution at the required angular position. Angular positions from $\theta = 0^o$ to 105^o in 15^o increments, were investigated at different rotational speeds. An angle of $\theta = 0^o$ corresponds to the vertical laser light sheet intersecting the mid-point of the leading impeller.

For each condition 500 image pairs were taken to produce instantaneous velocity vector maps. Phase-resolved measurements were acquired at impeller speeds of 200 and 400 rpm whilst time-resolved measurements were obtained at rotational speeds between 200 and 400 rpm in 50 rpm increments.

2.3.2 Sources of error & uncertainty

A number of sources of error must be considered when carrying out PIV experiments. Laser alignment is a very pertinent source of error uncertainty when conducting PIV measurements. The laser was fired at a reduced intensity and aligned with the glass tank and bioreactor impeller shaft (via visual inspection) prior to any acquisition. A spirit level was used to ensure that all components of the experiments were precisely horizontal. With regards to phase-resolved acquisitions, the light sheet was aligned to a marked position on the centre of an impeller blade. This was achieved by rotating the impeller at 1 rpm and carefully aligning the light sheet to the marker whilst controlling the impeller rotation. Manual alignment of the laser is a predicted source of error. Subsequent phase-resolved angular positions were obtained by adjusting the time delay of the laser emission (determined using the known impeller rotation rate and the time taken to complete one revolution). The timing of phase-resolved image pair acquisitions, was measured to be accurate to three decimal places of a second

2.4 Pneumatic bioreactor velocity measurements

2.4.1 PIV experimental set-up & data acquisition

The PBS 3 vessel has a rectangular base and therefore PIV experiments carried out in this system did not need to enclose the vessel in an external trough to minimise distortion. The laser light sheet was fired vertically and aligned to intersect the mid-point of the AirWheel^{TM}. The radial and axial coordinates are indicated in this investigation by *r* and *z*, respectively. Within the presented figures, the liquid height and vessel length are denoted as H_L and *L*, respectively. The systems origin is located at the bottom right of the vessel. The bioreactor was filled with a 2.5 L working volume and data was acquired at 20, 27, 33 and 38 rpm (*Re* = 6,194, 8,574, 10,371 and 11,870), corresponding to air flow rates of 100, 200, 300 and 400 mL/min, respectively. Time-resolved measurements were acquired for the PBS 3 at a frequency of 50 Hz. 250-500 image pairs were taken at each wheel speed investigated.

2.4.2 Sources of error

The spinning AirWheel^{TM} located inside the PBS 3 causes reflection and refraction of the light. This caused slight variation of the light intensity in the half of the bioreactor furthest away from the laser. The variation in the observed laser light intensity is a predicted source of error.

The air used to induce flow within the bioreactor was supplied by a 200 bar cylinder of compressed air (BOC Ltd, size: V) and controlled by a pressure valve and rotameter. The speed of the AirWheel^{TM} was measured using a magnetic RPM detection sensor (MD-BEST) that measured the frequency with which the magnet positioned on the AirWheel^{TM} rotated. Wheel rpm values were noted to vary by -/+ 0.5 rpm during operation.

2.5 Rocked bag velocity measurements

2.5.1 PIV experimental set-up & data acquisition

The fluid dynamics within a custom-built mimic of the Sartorius Cultibag RM bioreactor was investigated using PIV. The laser light sheet was positioned beneath the rocking platform in the vertical plane and aligned to the rocking axis. Given the size of the platform and camera, it was necessary to position the camera parallel to the plane of interest and facing a mirror positioned to view the measurement area.

A Cartesian coordinate system was used, with the radial and axial coordinates indicated in this investigation by *r* and z, respectively. The height and length of the acquired vector maps are indicated by *H* and *R*. *R* represents 50% of the Cultibag cavity total length. The platform angle relative to the horizontal ground is indicated by θ. The laser light sheet was positioned 8.5 cm from the outer edge of the mimic bag shape. The systems origin is located in the centre of the bioreactor length at the bottom (inner surface) of the mimic. The Perspex mimic was filled with 1.75 L of RO water, which corresponded to 50% of the working volume of the mimic. The orientation of the platform/mimic was determined by a gyroscopic sensor (Apple, USA). Phase-resolved measurements were acquired for the Cultibag mimic, with the laser optics, camera and acquisition system synchronised to a microswitch, enabling acquisition once per platform rock. A 12V geared motor (Parvalux, RS Components, UK) was used to rock the bed with a maximum output of 50 rpm. The motor was controlled by a boxed DC motor speed controller 12/24V (RS Components, UK). A DC regulated power supply (Rapid 85-1833) was used to power the motor and signal trigger. A schematic diagram of the experimental set-up is displayed in Figure 2.7. Images were acquired in $\theta = 4^{o}$ increments throughout a full rock, with ascending and descending directions of rocking motion being distinguished, and all angles relative to the horizontal ground. 500 image pairs were taken at each angle/platform direction. This procedure was repeated for fluid working volumes of 30, 40, 50 and 60%. Figure 2.8 highlights the platform angular positions and direction of motion, for the various datasets that were acquired.

2.5.2 Sources of error

During operation, the Cultibag RM has a total volume of 3.5 L, because it is inflated at 10 mbar overpressure. On creation of the plaster of Paris mould, the bag was filled to its maximum volume, in order to achieve the desired bag shape. As a result, during PIV investigation of the Perspex mimic, the Cultibag cavity was filled according to the total volume of the mimic i.e. 50% working volume equates to 1.75 L. The influence of varying fluid working volumes was investigated as stated previously (at 30%, 40%, 50% and 60% wv). 30% working volume within the mimic represented 1 L of fluid, however, lower fluid volumes were not conducive to producing adequate vector maps due to the small spatial acquisition area of the liquid. Hence the fluid acquisition area is significantly affected by the fill volume.

The laser light sheet was aligned at 8.5 cm from the edge of the bag shape. The laser was fired at a reduced power and positioned via visual inspection to the desired alignment on the Perspex mimic. Alignment of the laser light is a predicted source of error. The angles of the rocking platform positions were determined using a gyroscopic sensor (Apple, USA) which read the angular position to 1 decimal place. Only a quarter of the Cultibag cavity length could be analysed at any given time, due to the close proximity of the laser light to the Perspex mimic. As a result, the laser itself needed to be moved when measuring different portions of the mimic. Manual movement of the laser system during the acquisition process is a predicted source of error.

2.6 Statistical analysis

Given the sources of statistical variation in the fluid dynamics data that was obtained, the reproducibility of both time and phase-resolved PIV experiments was investigated using the CellReady. Data obtained on the same stirred vessel system on different experimental runs at the same conditions, differed by a maximum of 5% when measurements were obtained in the impeller zone. Measurements obtained in the bulk fluid (in the upper three quarters of the bioreactor) showed a slightly greater degree of variation (-/+10%). A single point in the impeller zone (z/H = 0.15 and r/R = 0.65) was analysed for statistical variation dependent upon the number of images acquired. The r.m.s. velocity (in the axial and radial direction, u'_{rz}) was calculated to

be $0.15U_{tip}$ for both a 250 and a 500 vector map dataset. Impeller rotation speeds were found to be accurate to 3 decimal places, based on the timestamp of acquired phase-resolved data.

Analysing an arbitrary point on the PBS vector plots (at z/H = 0.9 and d/D = 0.8) indicated a difference in the r.m.s. velocity of 1.3% between a 250 and a 500 image pair dataset. The ensemble-averaged velocity magnitude was $\overline{U}_{rz}$ = 0.04 ms^{-1} for both datasets.

Statistical analysis of the velocity magnitude values ($\overline{U}_{rz}$) was also performed in the Cultibag RM mimic at rocking angle $\theta = 4^{o}$, when the platform was descending. A difference of 0% in mean velocity magnitude was noted between a 250 and a 500 image pair dataset. Variation of the r.m.s. velocity levels was measured to be less than 0.1% of the measured $\overline{U}_{rz}$ at the same location, for sample sizes (number of acquired image pairs) ranging from N = 1 to 500.

2.7 Sources of error in PIV

The type of PIV used in this project is 2-dimensional, so the third component of velocity is not measured. This can lead to errors whereby the particles appear in and out of an image pair plane. As noted previously, validation steps are taken in order to mitigate against the production of such errors. In this project, the isotropic assumption was used to take into account the third component of velocity when determining specific parameters.

The PIV system uses Fast Fourier Transforms (FFT), which is based on the assumption that the particle input patterns are cyclic, thus correlations across the interrogation area boundary are handled using this assumption. For example, particles in the far right of an IA in frame 1, may correlate with particles that then come into view at the far left of frame 2, and the system may interpret this as a small displacement to the right. However, with suitable selections of both IA and particle displacement between image pairs, the "correct" particle displacement would typically produce a dominant correlation peak.

Given the wide range of fluid velocities within a given measurement area, if a constant time delay between image pairs is used then the cross-correlation peaks will

vary in size (relative to background noise). An appropriate time delay should then be used to ensure that an adequate signal-to-noise (SNR) is maintained throughout the whole measurement field.

As mentioned previously, the resolution of the acquired recordings will limit the degree with which small scales of turbulence (Kolmogorov) can be measured. This can result in an underestimation of parameters such as the energy dissipation rate. Methods used to compensate for this limitation are mentioned in Chapter 8.

2.8 Theoretical considerations

Instantaneous velocity vector data was exported and analysed using a MATLAB programme This section describes the equations used to obtain the fluid dynamic parameters in this thesis from the PIV velocity data.

Mean and Turbulent Velocity

A fluid is considered to be turbulent when it exhibits chaotic, random behaviour with regards to its various fluid parameters i.e. the three components of velocity, pressure, shear stress and temperature. Here, the fluctuating component (u) of instantaneous velocity (U) will be considered (Munson et al., 2002). Ensemble-averaged velocities $\overline{U}$ represent the mean whole flow field fluid velocities from a given vector map sample size. In this section, axial, radial and tangential components of velocity are represented by r, z and θ respectively, respectively.

$$\overline{U} = \frac{1}{\mathrm{N}}\sum_{r=1}^{\mathrm{N}} U_r \quad (2.1)$$

The instantaneous velocities that constitute ensemble-averaged measurements can be decomposed to their ensemble-averaged ($\overline{U}$) and turbulent components (u) as follows:

$$U_r = \overline{U}_r + u_r \quad (2.2)$$

$$U_z = \overline{U}_z + u_z \quad (2.3)$$

The vector magnitude, denoted in this document as U_{rz} is calculated using both the axial (U_z) and radial (U_r) instantaneous velocity components**.**

$$U_{rz} = \sqrt{{U_r}^2 + {U_z}^2} \quad (2.4)$$

A measure of turbulence often used is the root-mean-square (r.m.s.) velocity (u'), shown below.

$$u'_r = \sqrt{\overline{u_r{}^2}} \qquad (2.5)$$

$$u'_{rz} = \sqrt{\frac{1}{2}\left(\overline{u_r{}^2} + \overline{u_z{}^2}\right)} \qquad (2.6)$$

Reynolds Shear Stress

The Reynolds stress field is defined as the apparent stress that results from the mean transport of fluctuating momentum by turbulent velocity fluctuations (Munson et al., 2002) and it can be obtained from the equation below.

$$-\rho\overline{u_r u_z} \qquad (2.7)$$

Where u_r and u_z represent the fluctuating component of radial and axial velocity, respectively.

Turbulent velocity can be further decomposed using phase-resolved PIV, where vector maps are acquired at specific impeller angular positions (Sharp and Adrian, 2001).

$$U = \overline{U}_\theta + u'' \qquad (2.8)$$

Here, $\overline{U}_\theta$ is the phase-resolved mean velocity, and the periodic fluctuations in flow (caused by the rotating impeller) can be determined as:

$$U_P = \overline{U}_\theta - \overline{U} \qquad (2.9)$$

Thus

$$u'' = u - U_P \qquad (2.10)$$

Since u'' represents the turbulent component of velocity with the periodic fluctuation removed, it is thus the turbulent velocity due to random fluctuations. This parameter can also be used to determine the Reynolds shear stress.

$$-\rho\overline{u''_r u''_z} \qquad (2.11)$$

Turbulent Kinetic Energy

Turbulent kinetic energy (TKE) can be defined as the mean kinetic energy per unit mass that is associated with eddies in turbulent flow. The TKE is characterised by

the measured r.m.s. velocity and can be quantified by the mean of the turbulence normal stresses (Gabriele et al., 2009). The TKE (k) can be determined from 3-D velocity data using the following equation:

$$k = \frac{1}{2}\left(\overline{u_r{}^2} + \overline{u_z{}^2} + \overline{u_\theta{}^2}\right) \qquad (2.12)$$

However, given that the PIV system that is to be used is 2-D, the third fluctuating component (u_θ) is estimated using the isotropic approximation (Gabriele et al., 2009):

$$\overline{u_\theta{}^2} = \frac{1}{2}\left(\overline{u_r{}^2} + \overline{u_z{}^2}\right) \qquad (2.13)$$

Thus the TKE can be found as follows:

$$k = \frac{3}{4}\left(\overline{u_r{}^2} + \overline{u_z{}^2}\right) \qquad (2.14)$$

$$k_\vartheta = \frac{3}{4}\left(\overline{u''{}_r^2} + \overline{u''{}_z^2}\right) \qquad (2.15)$$

Rate of Energy Dissipation

The rate of viscous dissipation of the turbulent kinetic energy was determined from calculation of the spatial fluctuating velocity gradients as defined by Hinze (1975):

$$\varepsilon = \nu\left[\begin{array}{l} 2\left(\overline{\left(\frac{\partial u_r}{\partial x_r}\right)^2} + \overline{\left(\frac{\partial u_z}{\partial x_z}\right)^2} + \overline{\left(\frac{\partial u_\theta}{\partial x_\theta}\right)^2}\right) + \overline{\left(\frac{\partial u_r}{\partial x_z}\right)^2} \\ + \overline{\left(\frac{\partial u_z}{\partial x_r}\right)^2} + \overline{\left(\frac{\partial u_r}{\partial x_\theta}\right)^2} + \overline{\left(\frac{\partial u_\theta}{\partial x_r}\right)^2} + \overline{\left(\frac{\partial u_z}{\partial x_\theta}\right)^2} \\ + \overline{\left(\frac{\partial u_\theta}{\partial x_z}\right)^2} + 2\left(\overline{\frac{\partial u_r}{\partial x_z}\frac{\partial u_z}{\partial x_r}} + \overline{\frac{\partial u_r}{\partial x_\theta}\frac{\partial u_\theta}{\partial x_r}} + \overline{\frac{\partial u_z}{\partial x_\theta}\frac{\partial u_\theta}{\partial x_z}}\right) \end{array}\right] \qquad (2.16)$$

The third component of the velocity was not measured in this work, hence Equation (2.16) was simplified under the assumption of statistical isotropy. The seven remaining components were calculated using Equations (2.17) to (2.19) (Baldi et al., 2002).

$$\overline{\left(\frac{\partial u_\theta}{\partial x_\theta}\right)^2} = \frac{1}{2}\left[\overline{\left(\frac{\partial u_r}{\partial x_r}\right)^2} + \overline{\left(\frac{\partial u_z}{\partial x_z}\right)^2}\right] \qquad (2.17)$$

$$\overline{\left(\frac{\partial u_r}{\partial x_\theta}\right)^2} = \overline{\left(\frac{\partial u_\theta}{\partial x_r}\right)^2} = \overline{\left(\frac{\partial u_z}{\partial x_\theta}\right)^2} = \overline{\left(\frac{\partial u_\theta}{\partial x_z}\right)^2} = \frac{1}{2}\left[\overline{\left(\frac{\partial u_r}{\partial x_z}\right)^2} + \overline{\left(\frac{\partial u_z}{\partial x_r}\right)^2}\right] \qquad (2.18)$$

$$\overline{\frac{\partial u_r}{\partial x_\theta}\frac{\partial u_\theta}{\partial x_r}} = \overline{\frac{\partial u_z}{\partial x_\theta}\frac{\partial u_\theta}{\partial x_z}} = \frac{-\frac{1}{2}\overline{\left(\frac{\partial u_r}{\partial x_r}\right)^2} + \left(-\frac{1}{2}\overline{\left(\frac{\partial u_z}{\partial x_z}\right)^2}\right)}{2} = -\frac{1}{4}\left[\overline{\left(\frac{\partial u_r}{\partial x_r}\right)^2} + \overline{\left(\frac{\partial u_z}{\partial x_z}\right)^2}\right] \quad (2.19)$$

By substituting Equations (2.17) to (2.19) into Equation (2.16), Equation (2.20) was obtained and was used to estimate the energy dissipation rate of the turbulent kinetic energy.

$$\varepsilon = \nu\left\{2\overline{\left(\frac{\partial u_r}{\partial x_r}\right)^2} + 2\overline{\left(\frac{\partial u_z}{\partial x_z}\right)^2} + 3\overline{\left(\frac{\partial u_r}{\partial x_z}\right)^2} + 3\overline{\left(\frac{\partial u_z}{\partial x_r}\right)^2} + 2\overline{\frac{\partial u_r}{\partial x_z}\frac{\partial u_z}{\partial x_r}}\right\} \quad (2.20)$$

The energy dissipation rate can then be used to determine the Kolmogorov length scale (η) (Landahl and Mollo-Christensen, 1992), where ν is the fluids kinematic viscosity:

$$\eta = \left(\frac{\nu^3}{\varepsilon}\right)^{1/4} \quad (2.21)$$

Vorticity

Vorticity can be expressed as the amount of circulation/rotation, or more specifically the local angular rate of rotation within a fluid (Clancy, 1975). The flow within stirred tank reactors can be characterised by a strong radial jet, large tank-scale ring vortices and small-scale blade tip vortices (Hill et al., 2008). Thus, the structure of these vortices (in terms of size and velocity) must be determined in order to ascertain the specific differences between the flow field within single-use stirred tank and other SUB platforms.

Vorticity around the tangential θ -axis (ω_θ) is the average of the angular velocities in both the *r* and *z*-axis. The equation presented, ensures that anticlockwise rotation around the θ -axis is positive. The angular velocity of a plane (e.g. the *r*-axis), is determined by the change in velocity U_z over the change in distance, x_r, $\left(i.e.\ \frac{\partial U_z}{\partial x_r}\right)$, within δt.

$$\omega_\theta = \frac{1}{2}\left(\frac{\partial U_z}{\partial x_r} - \frac{\partial U_r}{\partial x_z}\right) \quad (2.22)$$

Reynolds Number

The Reynolds number (*Re*) is a dimensionless quantity used to distinguish between laminar and turbulent flow. The Reynolds number is defined as a measure of the ratio of inertia forces on a fluid to the viscous forces on the fluid (Munson et al.,

2002). The following equation is used to calculate the Reynolds number of a flow in a stirred tank, with *D* representing the impeller diameter and *N* the impeller rotation rate (revolutions per second):

$$Re = \frac{\rho N D^2}{\mu} \qquad (2.23)$$

2.9 Cell culture methods

2.9.1 Materials

During GS-CHO cell cultures, 100 mL of 1% antifoam C Emulsion (Sigma, A8011), 500 mL of 100 mM Sodium bicarbonate base and culture feed comprising 100 mL of 10 times concentrated CD-CHO (Invitrogen, Paisley UK) with a glucose concentration of 150 g/L were used.

For the purposes of HPLC analysis: 1 L of buffer A (20 mM sodium phosphate) was used with the pH of the solution adjusted to 7 using 2 M HCl; 1 L of buffer B (20 mM glycine) was used with the pH of the solution adjusted to 2.8 using 2 M HCl.

2.9.2 Cell Culture Preparation and Operation

Cell cultures were conducted within the Sartorius BIOSTAT® B-DCU, BIOSTAT® Cultibag RM and the Mobius® CellReady. For all cell cultures performed, a Glutamine Synthetase Chinese Hamster Ovary (GS-CHO) cell line (CY01) expressing IgG_4 B72.3 (Lonza Biologics, Slough, UK) was used. Cells were grown in Chemically Defined (CD) CHO medium (Invitrogen, Paisley UK). The inoculum was prepared in disposable vented cap shake flasks and incubated using a Galaxy S incubator (Wolf Laboratories, York, UK) at 37^{o}C, 5% (v/v) CO_2 producing 10% of the total cell culture volume. The airflow rate was set constant at 0.1 vvm in the CellReady and dissolved oxygen tension (DOT) was set to a minimum of 30% and was controlled using air, N_2 and O_2. A solution of 10 x concentrated CD-CHO medium with 150 g/L of glucose was used to feed the cells once the glucose concentration of the cell culture dropped below 2 g/L. All cell cultures involved the preparation of inoculum to 10% of the cell culture volume, with day 0 culture cell

densities of $0.2x10^6$ cells/mL. Mammalian cell cultures were 14 days in length, with daily sampling and analysis.

The pH within CellReady experiments was set at 7 and controlled using CO_2 and 100 mM sodium bicarbonate. Cell culture experiments were performed at different impeller speeds and liquid volumes, as shown in Table 2.2.

Table 2.2: Operating conditions used for the cell culture experiments in the CellReady bioreactor

Operating Conditions			
Working Volume (L)	1	2.4	2.4
Impeller Rate (rpm)	350	200	80
Reynolds Number (*Re*)	38.057	21.747	8,699
Impeller Tip Speed (ms^{-1})	1.396	0.798	0.319
Power Per Unit Volume (W/m^3)	152.98	11.89	0.76

Cell culture experiments in the Sartorius 5 L BIOSTAT bioreactor were conducted at N = 260 rpm (corresponding to Re = 17,528). Air flow rate was maintained constant at 0.02 vvm and the DOT was controlled at a minimum of 30% using air, N_2 and O_2. The pH was maintained at 7 and controlled using CO_2 and 100 mM sodium bicarbonate. The k_La value, as measured via the dynamic gassing-out method, was found to be 5 hr^{-1} at the operating conditions used in this work. The BIOSTAT cell culture was used as a benchmark for culture performance.

Cell culture experiments in the Sartorius BIOSTAT Cultibag RM bioreactor were conducted at N = 25 and 42 rpm. The bag was filled to a working volume of 1 L. Air flow rate was maintained constant at 0.1 vvm and the DOT was controlled at a minimum of 30% using air, N_2 and O_2. The pH was maintained at 7 and controlled using CO_2 and 100 mM sodium bicarbonate. The k_La values, as measured via the dynamic gassing-out method, were found to be 11 hr^{-1} and 33 hr^{-1} at N = 25 and 42 rpm, respectively.

2.10 Analytical techniques

Daily samples were withdrawn from the CellReady, BIOSTAT and Cultibag RM and analysed for viable cell concentration and cell viability (trypan blue exclusion method) using a ViCell (Beckman Coulter, High Wycombe, UK). A CASY analyzer (Innovatis, Bielefeld, Germany) was used to determine the cell size distribution. For each condition measurements were repeated 5 times and the mean and standard deviation values calculated. The cell size frequency was normalised by the number of counts associated with the maximum cell diameter frequency. The measured cell diameter ranges were set at 13.5-40 µm and 7.5-13.5 µm for viable and non-viable cells, respectively.

Cell culture samples were centrifuged at 13200 rpm for 10 minutes in a Microcentrifuge 5415 R system (Eppendorf North America, USA) in order to separate the cells from the supernatant. A Nova Bioprofile 400 Analyser (Nova Biomedical, Waltham, MA, USA) was used to measure the concentration of metabolites present in the sample supernatant, including glutamine, glutamate, glucose and lactate, as well as ammonium, sodium and potassium ion concentrations and osmolality.

The monoclonal antibody IgG_4 concentration was determined by protein G-HPLC analysis using an Agilent 1200 HPLC system (Agilent Technologies, South Queensferry, UK). 200 µL culture supernatant samples were prepared and loaded onto a 96-well plate (diluted 1 to 2 in 20 mM Sodium Phosphate). 100 µL of the sample was injected on to a 1 mL HiTrap protein G column (GE Healthcare, Pittsburgh, PA) and washed with 20 mM sodium phosphate buffer (at pH 7), with the analysis being performed at a flow rate of 1 ml/min. Samples were eluted using a glycine buffer (20 mM, adjusted to pH 2.8) and the elution peak was measured by UV detection at 280 nm. The peak corresponding to the IgG_4 (at 5.7 min) was integrated and the antibody concentration determined using a standard calibration curve.

To analyse the data, the peak area (PA) for IgG at 280nm at 5.7 min was obtained. To determine the IgG titre (g/L) the following equation was used:

$$\text{Titre (g/L)} = [\text{DF} \times \text{PA @ 280nm}]/2100 \qquad (2.23)$$

DF – Dilution factor = 2

IgG calibration for converting PA to g/L = 2100

Cell specific daily productivity was determined using the integral viable cell concentration (IVC), as shown in Equation 2.24 (Smales and James, 2005).

$$IVC_{i+1} = 0.5 \times (C_{i+1} + C_i) \times (t_{i+1} - t_i)/24 + IVC_i \qquad (2.24)$$

A plot of IgG_4 concentration (pg/ml) vs. IVC (cells.day/ml) was produced, and a linear curve fitted through the culture period to determine the cell specific productivity ($pg.cell^{-1}.day^{-1}$).

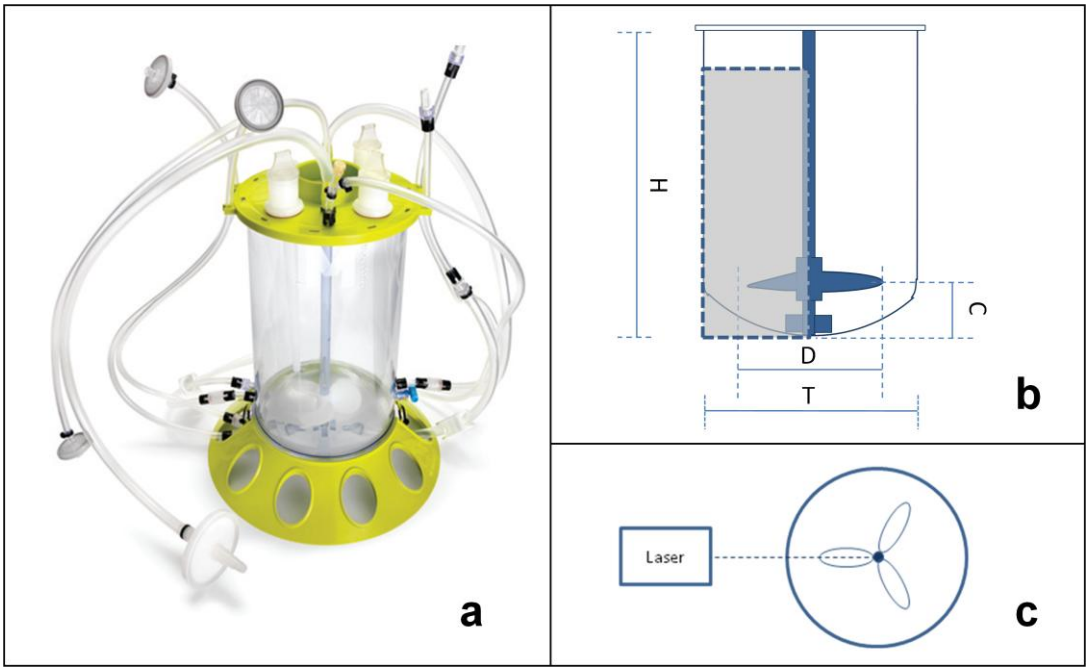

Figure 2.1: a) Mobius® 3 L CellReady Bioreactor. Image from www.millipore.com, accessed 17.02.2012; b) schematic diagram of bioreactor; c) top-down view of bioreactor and laser.

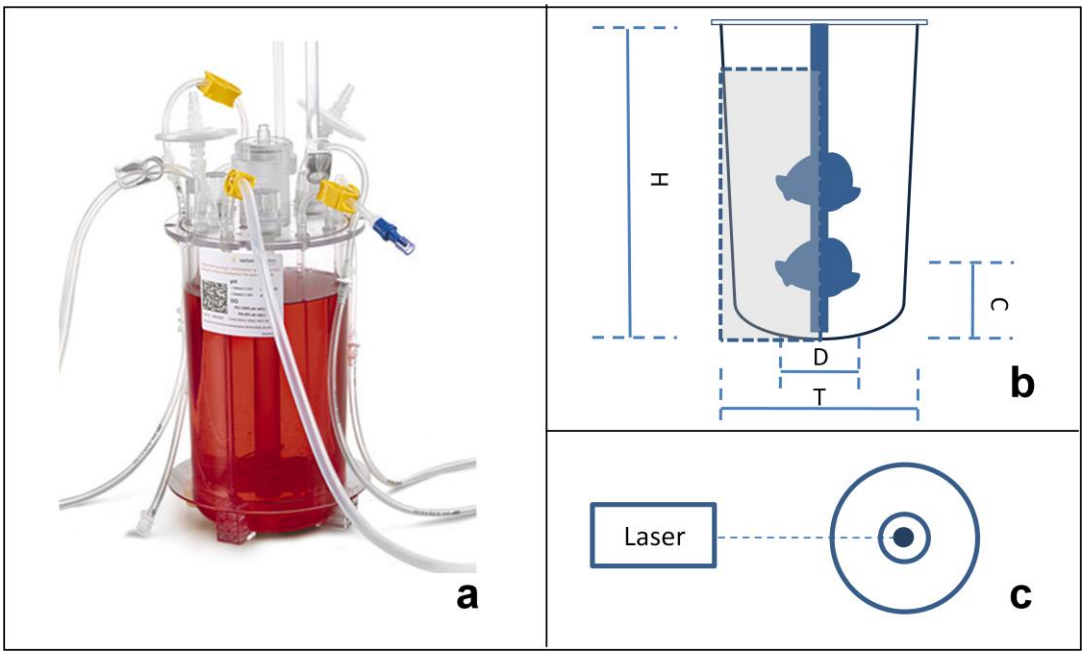

Figure 2.2 a) 2 L UniVessel® SU bioreactor. Image from www.sartorius.co.uk, accessed 13.02.2014; b) schematic diagram of bioreactor; c) top-down view of bioreactor and laser.

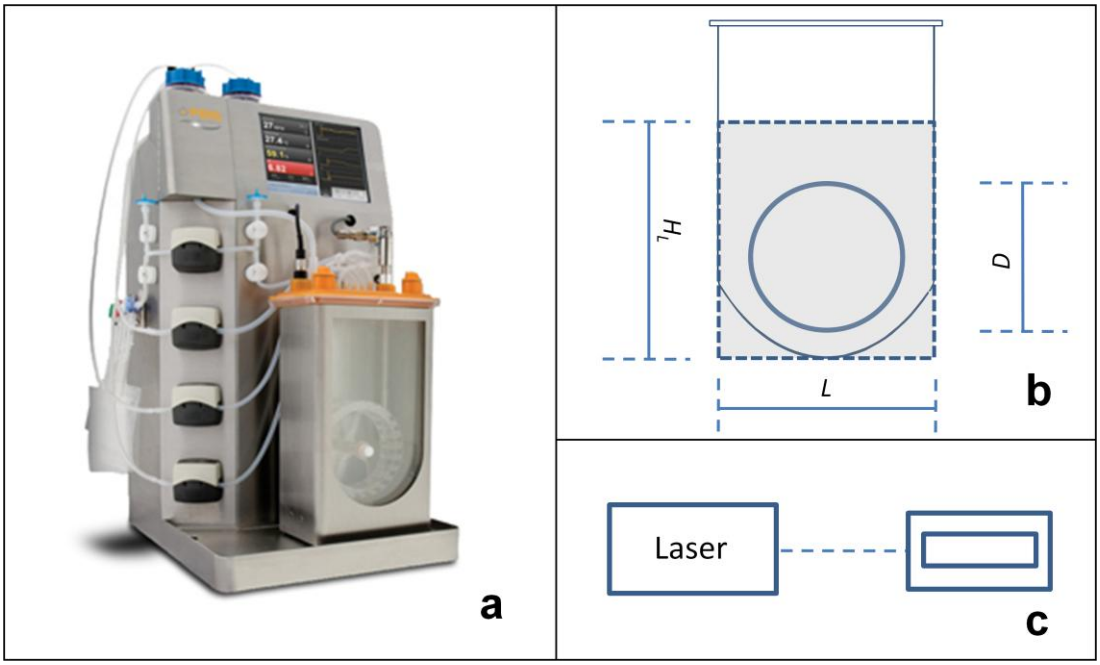

Figure 2.3: a) PBS Biotech® 3 L bioreactor (image from www.pbsbiotech.com, accessed 13.02.2014); b) schematic diagram of bioreactor; c) top-down view of bioreactor and laser.

Figure 2.4: Sartorius BIOSTAT® Cultibag RM rocking platform and control tower (image obtained from www.sartorius.co.uk, accessed 20.02.2014).

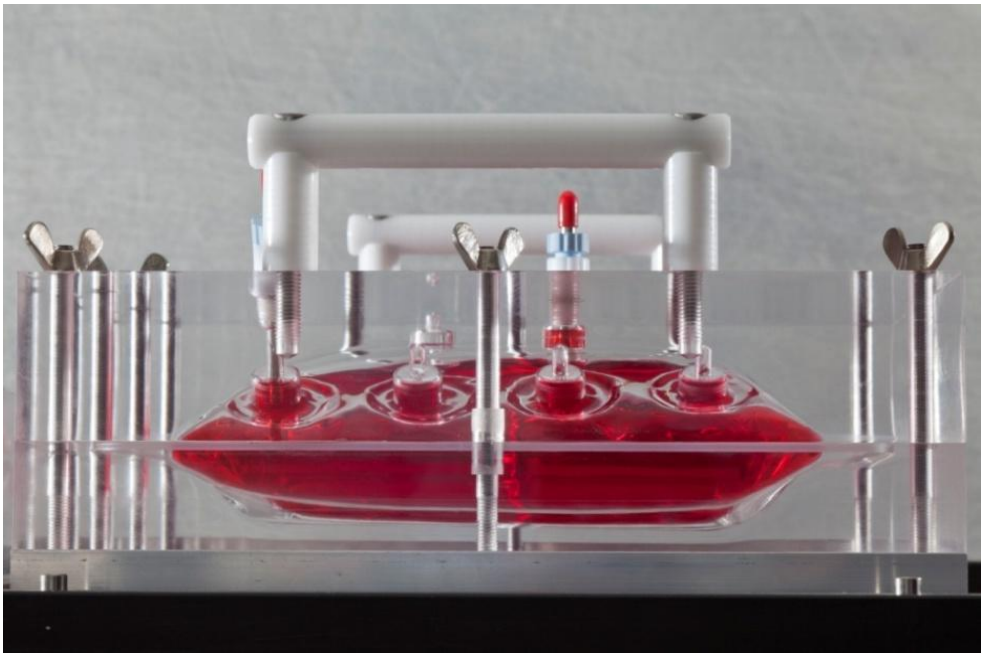

Figure 2.5: Image of the Perspex mimic of the inflated BIOSTAT® Cultibag RM bag.

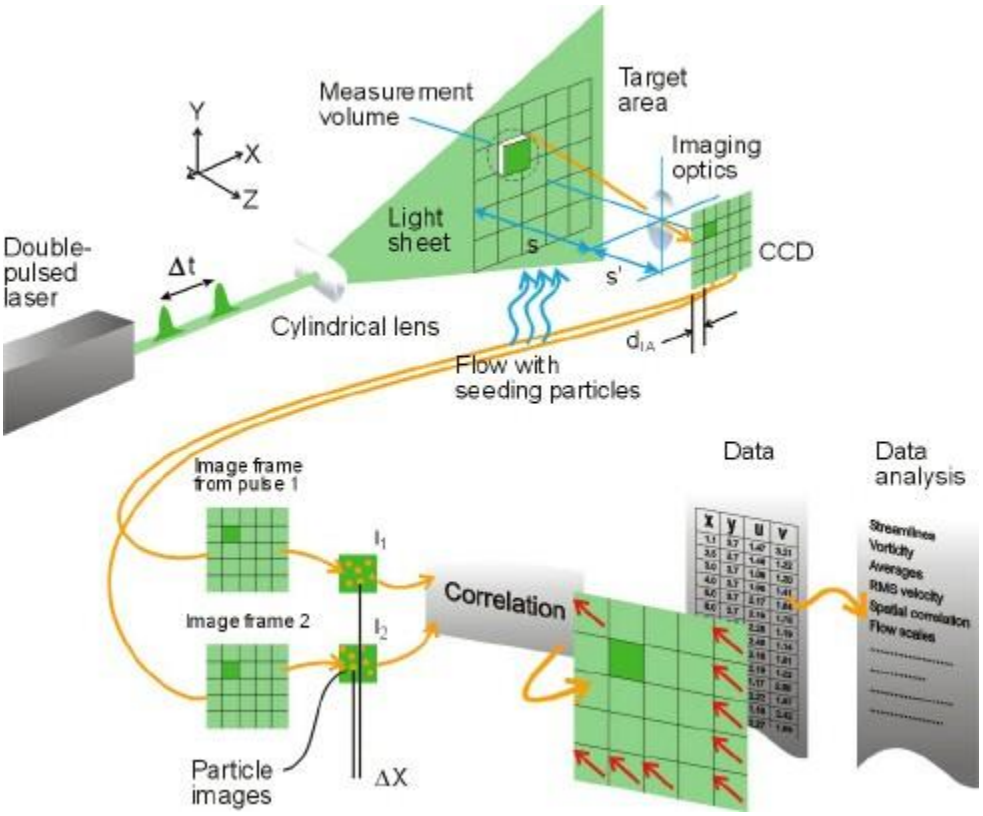

Figure 2.6: Diagram describing acquisition principles of PIV, and post-processing procedures (image obtained from www.dantecdynamics.com, accessed 20.02.2014).

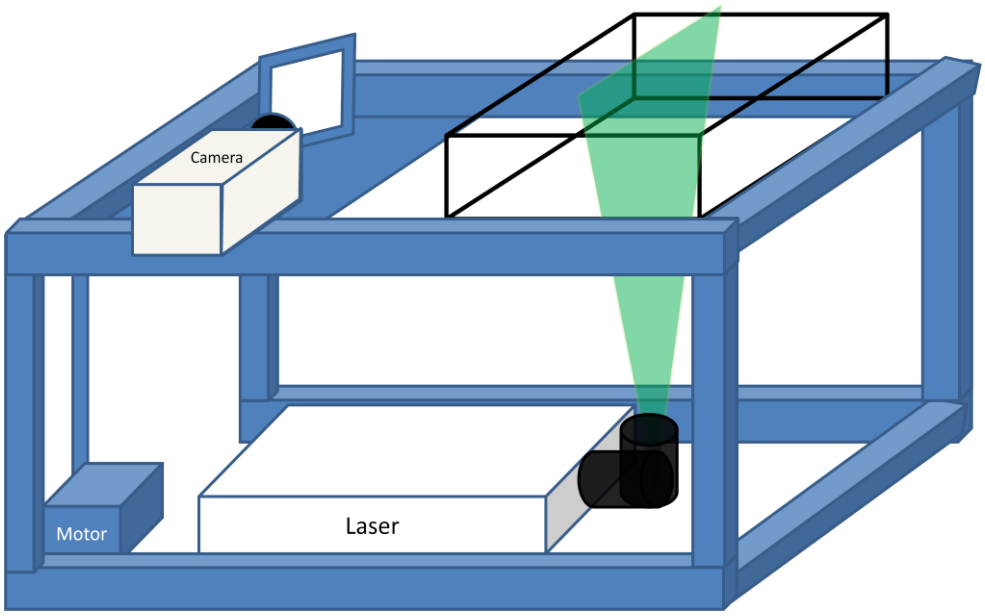

Figure 2.7: Cultibag RM PIV experimental set-up

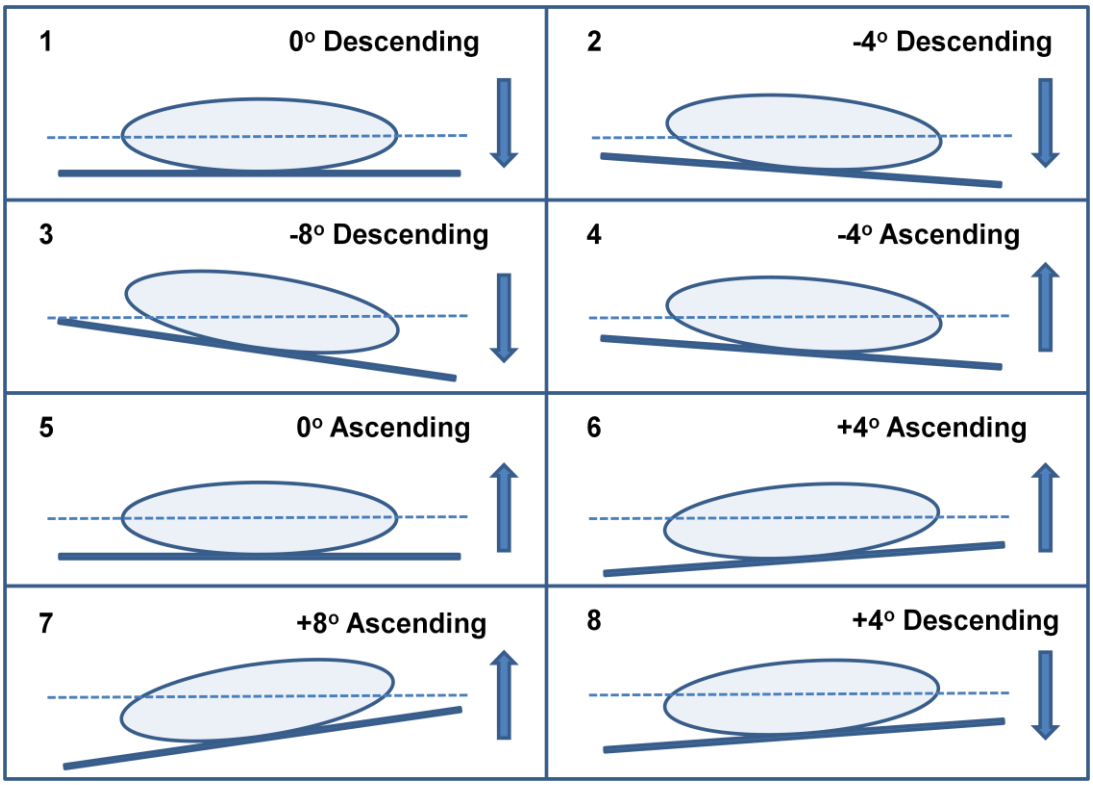

Figure 2.8: Vector map notation stating vector map number along with corresponding angle and direction of movement.

Chapter 3 On the fluid dynamics of the Mobius® 3 L CellReady

3.1 Introduction

The 3 L CellReady was one of the first rigid stirred tank SUB to be released on the market and has been widely employed for process development as its geometrical configuration facilitates process translation to larger scales of operation. It is part of EMD Millipore's family of Mobius® CellReady SUBs, including 50 L and 200 L vessels suitable for pilot-scale and clinical-scale applications. Recently a few single-use equipment manufacturers have invested in larger scale systems (examples include the 500 L Pneumatic Bioreactor System and 500 L GE WAVE Bioreactor™), however greater process predictability and robust scale translation methods must be ensured if laboratory scale single-use bioreactor systems are to be used as scale-down models at the development stage.

Kaiser et al. (2011a) used Computational Fluid Dynamic (CFD) approaches to determine engineering characteristics such as mixing time, power input and oxygen transfer within the 3 L Mobius® CellReady bioreactor. The marine impeller fitted within this bioreactor was found to produce an up-pumping circulation loop directed 25^{o} above the horizontal plane, with the fluid velocity dominated by its radial component. In addition, gas distribution was found to be significantly heterogeneous, with significant flooding of the impeller observed (up to an impeller rate of N = 200 rpm). A stagnant zone of fluid velocities close to 0 ms^{-1} was also observed at the drain inlet, which led to cell sedimentation and accumulation in this region (Kaiser et al., 2011a).

In this chapter, for the first time, a PIV system is used to investigate the flow characteristics within a commercial single-use bioreactor, namely the 3 L Mobius® CellReady. The PIV study was conducted within the actual vessel, rather than a purpose-built mimic. For this reason, some areas of the bioreactor were not optically accessible and could not be obtained. These regions are located at the curvature of the base, and near the bottom of the vessel.

Results included in this chapter are presented in Odeleye et al. (2014) entitled: 'On the fluid dynamics of a laboratory scale stirred single-use bioreactor', Chemical Engineering Science, vol. 111 p299-312.

When the power number (P_O) of an impeller in a stirred tank becomes constant upon increasing the Reynolds number, it is generally accepted that fully turbulent flow is present (Rushton et al., 1950). However, the degree of turbulence present within a system depends on assumptions of steady state, local isotropy and high Reynolds number. These conditions often apply only in the region close to the impeller (Kresta, 1998). In a Rushton agitated tank, the magnitudes of the convective and turbulent flows are very high within the impeller region, in comparison with the bulk of the fluid (Rutherford et al., 1996). Wernersson and Tragardh (1998) used Constant Temperature Anemometry (CTA) to indicate that an increase in tip speed had a greater effect on velocities measured in the impeller zone, than in the bulk fluid. This is important when scaling stirred bioreactors, given that the ratio of impeller zone and bulk fluid flow characteristics may not remain constant upon scale-up.

The work presented in this chapter aims to carry out a rigorous fluid dynamic study of the flow within a novel single-use bioreactor (3L Mobius® CellReady) in order to improve the current understanding of the flow pattern, mixing efficiency and velocity characteristics in the vessel. The variation of flow characteristics within the bioreactor in relation to *Re* will be reported. Such knowledge will subsequently be used to investigate the impact of the operating conditions on the performance of a Chinese Hamster Ovary (CHO) mammalian cell line in Chapter 7.

The experiments conducted in this chapter were carried out using the PIV technique described in Chapter 2. A cylindrical coordinate system is used, with the radial, axial and azimuthal coordinates indicated in this work by r, z and θ, respectively. The systems origin is located in the centre of the bioreactor bottom and $\theta = 0^o$ corresponds to the vertical plane intersecting the centre of the blade. Both time and phase-resolved measurements were obtained. These were then post-processed using a MATLAB program to determine different fluid dynamic characteristics.

3.2 Whole flow field characteristics

A Particle Image Velocimetry (PIV) system, described in Chapter 2, was used to obtain time-resolved and phase-resolved velocity data. A description of the whole flow field occurring inside the stirred Mobius CellReady bioreactor is provided in this section. The first part of the analysis is carried out for a standard configuration

corresponding to a fill volume of 2.4 L and an impeller rotational speed of 200 rpm (*Re* = 21,747). In the subsequent sections, this analysis is extended to a range of impeller speeds (*N* = 80 to 350 rpm, *Re* = 8,699 to 38,057) and phase-resolved data obtained at *N* = 120 rpm, *Re* = 13,048 are presented.

The two-dimensional (2-D) ensemble-average velocity field with vectors superimposed and contour plot of velocity turbulence are shown in Fig. 3.1. Fig. 3.1a shows the impeller inducing an upward flow at a trajectory of approximately 26^{o} with respect to the horizontal plane, the fluid then impinges on the wall at a vertical position of *z/H* = 0.15, at which point the fluid divides into two counter-rotating vortices in the regions below and above the impeller. The vortex located below the impeller plane is characterised by ensemble-averaged velocities up to $0.25U_{tip}$. This value is significantly lower than the $0.55U_{tip}$ measured by Gabriele et al. (2009) using an up-pumping 45^{o} 6-bladed PBT (*D/T* = 0.45), but it is in good agreement with the $0.26U_{tip}$ measured by Baldi et al. (2002) with a down-pumping 3-bladed hydrofoil axial impeller (*D/T* = 0.33 and a trailing edge angle of approximately 10^{o}) and to the $0.25U_{tip}$ measured by Plion et al. (1985) using Laser Doppler Anemometry (LDA) in a reactor stirred by a propeller. In the CellReady bioreactor the top circulation loop is weaker and achieves approximately a height of *z/H* = 0.5 before turning downwards towards the impeller region. The regions in correspondence with the vortex centre and on the top of the vessel above *z/H* = 0.5 are characterised by a limited degree of mixing and r.m.s. velocity levels below $0.05U_{tip}$ (Fig. 3.1b). The presence of a circulation loop occupying the bottom quarter of the tank has also been reported by Kaiser et al. (2011a) simulations. A difference of up to 80% between the impeller zone and bulk fluid r.m.s. velocity levels can also be observed from Figure 3.1b. The velocity magnitude decomposed to its axial and radial component is shown in Figure 3.2. The dominance of the radial component of velocity in the impeller exit stream is in good agreement with the work of Kaiser et al. (2011a). The axial velocity component is dominant beneath the impeller and at the bioreactor wall up to *z/H* = 0.5.

3.3 Impeller stream characteristics

The velocity field data presented have helped elucidate the whole flow field occurring in the 3 L CellReady bioreactor. It was then deemed necessary to investigate in more detail the flow near the impeller where the greatest turbulence and stress levels are likely to occur. A description of the flow occurring inside the impeller zone of the Mobius® CellReady bioreactor is provided in this section.

3.3.1 Spatial variation of flow characteristics

The two-dimensional (2-D) ensemble-averaged velocity contour and superimposed vectors direction is shown in Figure 3.3, where a maximum velocity of $0.25U_{tip}$ is observed in the impeller discharge stream (at approximately r/R = 0.65 and z/H = 0.15). In Fig. 3.3, an upward flow induced by the impeller is present at a trajectory of approximately 26^o (25^o is noted by Kaiser et al. (2011a)) with respect to the horizontal plane, the fluid then impinges upon the wall at a vertical position of z/H = 0.15, at which point the fluid divides into two counter-rotating vortices in the planes below and above the impeller. The ensemble-averaged contour plot shown in Figure 3.3 can be directly compared with the CFD simulations of Kaiser et al. (2011a) which is the only work available in literature that provides a qualitative study of the flow in the 3 L Mobius® CellReady impeller stream. The current results are in good agreement with their simulations, characterised by maximum velocities of $0.25U_{tip}$ at an impeller speed of N = 200 rpm for a fluid of similar viscosity.

Figure 3.4 shows the r.m.s. of the axial and radial velocity components. The maximum values of the r.m.s. velocity in the axial and radial directions (u'_z and u'_r) are $0.15U_{tip}$ and $0.11U_{tip}$, respectively (Figure 3.4). These values are in good agreement with the corresponding r.m.s. values of $0.12U_{tip}$ and $0.15U_{tip}$, respectively, obtained by Aubin et al. (2004) in the fluid discharge stream of an upward pumping 45^o pitched blade turbine ($D = 0.5T$).

The spatial variation of ensemble-averaged velocity and r.m.s. velocity levels were assessed in the impeller discharge zone. Ensemble-averaged and r.m.s. velocity values were measured and are presented, with vertical and horizontal profiles in Figures 3.5 and 3.6. The maximum radial velocity and r.m.s. radial velocity values

($\overline{U}_r/U_{tip}$ and u'_r/U_{tip}) were 0.26U_{tip} and 0.13U_{tip}, respectively. Radial velocities approach zero above a height of *z/H* = 0.153 and from radial locations between *r/R* = 0.652 to 1, whilst axial velocities change direction at *z/H* = 0.172 and *r/R* = 0.841. The vertical profile of the radial velocity reaches -0.003U_{tip} at approximately *z/H* = 0.20 and remains constant towards the upper regions of the bioreactor. The maximum axial velocity and r.m.s. axial velocity values ($\overline{U}_z/U_{tip}$ and u'_z/U_{tip}) were found to be 0.06U_{tip} and 0.15U_{tip}, respectively. The radial component of the velocity in the impeller zone is higher than the axial (as noted by Kaiser et al. (2011a), whilst r.m.s. axial and r.m.s. radial velocities in the impeller discharge stream are comparable. The maximum radial velocity is found close to the impeller tip at a height of *z/H* = 0.15, and decreases linearly from *r/R* = 0.75 to 1.0 with a gradient of 0.521. This is in contrast to the work of Van Der Molen and Van Maanen (1978), where the radial velocity at the impeller plane decreased exponentially, with respect to *r/R* in a vessel housing a six-bladed Rushton turbine. The relationship is described by Equation 3.1:

$$\frac{U_r}{U_{tip}} = 0.85\left(\frac{r}{R}\right)^{-\frac{6}{7}} \qquad (3.1)$$

The r.m.s. radial velocity levels were found to change from between 0.08 to 0.11U_{tip} at radial locations from *r/R* = 0.58 to 0.98.

3.3.2 Variation of impeller stream velocity & turbulence with *Re*

Figure 3.7 shows the ensemble-averaged velocity and vorticity at impeller rates of *N* = 80, 200 and 350 rpm (representing *Re* = 8,699, 21,747 and 38,057, respectively), whilst Figure 3.8 shows both the r.m.s. axial velocity and r.m.s. radial velocity for the same conditions. It is noted from Figure 3.7 that the height of the primary circulation flow induced by the impeller of the CellReady remains largely consistent at varying *Re*. This correlates well with the work of Bittorf and Kresta (2000), where it is shown that the main active zone of circulation for an axial impeller (which covers a height of 2*T*/3) is constant and does not depend on impeller diameter (between 0.2*H* and 0.6*H*) or impeller speed (*Re* = 13,500 to 196,000). In the aforementioned study, increasing the impeller speed raised the magnitude of the fluid

velocity values, not the dimensionless trend. The location of the active impeller zone is dependent upon the impeller clearance (C_1) from the tank bottom, as well as the fluid discharge angle and the point at which the fluid impinges upon the wall (Bittorf and Kresta, 2000).

Multiphase flow measurements in the presence of the gas phase were not conducted in this work, however it is generally thought that the impeller speed will have an impact upon the gas phase distribution. Visual observations of two-phase flow have suggested that significant flooding of the impeller is likely to occur in the CellReady bioreactor at impeller speeds below N = 200 rpm (as noted by Kaiser et al. (2011a)). However, the type of impeller was found to have a significant impact upon the bubble breakage efficacy and gas flow pattern (Martín et al., 2008). The impact of a propeller on the gas size distribution within a stirred tank reactor was evaluated by Martín et al. (2008). In this work the propeller is observed deflecting (or redirecting) the bubbles rather than retaining them on the blade and breaking them. The bubble deformation, breakage and coalescence were shown to occur during entrainment of the gas phase beneath the propeller. The presence of two counter-rotating regions of flow in the CellReady suggests that entrainment of the gas phase may occur at impeller speeds higher than N = 200 rpm, thus leading to a broad distribution of bubble sizes and a gradient of oxygen concentration across the height of the vessel.

Figures 3.9 and 3.10 show the variation of the axial and radial ensemble-averaged velocity and r.m.s. velocity, at different impeller speeds (ranging from N = 80 to 350 rpm) and axial locations z/H = 0.150 to 0.231. In this work, velocity and r.m.s. velocity levels vary linearly with impeller speed. The impeller speed has a much greater impact on the radial velocity in the impeller stream, compared to the bulk zone (z/H = 0.231). This difference is much less pronounced with regards to the axial velocity component. In addition, r.m.s. axial and r.m.s. radial velocities closer to the impeller are much more influenced by the impeller speed (r/R = 0.637 and z/H = 0.150), with u'_r/U_{tip} and u'_z/U_{tip} remaining constant and equal to 0.10 and 0.12, respectively, at r/R = 0.637 and z/H = 0.150. Both the r.m.s. axial and r.m.s. radial velocity values reduce down to approximately $0.03U_{tip}$ from z/H = 0.204 upwards (in the vertical plane intersecting r/R = 0.637).

3.3.3 Phase-resolved flow characteristics

The 2-D phase-resolved velocity fields ($\bar{U}_{rz}/U_{tip}$) and contour plots of the tangential component of the vorticity (ω_θ /N) are shown in Figures 3.11 and 3.12 at phase angle increments of 15^o and at N = 120 rpm (Re = 13,048). Periodic fluctuations in velocity fields and vorticity were observed due to the blade passage. It can be noted from Fig. 3.11 that a trailing vortex develops from the tip of the blade at an angle of 15^o after the blade passage, detaching from the tip of the blade at θ = 30^o and decreasing in strength after a complete blade passage (θ = 60^o). The vortex originating from the passing blade is visible in Fig. 3.11b at a location z/H = 0.11 and r/R = 0.78, moving towards the left-hand side as the blade progresses. The trailing tip vortex rotates in an anti-clockwise direction with dimensionless vorticity (ω_θ/N) values of over 40 being measured. Above the impeller blade fluid is ejected outwards axially and radially, whilst beneath the impeller is an influx of liquid upwards towards the blade. The fluid ejected from the blade impinges on the bioreactor inner wall, with a portion of the fluid flowing downwards, thus inducing the counter-clockwise rotating fluid experienced in the lower quarter of the bioreactor. It is noteworthy that in the case of an air sparged bioreactor the counter-rotating flow regimes (composed of the bottom quarter and upper three-quarters of the bioreactor liquid) would result in a larger gas residence time (Sardeing et al., 2004), with air bubbles becoming entrained within the lower ring vortex.

Figure 3.13 shows the locations of the trailing tip vortex centre at varying impeller speeds of 200, 250 and 350 rpm (Re = 21,747, 27,184 and 38,057) and impeller angle increments of 15^o. The radial location of the blade tip vortex was determined by measuring the highest vorticity found in the centre of the tip vortex. The radial movement of the vortex away from the impeller tip (up to a distance of 0.10T from the impeller tip) correlates with the work of Khopkar et al. (2004), where a 6-bladed Rushton turbine (D = T/2) was studied using PIV. It however slightly contrasts with the trailing vortex profile observed by Schaefer et al. (1998) whereby a down-pumping 4-bladed pitched (45^o) turbine in a cylindrical vessel (D = 0.329T) was investigated using LDA. In Schaefer's work, the vortex was noted to spread radially by less than 0.0015T, along with a 20^o downward inclination relative to the horizontal plane. The path of the trailing tip vortex and its wake does not change

significantly as the impeller rate is increased from N = 200 to 350 rpm. The maximum vorticity within the impeller zone is associated with the trailing tip vortex. Given the relatively high impeller to tank diameter ratio present in the CellReady bioreactor, the radial path travelled by the vortex is reasonably small, thus the impact of an increase or decrease in *Re* upon vortex radial trajectory is not significant.

3.3.4 Turbulent kinetic energy and energy dissipation study

The velocity field data presented in Section 3.3.1 have helped elucidate the whole flow field and impeller zone flow pattern and turbulence characteristics occurring in the 3 L CellReady bioreactor. It is now necessary to investigate in more detail the additional flow characteristics near the impeller where the greatest turbulence and stress levels are likely to occur. An important parameter is the turbulent kinetic energy (k). It should be noted that in this work the isotropic assumption was used to determine the third fluctuating velocity component (u_θ) and k was calculated as shown in Chapter 2, section 2.8.

Figure 3.14 shows a contour plot of ensemble-averaged k at N = 200 rpm. The plot indicates a difference of up to 12 times between k in the bulk and impeller zone. k values scaled linearly with U_{tip}^2, in the impeller speed range considered. A maximum k_θ value of up to $0.03U_{tip}^2$ was found from phase-resolved data in the impeller exit stream. The maximum k values obtained in this work are greater than the maximum k of $0.02U_{tip}^2$ observed by Aubin et al. (2004) for an axial up-pumping 6-blade pitched bladed (45^o) turbine. Gabriele et al. (2009) measured turbulent kinetic energy values near a 45^o pitched blade turbine and found a maximum k of $0.071U_{tip}^2$ at a similar distance from the impeller tip (approximately $0.12T$) than that observed in this work (approximately $0.10T$). Figure 3.15 shows the profiles of k with respect to impeller rotation rate (N = 80 to 350 rpm) at axial location z/H = 0.153 and radial locations r/R = 0.616 to 0.969. Figure 3.16 shows the profiles of k with respect to impeller speed (N = 80 to 350 rpm) at radial location r/R = 0.637 and axial locations from z/H = 0.125 to 0.222. Given the horizontal dimensionless profiles presented, it is clear that k scales linearly with U_{tip}^2 at the impeller rates investigated and at the locations represented. However, there is significant spatial variation in the axial direction, which correlates with the significant radial velocity component of the

marine scoping impeller. Therefore, the same conclusion (as determined from Figure 3.10) of a significantly greater influence of the impeller on the impeller stream *k*, compared to the bulk fluid *k* can be drawn from Figures 3.15 and 3.16.

The Reynolds stress field is defined as the apparent stress that results from the mean transport of fluctuating momentum by turbulent velocity fluctuations (Munson et al., 2002). Figures 3.17a and b present the variation of the ensemble-averaged dimensionless Reynolds stress $\frac{(\rho\overline{u_i u_j})}{(\rho\overline{u_i u_j})_{max}}$ and the turbulent kinetic energy within the impeller zone as the impeller rate is increased from 80 to 350 rpm (*Re* = 8,699 to 38,057). Data in Figure 3.17 was obtained by taking the mean of the velocity values obtained at 8 different impeller blade angles. Each data point represents the average of 2000 vector maps. In addition, each data point in Figure 3.17 represents the average of values obtained in the region comprised between *r/R* = 0.57 and 0.77 and *z/H* = 0.11 to 0.13. The ensemble-averaged k/U_{tip}^2, calculated in the impeller zone region between *r/R* = 0.57 and 0.77 and *z/H* = 0.11 to 0.13, remained constant at a value of 0.015-0.016U_{tip}^2 at varying *Re* (Fig. 3.17b). As observed in Figure 3.9, ensemble-averaged velocities values were found to be linear with U_{tip} for the range of Reynolds numbers investigated. In contrast the variation of Reynolds stress with *Re* was found to be exponential. The Reynolds stress can be calculated from the product of the fluctuating components of the instantaneous velocity field, thus the level of Reynolds stress in the bioreactor increases significantly as the impeller rotational speed increases. Values of up to 2.5 Pa at 350 rpm were measured. This is greater than the 0.4 Pa observed for a 3.5 L BIOSTAT® B-DCU STR (*H* = 190, *T* = 0.79*H* and *D* = 0.57*T*) housing a 3-bladed pitched elephant ear impeller at *N* = 150 rpm (Sorg et al., 2011). This is well below the conditions (i.e. > 150 Pa) noted by Godoy-Silva et al. (2009) that results in a fatal response by CHO (GS) cells to the hydrodynamic stress, and lower still than the shear stress (approximately 6 Pa) that resulted in a change in recombinant protein glycosylation profile (Godoy-Silva et al., 2009a).

Figure 3.18 shows the variation of the normalised energy dissipation rate ε/N^3D^2 with *Re* obtained from ensemble-averaged data (within the region *r/R* = 0.54 to 0.79 and *z/H* = 0.13 to 0.17). The dimensionless energy dissipation rate (ε/N^3D^2) decreases as the Reynolds number is increased. Table 3.1 shows maximum energy

dissipation rate data extracted from the previous works of Baldi and Yianneskis (2004); Zhou and Kresta (1996). Baldi and Yianneskis (2004) showed that ε_{max}/N^3D^2 reach values of approximately 11 at the lower Reynolds numbers investigated (15,000 to 20,000), whilst Zhou and Kresta (1996) note values below 3 at Reynolds numbers greater than 37,500. The accuracy of the energy dissipation rate measurement depends on the spatial resolution of the vector fields obtained, thus as the energy dissipation rate increases, the proportion of the actual energy dissipation rate that is measured will decrease (Baldi et al., 2002). Baldi and Yianneskis (2004) used the spatial fluctuating velocity gradients method (Hinze, 1975) to estimate the energy dissipation rate (as is the method used in this study), whereas Zhou and Kresta (1996) used the dimensional method. Therefore, obtaining a method that can estimate the ε to as great an accuracy as possible, will be imperative to enhance comparability between different mixing systems.

Table 3.1: Variation of Maximum Normalised Energy Dissipation Rate (ε_{max}/N^3D^2) at Varying *Re*

	Re	ε_{max}/N^3D^2		***Re***	ε_{max}/N^3D^2		***Re***	ε/N^3D^2
(Baldi and Yianneskis, 2004) Rushton Turbine	15,000	11	(Zhou and Kresta, 1996) Pitched Blade Turbine	37,500	2.47	**This Study** Marine Scoping Impeller	8,699	3.07
	20,000	11		50,400	2.36		10,873	2.83
	25,000	9		60,900	2.62		13,048	2.63
	30,000	10		73,600	2.33		21,747	1.81
	35,000	7		84,000	2.44		27,184	1.59
							32,620	1.34
							38,057	1.07

3.4 Concluding Remarks

The results obtained using the PIV system presented have helped elucidate some of the flow characteristics in the 3 L Mobius® CellReady and their variation with the impeller speed. The upward-pumping 3-bladed impeller within the CellReady engenders two counter-rotating flow regimes. This in turn contributes to the wide range of turbulence levels observed between the lower quarter and upper three quarters of the fluid. The radial dominance of the impeller ensures that the influence of the impeller on flow characteristics (e.g. velocity, turbulence and energy dissipation rate) decreases further from the impeller radial plane. The whole flow

field quantification of hydrodynamic parameters such as turbulent kinetic energy and energy dissipation within a bioreactor using PIV allows a comparative analysis across multiple single-use bioreactor platforms, thus enhancing knowledge of cross-compatibility and scalability of single-use technology. The aim for the future would be to elucidate the fluid dynamic parameters that are both pertinent to cell culture behaviour and applicable to the array of different mixing strategies available on the market. This would engender greater efficacy in scale-up procedures, in addition to cross-compatibility between bioreactor types. The following chapter will examine the hydrodynamic conditions within a dual-impeller rigid stirred bioreactor. This would offer a significantly different environment for investigation, considering the interaction between the two impeller discharge flows.

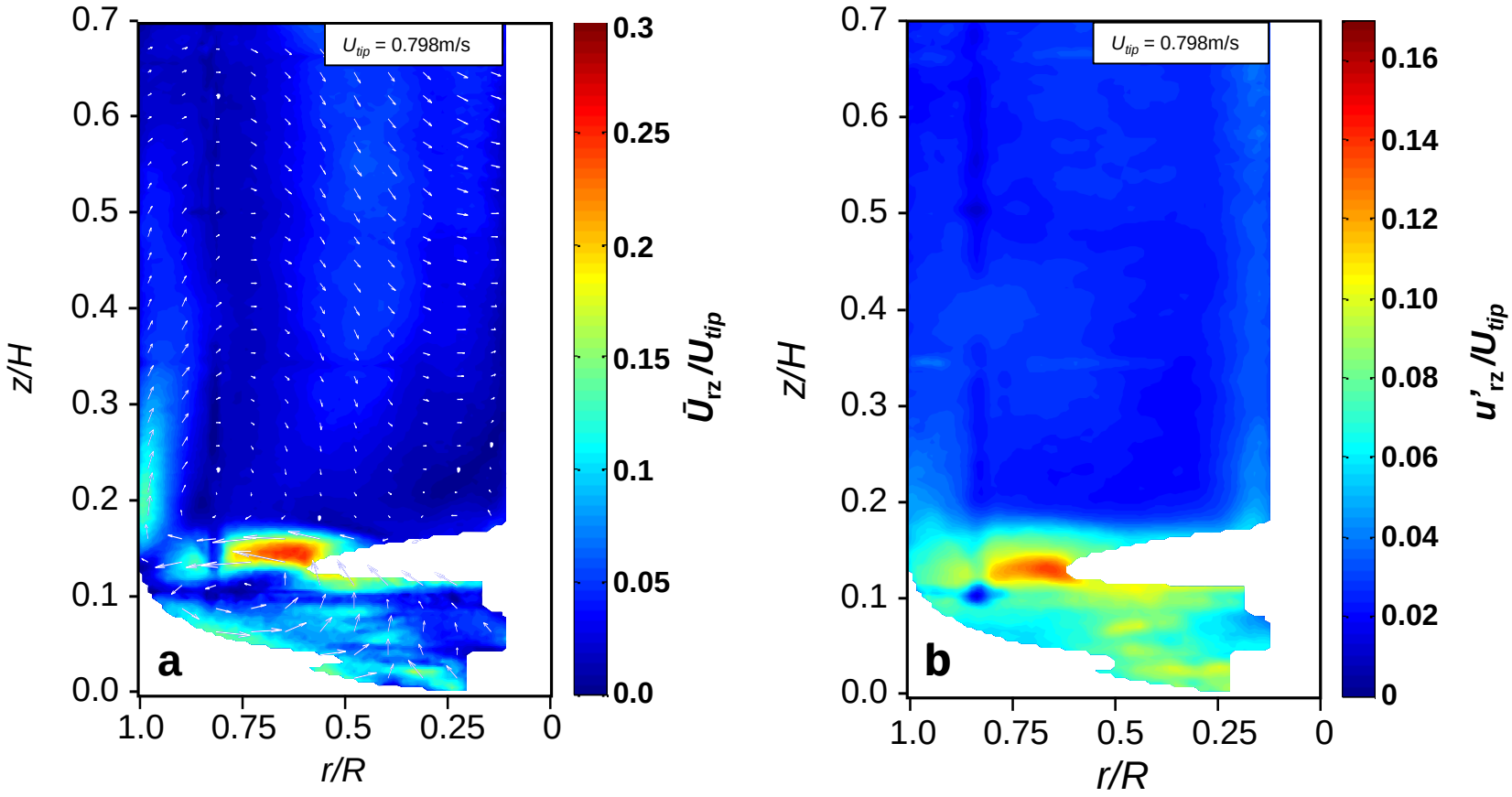

Figure 3.1: a) Ensemble-averaged velocity magnitude contour plot (N = 200 rpm, Re = 21,747, V_L = 2.4 L); b) r.m.s. velocity (in axial and radial direction) contour plot (N = 200 rpm, Re = 21,747, V_L = 2.4 L).

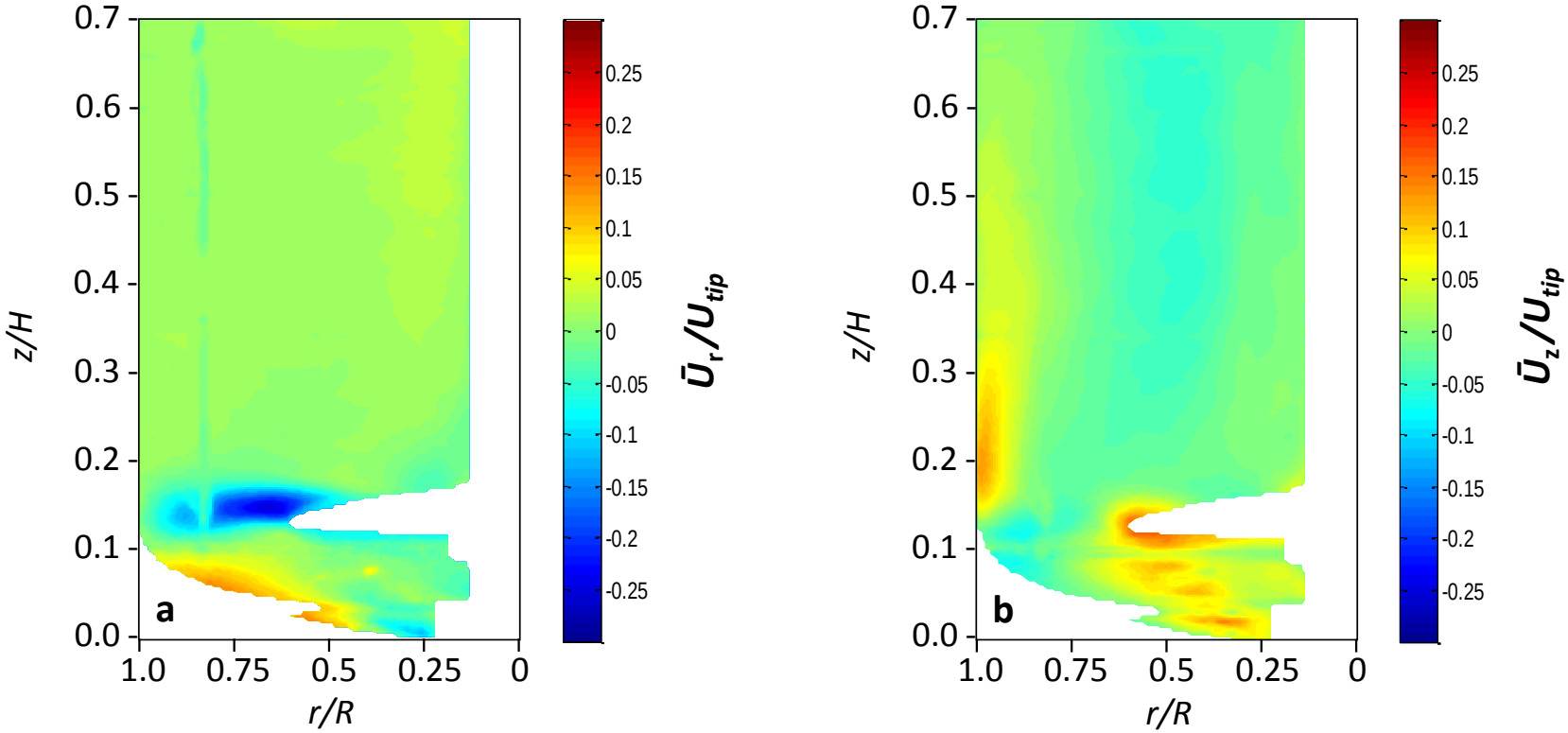

Figure 3.2: a) Ensemble-averaged radial velocity contour plot (N = 200 rpm, Re = 21,747, V_L = 2.4 L); b) ensemble-averaged axial velocity contour plot (N = 200 rpm, Re = 21,747, V_L = 2.4 L).

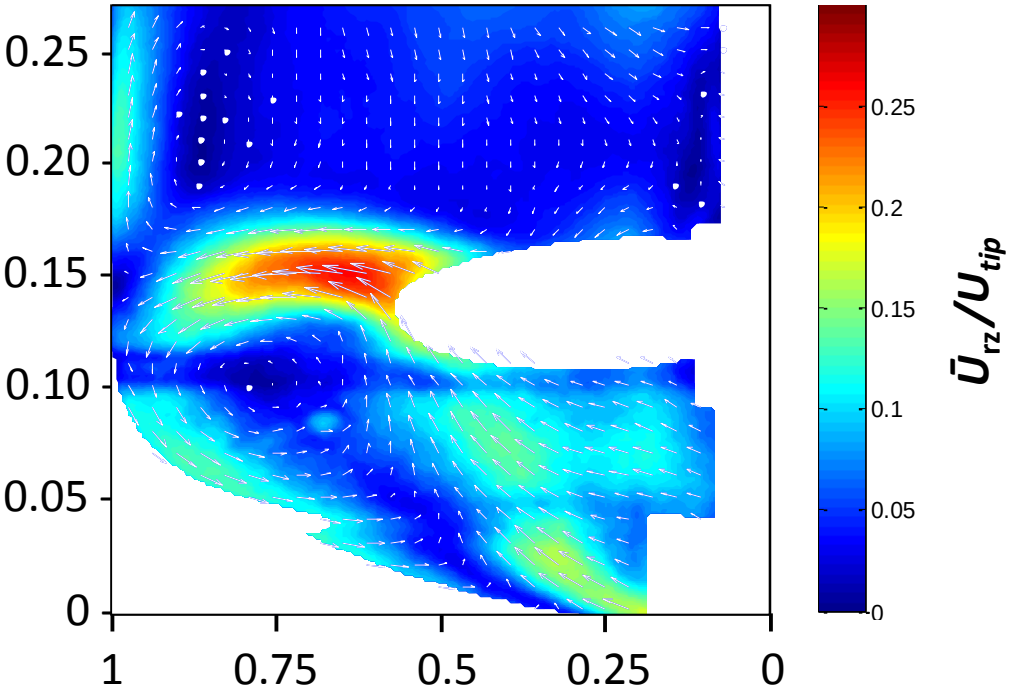

Figure 3.3: Ensemble-averaged velocity contour plot (N = 200 rpm, Re = 21,747, V_L = 2.4 L) with velocity vectors superimposed.

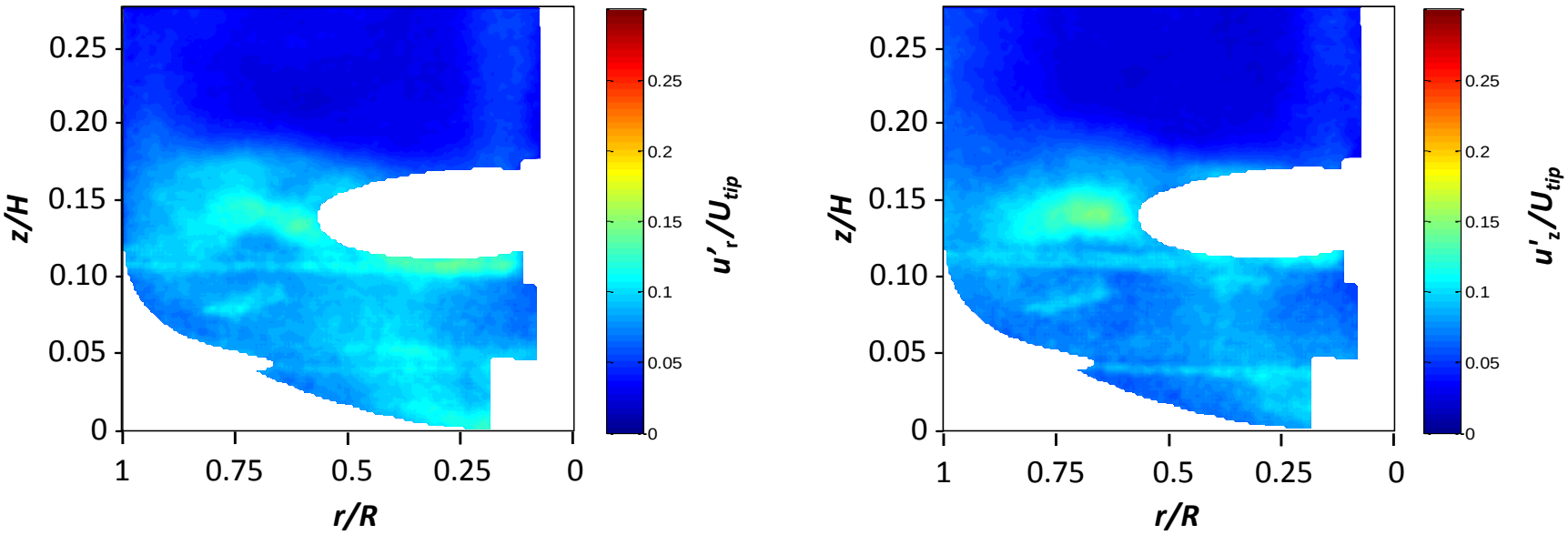

Figure 3.4: a) Ensemble-averaged contour plot of r.m.s. velocity in the radial direction (N = 200 rpm, Re = 21,747, V_L = 2.4 L); b) ensemble-averaged contour plot of r.m.s. velocity in the axial direction (N = 200 rpm, Re = 21,747, V_L = 2.4 L).

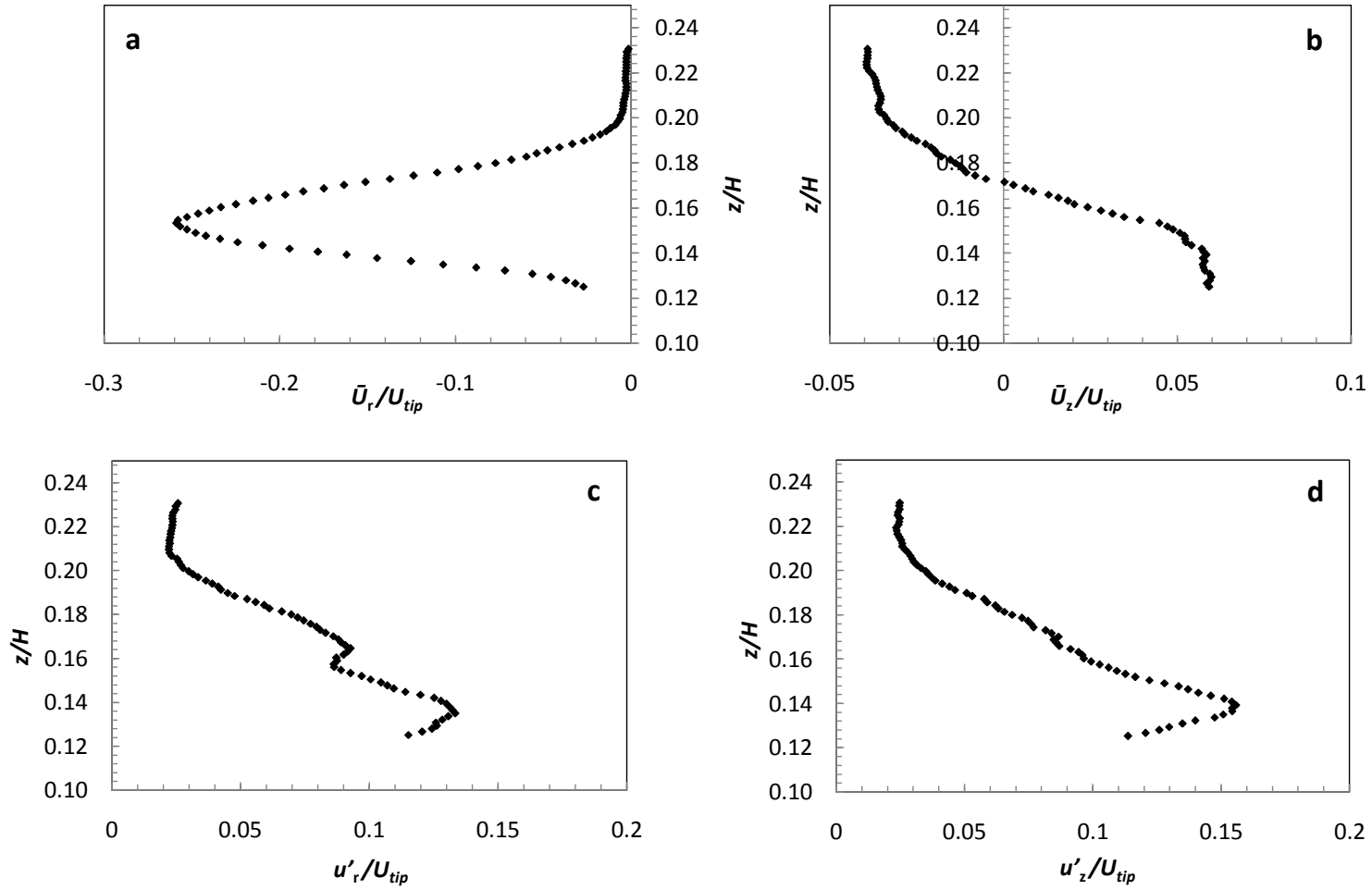

Figure 3.5: Axial and radial velocity and r.m.s. velocity profiles in the impeller exit stream at N = 200 rpm, Re = 21,747, V_L = 2.4 L. Vertical profiles are taken at r/R = 0.637: a) vertical profile of radial velocity; b) vertical profile of axial velocity; c) vertical profile of the r.m.s. radial velocity; and d) vertical profile of the r.m.s. axial velocity.

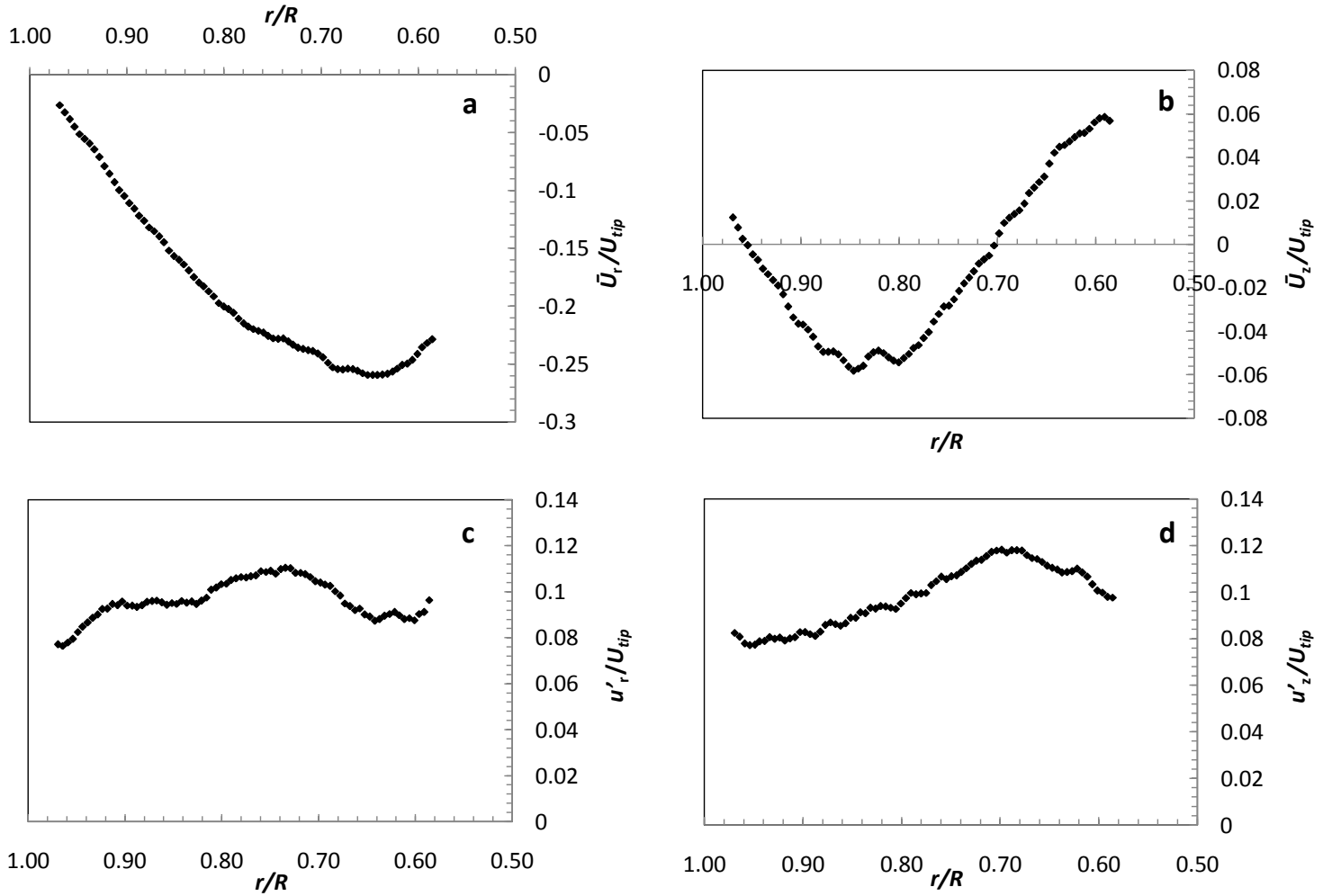

Figure 3.6: Axial and radial velocity and r.m.s. velocity profiles in the impeller exit stream at N = 200 rpm, Re = 21,747, V_L = 2.4 L. Horizontal profiles are taken at z/H = 0.153: a) horizontal profile of radial velocity; b) horizontal profile of axial velocity; c) horizontal profile of the r.m.s. radial velocity; d) horizontal profile of the r.m.s. axial velocity.

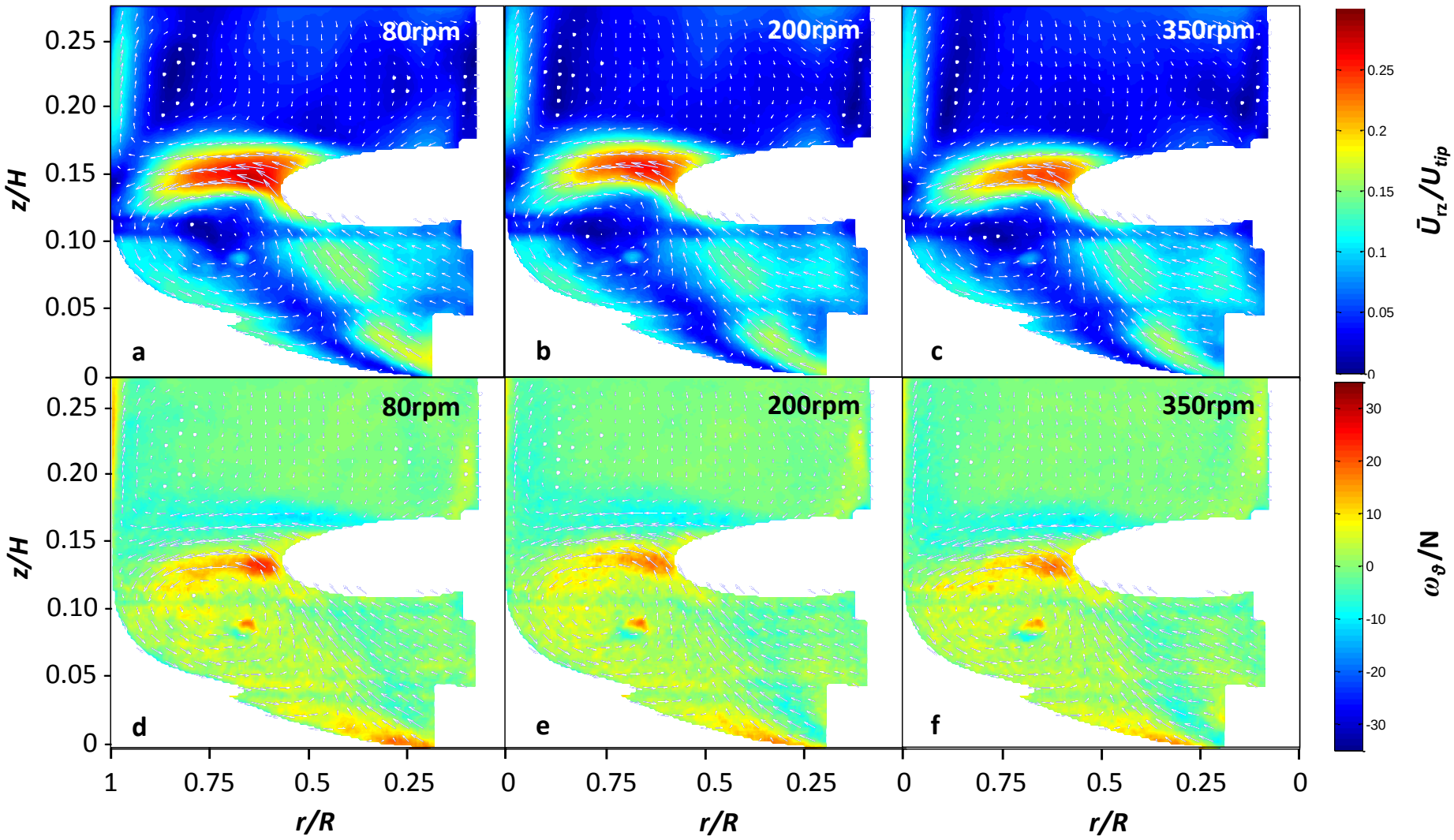

Figure 3.7: Ensemble-averaged velocity magnitude (a-c) and vorticity (d-f) contour plots (N = 80, 200 and 350 rpm, V_L = 2.4 L) with superimposed velocity vectors.

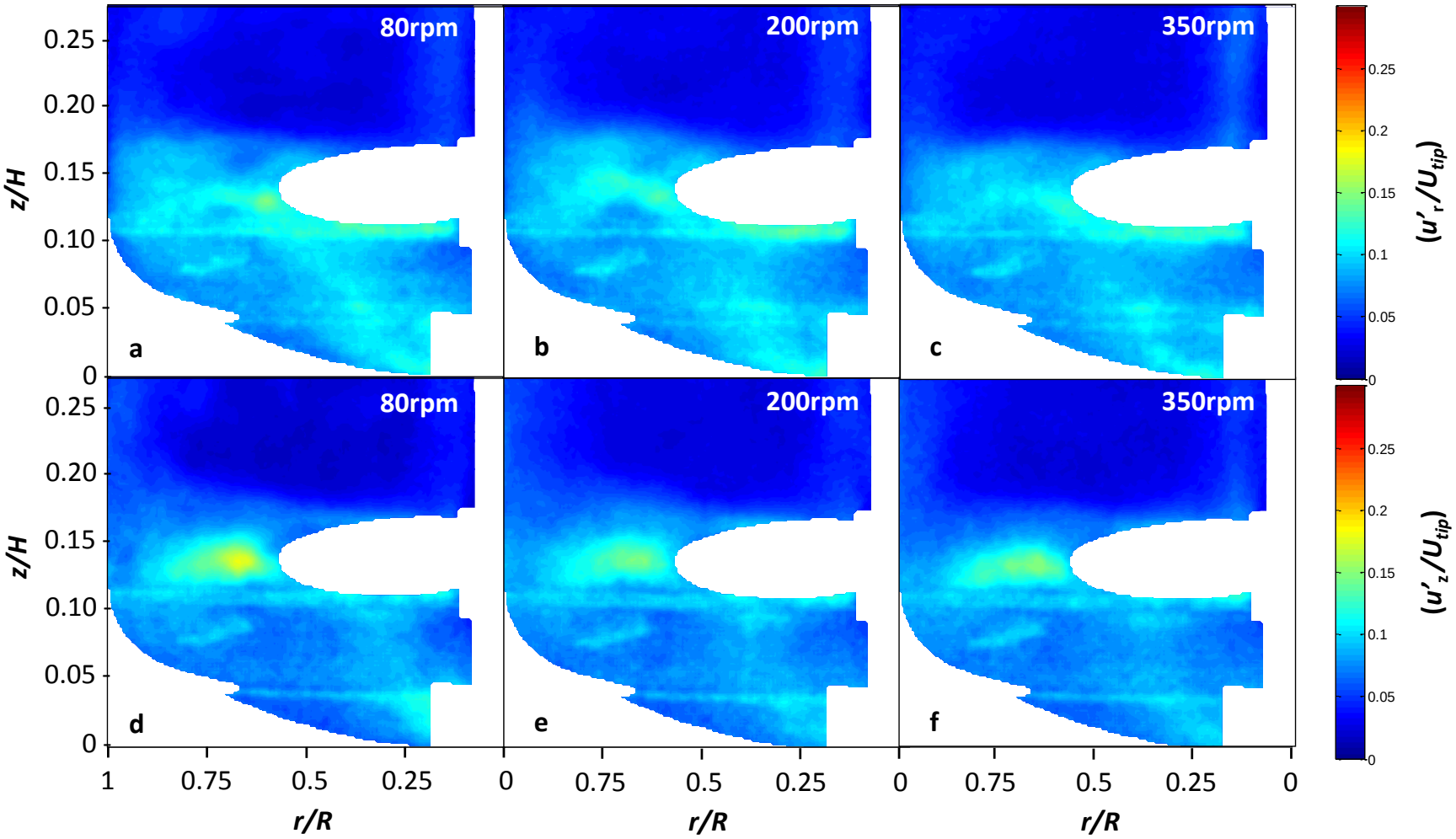

Figure 3.8: Ensemble-averaged contour plots of the r.m.s. axial velocity (a-c) and the r.m.s. radial velocity (d-f). Contour plots obtained at N = 80, 200 and 350 rpm, V_L = 2.4 L.

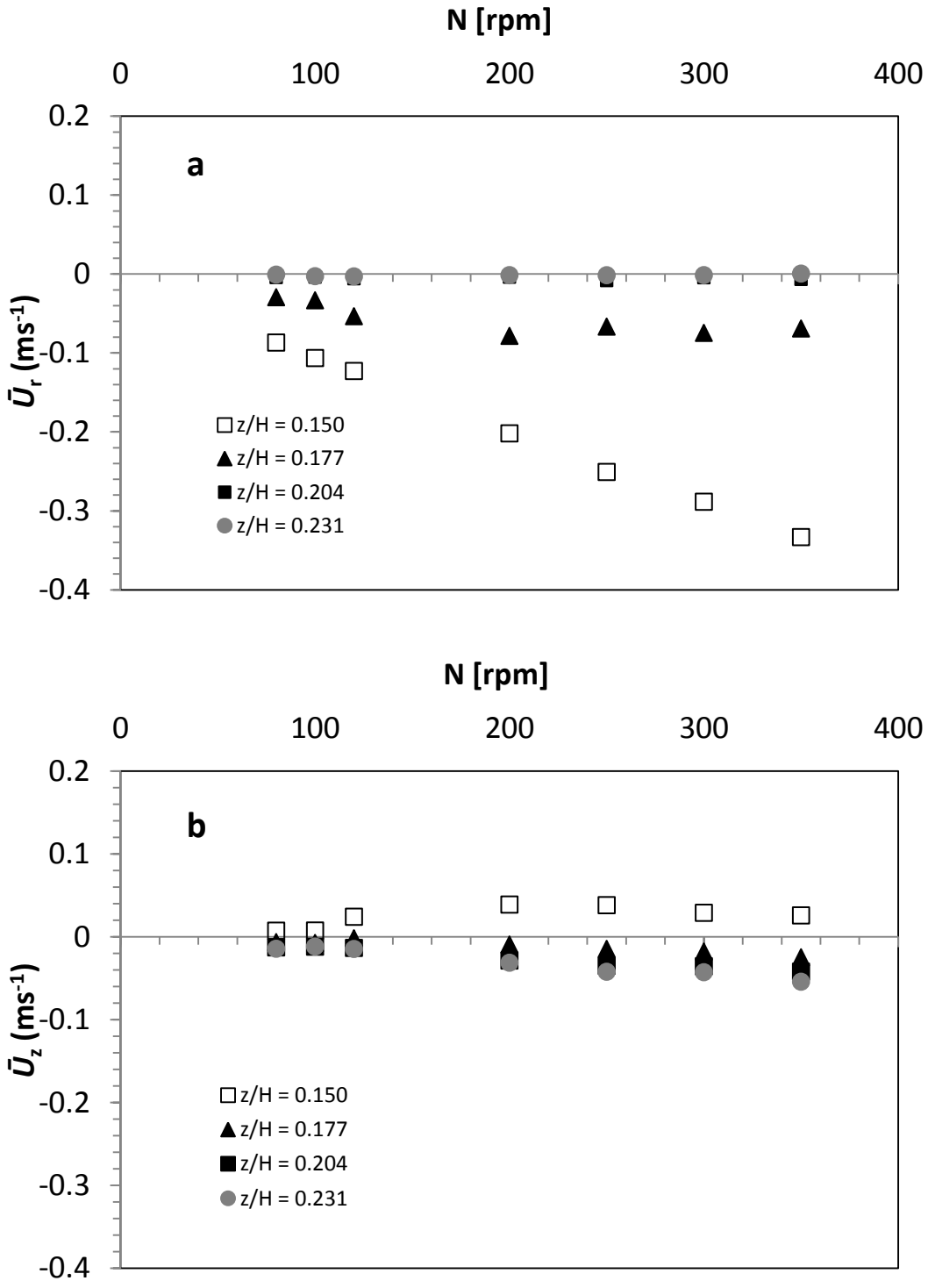

Figure 3.9: Variation of ensemble-averaged radial (a) and axial (b) velocity with impeller speed (rpm) at radial location r/R = 0.637 and different axial locations.

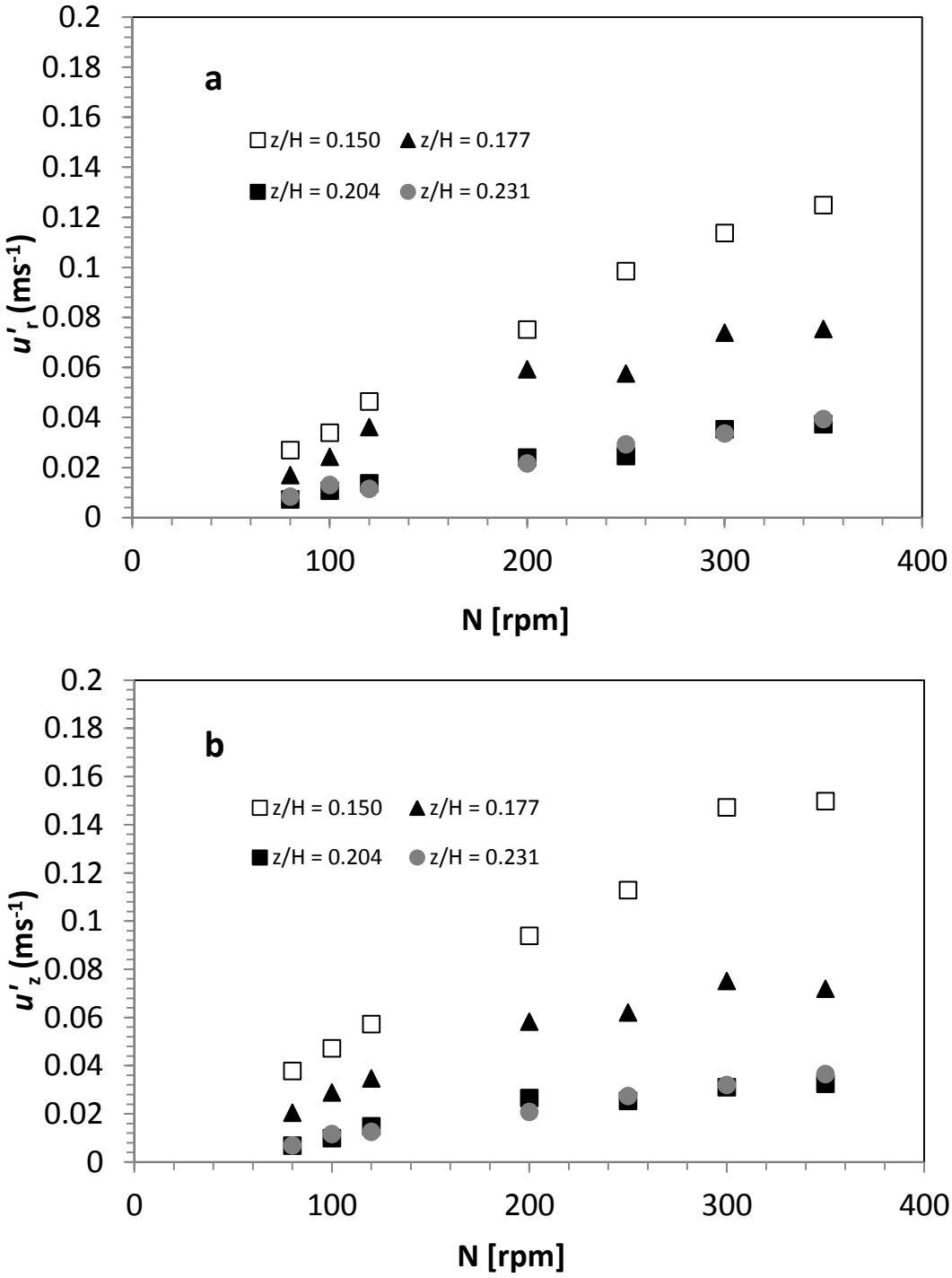

Figure 3.10: Variation of ensemble-averaged radial (a) and axial (b) r.m.s. velocity with impeller speed (rpm) at radial location r/R = 0.637 and different axial locations.

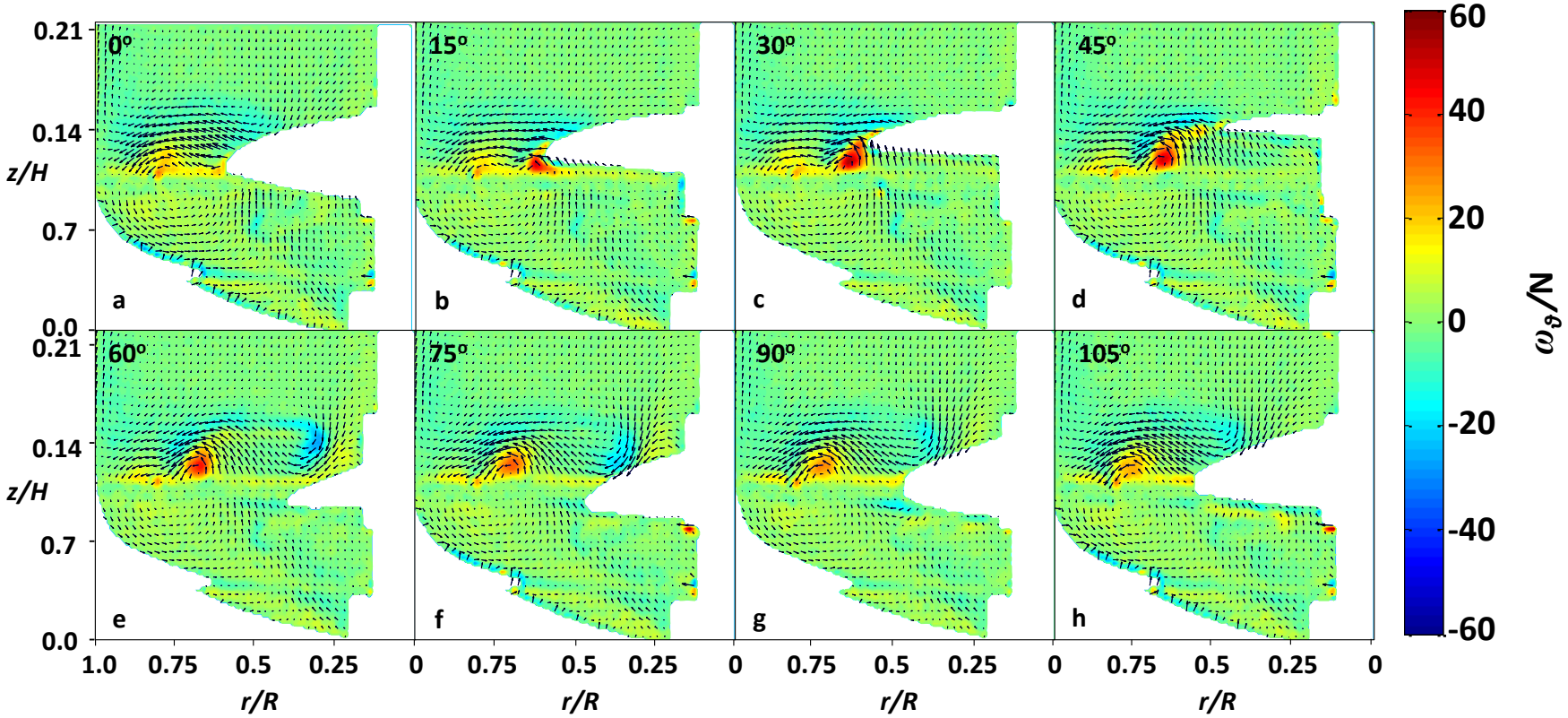

Figure 3.11: Contour plots of phase-resolved vorticity at N = 120 rpm in the vertical plane with angles relative to the leading blade: a) $\theta = 0^o$; b) $\theta = 15^o$; c) $\theta = 30^o$; d) $\theta = 45^o$; e) $\theta = 60^o$; f) $\theta = 75^o$; g) $\theta = 90^o$; h) $\theta = 105^o$.

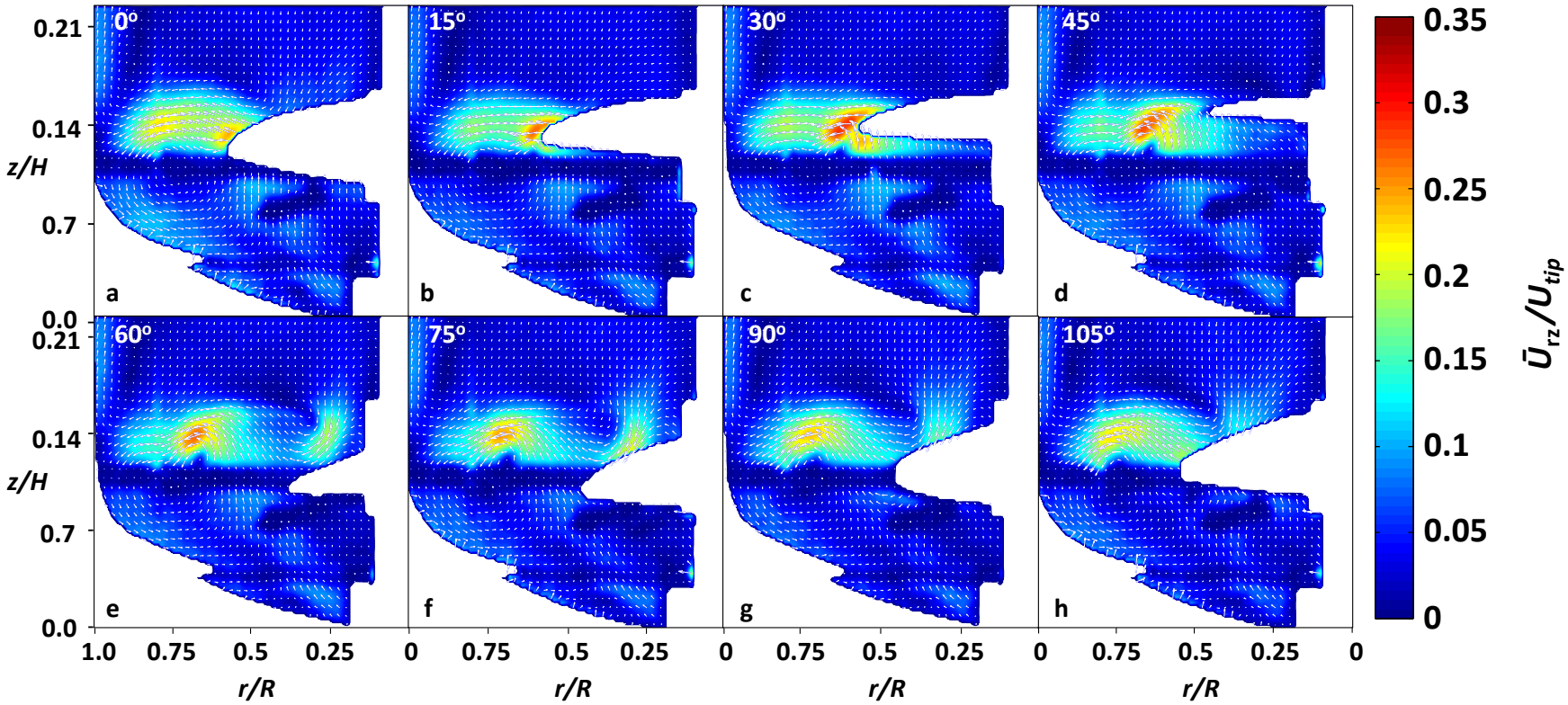

Figure 3.12: Contour plots of phase-resolved velocity magnitude at N = 120 rpm with velocity vectors superimposed, in the vertical plane with angles relative to the leading blade: a) $\theta = 0^o$; b) $\theta = 15^o$; c) $\theta = 30^o$; d) $\theta = 45^o$; e) $\theta = 60^o$; f) $\theta = 75^o$; g) $\theta = 90^o$; h) $\theta = 105^o$.

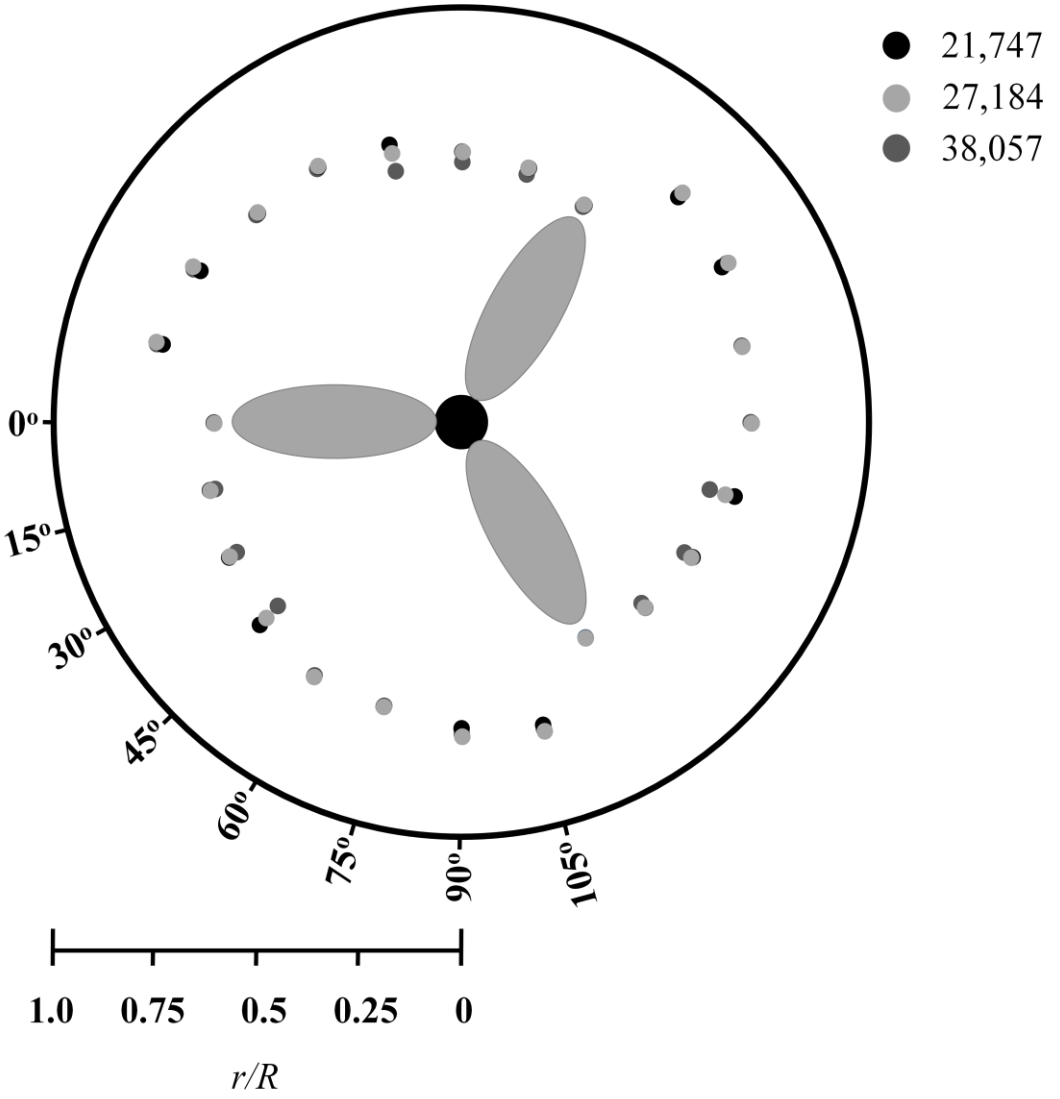

Figure 3.13: The radial location of the trailing tip vortex centre (top-down perspective) at θ = 0°, 15°, 30°,45°,60°,75°,90°, and 105°, for different Reynolds numbers.

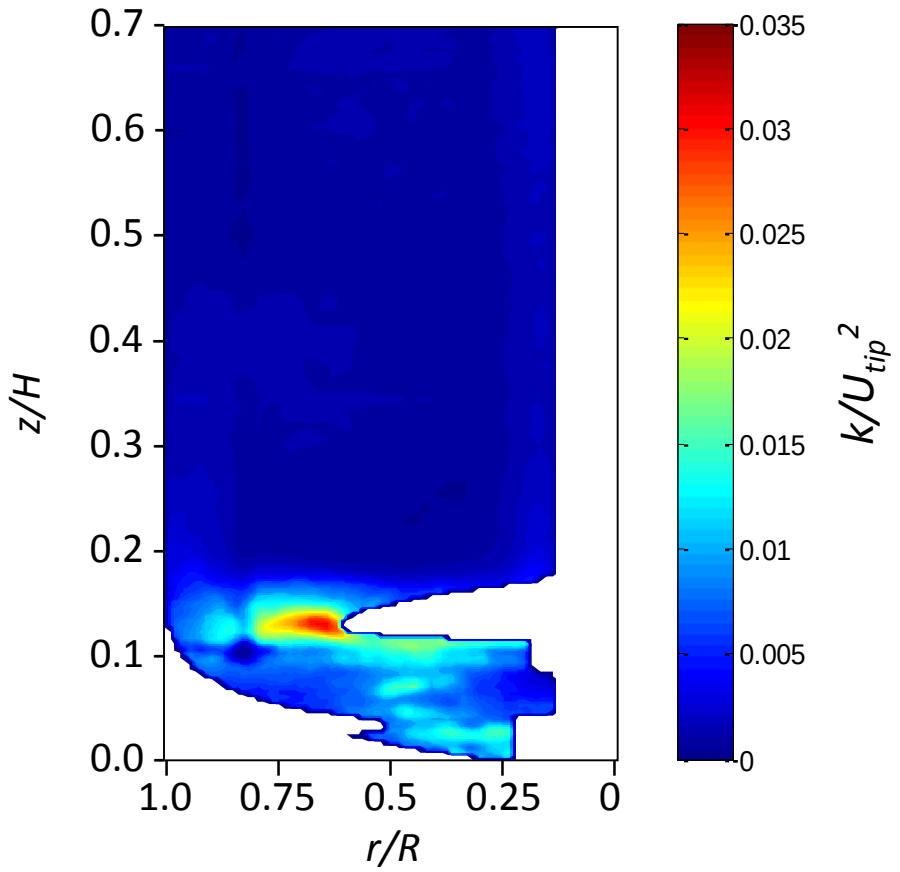

Figure 3.14: Ensemble-averaged turbulent kinetic energy (k/U_{tip}^2) contour plot obtained at N = 200 rpm, Re = 21,747, V_L = 2.4 L.

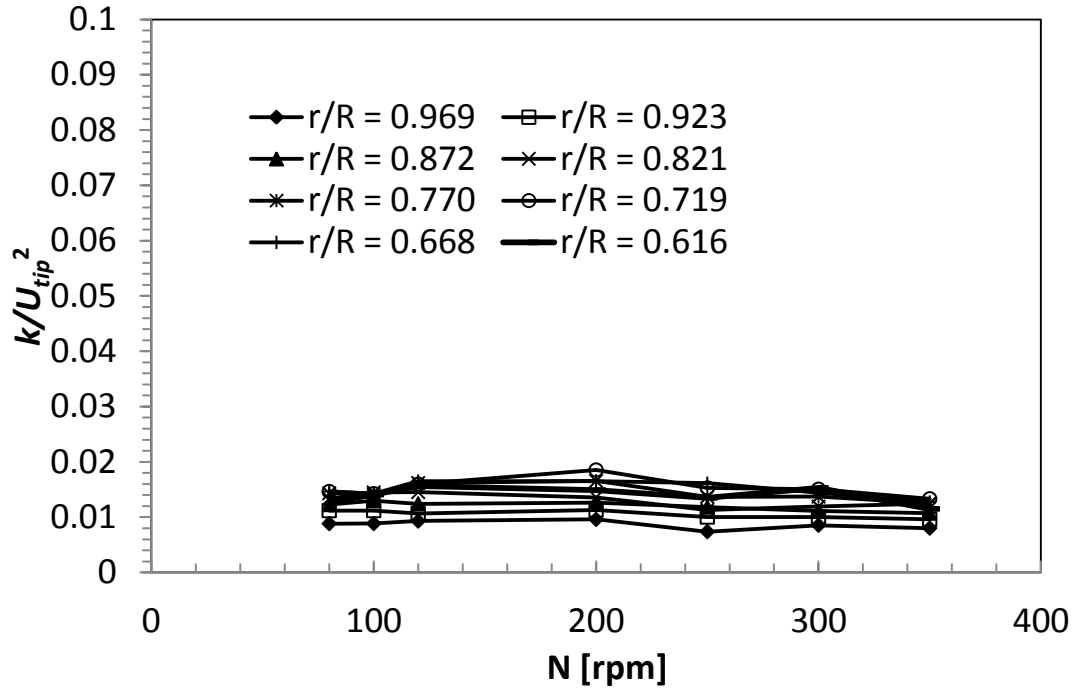

Figure 3.15: Profiles of turbulent kinetic energy with respect to impeller rotation rate (rpm) at position z/H = 0.153. Data is shown for N = 80, 100, 120, 200, 250, 300 and 350 rpm.

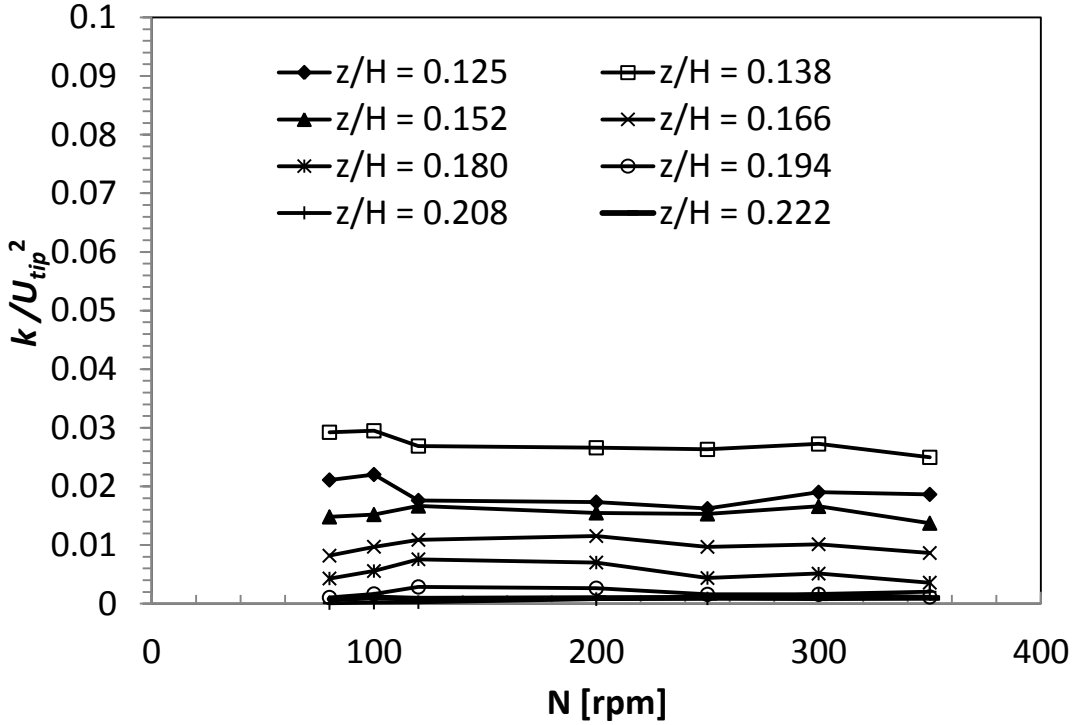

Figure 3.16: Profiles of turbulent kinetic energy with respect to impeller rotation rate (rpm) at position r/R = 0.637. Data is shown for N = 80, 100, 120, 200, 250, 300 and 350 rpm.

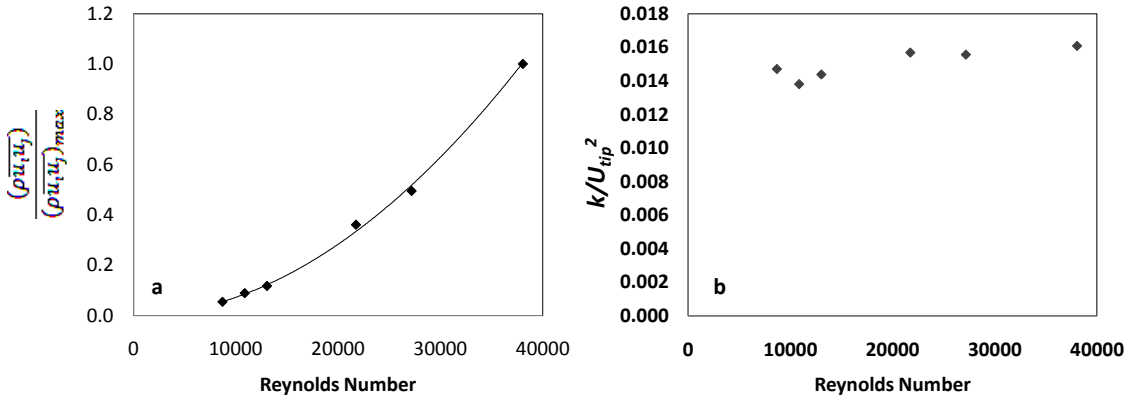

Figure 3.17: (a) Reynolds Stress and (b) turbulent kinetic energy in a selected impeller region.

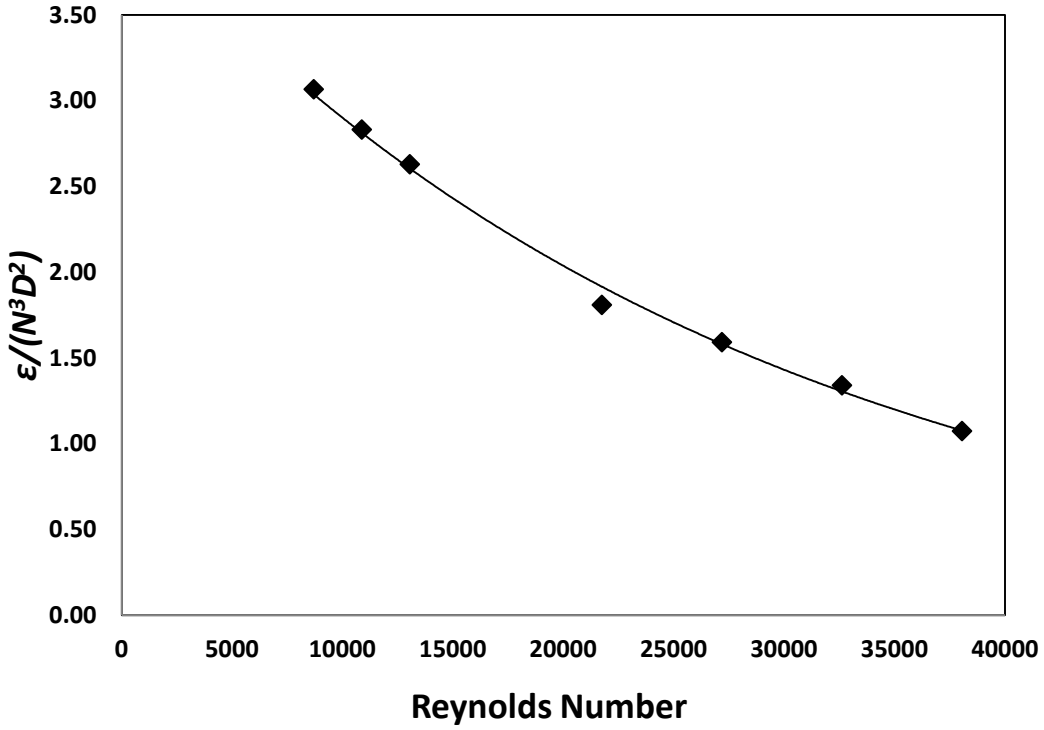

Figure 3.18: Ensemble-averaged ε/N^3D^2 within the impeller region (r/R = 0.54 to 0.79; z/H = 0.13 to 0.17).

Chapter 4 On the Fluid Dynamics of the 2 L UniVessel® SU

4.1 Introduction

The 2 L UniVessel® SU is a stirred double-impeller single-use bioreactor with a fluid working volume range of 0.6 to 2 L (2.6 L total volume). The UniVessel is compatible with the standard bench scale BIOSTATB-DCU-II controller and can be used interchangeably with existing glass vessels. The UniVessel® SU Connection Box, allows the sensors to be interfaced with nearly any bioreactor controller. The bioreactor is suitable for mammalian cells, stem cells, insect cells and plant cells. This system is typically used for process development and optimisation, in addition to the production of seed cultures and cell banks. The BIOSTAT line also includes single-use bioreactors with volumes up to 1000 L (BIOSTAT® STR).

The whole flow field 2-D characterisation of the fluid flow conditions within the 2 L UniVessel® SU was carried out using Particle Image Velocimetry. This study represents the first PIV investigation of a dual-impeller single-use bioreactor, which has the potential of providing better mixing at a greater power input. The PIV study was conducted within a custom-made optically accessible vessel, purposely made for this study by Sartorius Stedim. The vessel has an internal diameter T = 130 mm and height H = 242 mm, and houses a down-pumping dual pitched (30^o) blade segment impeller configuration, with a diameter of 54 mm ($D = 0.42T$). The impellers have a separation of $C_2 = 0.54T$, with an off-bottom clearance of 47.3 mm ($C_1 = 0.36T$).

The dual-impeller configuration is an important aspect of this vessel, as multiple impeller systems are commonly used within larger scale operations (Pan et al., 2008). The interaction between the flow fields generated by each impeller, as well as the energy dissipated by the impellers, can vary between configurations due to impeller geometry, flow direction and spacing. The flow between two Rushton turbines, as measured using Laser Doppler Anemometry (LDA), was found to be strongly influenced by the distance between the two impellers (Rutherford et al., 1996). Velocity distribution was noted to be very different from that of a single impeller when the distance between the impellers was relatively small (Mishra and Joshi, 1994). From an LDA study of a dual Rushton impeller system, Rutherford et

al. (1996) observed that the clearance of the lower blade from the tank bottom (C_1), the separation of the two blades (C_2) and the submergence of the upper impeller from the top of the liquid height (C_3) all strongly affect the flow regime. When these geometric parameters were varied, three stable and four unstable flow patterns were observed. The stable flow regimes were investigated further and characterised as "parallel", "merging" and "diverging" flow patterns. "Parallel" flow exhibited impeller induced vortices acting independently of one another. "Merging" flow showed impeller streams flowing toward each other and merging. The "diverging" flow pattern was observed when a low position was used for the lower impeller, resulting in the production of one large and one small ring vortex by the lower impeller (Rutherford et al., 1996). Flow patterns and turbulence scaled well when comparing vessels of $T = 100$ mm and 294 mm (with $D = T/3$ for both systems). Given the complex flow interactions present at varying geometries and configurations, prediction of the flow characteristics of mixing vessels operating with dual-impeller systems has proved difficult (Rutherford et al., 1996).

This study will aim to improve understanding of the flow pattern, mixing efficiency and velocity characteristics within the UniVessel, and the flow interactions that occur between the two impeller flow discharges. The variation of flow characteristics within the vessel in relation to *Re* will also be presented. The vessel geometry and impeller type used for this bioreactor facilitates comparisons with traditional stirred vessels used in the biopharmaceutical industry for mammalian cell cultures applications. In addition, whole flow field quantification studies using dual-impeller stirred tanks are limited, and even more so studies using pitched blade turbines. Results obtained in this Chapter were collected using the PIV technique described in Chapter 2.

4.2 Whole flow field characteristics

A Particle Image Velocimetry (PIV) system, described in Chapter 2, was used to obtain time-resolved and phase-resolved velocity data. A description of the whole flow field regime in the vertical plane inside the 2 L UniVessel is provided in this section. The first part of the analysis is carried out for a standard configuration corresponding to a fill volume of 2 L. In the subsequent sections, this analysis is

extended to a range of impeller speeds (N = 200 to 400 rpm, Re = 10,904 to 21,808) as well as phase-resolved data (obtained at impeller speeds N = 200 rpm and 400 rpm). Results will be compared with a relevant CFD investigation into the Sartorius UniVessel (Kaiser et al., 2011b), in addition to published works regarding fluid dynamic studies of dual-impeller stirred vessels.

4.2.1 Whole flow field characteristics

The two-dimensional (2-D) ensemble-averaged velocity vector field is given in Fig. 4.1 at N = 200 rpm and Re = 10,904. The figure shows both impellers inducing a downward flow at a trajectory ranging from vertically downwards to -26.5^{o} with respect to the horizontal plane. The fluid flows radially from the lower impeller and impinges on the wall at a vertical position of z/H = 0.13, at which point the fluid divides into two counter-rotating vortices in the regions below and above the lower impeller radial plane. The upper impeller discharges fluid at the same angle, with the lower radial portion of its clockwise rotation fluid present above z/H = 0.35. Flow from the upper impeller does not split at the wall, but continues to flow upwards due to the up-flow of fluid induced by the lower impeller. Figure 4.2 is a contour plot of velocity magnitude (N = 300 rpm, Re = 16,456 and U_{tip} = 0.848 ms^{-1}), with velocity vectors superimposed. The impeller discharge zones are characterised by ensemble-averaged velocities up to 0.35U_{tip}. This value is comparable with the maximum velocities of 0.4U_{tip} in the discharge of a segment pitched blade impeller in a single-use UniVessel®, calculated using CFD (Kaiser et al., 2011b). The vessel used in the aforementioned study houses a dual-impeller combination of a Rushton turbine (RT) lower impeller, and a segment pitched blade turbine (upper impeller). The fact that this study utilises a RT lower impeller, hinders comparison of the whole flow field characteristics of the present study with that of Kaiser et al. (2011b). Zhu et al. (2009) studied a model aerated vessel with a 3-bladed "elephant ear" impeller using PIV. The Elephant Ear impeller was housed by a cylindrical vessel with dimensions; T = 15 cm, D = 0.45T, $T = H_L$, and C = 0.25T. The discharge velocities in both their up-pumping and down-pumping unaerated investigations show good agreement with the present study, with maximum values in the order of 0.4U_{tip} observed. The velocity decreases to about 0.25U_{tip} in the bulk of the impeller discharge fluid, which is higher than the 0.15U_{tip} noted in the bulk clockwise circulation loops of the

UniVessel (r/R = 0.9). However, this reduced velocity value adjacent to the lower impeller (z/H = 0.11, r/R = 0.5 to 0.85) is likely due to the obstructed view around the lower portion of the bioreactor (r/R = 0.11). With regards to the upper impeller induced circulation loop, velocities are reduced in the region around z/H = 0.37 and r/R = 0.56, due to the interaction of the two clockwise circulatory loops induced by the impellers. Ensemble-averaged velocities above z/H = 0.5 were low compared with the impeller discharge zone, with values of approximately 0.04 to 0.07U_{tip} noted. The clockwise rotating fluid (level with the lower impeller) flows towards the upper impellers discharge flow. Due to the close proximity of the two impellers, the radial discharge flow from the upper impeller interacts with the flow induced by the lower impeller at a height of z/H = 0.3 to 0.35. For this reason, the upper impeller discharge flow face greater resistance before it reaches the internal vessel wall. The upward flow close to the vessel wall induced by the lower impeller continues to flow upwards. There is a slight inversion of the flow away from the wall at approximately z/H = 0.35, where the two clockwise rotation loops from both impellers meet and interact further inside the vessel (r/R = 0.70 to 0.45). The flow at the wall then realigns to its vertical direction (from z/H = 0.4 upwards) and continues to flow up the vessel, until its direction becomes radial (at r/R = 0.55) and turns towards the upper impeller.

The maximum velocity magnitude values ($\bar{U}_{rz}$) noted in both impeller discharge zones (0.35U_{tip} and 0.30U_{tip} for the upper and lower impellers, respectively), indicate that the flow generated by upper impeller is slightly greater than that of the lower impeller. This can be explained by the resistance in flow that the lower clockwise flow field faces as a result of the incoming fluid pumped by the upper ring vortex. The "merging" flow conditions caused by the two large clockwise vortex structures, results in an axial component of velocity directly above the lower impeller that is lower than the equivalent region directly above the upper impeller. This greater axial velocity above the upper impeller results in greater momentum, which in turn facilitates a higher impeller discharge velocity.

Figure 4.3 is a contour plot of the ensemble-averaged velocity decomposed to its axial and radial components. The axial velocity component is noted to be dominant in the impeller zone and at the vessel wall. The specific regions being between z/H = 0.15 to 0.3 and z/H = 0.4 to 0.5, both at r/R = 0.90 to 0.75 and 0.50 to 0.25 (at

N = 300 rpm, Re = 16,456). Axial velocities at the impeller attain values of over -0.3U_{tip} (negative values represent downward flow direction), whilst at the wall up to 0.075U_{tip}. This agrees to a certain extent with the work of Zhu et al. (2009) whereby axial velocities in the impeller discharge zone of an "Elephant Ear" impeller attained values of approximately -0.35U_{tip}, whilst the axial fluid velocity at the wall remains in the region of 0.3U_{tip} on the impeller radial plane. The lower velocities at the UniVessel wall may be due to the interaction of clockwise rotating circulatory loops induced by the impellers, since both discharge and wall velocities will experience resistance to their flow.

Figure 4.4 shows contour plots of r.m.s. axial and radial velocity, at N = 300 rpm. The turbulence is observed to be greater for the axial component, with r.m.s. axial velocity values in the region of 0.13U_{tip} (at z/H = 0.10 to 0.72 and r/R = 0.15 to 0.93), whilst r.m.s. radial velocity is noted to be 0.10U_{tip} in the same region. It should be stated that due to the curved nature of the bioreactor base, and the distortion this causes, the level of turbulence and velocity measured in the region below z/H 0.10 is reduced. The r.m.s. axial and r.m.s. radial velocities measured were equivalent for both the discharge and the suction zone. This is in contrast to the work of Khan et al. (2006) where both 2-D and 3-D PIV were used to measure the velocity characteristics in a stirred tank with a four bladed down-pumping PBT (45^o), four baffles, T = 290 mm, D = T/3 and an impeller clearance C_1 = T/3 from the base of the tank. R.m.s. axial and radial velocity in the impeller discharge stream were 0.21 and 0.15U_{tip}, respectively, whilst above the impeller in the suction zone, r.m.s. axial and radial velocity were approximately 0.06 and 0.09U_{tip}, respectively, from 2-D PIV measurements (Khan et al., 2006).

4.2.2 Phase-resolved velocity and vorticity characteristics

The 2-D phase-resolved velocity fields ($\tilde{U}_{rz}/U_{tip}$) and contour plots of the vorticity around the tangential axis (ω_θ/N) are shown in Figures 4.5 and 4.6 at phase angle increments of 15^o and at N = 200 rpm (Re = 10,904), allowing periodic changes to the velocity fields and vorticity to be observed. The phase-resolved velocity measurements indicate that the maximum impeller induced velocities occur at angular positions θ = 60 to 105^o), near the impellers (in the radial region of

r/R = 0.30). These velocities extend to a radial location of r/R = 0.38. This differs considerably from the flow observed within the CellReady (shown in Chapter 3), in which the maximum impeller induced velocities extend from the impeller tip (r/R = 0.5) to r/R = 0.75, over the course of a single impeller revolution. This indicates that the high velocity impeller discharge fluid reduces quite abruptly at r/R = 0.4. This is likely due to the increased turbulence and flow resistance in the bulk fluid caused by the interacting impeller induced flow regimes.

In Fig. 4.6 the (clockwise rotating) trailing vortex is observed originating from the tip of the blade at an angle of 60^o after the leading blade passage at location z/H = 0.44 and r/R = 0.45, with its wake remaining close to the blade as the impeller rotates. Once fully emerged, the radius of the vortex remains constant as the impeller rotates, with a consistent dimensionless angular rate of rotation of ω_θ/N = -12 (negative vorticity values represent clockwise rotation). The vortex does not migrate radially by a significant distance from the impeller tip, and appears to follow the circumferential path of the impeller blade. Schaefer et al. (1998) used PIV to investigate vortical structures around a down-pumping 45^o PBT in a vessel of T = 152 mm, D = 0.329T, C_1 = 0.33T and four baffles 0.1T in width. This study found that the trailing vortex originates at the side and upper tip of the blade, and that the radius of the trailing tip vortex decayed linearly as the impeller rotated. The vortex axis extends radially by less than 0.0015T, and was inclined by 20^o relative to the horizontal axis, whilst the circumferential velocity around the trailing vortex edge was up to 0.55U_{tip} (Schaefer et al., 1998). Ensemble-averaged vorticity in the present study attained values of approximately 37.5 s^{-1} at N = 300 rpm, whilst maximum dimensionless vortices remained in the region of ω_θ/N = 7 to 10 in the impeller discharge zone for the range of impeller speeds investigated (N = 200 to 400 rpm). This compares well with Zhu et al. (2009), where ensemble-averaged vorticity in their "Elephant Ear" stirred system were in the region of 30 to 40 s^{-1} (this measurement was taken at N = 300 rpm, thus a dimensionless vorticity of ω_θ/N = 6 to 8) in the impeller discharge zone.

4.3 Flow variation with respect to Re

Figure 4.7 shows velocity vector plots of the fluid at N = 200, 250, 300, 350 and 400 rpm. Here, the dominance of the axial velocity at the impeller discharge zone becomes more pronounced as the impeller rate increases. As a result, the lower clockwise circulatory loop reduces from a vessel height of z/H = 0.35 (at Re = 10,904) to z/H = 0.25 (at Re = 21,808), due to the down-flow produced by the upper impeller. This causes significant spatial variation of the fluid velocity. The variations in flow pattern can be explained by the positioning of the lower impeller. Fluid accelerated radially by the lower impeller, divides at the bioreactor wall to flow in both upward and downward directions. This division in flow creates an counter-clockwise flow structure as well as the clockwise flow already mentioned. As a result, the upper impeller discharge stream possesses greater momentum, upon contact with the circulated fluid originating from the lower impeller. This difference in momentum flux becomes more pronounce at the higher impeller speeds. Promoting further "merging" flow conditions, and ensuring enhanced distribution of turbulent flow throughout the vessel.

The interaction between the two primary circulatory loops (causing the "merging" regions of fluid flow) is present from the lowest impeller rate of N = 200 rpm. For this reason, the dimensionless r.m.s. velocity in the upper, midpoint and lower impeller discharge zones, remain constant between impeller speeds of N = 200 to 400 rpm. Figure 4.8 shows the mean r.m.s. axial and radial velocity in the upper impeller zone (UIZ), midpoint impeller zone (MIZ) and lower impeller zone (LIZ). The UIZ refers to the region within z/H = 0.44-0.48 and r/R = 0.39-0.51, the MIZ is the area within z/H = 0.31-0.34 and r/R = 0.39-0.51 and the LIZ is the region comprising z/H = 0.16-0.19 and r/R = 0.39-0.51. The figure shows a linear increase of r.m.s. (axial and radial) velocity in the range of impeller rates investigated. There is relatively little difference between the r.m.s. radial velocities in the different zones highlighted (1-10%), however there is greater disparity regarding r.m.s. axial velocities. At N = 200 rpm, a difference in r.m.s. axial velocity of up to 40% is noted, which then reduces at the higher impeller rates (1-15% difference at N = 400 rpm). Furthermore, regarding turbulence levels at the higher impeller rates, there is greater spatial spread of the maximum turbulence levels from the impeller to the

bioreactor wall. Augmenting the spatial uniformity of turbulence levels in the fluid. This was also observed in Devi and Kumar (2013), where CFD was used to observe a "merging" flow regime induced by a dual-Rushton turbine (6 blades) stirrer with a separation of $C_2 = 0.315T$. Their CFD investigation of the dual-impeller system indicate that maximum turbulence occurred in close proximity to the blade in non-"merging" conditions, whilst the maximum turbulence encompassed a much broader spatial region, between the impellers during "merging" flow conditions. This observation only occurred when the impeller spacing was at the lowest in their investigation ($C_2 = 0.315T$), which was much smaller than the $C_2 = 0.54T$ in the UniVessel. The study suggested that a 6-bladed CD-6 (concave impeller) dual-impeller system would require a closer proximity of impellers in order to observe the required "merging" flow interactions, thus highlighting the importance of impeller type as well as proximity in observing the different flow structures in dual-impeller systems (Devi and Kumar, 2013).

Figures 4.9 and 4.10 show radial profiles of dimensionless axial and radial velocity ($\bar{U}_z/U_{tip}$ and $\bar{U}_r/U_{tip}$) in the upper and lower impeller planes, with values given at impeller speeds of N = 200, 250, 300, 350 and 400 rpm. The profiles extend from radial locations r/R = 0.21 to 0.91 at axial locations of z/H = 0.47 and z/H = 0.20 for the upper and lower impeller planes, respectively. With regards to the axial velocities, the radial variation of velocity scale well from N = 200 to 300 rpm, with high downward velocities of approximately $-0.3U_{tip}$ occurring at a radial location of r/R = 0.37 for both impeller planes. This high downward axial velocity then shifts from a radial location of r/R = 0.38 to 0.35 (at N = 350 and 400 rpm), again for both impeller planes. Regarding the lower impeller plane, the maximum velocities remain constant for all impeller speeds. However, in the upper impeller plane, the maximum downward axial velocities increase from $0.30U_{tip}$ to approximately $0.33U_{tip}$ at N = 350 to 400 rpm. These results indicate the shift in the axial component of velocity close to the impeller as the agitation rate increases to 350 and 400 rpm, putting a greater downward flow upon the lower ring vortex. The radial profiles of the radial velocities show greater variation with impeller speed. Radial profiles are relatively consistent again for impeller speeds N = 200 to 300 rpm, where velocities at r/R = 0.20 are approximately $-0.30U_{tip}$ in both impeller planes. These velocities then change direction towards the bioreactor wall and attain values of up to $0.2U_{tip}$.

This changes dramatically at impeller speeds of N = 350 and 400 rpm, for both the upper and lower impeller plane. At z/H = 0.20, the direction of radial flow alternate between r/R 0.20 to 0.68, after which the flow stabilises close to zero towards the wall. Regarding the upper impeller plane (z/H = 0.47), radial velocities start at $0.008U_{tip}$ at r/R = 0.20, and then shift in direction to a value of $-0.06U_{tip}$ at r/R = 0.49, before which the fluid changes direction again with a velocity of up to $0.01U_{tip}$ towards the vessel wall. Both Figures 4.9 and 4.10 indicate that the increase in impeller rotation rate has a more significant impact upon the fluid flow regime induced by the upper impeller.

Figures 4.11 and 4.12 show the r.m.s. axial and r.m.s. radial velocity profiles, at the same location as the ensemble-averaged axial and radial velocities shown in Figures 4.9 and 4.10. For the Reynolds numbers tested, the r.m.s. profiles at N = 200, 250 and 300 rpm are consistently similar, however, a shift in turbulence distribution takes place at N = 350 and 400 rpm. As noted in Figure 4.11, u'_z/U_{tip} profiles presented in both impeller planes selected, show a significant drop (commencing at a radial location of r/R = 0.48) from u'_z/U_{tip} = 0.14, to as low as 0.04 (at r/R = 0.74) towards the bioreactor wall (at N = 200 to 300 rpm). However, as the impeller rate increases to N = 350 rpm the profiles change. Extending from r/R = 0.47 to 0.74, the u'_z/U_{tip} decreases to a lesser degree and attains greater values (than at N = 200 to 300 rpm) with u'_z/U_{tip} = 0.10 at r/R = 0.74. The u'_z/U_{tip} profile at z/H = 0.20 begins to decrease closer to the impeller (from r/R = 0.32) when the impeller rate is increased to N = 350 and 400 rpm. Thus, the upper impeller appears to produce axial turbulence with greater spatial homogeneity (when the impeller rate is increased), whilst the lower impeller shows a shift in the turbulent flow structure when *Re* increases. Similar features are observed in Figure 4.12, with a greater degree of uniformity observed at the upper impeller plane (z/H = 0.47) at the higher impeller rates (N = 350 and 400 rpm), whilst the reduction in r.m.s. radial velocity away from the lower impeller is slightly more pronounced than its r.m.s. axial velocity counterpart. Again the interacting flow regimes would have a role to play in the disparity seen in the radial profiles of r.m.s. velocity in both impeller planes. With the upper impeller generating greater velocities and spatial uniformity of r.m.s. velocity, whilst the lower impeller maintains similar velocity and turbulence throughout the impeller rpm range, along with a more compact circulatory loop. This

difference in flow regime at agitation speeds N = 350 and 400 rpm, as highlighted in Figure 4.7, is caused by the positioning of the lower impeller; and the division in fluid momentum produced as the lower impeller flow discharge impinges upon the wall.

4.3.1 Ensemble-averaged vs. phase-resolved TKE

Figure 4.13 shows contour plots of dimensionless turbulent kinetic energy (k/U_{tip}^2) from ensemble-averaged time-resolved measurements at both N = 200 and 400 rpm. Ensemble-averaged k measurements indicate maximum values of approximately $0.025U_{tip}^2$ in the region surrounding the impellers. These values are in agreement with the $k_{max} = 0.025U_{tip}^2$, determined by Zhu et al. (2009) for an unaerated down-pumping "Elephant Ear" stirrer. Within the UniVessel, at N = 200 rpm, the maximum k reduces significantly past r/R = 0.4, and does not extend axially beyond the height of the impellers. At higher impeller rates, the spatial spread of the higher k values increase. The k values of $0.02U_{tip}^2$ associated with fluid in the proximity of the blades, extend to a radial location of r/R = 0.5, as well as axial extension from z/H = 0.1 to 0.65.

The spatial distribution of ensemble-averaged k increases from N = 200 to 250 rpm, and remains relatively constant beyond N = 250 rpm. The ensemble-averaged phase-resolved and ensemble-averaged time-resolved turbulent kinetic energy contour plots are shown in Figure 4.14, for N = 400 rpm. Both plots maintain similar values of k/U_{tip}^2, in particular in the bulk fluid. As was indicated in the previous section, the maximum velocities noted in Figure 4.5 at varying impeller angular positions, do not extend radially by a significant amount. Given that the phase-resolved ensemble-averaged k, represents the turbulent kinetic energy with the impeller induced periodic component of fluctuating velocity removed (leaving only the random turbulence), the similarity in both the ensemble-averaged time-resolved and phase-resolved k indicates that fully turbulent conditions exist in the bulk of the fluid, with both impeller induced flows simultaneously interacting as the impeller rotates. This subsequently leads to the maximum turbulence levels being present in a greater proportion of the fluid, and further highlights the importance of the "merging" flow

resulting from the proximity of the two impellers (as observed by Rutherford et al. (1996)).

4.4 Concluding remarks

Application of PIV to investigate the flow within a dual-impeller PBT (30^o), has enabled a unique insight into a bioreactor configuration used at a variety of production scales. Dual-impeller systems are typically used for larger scales of operation as opposed to bench-scale systems, thus allowing for enhanced understanding of the flow regime akin to that of pilot-scale operations.

Previous laser-based investigations into dual-impeller systems are few and typically conducted in tanks agitated by Rushton turbines (Mishra and Joshi, 1994; Rutherford et al., 1996), whereby both stable and unstable flow regimes have been observed. The PBT (30^o) employed within the 2 L UniVessel and the proximity between the two impellers induce "merging" flow regimes, in which interacting flow structures create high turbulence zones (with reduced velocity) encompassing a broader spatial scale than that of a single-impeller system (Zhu et al., 2009). This creates a more narrow range of r.m.s. velocity values within the fluid, resulting in greater consistency when comparing whole-field turbulence at different agitation rates. It should be noted, that certain artefacts have obstructed a completely clear view of certain regions i.e. the curved base of the bioreactor, or the light distortion present in the outer region of the bioreactor.

Although turbulence levels remain consistent, the interacting flows cause a distinct change in the flow regime at varying impeller rates, with the axial component of the upper impeller compressing the clockwise rotating fluid pumped by the lower impeller. This would have implications for varying the flow path of cells and the gas phase. The change in flow regime in the lower ring vortex could cause the fluid being pumped by the lower impeller to not fully circulate, and for the fluid to simply travel up the side of the vessel (or flow in the low velocity area where the flow interaction occurs), until it reaches the top of the vessel and subsequently directed downwards by the upper impeller. All these considerations and observations are important for understanding the flow conditions experienced by animal cells.

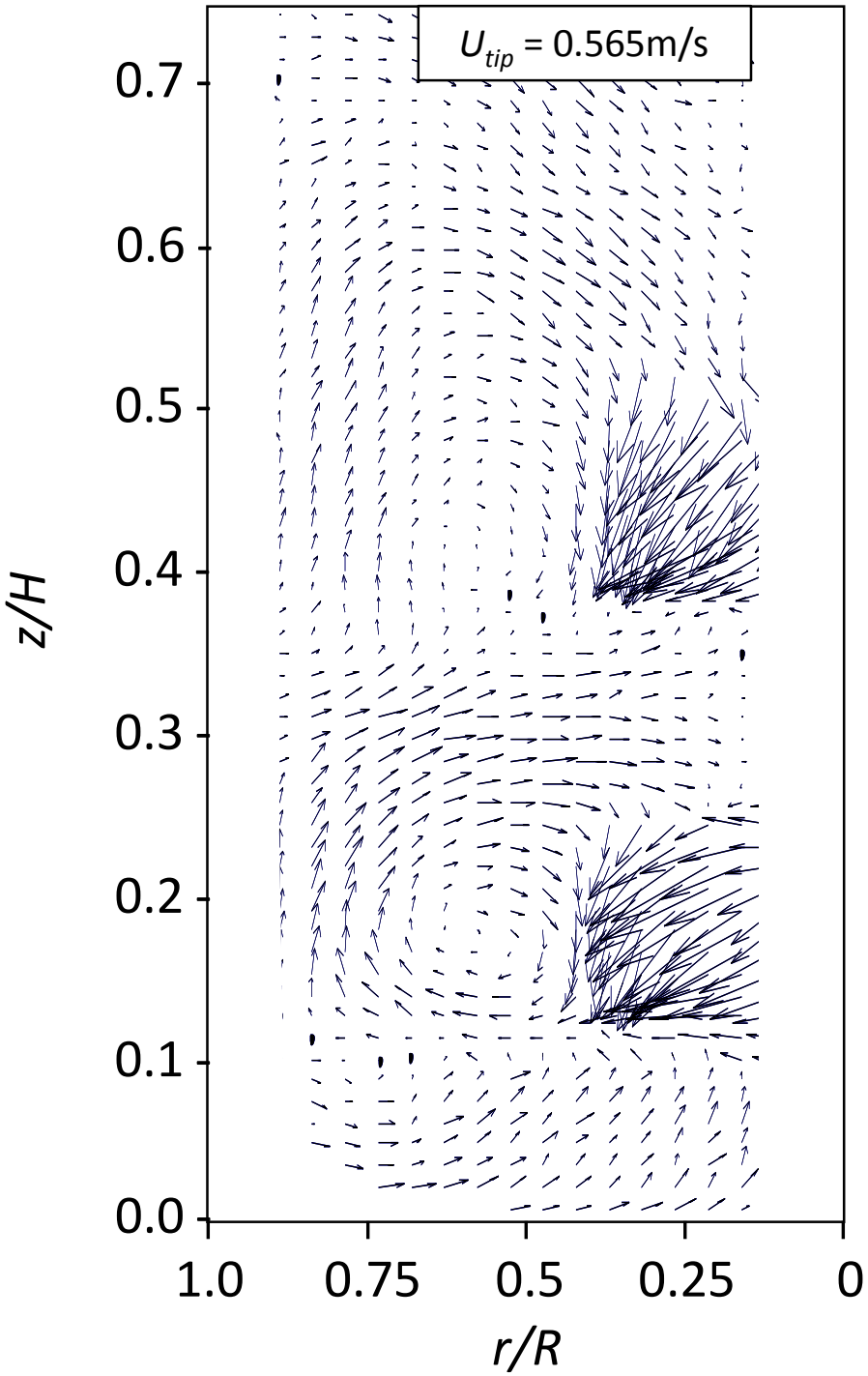

Figure 4.1: Ensemble--averaged vector plot of fluid velocity magnitude at N = 200 rpm (Re = 10,904 and U_{tip} = 0.565 ms^{-1}).

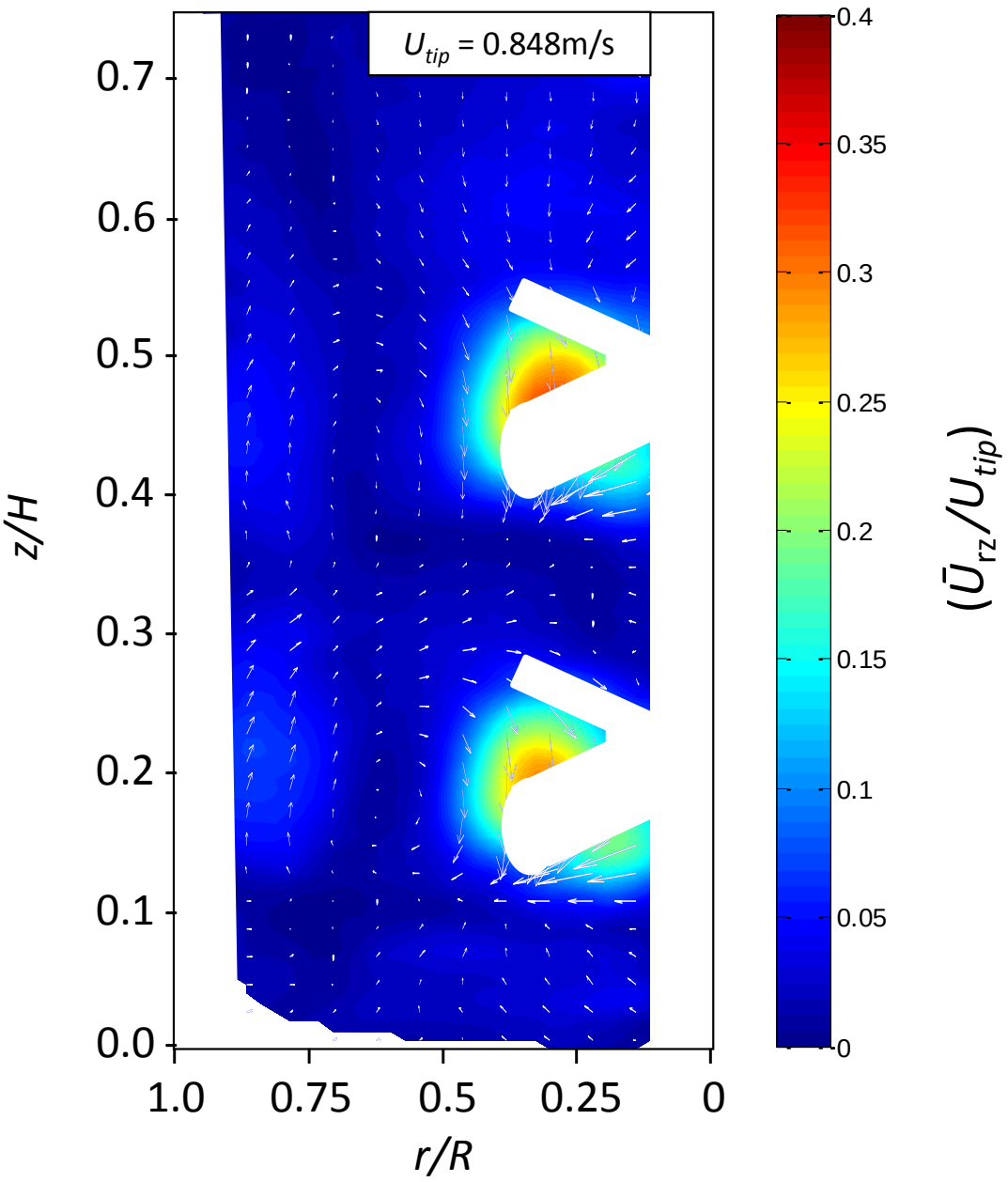

Figure 4.2: Ensemble-averaged velocity magnitude contour plot (N = 300 rpm, Re = 16,456, V_L = 2.0 L) with superimposed velocity vectors.

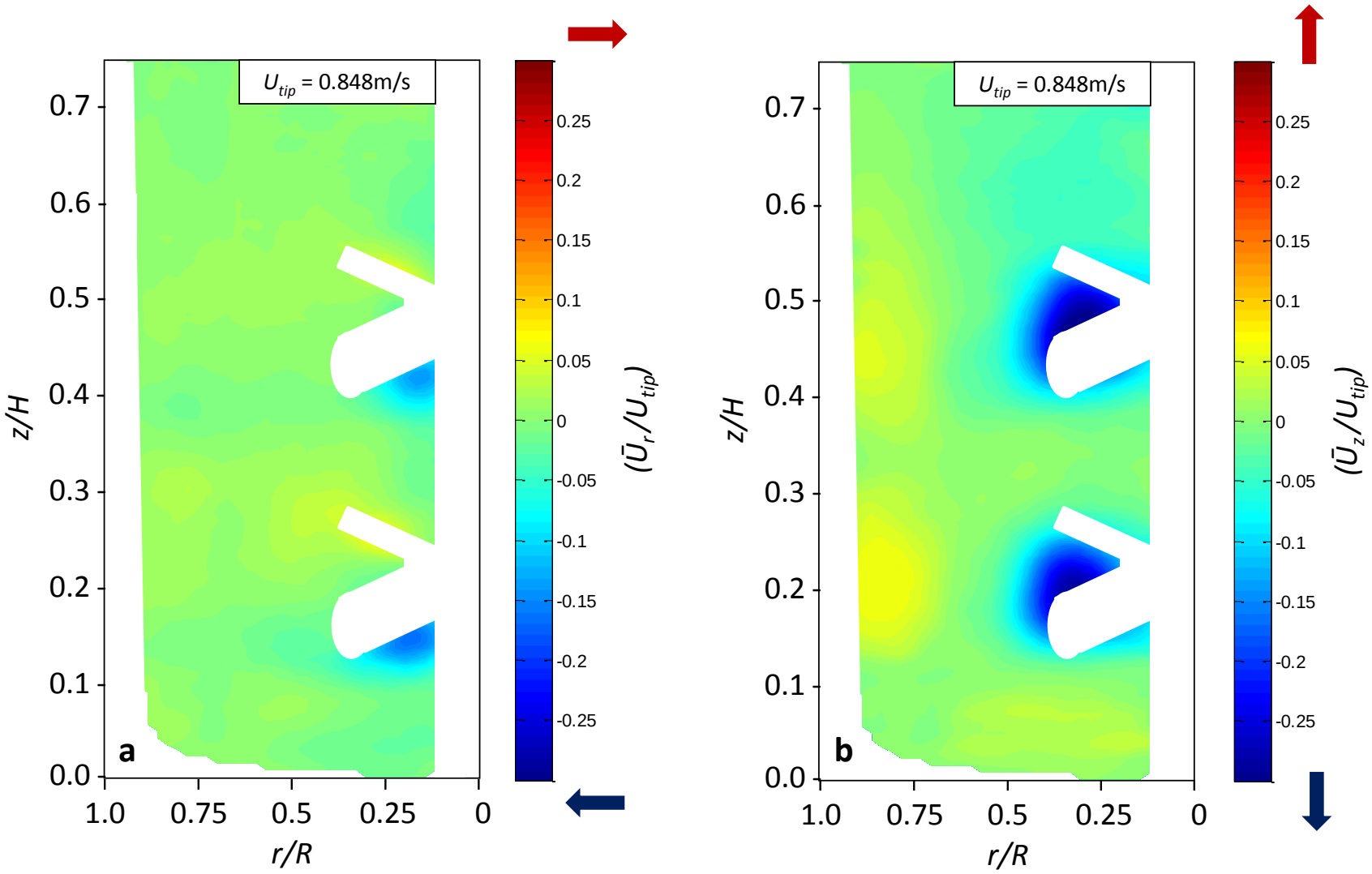

Figure 4.3: a) Ensemble-averaged radial velocity contour plot and b) ensemble-averaged axial velocity contour plot (N = 300 rpm, Re = 16,456, V_L = 2.0 L).

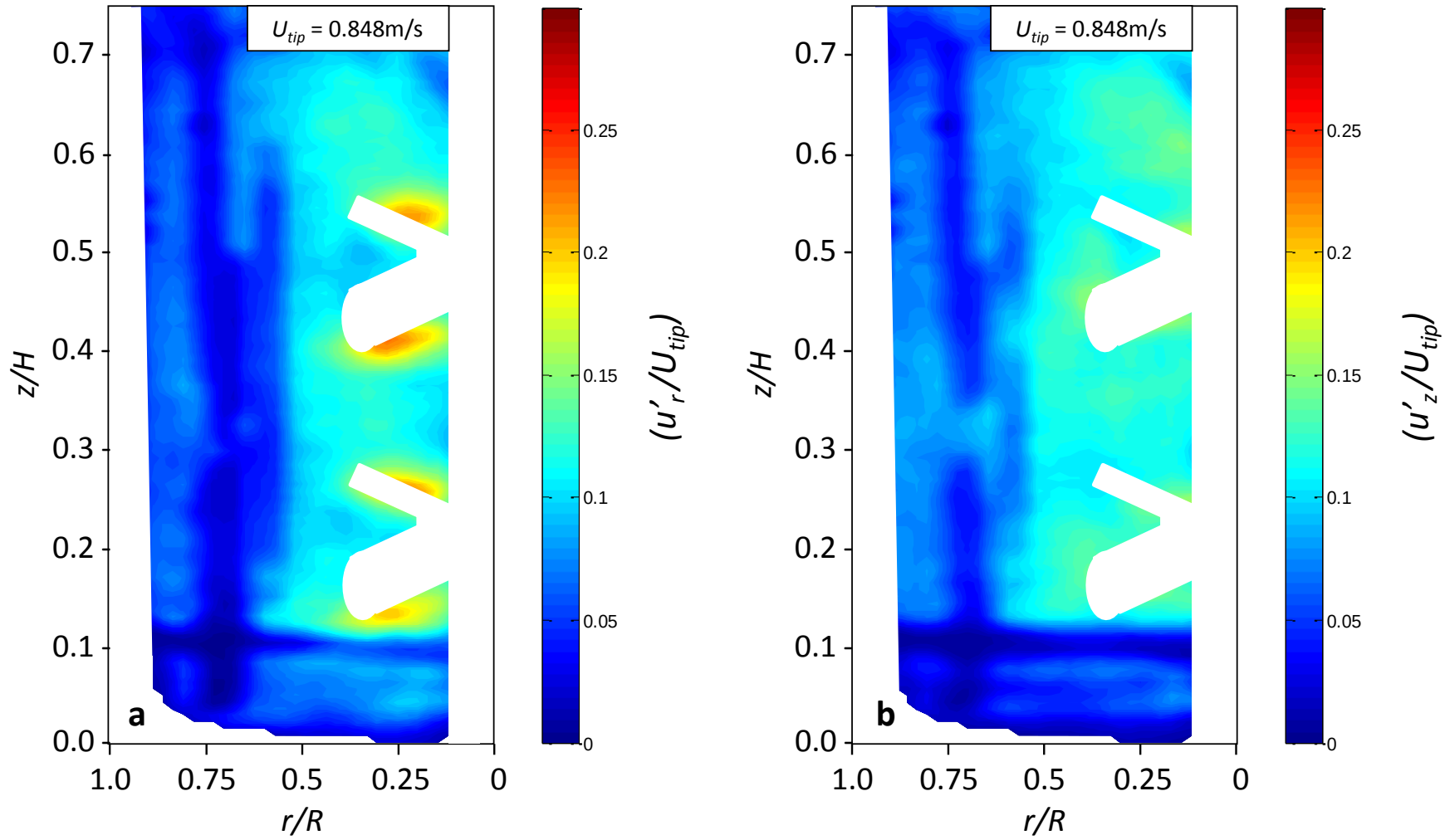

Figure 4.4: a) Ensemble-averaged r.m.s. radial velocity and b) ensemble-averaged r.m.s. axial velocity contour plots (N = 300 rpm, Re = 16,456, V_L = 2.0 L).

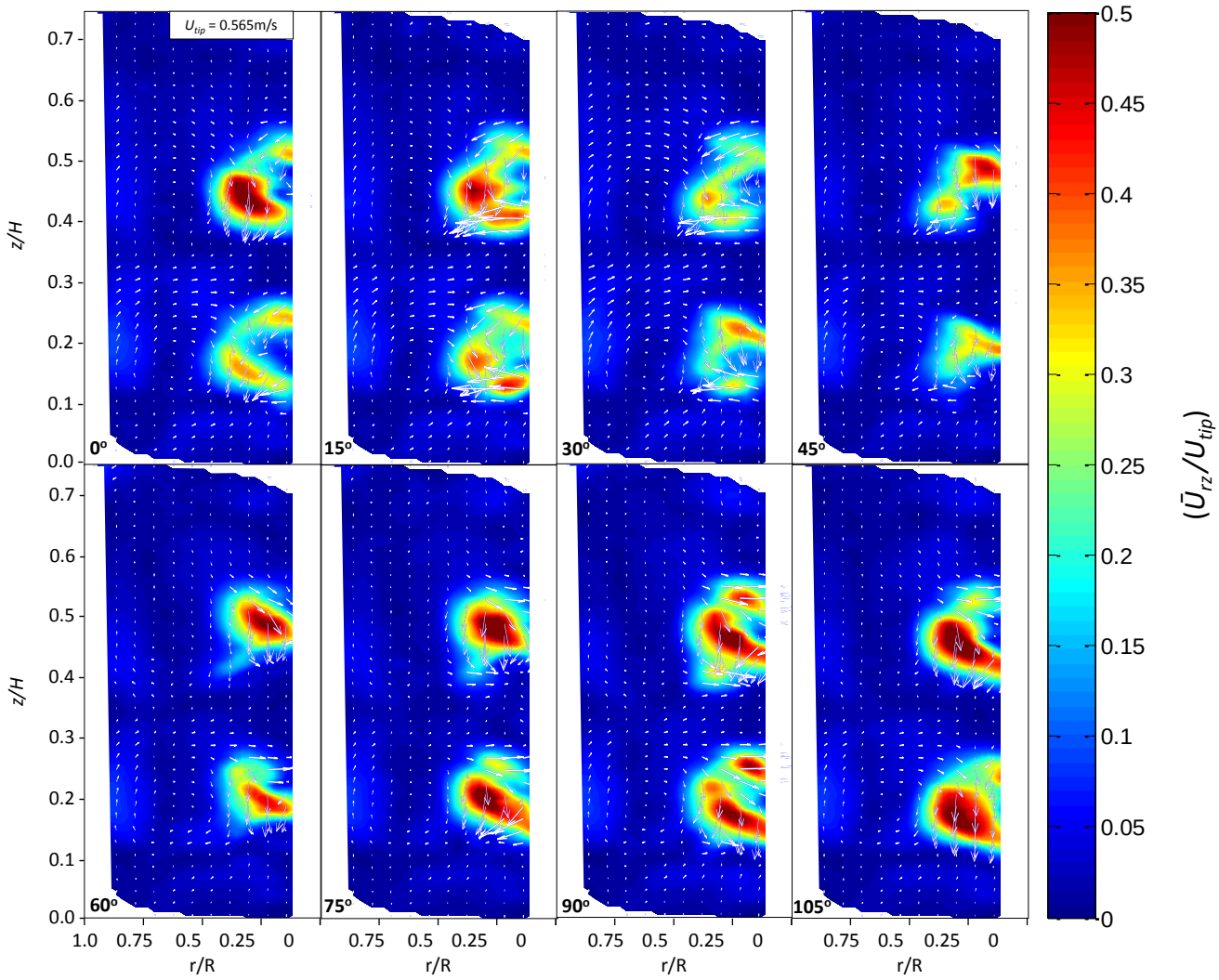

Figure 4.5: Phase-resolved contour plots of the velocity magnitude at N = 200 rpm (Re = 10,904) with velocity vectors superimposed, in the vertical plane with angles relative to the leading blade: θ = 0°, 15°, 30°, 45°, 60°, 75°, 90° and 105°.

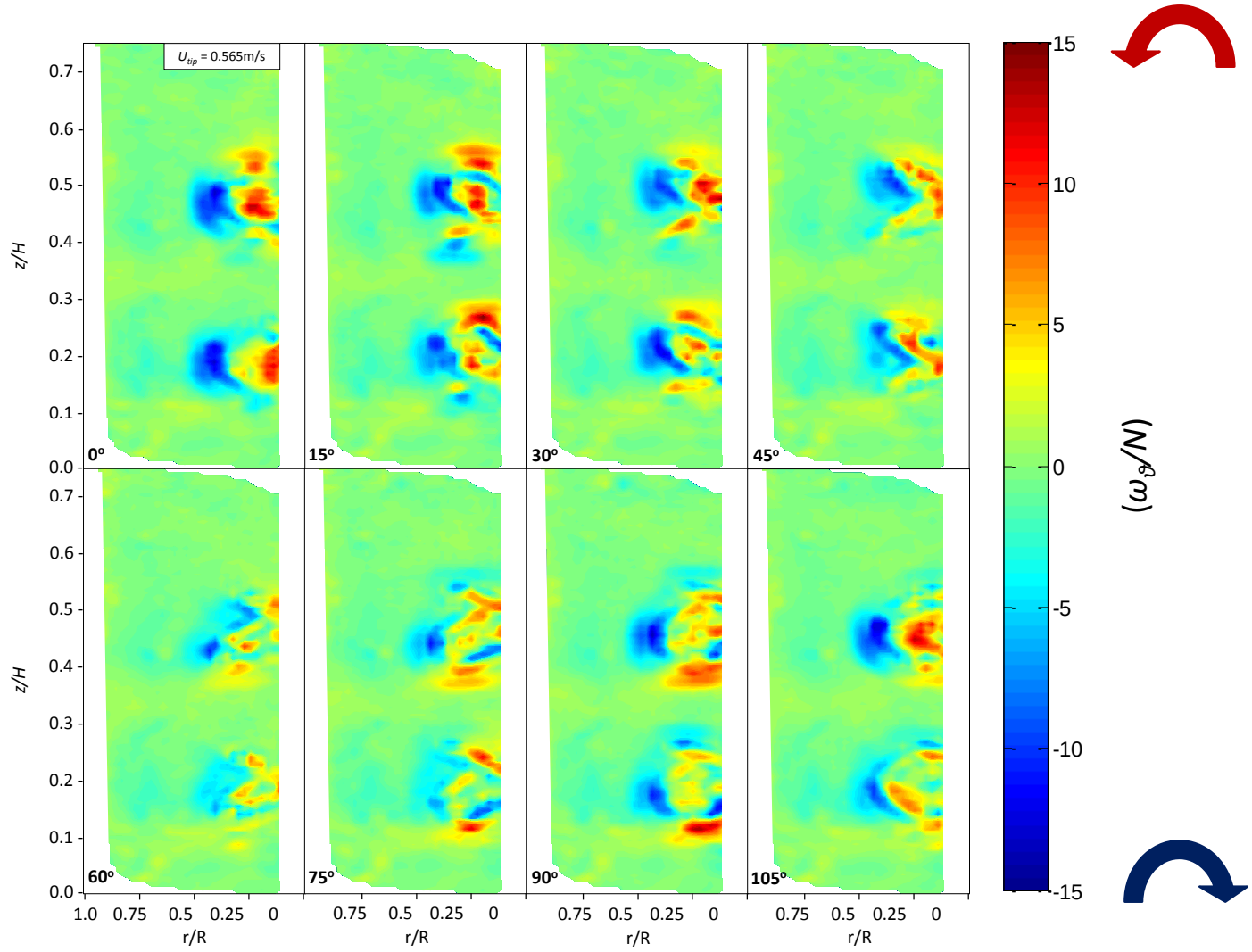

Figure 4.6: Phase-resolved contour plots of vorticity at N = 200 rpm (Re = 10,904) in the vertical plane with angles relative to the leading blade: θ = 0°, 15°, 30°, 45°, 60°, 75°, 90° and 105°.

.

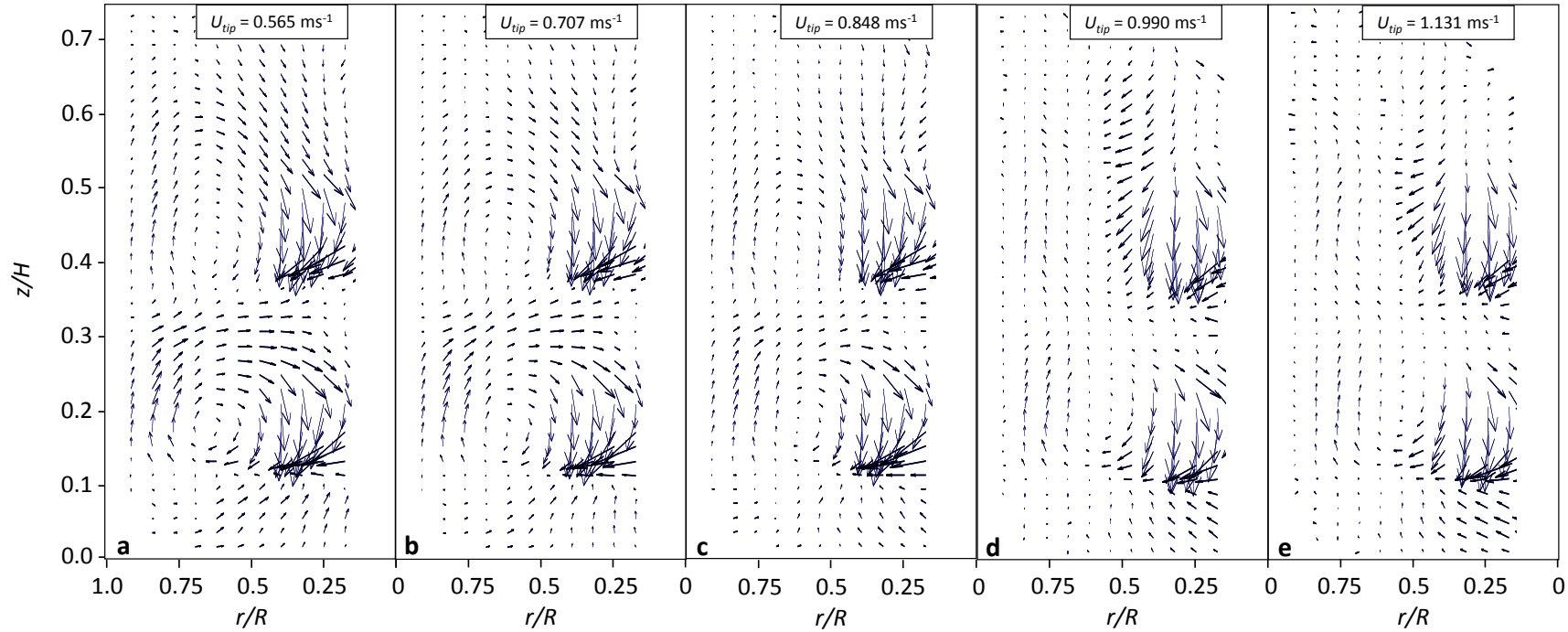

Figure 4.7: Vector plots of ensemble-averaged velocity at: a) N = 200 rpm (Re = 10,904); b) N = 250 rpm (Re = 13,630); c) N = 300 rpm (Re = 16,356); d) N = 350 rpm (Re = 19,082) and e) N = 400 rpm (Re = 21,808).

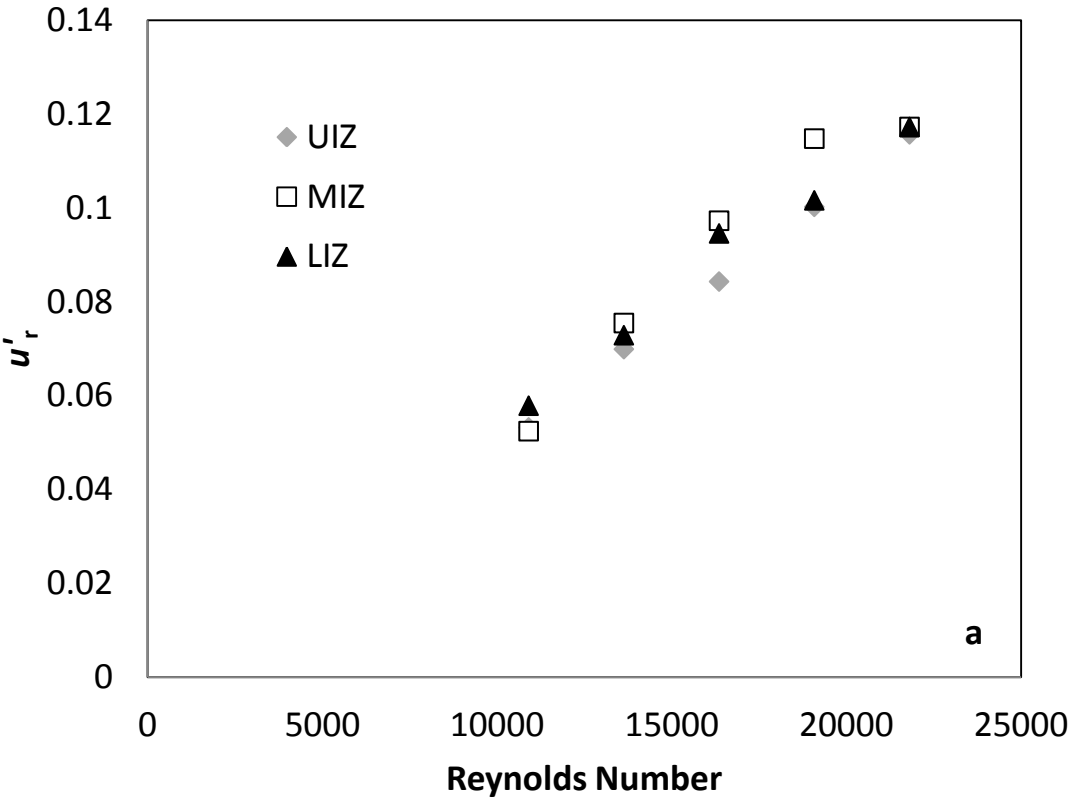

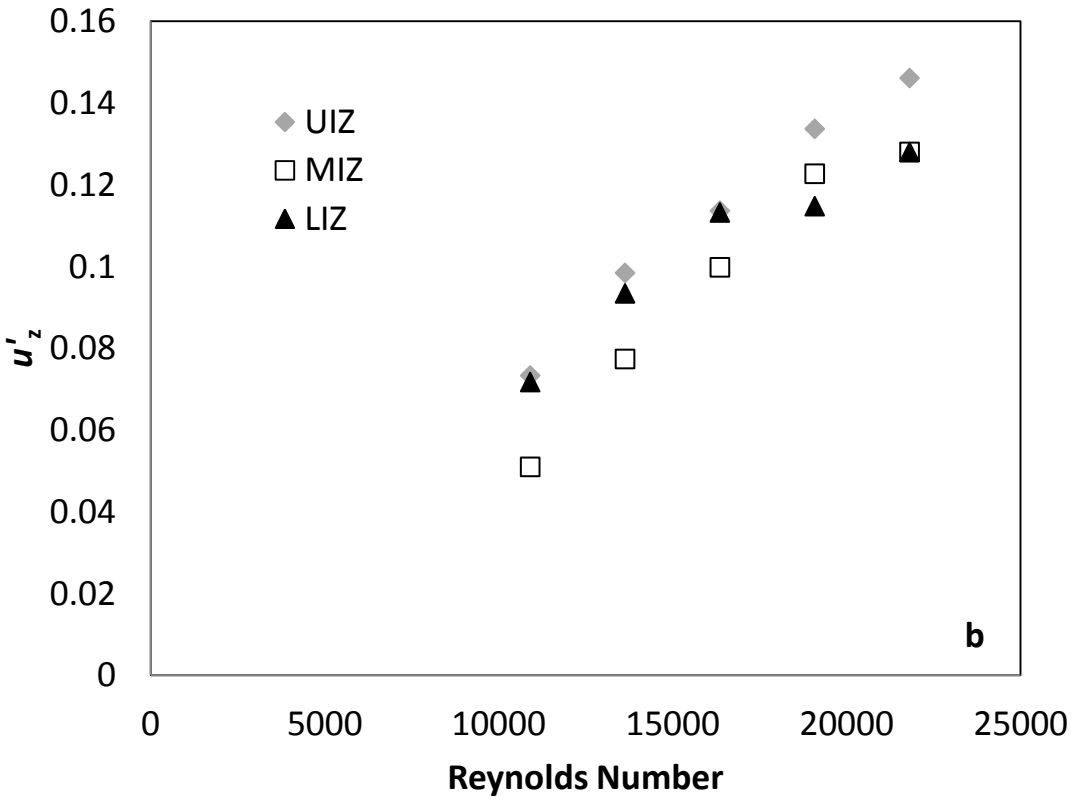

Figure 4.8: (a) r.m.s. radial velocity and (b) r.m.s. axial velocity at varying impeller rates. Data represents mean values in the following regions: z/H = 0.44 to 0.48 and r/R = 0.39 to 0.51 for UIZ, z/H = 0.31 to 0.34 and r/R = 0.39 to 0.51 for MIZ and z/H = 0.16 to 0.19 and r/R = 0.39 to 0.51 for LIZ.

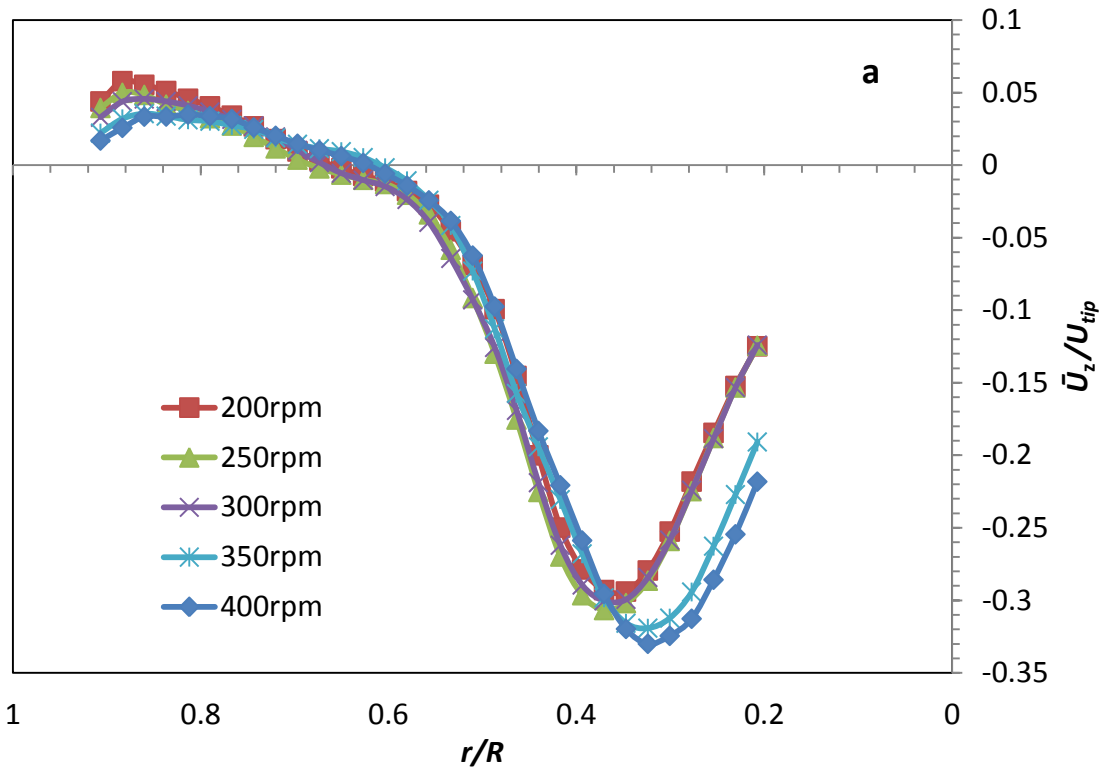

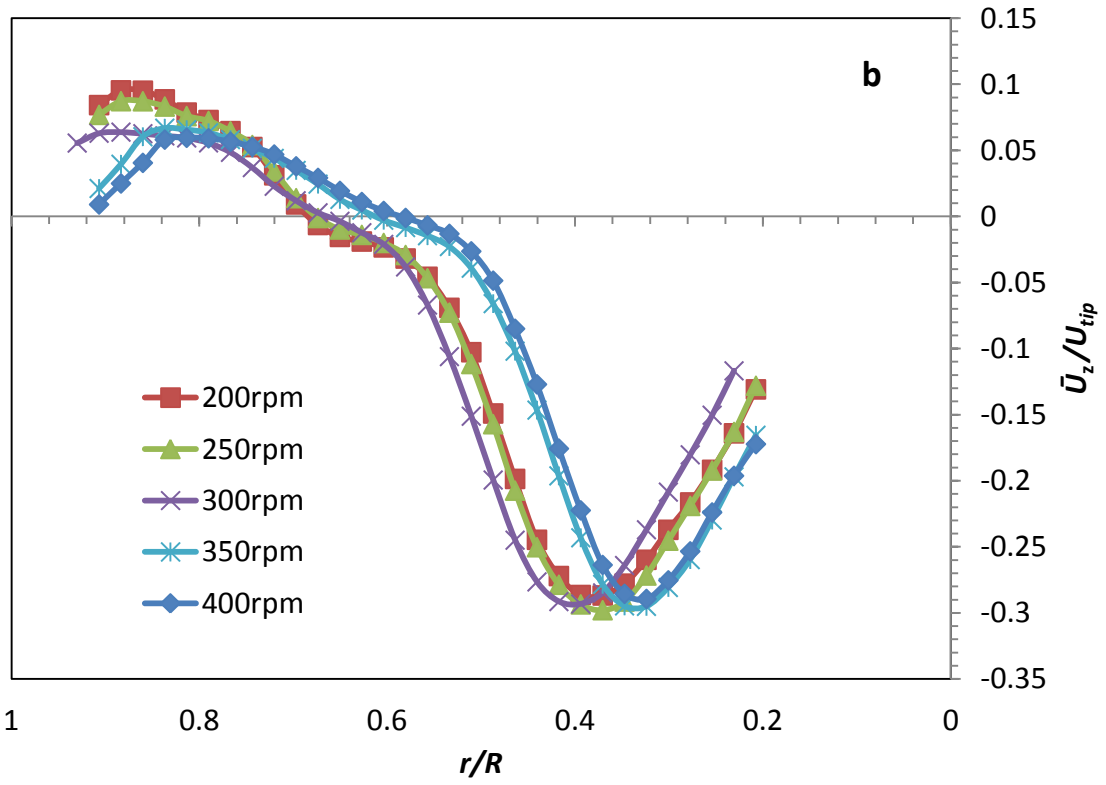

Figure 4.9: Radial profile of axial velocity in upper and lower impeller plane at impeller speeds of N = 200, 250, 300, 350 and 400 rpm: (a) profile extends from radial locations r/R = 0.21 to 0.91 at an axial location of z/H = 0.47 and (b) profile extends from radial locations r/R = 0.21 to 0.91 at an axial location of z/H = 0.20.

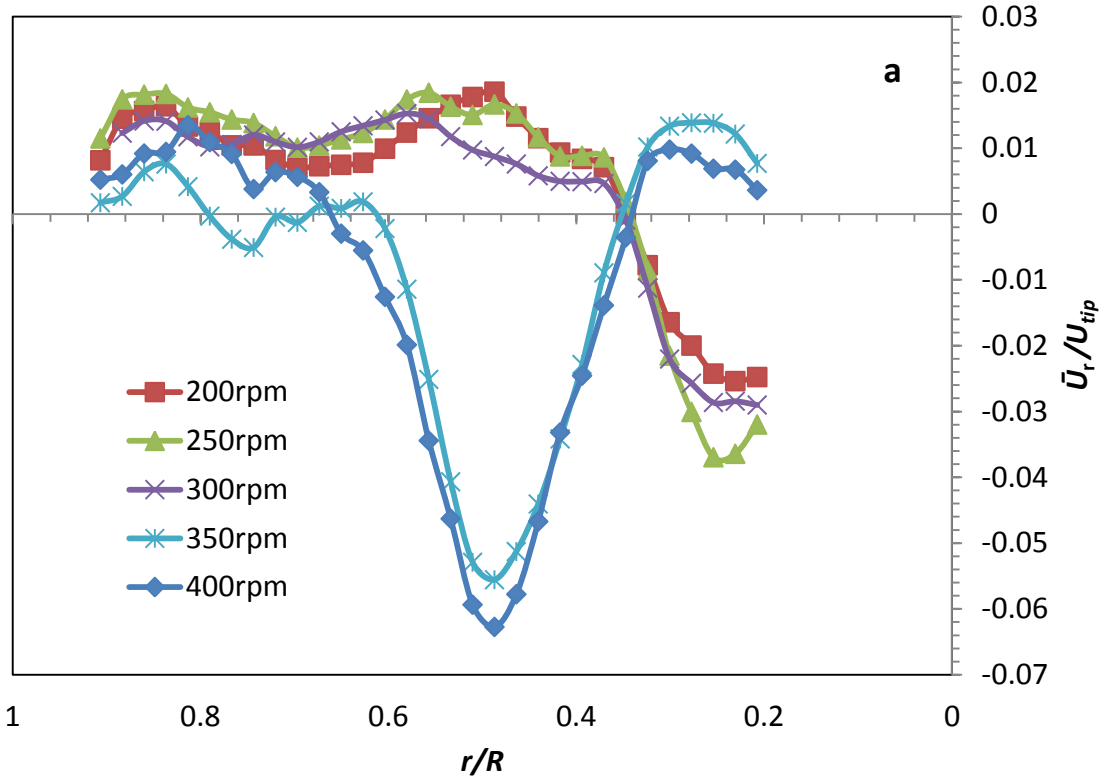

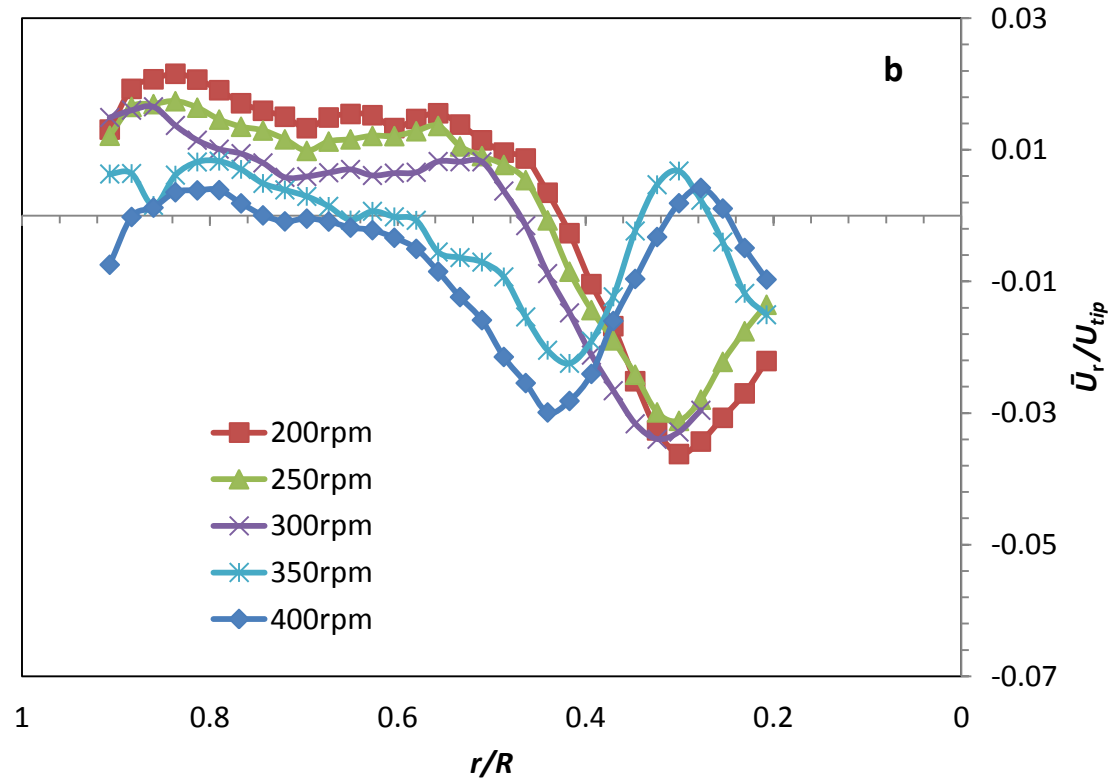

Figure 4.10: Radial profile of radial velocity in upper and lower impeller plane at varying impeller speeds of N = 200, 250, 300, 350 and 400 rpm: (a) profile extends from radial locations r/R = 0.21 to 0.91 at an axial location of z/H = 0.47 and (b) profile extends from radial locations r/R = 0.21 to 0.91 at an axial location of z/H = 0.20.

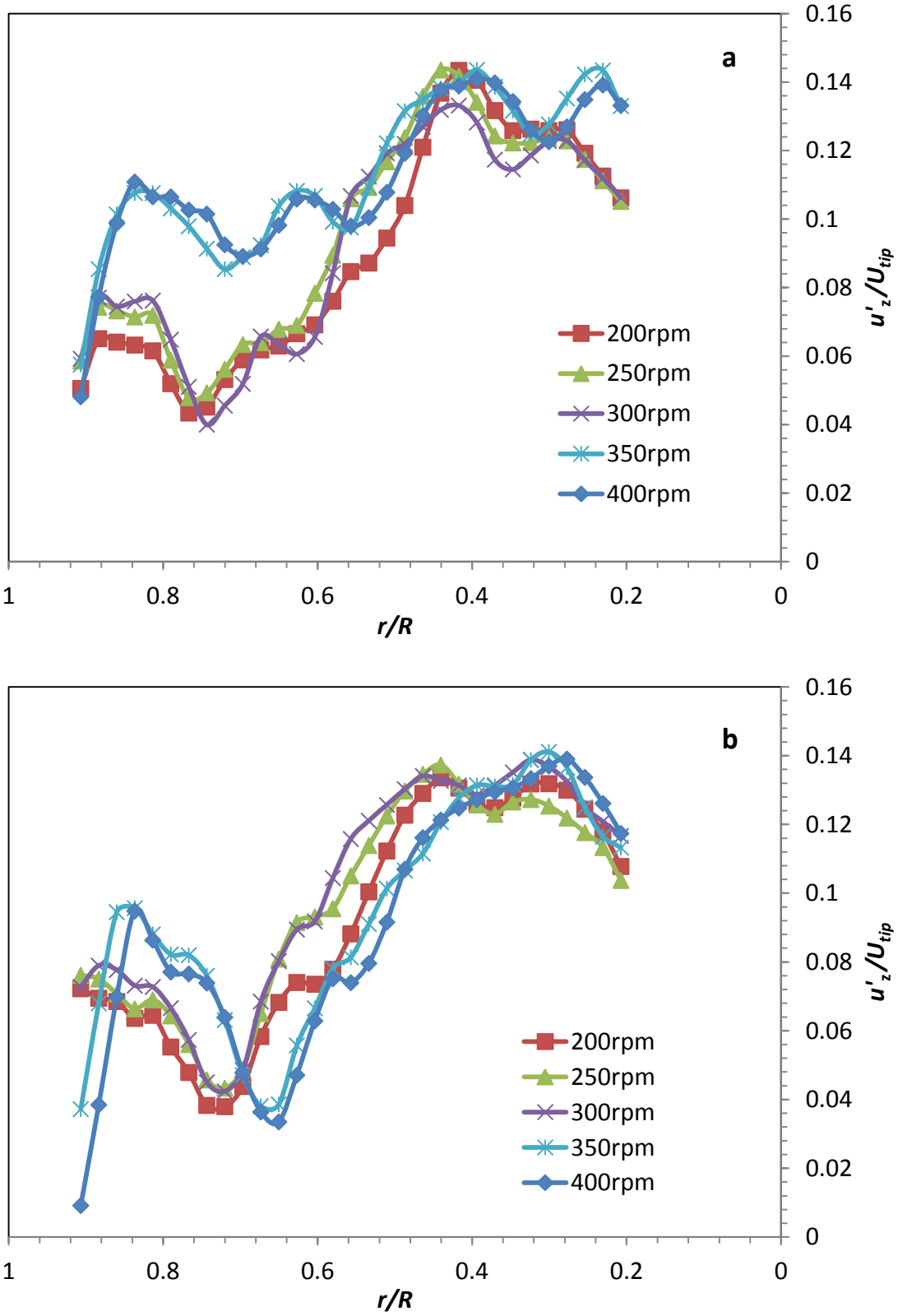

Figure 4.11: Radial profile of r.m.s. axial velocity in upper and lower impeller plane at impeller speeds of N = 200, 250, 300, 350 and 400 rpm: (a) profile extends from radial locations r/R = 0.21 to 0.91 at an axial location of z/H = 0.47 and (b) profile extends from radial locations r/R = 0.21 to 0.91 at an axial location of z/H = 0.20.

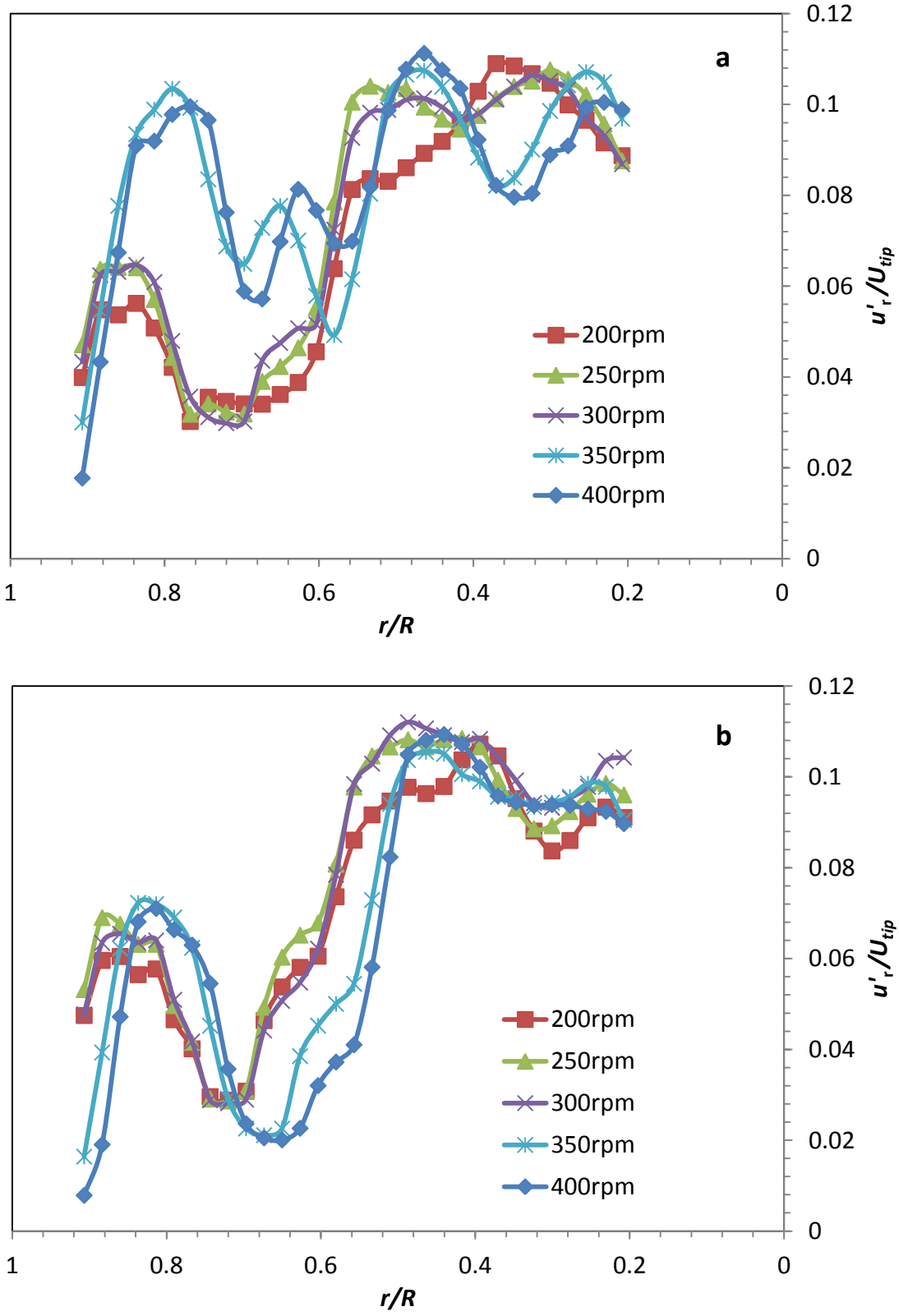

Figure 4.12: Radial profile of r.m.s. radial velocity in upper and lower impeller plane at impeller speeds of N = 200, 250, 300, 350 and 400 rpm: (a) profile extends from radial locations r/R = 0.21 to 0.91 at an axial location of z/H = 0.47 and (b) profile extends from radial locations r/R = 0.21 to 0.91 at an axial location of z/H = 0.20.

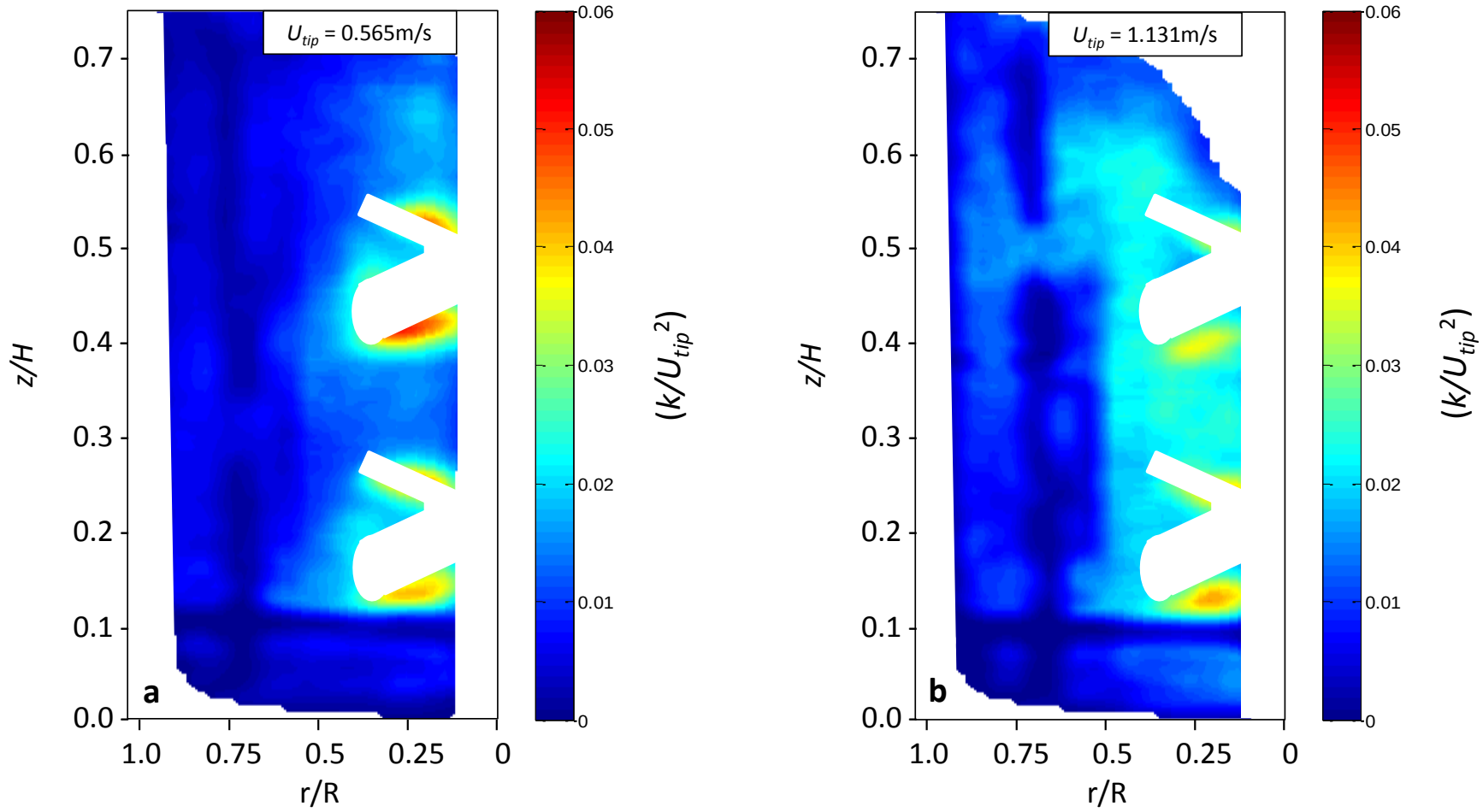

Figure 4.13: Ensemble-averaged turbulent kinetic energy contour plots at; a) N = 200 rpm Re = 10,904 and V_L = 2.0 L; and b) N = 400 rpm, Re = 21,808 and V_L = 2.0 L.

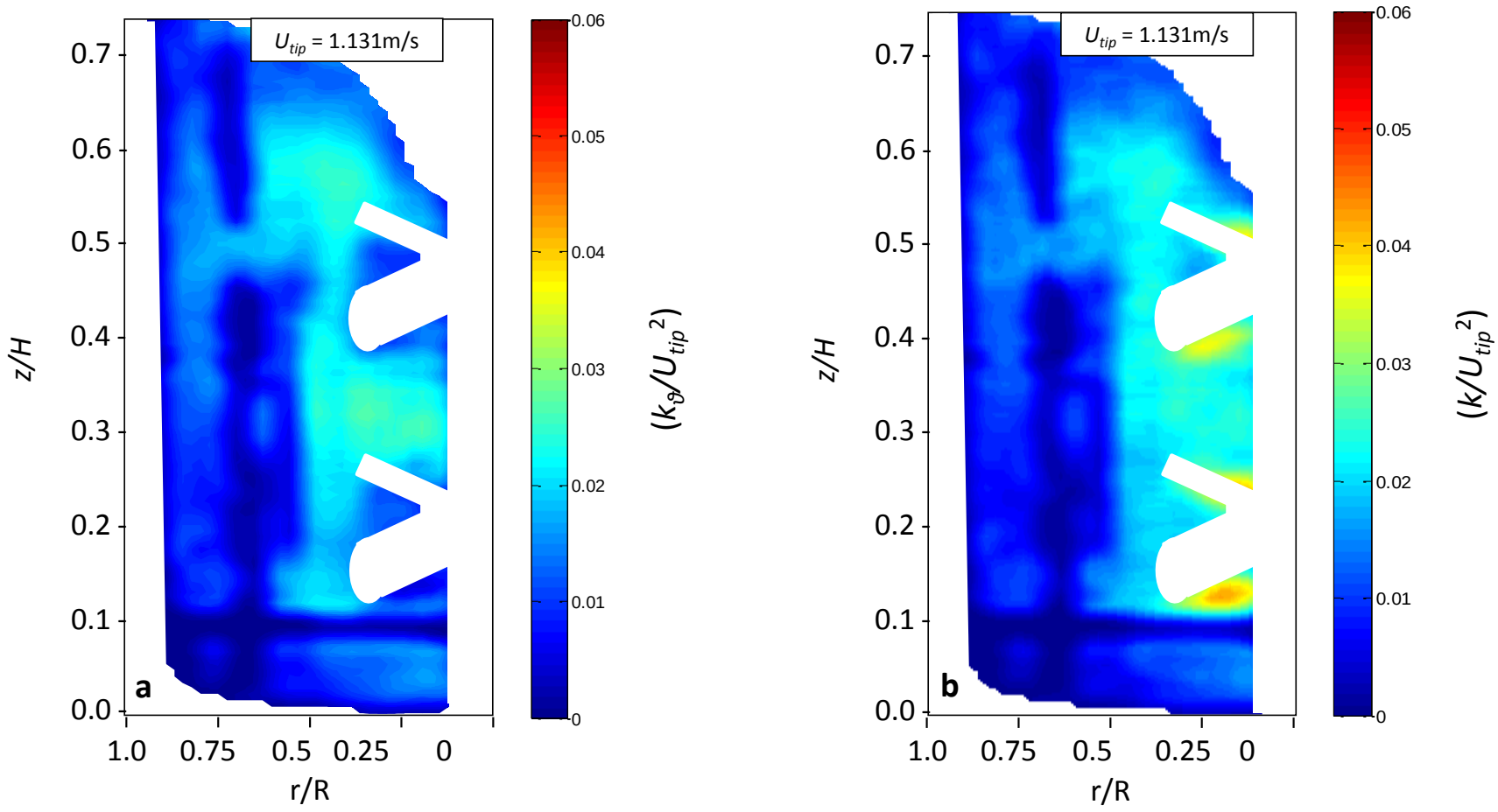

Figure 4.14: a) Ensemble-averaged (from phase-resolved measurements) turbulent kinetic energy contour plot (N = 400 rpm, Re = 21,808 and V_L = 2.0 L); and b) ensemble-averaged (from time-resolved measurements) turbulent kinetic energy contour plot (N = 400 rpm, Re = 21,808 and V_L = 2.0 L).

Chapter 5 On the Fluid Dynamics of the 3 L PBS Biotech® PBS 3

5.1 Introduction

Pneumatically driven bioreactors have become increasingly utilised in fermentation processes due to their simple designs, cheaper manufacture, low power consumption, and the savings in operating and capital costs these advantages create (Chisti and Moo-Young, 1987; Thomasi et al., 2010). Airlift and bubble column bioreactors are the most typical and widely used among the pneumatic bioreactor family. Such systems are typically used for plant cells and filamentous microorganisms (Thomasi et al., 2010), as well as anchored and suspended animal cell cultures (Chisti, 1998).

It is generally noted in literature that pneumatic bioreactor systems exhibit a lower shear stress compared with traditional bioreactors at similar oxygen transfer conditions (Thomasi et al., 2010). For operations in which shear-sensitive cells are cultivated, this is an important characteristic. However, such assertions regarding the stress environment require operational results and extensive characterisation. This is due to the fluid dynamics being dependent upon on bioreactor geometry, mixing mechanisms, bioreactor operational conditions, in addition to the rheological properties of the system (Thomasi et al., 2010). For this reason, a recently marketed pneumatic reactor, the PBS Biotech® PBS 3, has been included in this study and results will be presented in this chapter.

The PBS bioreactor is a pneumatically driven bioreactor where mixing is achieved through the buoyancy of bubbles, that turn a novel AirWheel™. This mixing mechanism facilitates a smaller footprint, whilst providing the mixing and oxygen transfer necessary for CHO cell growth (Kim et al., 2013). Vessels can range from 3 to 500 L in size. The aim of this experiment is to investigate the flow characteristics induced by the novel mixing mechanism of the PBS 3. This study will be focussed on PIV measurements obtained in the central vertical plane. It should be noted that when performing PIV, the gas phase of a two-phase system can cause distortion of the laser light sheet. However, given that the aeration induces the mixing, it could not be avoided in this case and it was deemed necessary to obtain results indicative

of the turbulent and mean flow present in the bioreactor under real operating conditions.

A Cartesian coordinate system is used, with the radial and axial directions indicated in this investigation by *r* and *z*, respectively. The liquid height and vessel length are denoted as H_L and *L*, respectively. The laser light sheet intersects the midpoint of the bioreactor width (50 mm from the front surface of the vessel).

5.1 Whole flow field characteristics

A Particle Image Velocimetry (PIV) system, described in Chapter 2, was used to obtain time-resolved velocity data. A description of the whole flow field regime in the vertical plane inside the 3 L PBS is provided in this section. The first part of the analysis is carried out for a standard configuration corresponding to a fill volume of 2.5 L and a wheel rotational speed of 20 rpm (*Re* = 6,194). In the subsequent sections, this analysis is extended to a range of impeller speeds (*N* = 20 to 38 rpm, *Re* = 6,194 to 11,870). In the Reynolds number calculation, the AirWheel^{TM} has been considered to act as an impeller in a traditional stirred bioreactor. Thus the diameter (*D*) is taken as the wheel diameter and the rotation rate (*N*) as the wheel rotational speed. The Reynolds number calculation for a stirred tank is shown in Chapter 2, Equation 2.23:

5.1.1 Flow regime

The mean flow present in a vertical plane intersecting the midpoint of the pneumatic wheel was investigated first to confirm the velocity directions expected in this bioreactor. The AirWheel^{TM} has a diameter of *D* = 130 mm and occupies the majority of the reactor space. The wheel design and orientation ensures that the flow will primarily occur in the *r*-*L* plane (i.e. the vertical plane in-line with the AirWheel^{TM}). The ensemble-averaged velocity contour plot is shown in Figure 5.1 for an air flow rate of 100 ml/min (corresponding to *N* = 20 rpm), U_{Wheel} = 0.13 ms^{-1} and 2.5 L working volume. Velocity values of up to 1.0U_{Wheel} represent the velocity of the AirWheel^{TM}. As expected, the fluid velocity gradually reduces further from the wheel. Ensemble-averaged velocities in the vertical plane achieve the highest

values in correspondence to r/L = 0.63 and z/H_L = 0.8 where the gas bubbles are released from the wheel and rise to the surface. Fluid velocities in this gas discharge region are up to $0.7U_{Wheel}$ (U_{wheel} is determined at the outer edge of the wheel using the circumference of the wheel and its rotational speed). This region of high velocity (compared with the upper corners of the bioreactor) does not appear to be observed in CFD investigations carried out for a 10 L PBS bioreactor operating at 20 rpm (U_{wheel} = 0.24 ms^{-1}) (Eibl and Eibl, 2011). The aforementioned study used the Euler granular approach and a low aeration rate in order to reduce the influence of the gas phase upon the fluid flow pattern so that its effect could be disregarded. Near the liquid surface, the fluid moving vertically upwards impinges on the surface and flows radially around the wheel. A vortical structure rotating clockwise is apparent within the region between z/H_L = 0.8 to 0.95 and r/L = 0.25 to 0, before the fluid at the wall flows down adjacent to the wheel and is re-circulated around it. As a result of the upward flow caused by the buoyant bubbles, there is a zone of low velocity (as low as $0.10U_{wheel}$) away from the gas discharge zone towards the upper left corner of the bioreactor. This feature indicated by the PIV measurements agrees with the CFD simulations made by Eibl and Eibl (2011), where fluid velocities reduce to as low as 10% of the wheel speed in the periphery of the fluid (in the upper corners of the vessel). The flow pattern within the wheel rotates around the centre of the wheel. The velocities gradually decrease from U_{wheel} = 0.13 ms^{-1} (with respect to the wheel perimeter), from 0.6 to $0.35U_{Wheel}$ between r/L = 0.8 to 0.6 (at z/H_L = 0.47), down to values close to zero at the centre of the wheel. The impact of "sails" located in the middle of the AirWheel^{TM} upon the tangential component of velocity was not obtained in this study, as the wheel itself would have caused distortion to the laser light with subsequent inaccuracies in the velocity measurement. However, Eibl and Eibl (2011) noted that the fluid velocities within the diameter of the wheel was dependent upon the angle, shape and number of sails in the wheel.

Figures 5.2 and 5.3 show the axial and radial components of ensemble-averaged velocity and r.m.s. velocity within the PBS. Indeed the dimensionless velocities at the wheel are consistent with the measured U_{wheel}, whilst fluid velocities gradually reduce further away from the AirWheel^{TM}. Radial velocities in the upper regions of the PBS above the wheel maintain values of approximately 0.1 to $0.2U_{Wheel}$. The axial velocities near the gas phase exit path, show higher values in the region of 0.4

to $0.6U_{Wheel}$, with axial velocities closer to $0.20U_{Wheel}$ at the opposite side of the bioreactor. There is much spatial variation in relation to the r.m.s. velocities (u'_r and u'_z); with both axial and radial components varying between 0.2 to $0.4U_{Wheel}$ throughout the majority of the fluid. Areas of increased r.m.s. velocity (0.6 to $0.7U_{Wheel}$) occur at the exit path of the gas phase (within the region r/L = 0.60 to 0.65 and z/H_L = 0.7 to 1.0) as they are released from the AirWheel™.

5.1.2 Turbulence and Reynolds stress

Figure 5.4 shows a contour plot of turbulent kinetic energy (normalised to the square of the wheel speed) at operating conditions of air flow rate 100 ml/min, N = 20 rpm, U_{wheel} = 0.13 ms^{-1} and 2.5 L working volume. As observed from Fig. 5.4, the spatial variation of k within the bioreactor is relatively homogenous. Typical bulk fluid values are approximately $0.2U_{Wheel}^2$, rising to $0.8U_{wheel}^2$ in the gas phase discharge at the fluid surface. The larger values of k measured at these conditions (0.014m^2s^{-2}) are 50% lower than the maximum k of $0.025U_{tip}^2$ observed in a stirred tank by Zhu et al. (2009). In this study, an Elephant Ear impeller was housed by a cylindrical vessel (operating at 300 rpm and un-aerated) with dimensions: T = 150 mm, D = 0.45T, $T = H_L$, and C = 0.25T, with the k/U_{tip}^2 equating to 0.028 m^2s^{-2}. The maximum PBS k measured is also lower than the 0.018 m^2s^{-2} noted in Chapter 3, determined using PIV in a 3 L CellReady (at 200 rpm and un-aerated), with vessel dimensions of: T = 137 mm, D = 0.56T, and C_1 = 0.22T. The maximum k noted in the gas discharge zone may also be attributed to the distortion of the laser upon transmission through the gas phase, which would have caused a significant degree of fluctuating correlation peaks during vector processing. The tangential component of velocity was not acquired in this study, due to the AirWheel™ and the resulting difficulty in obtaining optically clear images in this field of view. Thus, the isotropic assumption was used to determine turbulent kinetic energy (Gabriele et al., 2009), as shown in Equation 5.1.

$$k = \frac{3}{4}\left(\overline{u_r^2} + \overline{u_z^2}\right) \qquad (5.1)$$

Reynolds stress was calculated using equation 5.2 below and is shown in Figure 5.5 at 20 rpm (U_{wheel} = 0.13 ms^{-1}).

$$\rho\overline{u_r u_z} \qquad (5.2)$$

Reynolds stress values show a great degree of uniformity in the bulk fluid, with values in the region of 0.2-0.4 Nm^{-2}. These stress measurements are in good agreement with the estimated shear stresses of <0.5 Pa, determined by (Lee et al., 2011) using CFD (modelling on STAR CCM+ software) across bioreactor volume range of 3 to 2500 L. The highest stresses are seen in the gas discharge zone above the wheel, with values of up to 1.6 Nm^{-2}. Reynolds stresses of up to 1.6-1.8 Nm^{-2} are also noted at the wheel-liquid boundary. These maximum Reynolds stresses compare well with the maximum wall shear stresses of up to 1.7 Nm^{-2} observed by Eibl and Eibl (2011).

5.2 Flow characteristics vs. wheel speed

Figure 5.6 shows the variation of axial and radial velocity at N = 20, 27, 33 and 38 rpm, at different locations (r/L = 0.912, 0.714, 0.516, 0.319 and 0.121 and z/H_L = 0.875). Radial velocities showed a linear relationship with wheel speed, with the greatest influence of wheel speed applied to location r/L = 0.516. This influence then decreases further away from the central part of the vessel (r/L = 0.5). This is to be expected given that the maximum fluid velocities occur in the proximity of location z/H_L = 0.875 and r/L = 0.516, with radial velocities of over 0.10 ms^{-1} at N = 38 rpm measured. In contrast, the equivalent axial velocity variation at varying wheel speeds show very little change. This can be attributed to the fluid velocity in the region investigated, being limited by the buoyancy of bubbles. Axial velocities of up to 0.047 ms^{-1} occur at z/H_L = 0.875 and r/L = 0.912.

Figure 5.7 shows the variation of r.m.s. axial and r.m.s. radial velocity at N = 20, 27, 33 and 38 rpm and the locations stated in Figure 5.6. There appears to be a linear relationship between the r.m.s. values and wheel speed. At the locations measured, r.m.s. radial velocity attains a value of 0.03 ms^{-1} (at z/H_L = 0.875 and r/L = 0.319), whilst r.m.s. axial velocity reaches a level of 0.03 ms^{-1} (at z/H_L = 0.875 and r/L = 0.516). Although the r.m.s. velocity vs. wheel speed relationship appears linear, there is greater fluctuation with respect to r.m.s. axial velocity. There was not a great degree of isotropy between the r.m.s. axial and r.m.s. radial velocity at their respective locations, however given the lower levels of r.m.s. velocity measured,

there is a augmented propensity for variation in the values obtained. The relatively low degree of isotropy at the localised level, appears to result in a greater degree of spatial uniformity in the system. This is because locations with higher r.m.s. axial velocity, will have a corresponding lower level of r.m.s. radial velocity, and vice versa. However, this spatial uniformity could also be attributed to the small range (0.005 to 0.03 ms^{-1}) of both the r.m.s. axial and r.m.s. radial velocity noted.

5.3 Concluding remarks

The PBS bioreactor offers a novel mixing mechanism for cell culture applications, resulting in an environment with turbulence levels significantly lower than maximum values noted in conventional impeller stirred systems. The PBS wheel speed is limited by its mechanism of operation (buoyancy of bubbles). Although fluid velocities are not dissimilar to those found within equivalently scaled stirred tank SUBs. The reliance upon aeration for mixing also limits the turbulence levels, in addition to parameters such as mixing times and k_La, and the operational range it can achieve. Even though mixing time studies within the PBS scale well between 2 to 50 L vessels, mixing is highly dependent upon, and limited by, the air flow rate. Hence comparability with STRs is also difficult given the interdependency of oxygen transfer with mixing efficiency. In addition, traditional scaling parameters such as power input, mixing time and Reynolds number cannot be easily translated to stirred-tanks, as these parameters represent the whole fluid flow environment within the vessel. Which may also be significantly different at the localised level within a stirred tank. The mixing mechanism, lower stress and reduced turbulence levels in the PBS, enhance the degree of fluid dynamic uniformity throughout the fluid. For this reason, the utilisation of traditional parameters for scaling across the PBS product range may be suitable, because of the enhanced consistency regarding mixing time and oxygen transfer rates, across the PBS vessel sizes (Kim et al., 2013).

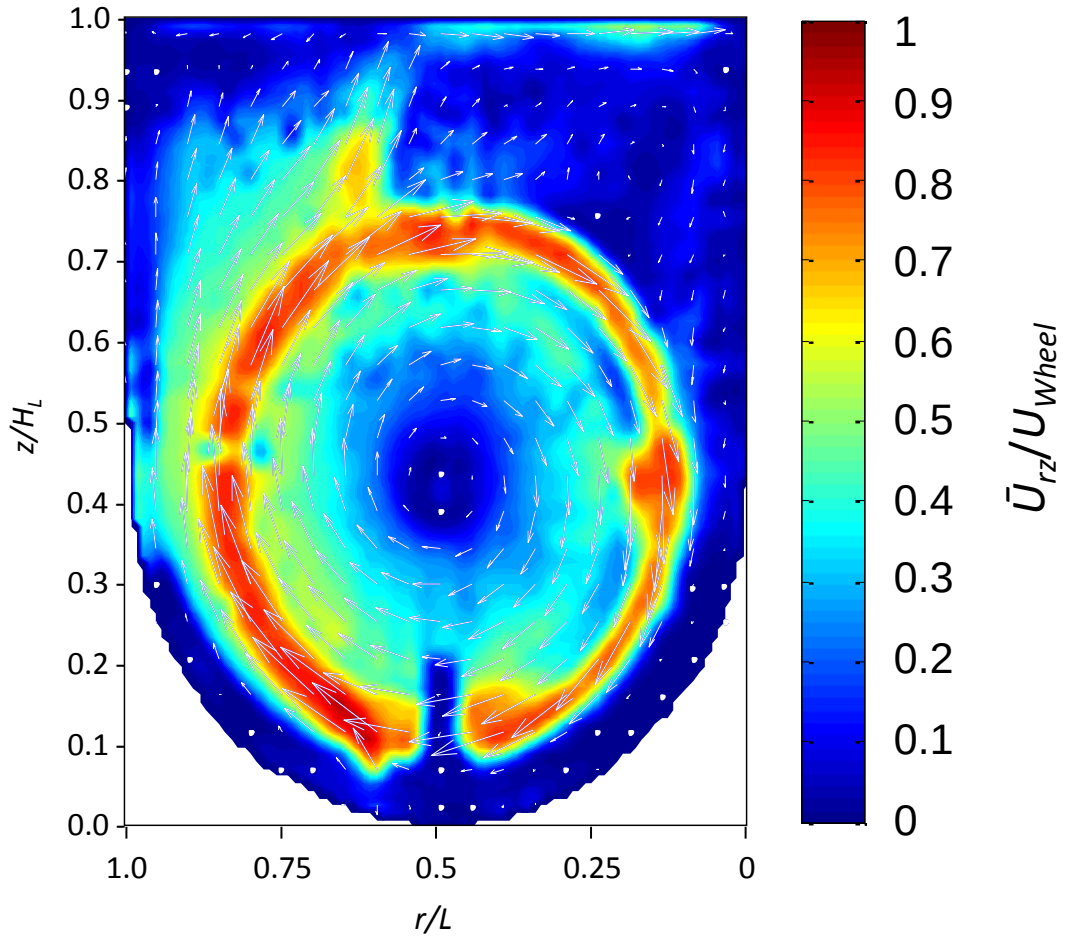

Figure 5.1: Ensemble-averaged velocity ($\bar{U}_{rz}/U_{wheel}$) contour plot with superimposed velocity vectors. Data obtained at 100 mL/min aeration, N = 20 rpm, U_{wheel} = 0.13 ms^{-1}, V_L = 2.5 L and Re = 6,194.

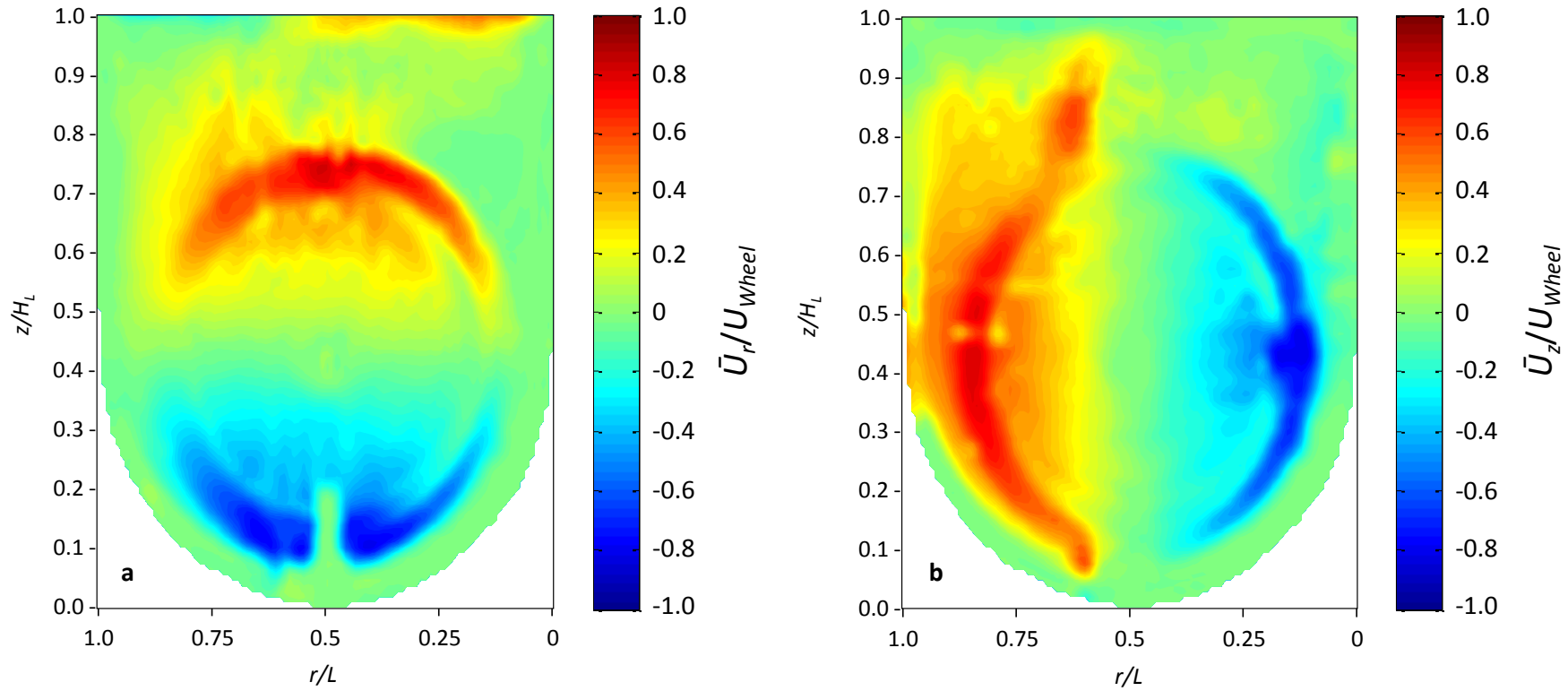

Figure 5.2: Ensemble-averaged; (a) radial ($\bar{U}_r/U_{wheel}$) and (b) axial ($\bar{U}_z/U_{wheel}$) velocity contour plots. Data obtained at 100 mL/min aeration, N = 20 rpm, U_{wheel} = 0.13 ms^{-1}, V_L = 2.5 L and Re = 6,194.

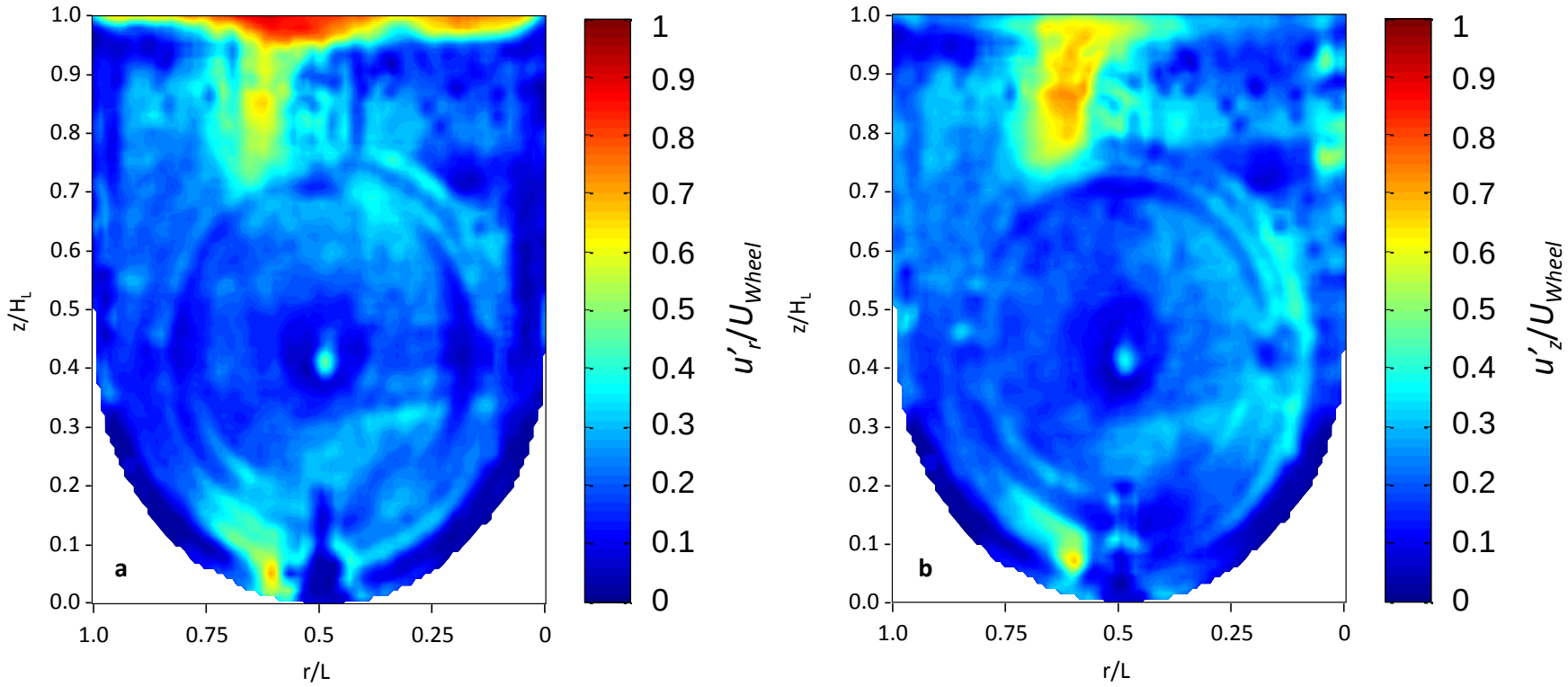

Figure 5.3: Ensemble-averaged r.m.s.; (a) radial (u'_r/U_{wheel}) and (b) axial (u'_z/U_{wheel}) velocity contour plots. Data obtained at 100 mL/min aeration, N = 20 rpm, U_{wheel} = 0.13 ms^{-1}, V_L = 2.5 L and Re = 6,194.

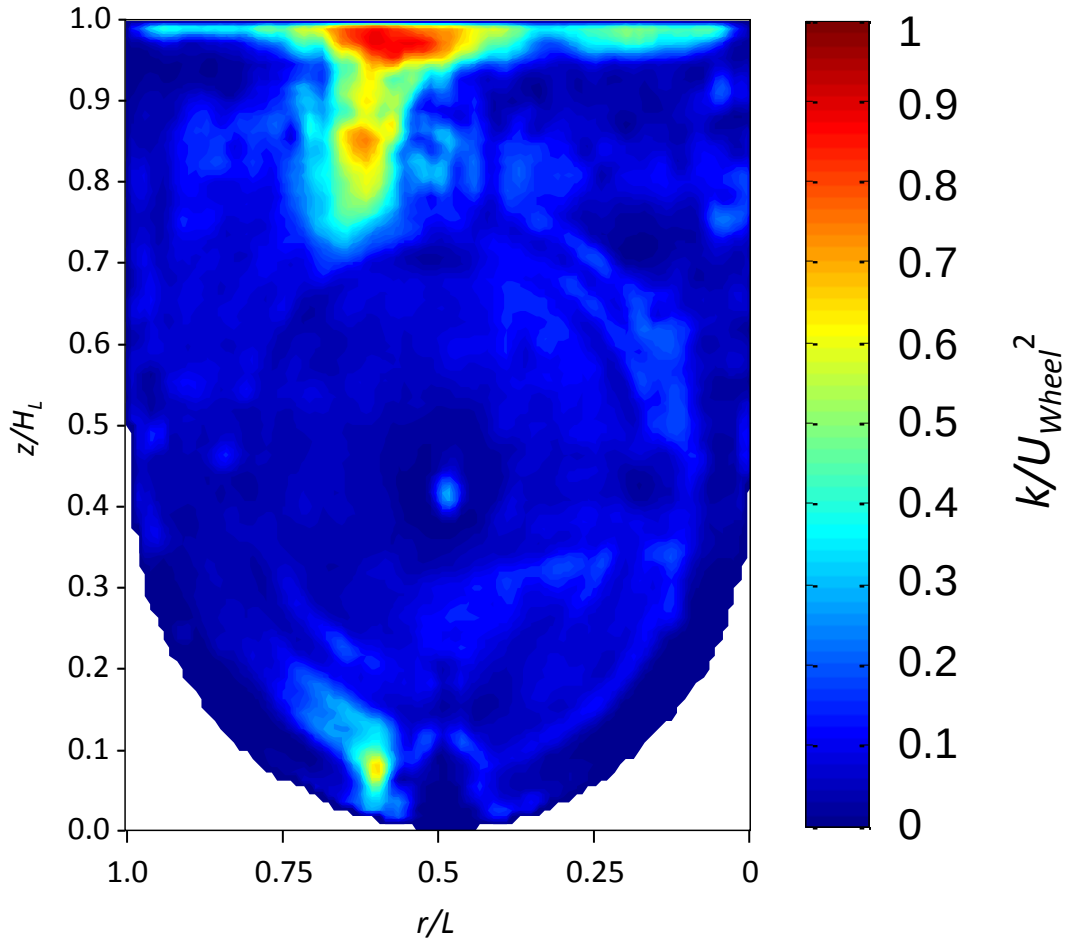

Figure 5.4: Ensemble-averaged turbulence kinetic energy (k/U_{wheel}^2) contour plot. Data obtained at 100 mL/min aeration, N = 20 rpm, U_{wheel} = 0.13 ms^{-1}, V_L = 2.5 L and Re = 6,194.

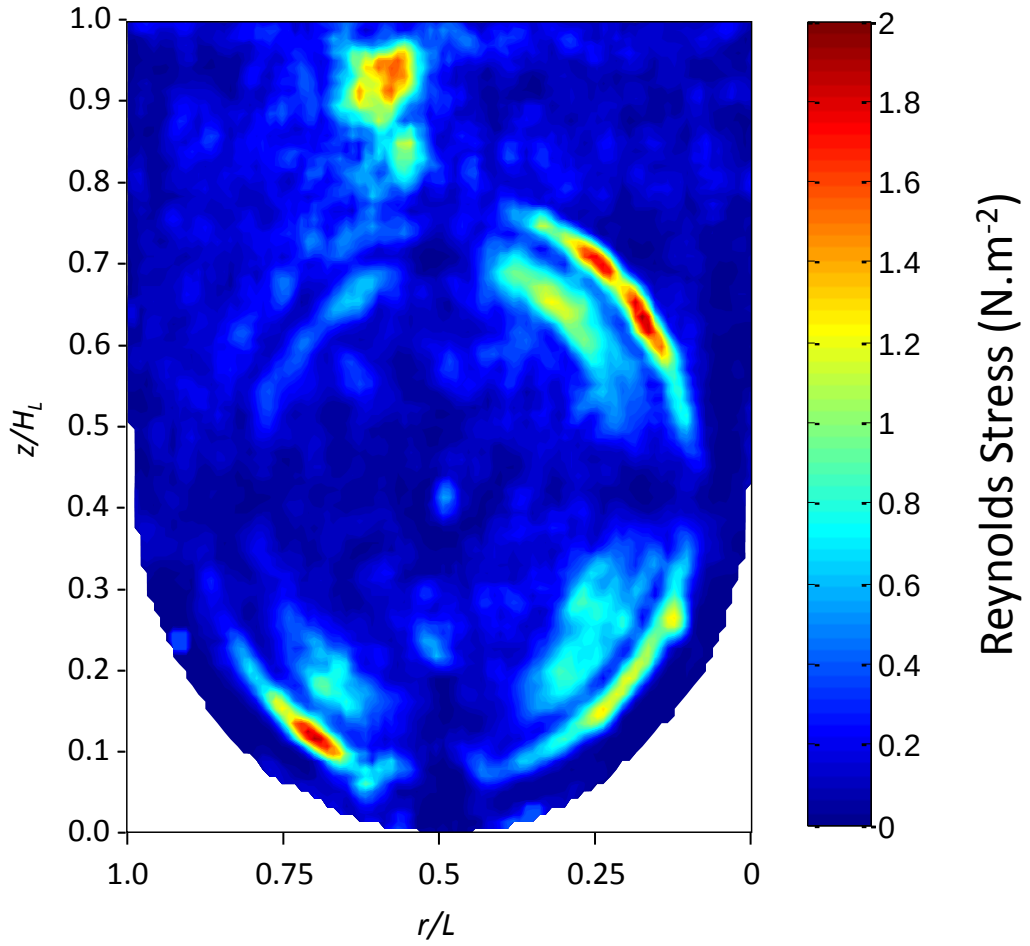

Figure 5.5: Ensemble-averaged Reynolds stress ($\boldsymbol{\rho \overline{u_r u_z}}$) contour plot. Data obtained at 100 mL/min aeration, N = 20 rpm, U_{wheel} = 0.13 ms^{-1}, V_L = 2.5 L and Re = 6,194.

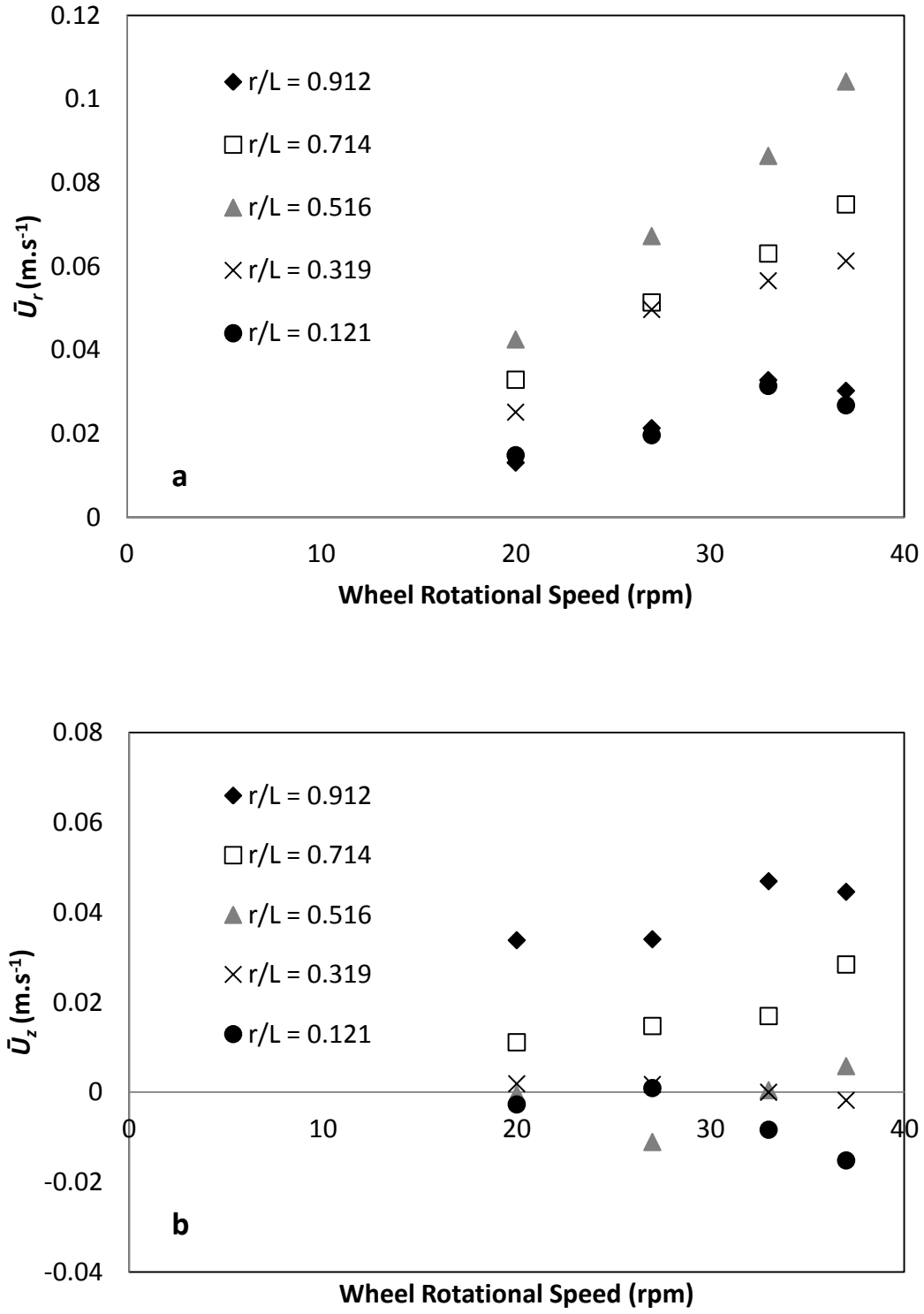

Figure 5.6: Axial and radial velocity at varying wheel speeds and locations. a) Radial velocity ($\bar{U}_r$) and b) axial velocity ($\bar{U}_z$). Data represents values at the following locations: r/L = 0.912, 0.714, 0.516, 0.319 and 0.121 all at z/H_L = 0.875.

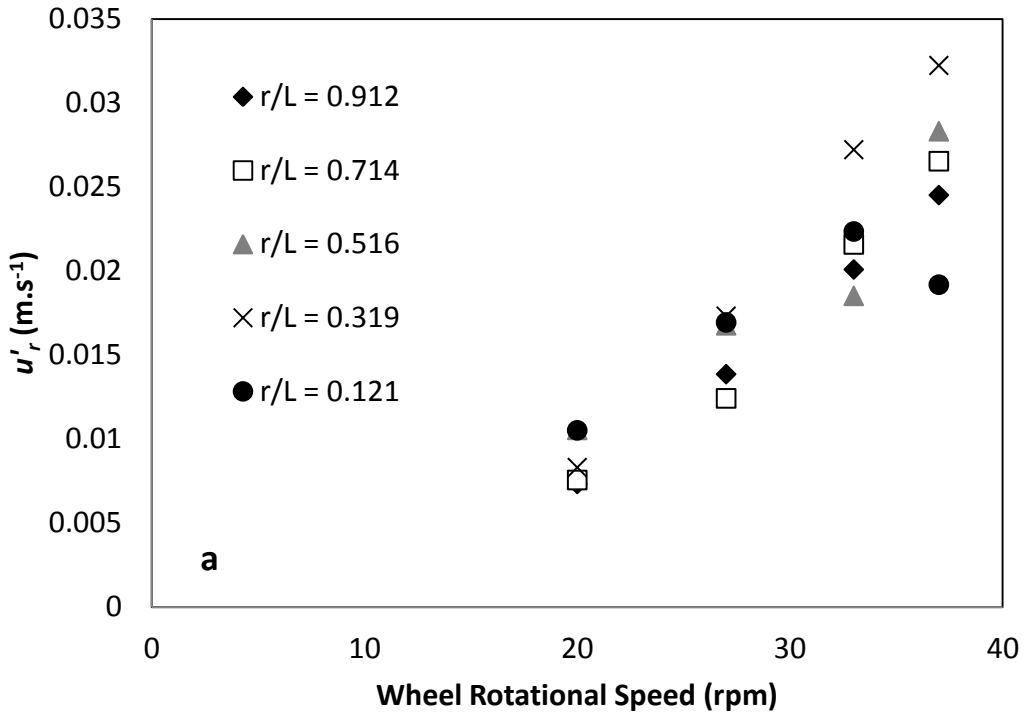

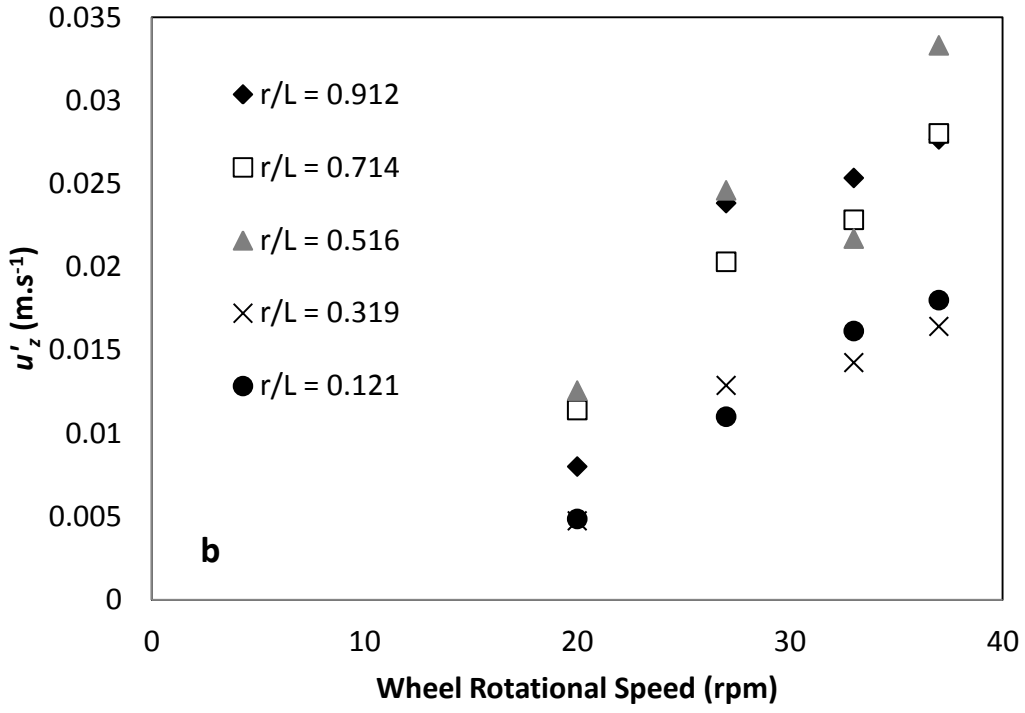

Figure 5.7: R.m.s. axial and r.m.s. radial velocities at varying wheel speeds and locations. a) r.m.s. radial velocity (u'_r) and b) r.m.s. axial velocity (u'_z). Data represents values at the following locations: r/L = 0.912, 0.714, 0.516, 0.319 and 0.121 all at z/H_L = 0.875.

Chapter 6 On the Fluid Dynamics of the Sartorius BIOSTAT® Cultibag RM

6.1 Introduction

The results obtained and presented in Chapters 3, 4 and 5 have helped to elucidate the whole flow field mixing characteristics within single-use bioreactors with stirred and pneumatically driven mixing. However, the release of the first rocked bag by Wave Biotech US in 1996 (GE Healthcare Life Sciences), has started a trend and a few more similar bioreactor products were released for upstream processing and cell culture applications. This chapter will focus on the engineering characterisation of the Sartorius BIOSTAT® Cultibag RM 20/50 bioreactor. The bioreactor comprises a disposable, flexible plastic bag which is available pre-sterilised via gamma-irradiation. The bag itself sits upon a rocking platform; this platform also houses the thermocouple that enables temperature control of the bag content. In operation, the Cultibag is partially filled with media and inflated with air through an inlet filter. The disposable contact material negates the cleaning validation requirements, thus significantly reducing costs in cGMP operations. The bioreactor also facilitates rapid installation and utilisation, thus making it favourable for process development and clinical manufacturing as well as minimising the time to market for biological products (Mikola et al., 2007).

It is generally accepted that the flow conditions within cell culture systems might have a strong influence on the cell density and product yield that is achieved. Control of cellular growth rates and cell damage are of particular importance for mammalian cell systems used for the production of therapeutic proteins. Given their high shear sensitivity, their aeration requirements and lower growth rates achieved, the selection of the appropriate flow conditions is crucial for the design and optimisation of the cell culture performance (Oncül et al., 2010). Despite this, very few studies have attempted to quantify the hydrodynamic conditions within this type of bioreactor. Eibl et al. (2009) proposed a modified Reynolds number to quantify the flow conditions within a BioWave® culture bag. The proposed modified Reynolds number included correction factors that account for differences in culture bag type, liquid volume, rocking angle, rocking rate and that aid in the comparison with *Re* generated

in stirred tanks (Eibl et al., 2009). In view of that, a Reynolds number for the Cultibag RM was not estimated in this study, due to the uncertainties arising from differences captured in these correction factors.

In an effort to characterise the flow conditions within the Wave Bioreactor®, Oncül et al. (2010) used Computational Fluid Dynamics (CFD), to study the flow pattern in both 2 L and 20 L volume bags. The study used the Volume of Fluid (VOF) method to account for the evolution of free fluid during three-dimensional and time-dependent computations. The VOF method is an Eulerian approach proposed by (Hirt and Nichols, 1981) and has been used in the prediction of a number of multiphase flows involving a free boundary. The flow within the bags investigated by Oncül et al. (2010) was reported to be laminar, thus eliminating the need for a turbulence model and reducing the computational demand. In order to validate the computational simulations, empirical measurements such as time-dependent measurements of liquid surface height and liquid velocities were carried out at different locations in the bag. Maximum velocities occurred when the bag was in a horizontal position. Greater velocities were noted in the 20 L bag than in the 2 L bag, whilst the higher velocities within the 20 L were observed near the bag bottom of the bag (maximum velocities were relatively constant at various heights of the 2 L bag). An estimation of shear stress was also obtained for a few selected locations, with the maximum value being approximately 0.01 Pa (Oncül et al., 2010). Such values are much lower than those reported for a stirred tank geometry (higher than 1 Pa) observed by Joshi et al. (1996).

Given the unconventional nature of the rocked bioreactor, the efforts made to estimate and/or quantify their hydrodynamic characteristics have been limited. The availability of publications on rocked bags is both pertinent and sparse. This chapter aims to describe the fluid dynamics within a 2 L Sartorius Cultibag mimic, as determined using Particle Image Velocimetry. Significant time and effort were devoted to the design of an exact reproduction of the bioreactor. The materials and methods employed to perform this investigation are outlined in Chapter 2. All PIV measurements obtained were phase-resolved due to the significant changes in flow and surface movement during the course of a rock. The notation used to identify each vector map, the platform angle and direction of motion have been discussed in Chapter 2, Section 2.5.

6.2 Results

6.2.1 Wave induced motion

Through visual inspection of the fluid flow in operation, it was observed that the fluid flow direction was either in-phase with the platform rocking motion or out-of-phase. It was noted that the out-of-phase motion is a consequence of a wave formed on the surface of the fluid, as the liquid rebounds off the end of the bag. A typical out-of-phase wave travels ahead of the rocking platform motion, and is initiated at the lower starting point of a rock (i.e. θ = -8^o). Figure 6.1 shows a graph of the wave's dimensionless (normalised by the full radial length of the Cultibag cavity, L = 310 mm) radial location across the length of the bag (recorded by visual inspection). Along with the dimensionless angular position (normalised by the selected rocking angle, θ = 8^o) of the platform. The normalised radial location of the wave refers to the wave's horizontal position relative to either end of the rocked bag mimic. The normalised angular position relates to the platform angle relative to the horizontal plane (0^o) and 8^o. Figure 6.1 indicates that the wave initiates at the start of a rock (θ = -8^o) and travels the length of the bag 0.70 seconds faster than the platform can undergo one half of a rock (at a rocking rate of N = 25 rpm).

Waves come in a variety of forms. One of the more common forms of waves is gravity waves on water. When a fluid is displaced either on the surface or internally, gravity will attempt to restore it to its state of equilibrium (Koch et al., 2010). Bryson (1964) describes two more wave categories, named expansion and compression waves. As the Cultibag platform is rocked, the fluid flows downwards due to gravity to the opposite side of the bag. In addition, the direction of fluid vorticity of the wave is opposite to that of the fluid direction (noted through PIV vorticity plots). This is indicative of an expansion wave (Bryson, 1964). Another observation that indicates an expansion wave in the Cultibag, is the lower trailing fluid velocity of the wave compared to the leading portion of the wave: In a typical compression wave, the fluid velocity behind the wave is greater than the fluid velocity ahead of the wave. For this reason, a compression wave will at some point overtake the fluid ahead and then topple over it (as seen in ocean waves) (Bryson, 1964).

6.2.2 Phase-resolved flow characteristics

Figure 6.2 displays the phase-resolved velocity ($\bar{U}_{rz}$) contour plot obtained at N = 25 rpm, V_L = 50% wv with velocity vectors superimposed. In this section, rpm refers to rocks per minute. The plots represent one half of the Cultibag mimic at rocking angles of 0^o, 4^o and 8^o both ascending and descending (denoted as + or -, respectively). Fluid velocities of up to 0.37 ms^{-1} are noted at an angle of $\theta = +4^o$ (platform ascending). The range of velocities experienced by the fluid can be observed in Figure 6.3, where the mean whole flow field velocity ($\bar{U}_{rz}$) is plotted in correspondence to the varying platform positions. As expected, velocity is lowest at platform angles of $\theta = -8^o$ and $+8^o$, given that the fluid is at the edge of the bag and the platform has decelerated to its lowest angular velocity prior to its change in direction. Whilst the maximum velocities exist at $\theta = -4^o$, $+4^o$ and 0^o (here the fluid is travelling the length of the bag and is able to accelerate). This is particularly true for the trailing fluid at an angle above the horizontal plane, as fluid at this point would have been accelerated for the longest period of time. The results obtained by Oncül et al. (2010) also indicate that the velocity is highest when the bag is aligned with the horizontal plane. The authors stipulate that this is due to the maximum angular speed of the platform at this position. In addition, the average velocity at the side of the bag was lower than in the middle, possibly due to the liquid motion being constrained by the walls of the bag (Oncül et al., 2010).

Figures 6.4 and 6.5 show the radial and axial velocity components, at N = 25 rpm and $\theta = 8^o$. It is clear that the flow is dominated by the radial velocity, with values up to 0.35 ms^{-1} noted. This is in contrast to the axial velocities of up to 0.1 ms^{-1} observed in each vector map. Figures 6.6 and 6.7 show the phase-resolved contour plots of r.m.s. radial velocity and r.m.s. axial velocity, respectively. The figures show that the r.m.s. radial velocities are more pronounced; though the higher levels of r.m.s. velocity are observed when the liquid height is lowest (i.e. the leading or trailing fluid at angles of $\theta = 4^o$ and 8^o). So although the radial velocity ranges from 0 to 0.35 ms^{-1} within a single rock, the r.m.s. velocity can vary between just 0.02 to 0.04 ms^{-1} in the majority of fluid throughout the course of a full rock.

6.2.3 Effect of fluid working volume on flow characteristics

Fluid working volume is an important variable that can sometimes be overlooked during cell culture. It is a parameter that varies depending on sampling and feeding procedures, thus having an impact upon power input per unit volume. For this reason, phase-resolved data within the Cultibag RM mimic was obtained at fluid working volumes of 30, 40, 50 and 60% wv. Figures 6.8 and 6.9 show the phase-resolved velocity magnitude ($\overline{U}_{rz}$) contour plots with superimposed vectors for each of the fluid working volumes and rocking angles investigated, whilst Figure 6.10 shows the velocity magnitudes ($\overline{U}_{rz}$) averaged over the whole measured flow field, for each phase angle and fluid working volume investigated. An analysis of the whole flow field velocity magnitude was carried out, where the mean velocity values obtained were averaged over the acquired area. The mean velocity decreases with increasing fluid working volume, as can be seen from Figure 6.10. Figure 6.11 shows whole flow field averaged velocities of 0.116, 0.105, 0.092, and 0.076 ms^{-1} for volumes of 30, 40, 50 and 60%, respectively. The increase in velocity at lower working volumes can be attributed to an associated reduction in resistance to flow caused by the surrounding fluid, as well as the increased amount of space for the fluid to accelerate. As noted in section 6.2.2, a higher velocity was observed at lower liquid heights and the same observation is noted at the varying fluid volumes. Furthermore, the maximum velocities measured at each fluid volume do not exceed the 0.37 ms^{-1} which was measured at 50% working volume. A polynomial regression of the data points was carried out and results presented in Figure 6.11. An equation for the curve can be found as shown below with 'y' representing the value of $\overline{U}_{rz}$ averaged over the whole field and 'x' the fluid working volume as a percentage of the vessel volume:

$$y = -1 \times 10^{-5}x^2 - 0.00017x + 0.13283 \qquad (6.1)$$

The derivative of Equation 6.1 was calculated with respect to x and Equation 6.2 was obtained:

$$\frac{\partial y}{\partial x} = -2 \times 10^{-5}x - 0.00017 \qquad (6.2)$$

Using Equation 6.2, the maximum whole-volume averaged velocity magnitude ($\bar{U}_{ij}$) is estimated to occur at a working volume of 17%, with a value of

$\bar{U}_{rz}$ = 0.12705 ms^{-1}. The estimated subsequent drop in velocity below 17% wv may be due to increased surface tension and friction forces (commensurate to the fluid volume) at the reduced fluid volumes.

The degree of uniformity in relation to turbulence at varying fluid volumes is also of significance. Axial profiles of r.m.s. axial and radial velocities are shown in Figures 6.12, 6.13, 6.14, and 6.15 for working volumes of 30, 40. 50 and 60%, respectively. Figure 6.12 indicates the largest range of r.m.s. radial velocities measured, extending from 0.02 to 0.11 ms^{-1} in vector map 4 and radial location r/R = 0.115. However, the extent of this range can, to a degree, be attributed to the increased fluctuations measured at the fluid/air and fluid/Perspex boundary. This is due to the laser light refraction caused by the differing refractive indices of the Perspex, water and air. A relatively small range can be noted for the r.m.s. axial velocity in Figure 6.12 at vector map 8, with values between u'_z = 0.01 to 0.03 ms^{-1} in the axial direction. The spread of r.m.s. radial velocity values in the axial direction becomes narrower as the working volume increases. This can be seen in Figure 6.15, where the u'_r ranges from 0.013 to 0.014 ms^{-1} between z/H = 0.05 and 0.26. Again, the r.m.s. velocity deviates at values close to the bag surface, due to the difficulty in capturing particles at the liquid/air boundary layer.

The turbulent kinetic energy averaged over all fluid areas measured at the various platform angles is shown in Figure 6.16. The whole flow field averaged k in the fluid increases as the fluid volume decreases due to the reduced resistance to flow, and the greater energy per unit volume drawn into the fluid. The force generated by the platform remains the same given that the rocking rate and angle are kept constant, so a greater amount of energy is transferred to fluid per unit volume. These turbulent kinetic energy values are 0.0010, 0.0015, 0.0021 and 0.0022 m^{2}s^{-2} at fill volumes of 60, 50, 40 and 30%, respectively. The spatial range of turbulent kinetic energy levels can also be observed in the contour plots at the varying fluid volumes (Figure 6.17). The contour plot shown in Figure 6.17 at a rocking angle of -4^o (descending) at 30% wv shows a k range of 0 to 1.8 m^{2}s^{-2}, whilst its counterpart at 60% wv displays a range of 0 to 0.7 m^{2}s^{-2}.

6.3 Concluding remarks

The application of Particle Image Velocimetry to study the fluid dynamics within a rocked bag vessel is a novel study. Typical fluid dynamics studies into this category of bioreactor have been limited to single point analysis of fluid flow properties and to Computational Fluid Dynamics investigations (Oncül et al., 2010). The investigation presented has enabled the quantification of whole flow field velocities and turbulent velocities at rocking angles in 4^o increments within one rock. The changing surface and platform angle results in a range of fluid velocities occurring over the course of a single rock. Whole flow field averaged velocity values ($\bar{U}_{rz}$) can vary from 0.03 to 0.20 ms^{-1} over the course of one rock. Whilst at a fluid working volume of 30% wv and rocking angle of -4^o (descending); u'_r values of up to 0.11 ms^{-1} are noted, along with u'_r values as low as 0.02 ms^{-1}. Although the full range of turbulence and velocity measured in the Cultibag is significant, there is a much greater degree of uniformity, when compared with the impeller region and the bulk fluid of a stirred tank.

Fluid velocity measurements exhibited greater spatial uniformity at 60% wv, due to the relatively smaller space available for the fluid to move within. This may have implications for oxygen transfer given the surface aeration mechanism. The enhanced turbulence levels at the lower working volumes studied in this work are also of importance to mass and oxygen transfer mechanisms. The lower fluid working volume would cause enhanced oxygen transfer efficiency, given the greater surface to volume ratio. The reduced volume would also lead to increased turbulence, although the range of turbulence levels would be narrower at a higher fluid volume.

The variation in turbulence and velocity noted in this chapter occurs within 1.2 secs (which constitutes half a rock) and repeat every 1.2 secs. Indeed, there are many different paths with which a cell can flow within the Cultibag, and from the data acquired, structures of flow entrainment or segregated flow are not visibly evident. Though, due to the rocking motion and changing fluid structure, there is a greater degree of hydrodynamic uniformity within the Cultibag compared with stirred tanks.

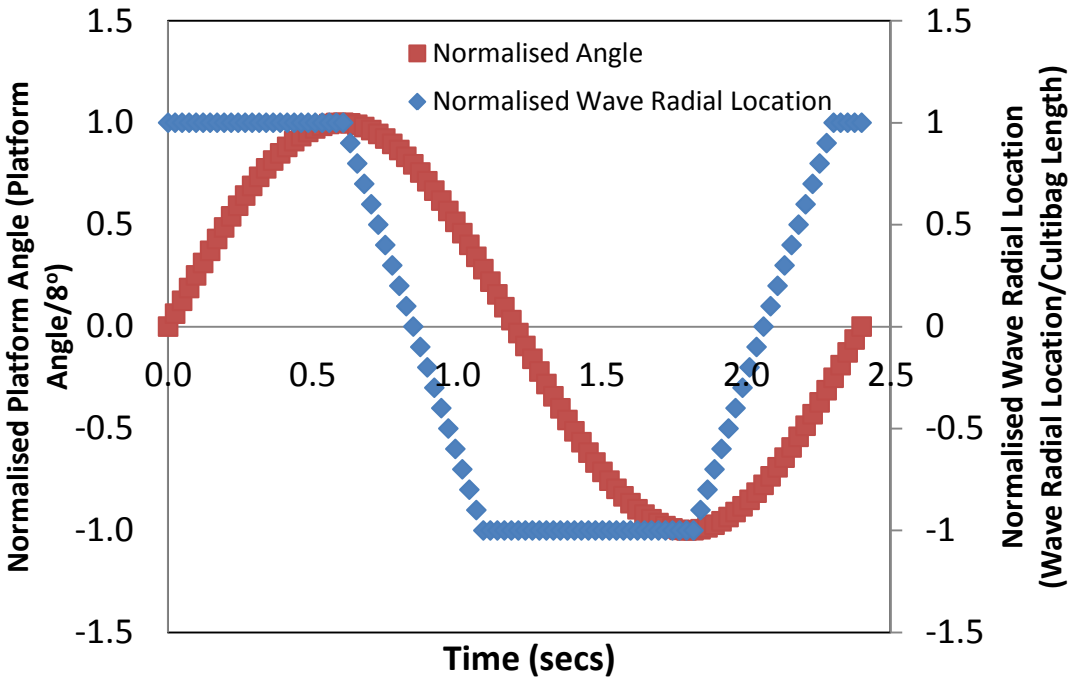

Figure 6.1: Profile plot of normalised platform angle over a single rock (2.4 seconds in duration) and radial location of the wave over a single rock. Rocking rate of 25 rpm and V_L = 50% wv.

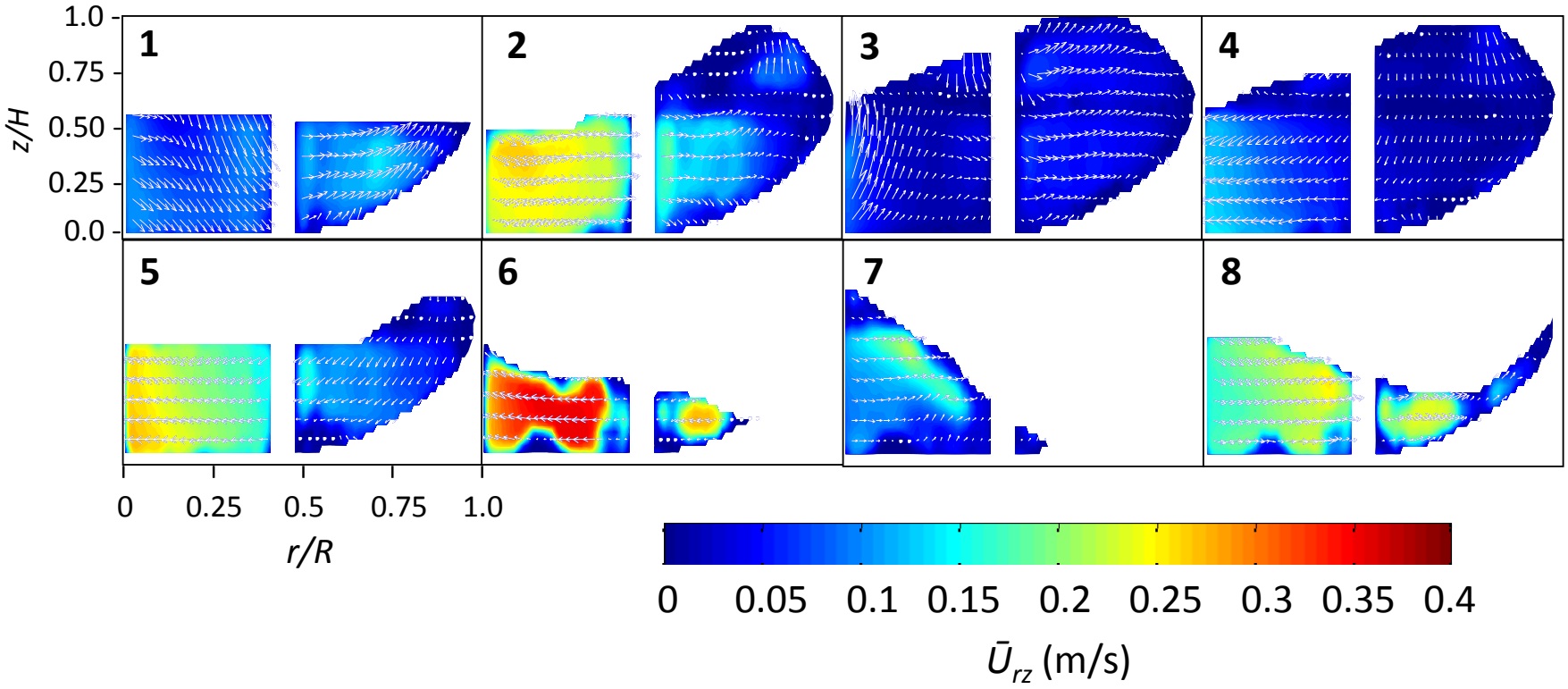

Figure 6.2: Phase-resolved velocity ($\bar{U}_{rz}$) contour plot obtained at N = 25 rpm, V_L = 50% wv with superimposed velocity vectors. Numbers 1-8 represent the platform angle and direction of motion as explained in Chapter 2

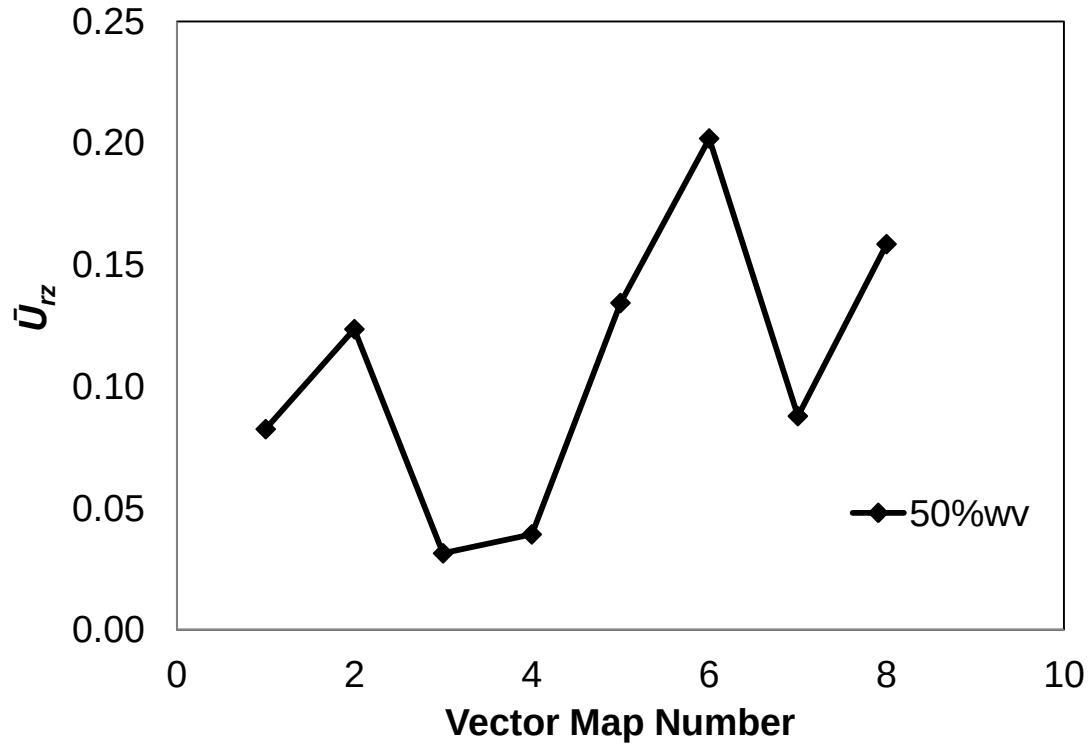

Figure 6.3: Mean vector map velocity measured using PIV at various platform angles.

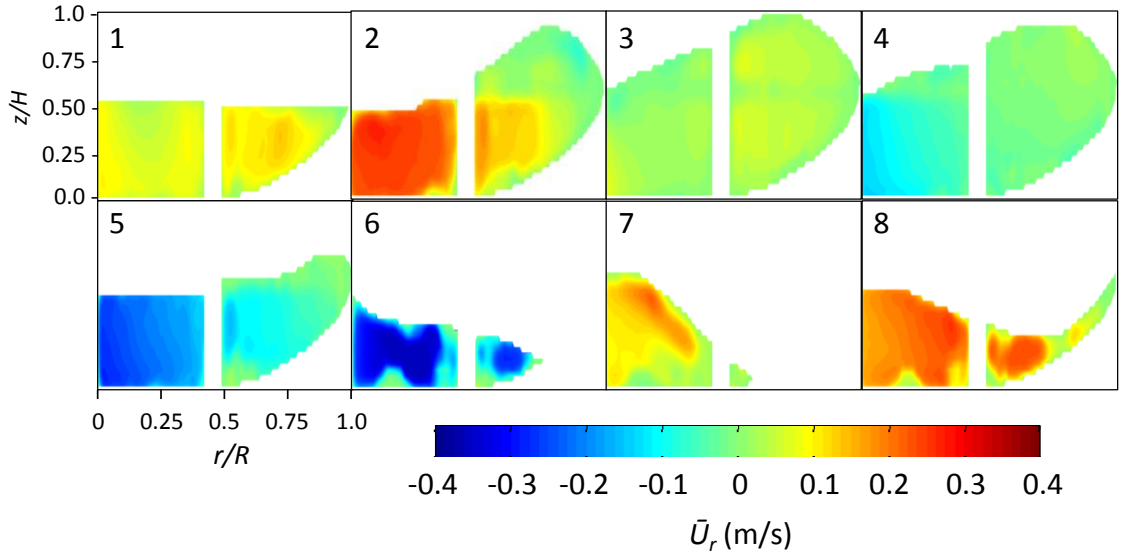

Figure 6.4: Phase-resolved radial velocity contour plots obtained at N = 25 rpm, V_L = 50% wv.

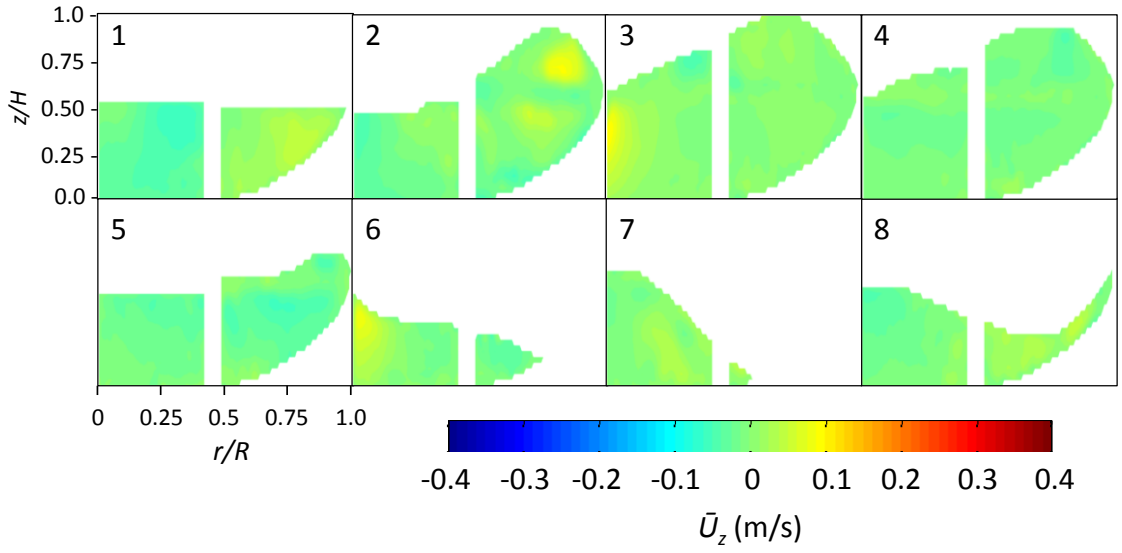

Figure 6.5: Phase-resolved axial velocity contour plots obtained at N = 25 rpm, V_L = 50% wv.

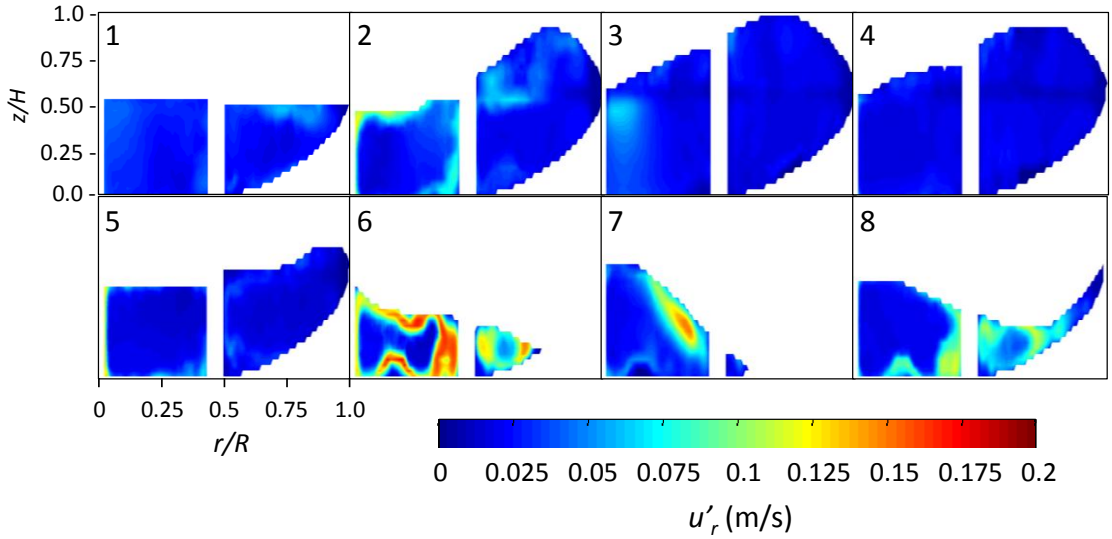

Figure 6.6: Phase-resolved r.m.s. radial velocity contour plots obtained at N = 25 rpm, V_L = 50% wv.

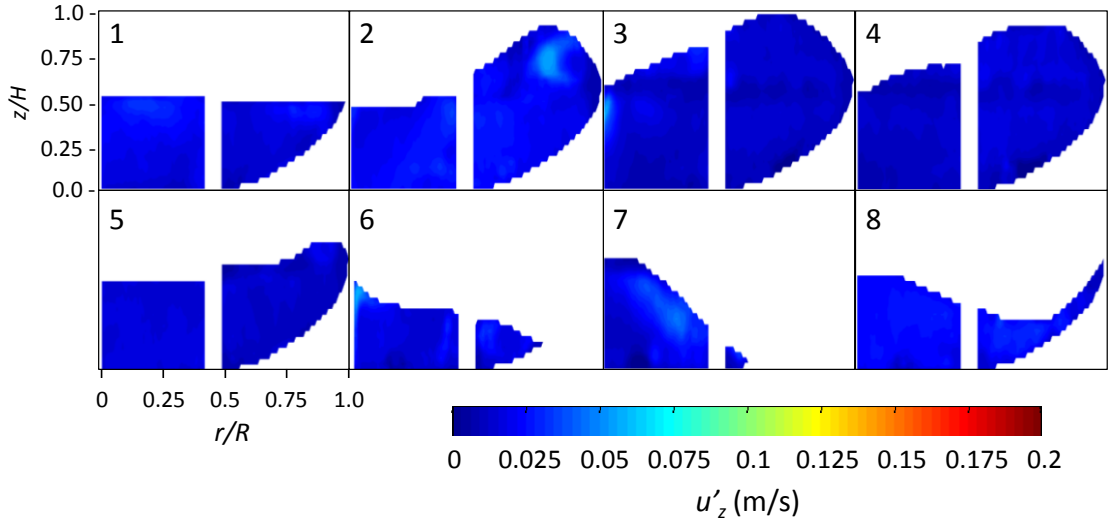

Figure 6.7: Phase-resolved r.m.s. axial velocity contour plots obtained at N = 25 rpm, V_L = 50% wv.

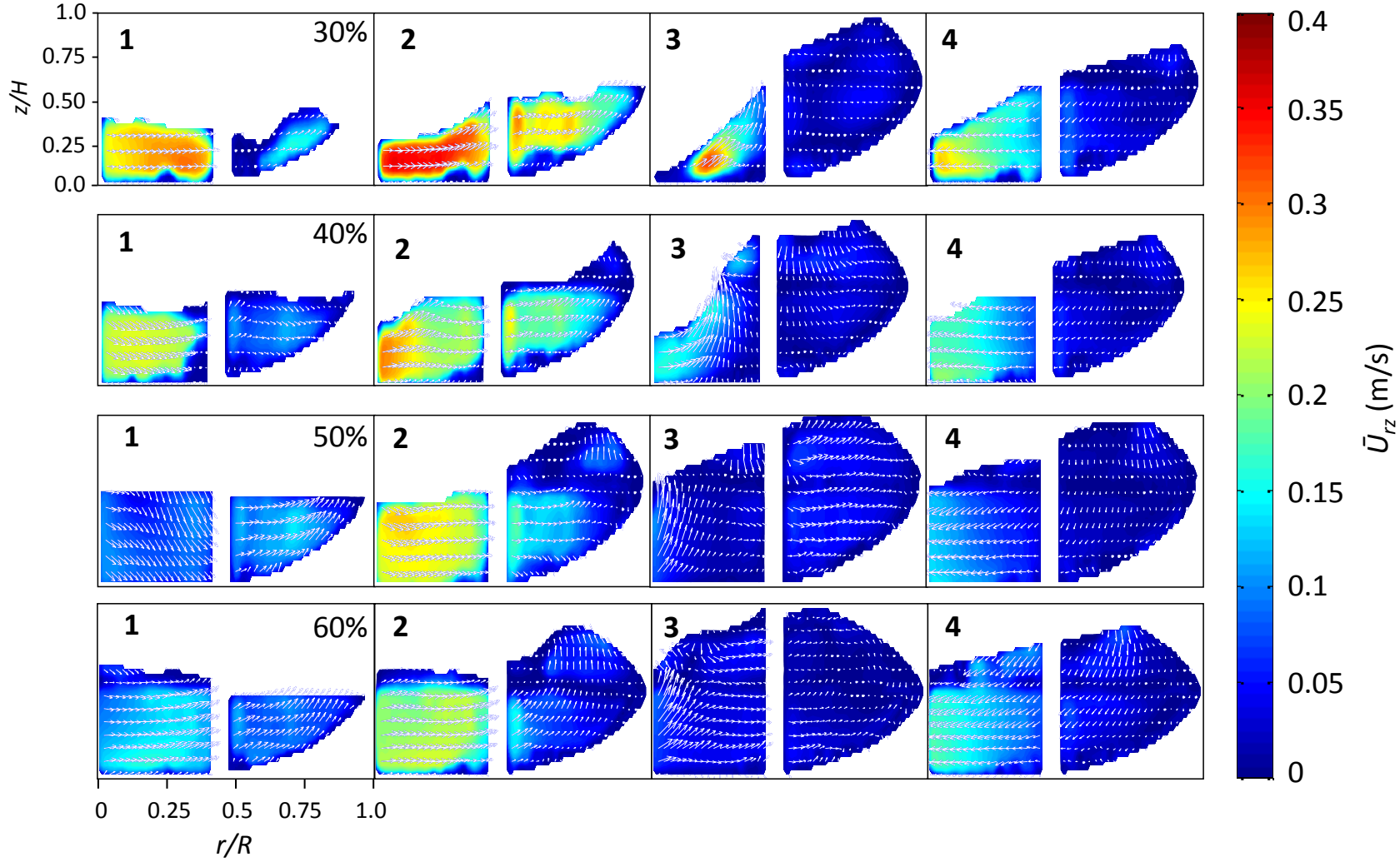

Figure 6.8: Phase-resolved velocity contour plots obtained at N = 25 rpm, V_L = 30, 40, 50 and 60% wv with superimposed velocity vectors.

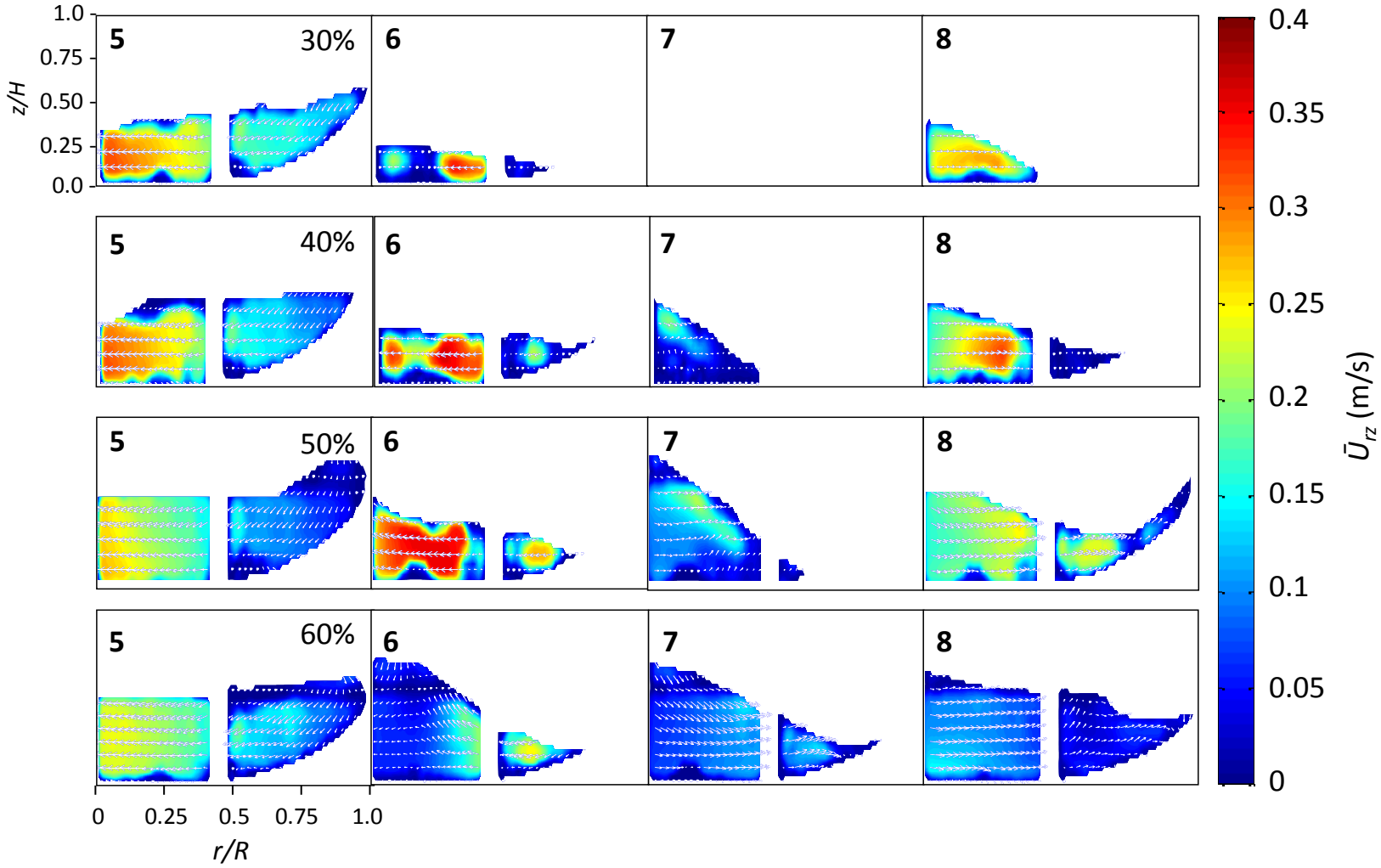

Figure 6.9: Phase-resolved velocity contour plots obtained at N = 25 rpm, V_L = 30, 40, 50 and 60% wv with superimposed velocity vectors.

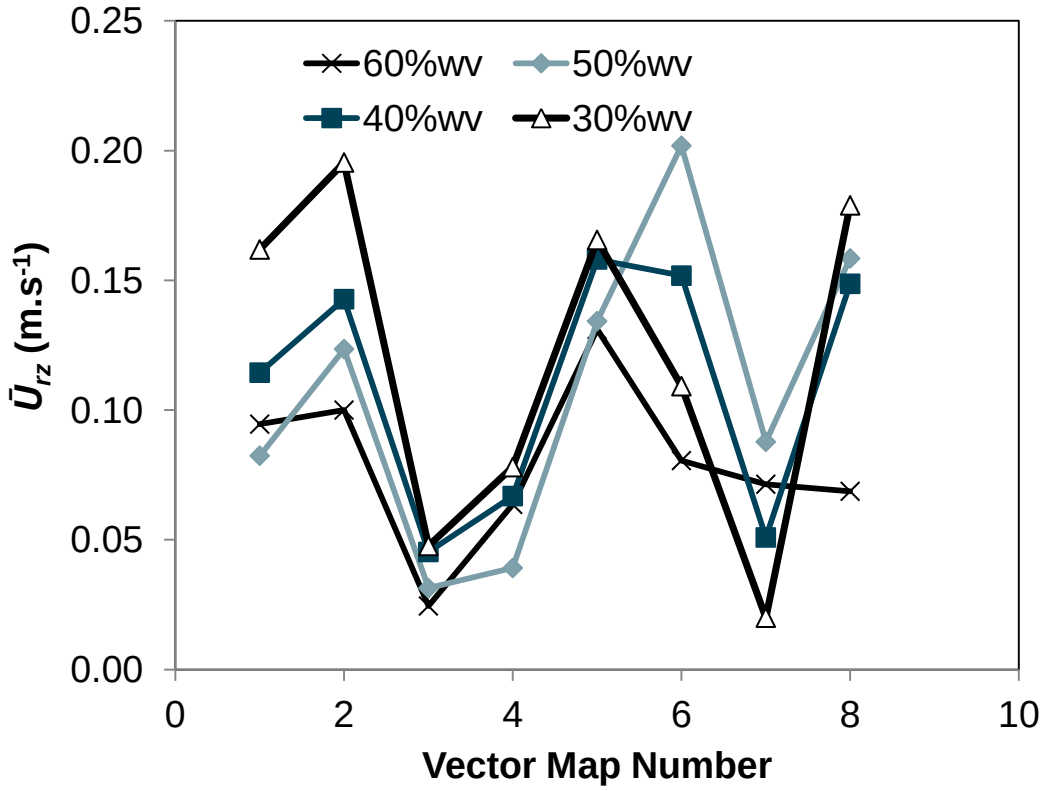

Figure 6.10: Whole flow field (averaged for whole vector map) velocity measured using PIV at various platform angles. Profiles are presented for fluid working volumes of V_L = 30, 40, 50 and 60%.

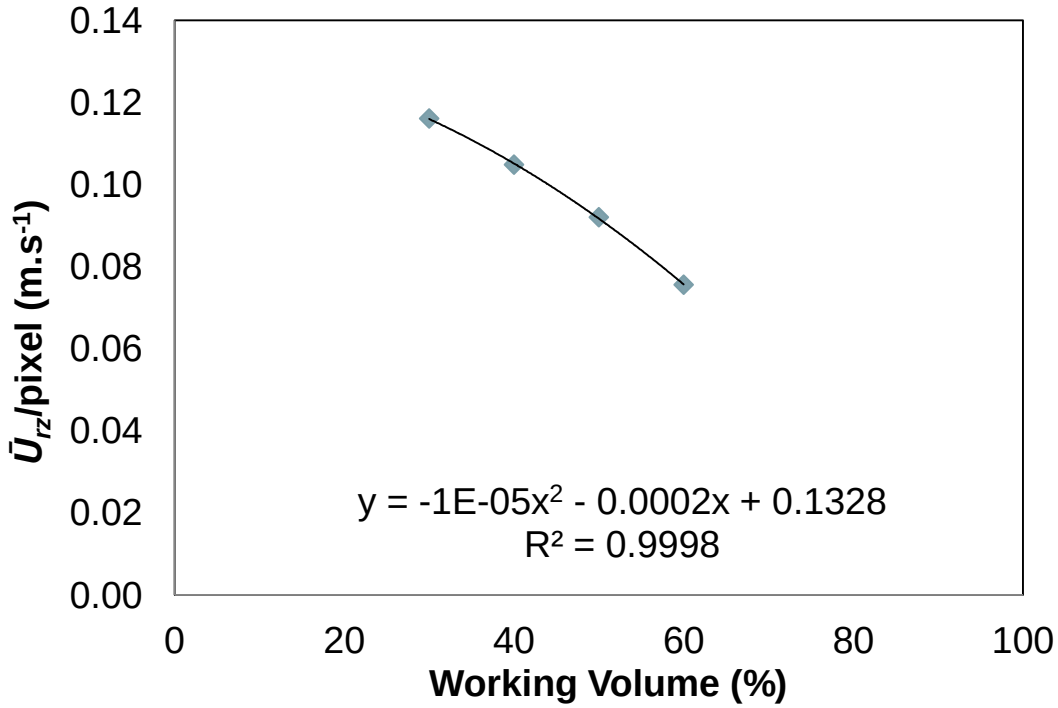

Figure 6.11: Velocity magnitude representative of the mean flow over the duration of a rock. Values shown are the mean velocities per pixel, for each of the four fluid working volumes investigated using PIV (V_L = 30, 40, 50 and 60% wv).

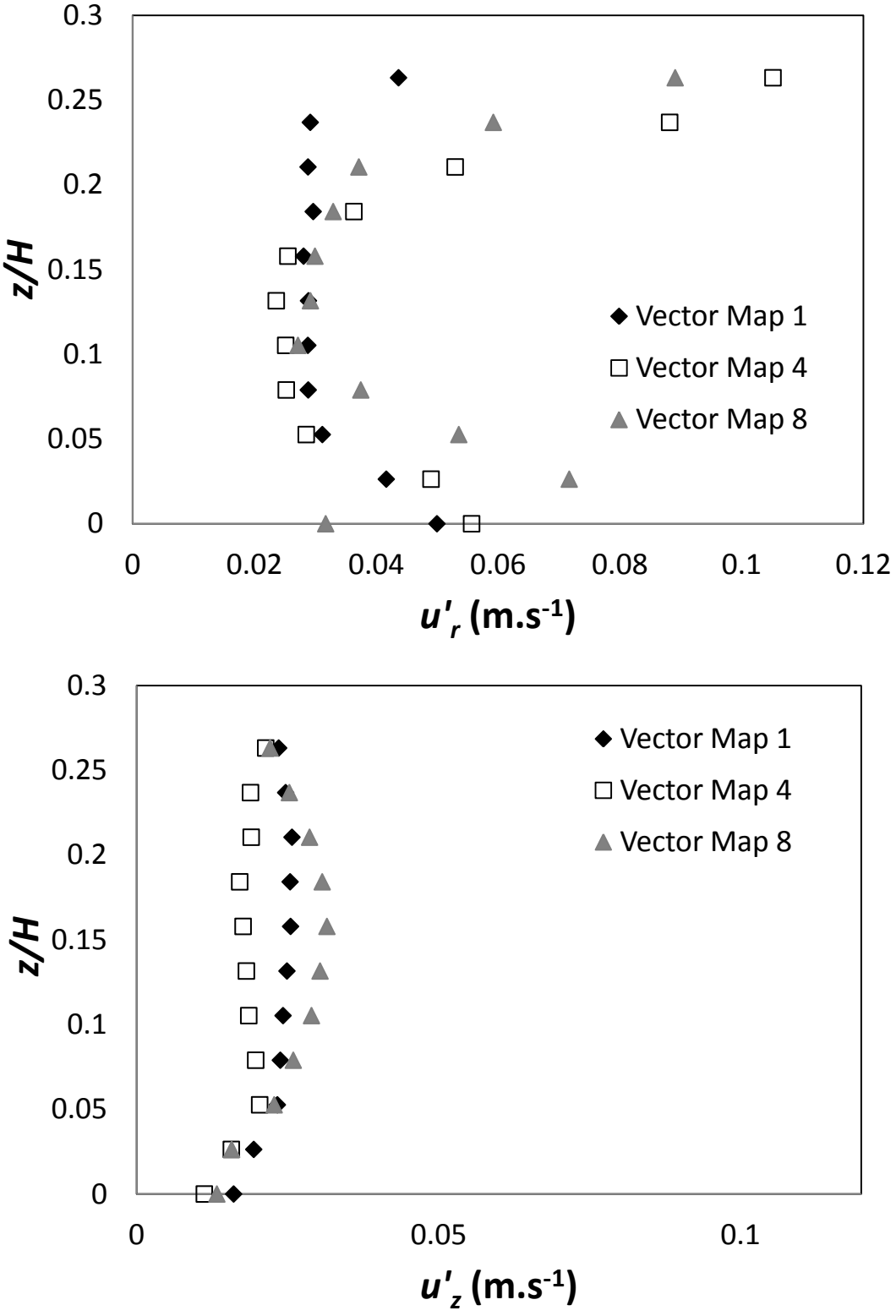

Figure 6.12: Axial profiles of a) r.m.s. radial velocity and b) r.m.s. axial velocity, for working volume V_L = 30% wv. Values are given for radial location r/R = 0.115.

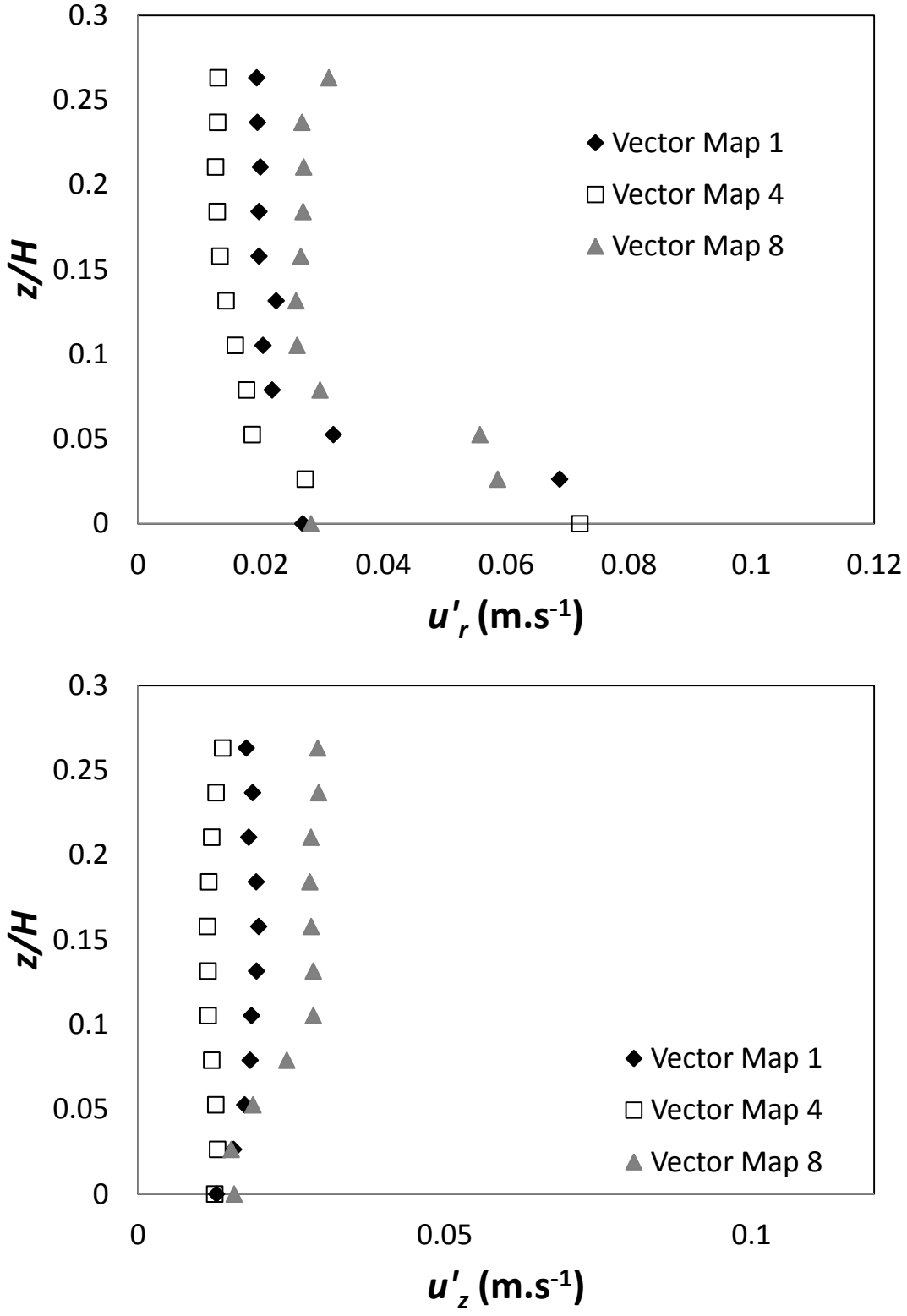

Figure 6.13: Axial profiles of a) r.m.s. radial velocity and b) r.m.s. axial velocity, for working volume V_L = 40% wv. Values are given for radial location r/R = 0.115.

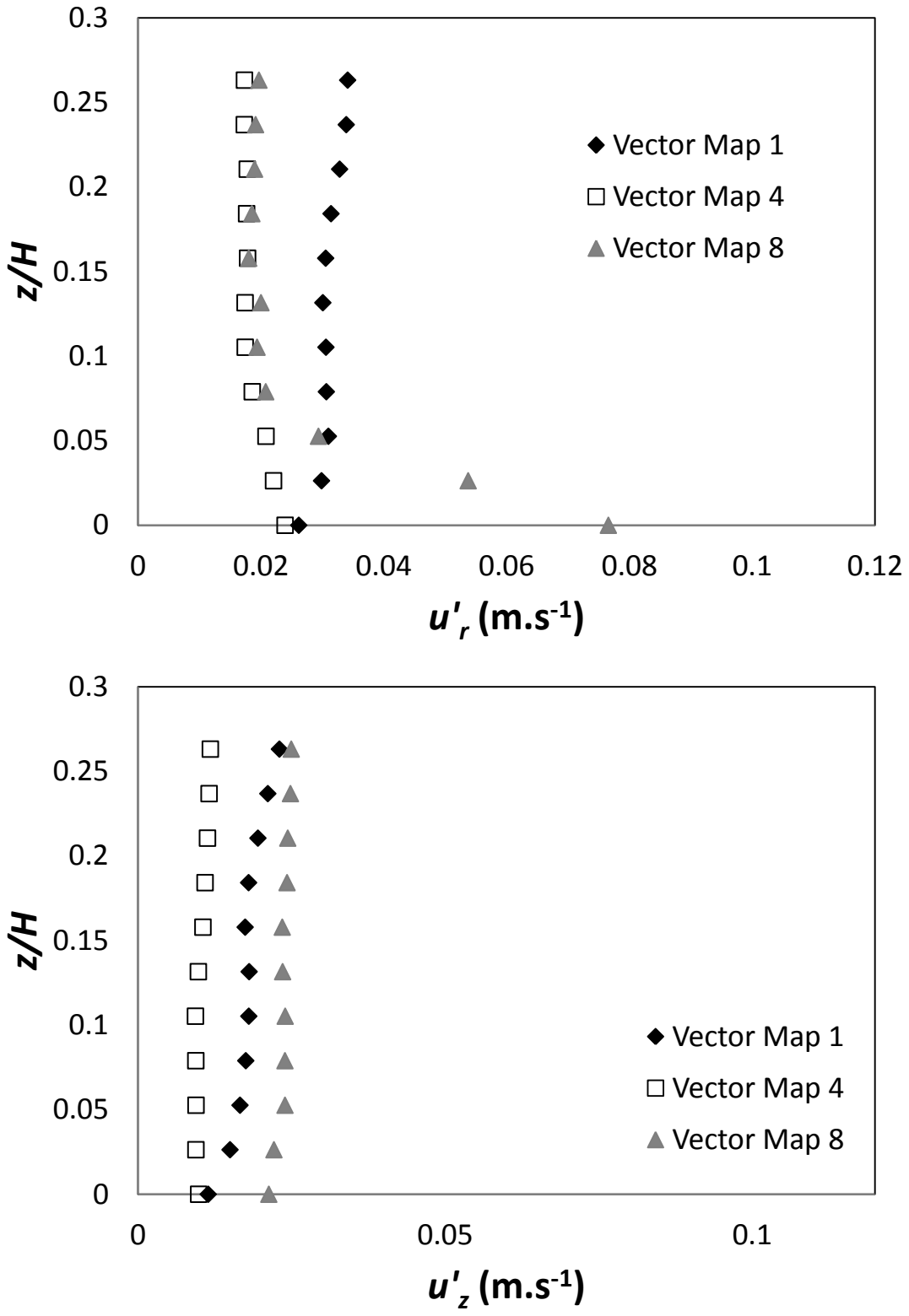

Figure 6.14: Axial profiles of a) r.m.s. radial velocity and b) r.m.s. axial velocity, for working volume V_L = 50% wv. Values are given for radial location r/R = 0.115.

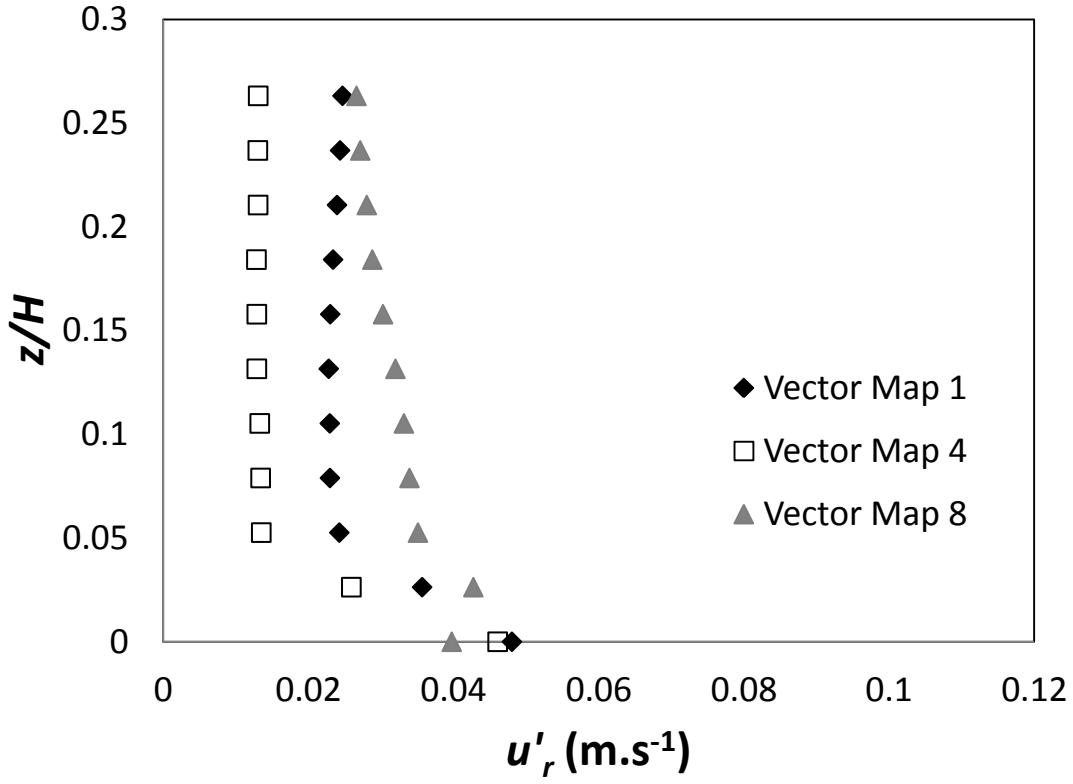

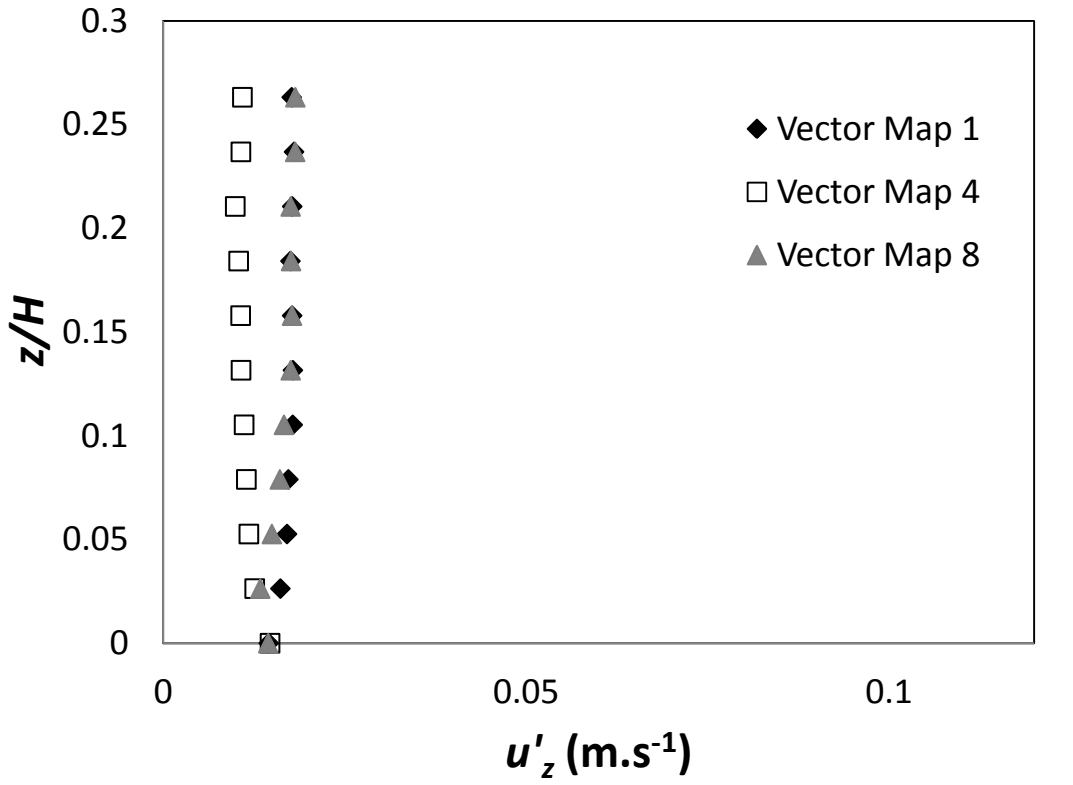

Figure 6.15: Axial profiles of a) r.m.s. radial velocity and b) r.m.s. axial velocity, for working volume V_L = 60% wv. Values are given for radial location r/R = 0.115.

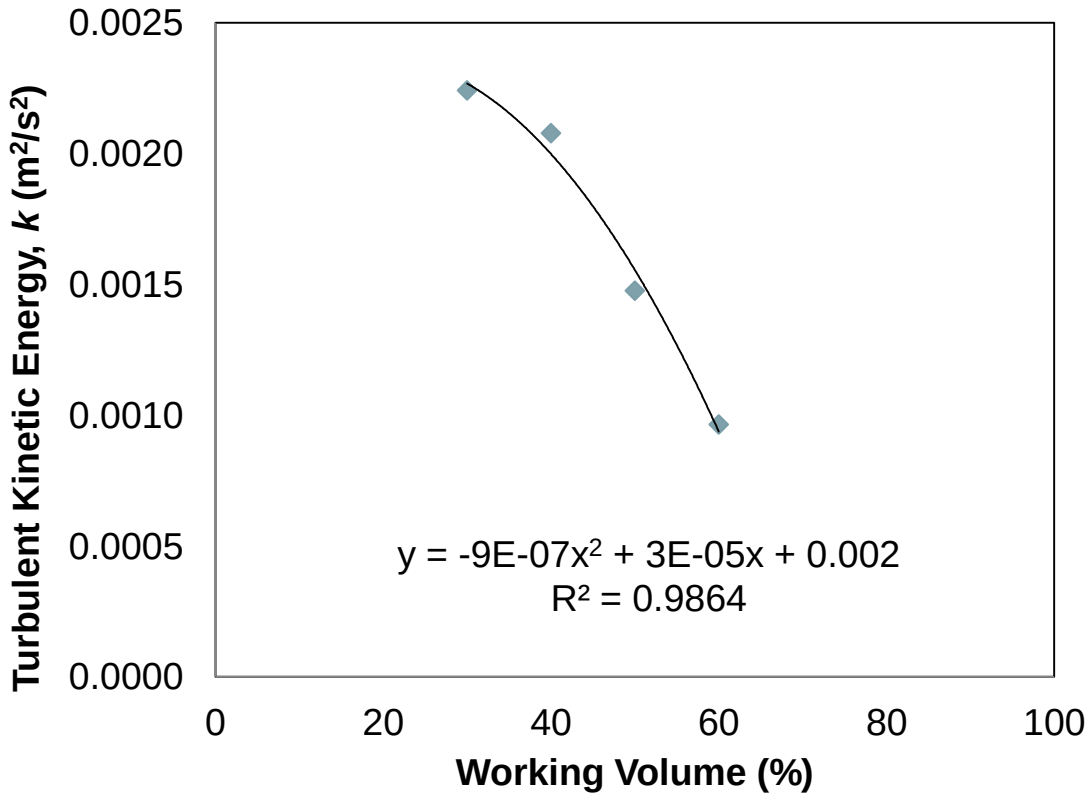

Figure 6.16: Turbulent kinetic energy (k) averaged over the whole fluid vector maps at the various rocking angles. Values shown are the mean velocities per pixel, for each of the four fluid working volumes investigated using PIV (V_L = 30, 40, 50 and 60% wv).

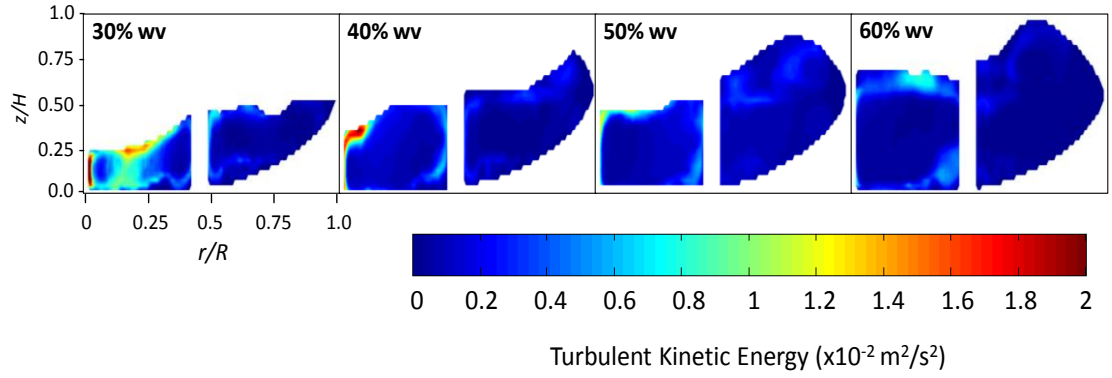

Figure 6.17: Phase-resolved contour plots of turbulent kinetic energy (m^2/s^2). Plots shown are determined at a rocking angle of -4°, descending, at fluid working volumes of 30, 40, 50 and 60%.

Chapter 7 Mammalian Cell Culture in Varying Hydrodynamic Conditions

7.1 Introduction

The whole flow field characteristics described in previous chapters for a range of single-use bioreactors have enabled the achievement of a unique knowledge platform upon which to compare process characteristics and corresponding cell culture performance within different systems. As noted in Chapter 1, previous works investigating cellular response to hydrodynamic stresses have largely been applied to characterising tolerance levels of animal cells to parameters such as EDR and shear stress. This chapter will focus on studying the effects of the varying hydrodynamic conditions in actual lab-scale SUBs upon mammalian cell culture performance.

Mammalian cell cultures are the primary source for a number of high-value biologics including antibodies, viral vaccines and hormones. Thus, the ability to understand and predict the behaviour of the different facets of mammalian cell cultures at varying conditions is pertinent for both scientific and commercial purposes (Sidoli et al., 2004). When characterising cellular performance and the biological responses to external stimuli, there are a multitude of interdependent parameters that can be used to understand the behaviour of cells. Metabolic flux analysis using isotopic tracers and mass spectrometry has been utilised to understand the metabolism of CHO cells during the varying stages of cell growth and death (Ahn and Antoniewicz, 2011; Sengupta et al., 2011). Through these studies, a significant increase in flux through the pentose phosphate pathway has been observed (Sengupta et al., 2011), in addition to reduced flux in the glycolytic pathway upon transition from growth to the non-growth phase of CHO cells (Ahn and Antoniewicz, 2011).

Metabolic profiles can provide an insight into the performance of a given culture. In particular, lactate production (and/or consumption) is typically monitored in industrial processes. This metabolite is normally produced in great quantities during the exponential phase of cell growth, its production then shifts to net

A significant amount of the results included in this chapter are presented in Odeleye et al. (2014) entitled: 'On the fluid dynamics of a laboratory scale stirred single-use bioreactor', Chemical Engineering Science, vol. 111 p299-312.

consumption when the stationary phase begins. The lactate production during the exponential phase can be attributed to the conversion of glucose to lactate (rather than being completely oxidised to CO_2 and H_2O, even when there is sufficient oxygen); the latter is known as the "Warburg effect" or aerobic glycolysis (Mulukutla et al., 2010). However, the latter shift to net lactate consumption is not a generic or universal phenomenon and is not something that can be easily controlled (Zagari et al., 2013). The rapid consumption of glutamine is also a notable characteristic of rapidly growing cells. This is a key energy source for the tricarboxylic acid cycle (TCA) cycle, however it may indicate the oxidation of glutamine to malic acid, which then is converted to pyruvate and subsequently lactate (Zagari et al., 2013).

This chapter investigates the impact of differing fluid dynamics, within two very different cell culture systems, upon a GS-CHO mammalian cell fed-batch culture. As previously mentioned, there are numerous aspects of CHO cell performance and behaviour that can be analysed, so for practical reasons, the assessment of CHO cell performance and behaviour was narrowed to characterising cell growth, metabolite concentration and protein productivity. The methods used to obtain the results presented in this chapter have been described in Chapter 2, section 2.9.

Cell culture experiments were performed in the 3 L Mobius® CellReady, for comparison with PIV measurements investigated in Chapter 3. A fed-batch culture was conducted within the Sartorius 5 L BIOSTAT® B-DCU, to provide data for comparison using traditional cell culture methods.

CellReady cell culture experiments were performed at different impeller speeds and liquid volumes, as shown in Table 7.1.

Table 7.1: Operating conditions used for the cell culture experiments in the CellReady bioreactor

Operating Conditions			
Working Volume (L)	1	2.4	2.4
Impeller Rate (rpm)	350	200	80
Reynolds Number (*Re*)	38,057	21,747	8,699
Impeller Tip Speed (ms^{-1})	1.396	0.798	0.319
Power Per Unit Volume (W/m^3)	152.98	11.89	0.76

A cell culture experiment in the Sartorius 5 L BIOSTAT bioreactor was conducted at N = 260 rpm (corresponding to Re = 23,858). Air flow rate was maintained constant at 0.02vvm and the DOT was controlled at a minimum of 30%. The k_La value, as measured via the dynamic gassing-out method, was found to be 5 hr^{-1} at the operating conditions used in this work. The BIOSTAT cell culture was used as a benchmark for culture performance, with the conditions used representing the laboratory established standard operating protocol (Mammalian Cell Lab, University College London) for GS-CHO cell cultures.

Sartorius Cultibag RM cell culture experiments in a 2 L bag were performed at different rocking speeds, maintaining a constant starting working volume, as shown in Table 7.2.

Table 7.2: Operating conditions used for the cell culture experiments in the Sartorius Cultibag RM bioreactor

Operating Conditions			
Run Number	1	2	3
Working Volume (L)	1	1	1
Rocking Rate (rpm)	25	25	42

7.2 CellReady cell cultures

7.2.1 Cellular Growth

In order to ascertain the performance of an antibody-producing CHO cell line within the CellReady in response to a change in hydrodynamic conditions, cell culture experiments were conducted in the bioreactor at the conditions described in Chapter 2. For each experiment cellular growth, protein productivity and metabolite production of fed-batch cell cultures at the conditions reported in Table 7.1 were obtained. The fluid working volume and impeller rotation speeds selected for the cell culture investigation are within the range recommended by the manufacturer Merck Millipore. Three impeller speed-liquid fill volume combinations were selected to represent the upper (350 rpm and 1 L), middle (200 rpm and 2.4 L) and lower (80 rpm and 2.4 L) levels of turbulence occurring within the CellReady. The

reduction of fluid working volume from 2.4 L to 1 L would serve to increase the frequency with which cells pass through the lower circulation loop characterised by higher turbulence levels and higher Reynolds stresses. For simplicity, these three experimental conditions will be referred to as 80rpm-1L, 200rpm-2.4L and 350rpm-1L. Figure 7.1 shows the viable cell growth profiles and cell viability at the three cell culture conditions tested. Cell growth and viability data of a benchmark cell culture conducted in a 5 L Sartorius bioreactor are also reported in Figure 7.1. For most operating conditions and bioreactor systems viable cell density reached values higher than $10x10^6$ cells/mL. The growth profile obtained from the cell culture conducted at 350 rpm and 1 L volume is characterized by a longer lag phase than the profiles obtained at the other conditions. An extended lag phase can indicate a period of adaptation and in this case might be an indication that cells are adapting to the higher turbulence levels present in the bioreactor at the 350rpm-1L condition. Under these conditions cells achieve a maximum concentration of over $11x10^6$ cells/mL, thus showing a similar profile to the other cultures in the exponential and stationary phase. This is in agreement with the work of Kunas and Papoutsakis (1990), whereby even in the presence of entrained bubbles (ranging from 50 to 300 μm) and impeller speeds of up to N = 700 rpm, good cell growth of hybridoma cultures was observed in a 2 L Setric Genie Bioreactor.

Particle size distribution was measured using a sample at the end of each cell culture experiment to determine whether the selection of the higher impeller speed and lower liquid volume combination had an impact on cell size. Mean particle diameters throughout the cell cultures are shown in Figure 7.2, whilst the particle size distribution on day 14 of the experiments (i.e. harvest) are shown in Figure 7.3. Interestingly, particle size experiments showed a significantly reduced maximum cell diameter of 16.23 μm obtained at 350rpm-1L conditions, whilst at 80rpm-2.4L and 200rpm-2.4L maximum cell diameters of 17.99 μm and 18.46 μm, respectively, were recorded. Godoy-Silva et al. (2009) have shown that cell size during culture is influenced by repetitive cycles of high hydrodynamic stress levels. In the aforementioned study, cells were cyclically subjected to a "torture chamber" with energy dissipation rate values of $6.4x10^6$ W/m^3, from day 4 of a 14 day CHO cell culture. The cell culture experiments were conducted within a 2 L (1 L working volume) bioreactor with dual pitched blade impellers (Applikon, Inc., Foster city,

CA) at N = 130 rpm. Cells not subjected to the "torture chamber" attained a final day mean cell diameter of approximately 18 µm, whilst those exposed to the repetitive increased energy dissipation rates were found to have a mean cell diameter of 17 µm. In addition to the influence of the rate of energy dissipation on cell size during culture, this finding is important in relation to the flow length scale to cell size ratio. It has been suggested that if the Kolmogorov length scale (flow length scale) is greater than the cell diameter, then cell damage should not occur (Scott et al., 2012), since cells would become entrained within the larger turbulent eddies rather than collide with turbulent eddies of size comparable to the cells.

7.2.2 Protein productivity

Figure 7.4 shows the IgG_4 concentration present in samples obtained daily throughout the duration of the 14 day-long cultures. The maximum recombinant protein concentration of 0.92 g/L was expressed by cells grown in the 5 L Sartorius bioreactor, while those cultivated in the CellReady at N = 200 rpm and V_L = 2.4 L obtained an IgG_4 titre of 0.87 g/L. Cell culture experiments conducted at 80rpm-2.4L and 350rpm-1L resulted in lower recombinant protein production of 0.77 g/L and 0.76 g/L, respectively (a reduction of 17% and 18% respectively in comparison to the benchmark Sartorius BIOSTAT experiment). Cells grown at the 80rpm-2.4L condition did not attain the same maximum cell density as their counterparts (200rpm-2.4L and 350rpm-1L). In the case of cells grown at N = 80 rpm it is possible that nutrient and oxygen limitations occurred due to insufficient mixing. As a result of the reduced *Re*, the cells began to form clusters which would have impacted upon nutrients transport to cells. The lower viable cell count observed at 80rpm-2.4L and the lower cell specific productivity found at this condition would have influenced the final IgG_4 titre. Based on the fluid dynamics investigations, Re = 21,747 corresponds to the onset of fully developed turbulent flow conditions along with gas phase entrainment, but it is likely that cells in regions above the impeller experienced significantly reduced mass transfer conditions. This disparity in fluid dynamic stress is even more pronounced between the two counter-rotating loops observed at 350 rpm. The reduced IgG_4 titre observed at 350rpm-1L is in agreement with the work of Nienow et al. (2013b) , where CHO cells grown within a 2 L STR were repeatedly subjected to a plug flow loop with increased specific power

input of up to $2.9x10^5$ W/m^3. The cells were circulated through the loop at a similar frequency with which they would circulate as a result of agitation at the large scale. Cells grown within the STR with and without the recirculation loop obtained cell densities within batch to batch experimental deviation, however, cells that were repeatedly exposed to increased specific power input showed a 20% reduction in IgG_4 titre and cell specific protein productivity.

7.2.3 Metabolite analysis

Profiles of metabolite concentrations (as described in section 2.4) were obtained for all cell culture runs. Figure 7.5 shows the lactate concentration profile for the three CellReady cell cultures conducted in this work. The lactate concentration reached the highest values of 3 g/L at 80rpm-2.4L. This correlates with the work of Sorg et al. (2011) which shows greater lactate production was obtained as the energy dissipation rate range becomes narrower. This highlights the importance of spatial and temporal regularity of the cells environment, not only with respect to oxygen and nutrients concentration but also with regards to energy dissipation. The lactate concentration profile observed at 200rpm-2.4L is the profile expected for the CHO cell line used in this work, where the lactate increases upon commencement of the cell exponential growth phase. This behaviour is associated with the metabolism of glucose through glycolysis, followed by the conversion of pyruvate to lactate due to insufficient oxygen during the exponential phase (Campbell and Reece, 2005). Subsequently, as the stationary phase progresses, lactate concentration becomes constant (indicating net lactate consumption) due to the cellular demand for a higher carbon source concentration. In the case of the cells grown at 350rpm-1L, lactate concentration reaches a maximum at day 7 (which coincides with the beginning of the stationary phase) and then decreases for the remainder of the culture. At this stage lactate is metabolised in the Krebs cycle, which may indicate one of two scenarios: an increase in the demand for pyruvate through the Krebs cycle, or reduced production of the pyruvate through glycolysis due to the sequestering of glucose within another metabolic pathway. The latter would result in a reduction in NADH and ATP production necessary for protein synthesis.

The overall glucose consumption as well as the cell specific consumption of glucose was lowest at 350rpm-1L condition (11 g/L of glucose consumed throughout the culture period, as opposed to 13 and 14 g/L consumed at 200rpm-2.4L and 80rpm-2.4L, respectively). Lactate consumption is typically a cellular response to a lack of glucose as a carbon source, however, adequate glucose levels (>2g/L) were maintained throughout the fed-batch cultures. Lactate consumption also coincides with a reduction in ammonium production (Li et al., 2012), which was evident in this work where ammonium concentrations of 2.45, 5.12 and 3.52 g/L were measured at 80, 200 and 350 rpm, respectively. The consumption of both glucose and lactate along with reduced IgG_4 productivity may be an indication that the higher turbulence levels at 350rpm-1L engendered the reallocation of glucose away from IgG_4 synthesis, towards more essential requirements. Table 7.3 shows cell specific productivity obtained during the stationary phase at the different conditions tested.

Table 7.3: Stirred Tank Bioreactor Cell Specific Productivity of IgG_4 (picograms per cell per day)

Bioreactor & Conditions	**IgG_4 ($pg.cell^{-1}.day^{-1}$)**
5 L STR 260rpm-3.5L	9.3
CellReady 80rpm-2.4L	9.0
CellReady 200rpm-2.4L	9.3
CellReady 350rpm-1L	8.2

The cell specific protein productivity at 350rpm-1L was 12% lower than the productivity obtained at 200rpm-2.4L, whilst the 80rpm-2.4L condition and the experiments conducted using the Sartorius bioreactor had cell specific productivities similar to that obtained at 200rpm-2.4L condition. This finding supports the aforementioned hypothesis about a possible change in glucose metabolism during the stationary phase. It can be postulated that the reason behind the shift from lactate production to consumption is oxidative stress. Oxidative stress is defined as a state of inequity within a cell where the reactive oxidative species becomes imbalanced in favour of the oxidant species. The adoption of high impeller rates and airflow inlet in the bioreactor may have resulted in locally high levels of oxygen leading to the oxidative stress phenomena (Mckenna, 2009). For this reason, cells may have reduced their utilisation of glucose for protein production in order to maintain a

reduced environment. Metabolic analysis of CHO cells has shown a stationary phase characterised by a reduced flux of glycolysis, net lactate uptake accompanied by significant glucose flux through the oxidative pentose phosphate pathway (oxPPP) (Ahn and Antoniewicz, 2011). This is in contrast to the exponential phase, where glycolysis contributes more (in comparison to the stationary phase) to ATP production (Ahn and Antoniewicz, 2011). The augmented oxPPP flux indicates a requirement of additional NADPH at the stationary phase to be used to counteract oxidative stress (Sengupta et al., 2011). Cells produce defensive enzymes such as glutathione peroxidise; these enzymes eliminate peroxides that accumulate within the cell, by oxidizing glutathione to glutathione disulfide. This is subsequently regenerated by NADPH reduction catalysed by glutathione reductase (Sengupta et al., 2011).

7.3 Sartorius Cultibag cell cultures

7.3.1 Cellular growth

Initial cell culture investigations within the Sartorius Cultibag involved establishing the reproducibility of the system and operating procedures when culturing GS-CHO cells at 25 rpm and 1 L working volume. At these conditions, the Cultibag cultures possessed a k_La value of 11 hr^{-1} (determined using the static gassing out method). Figure 7.6 shows the VCC and viability of the two runs at 25rpm-1L, showing viable cell density to reach values higher than $7x10^6$ cells/mL in both cases and a difference in cumulative IVC of less than 7%. The lag phase appears to last slightly longer in 25rpm-1Lv2 with the cells entering their exponential phase of cell growth on day 5 (whereas this occurs on day 4 of 25rpm-1Lv1). This slight difference can also be noted in the glutamate profiles shown in Figure 7.7, indicating that the metabolism of glutamate in 25rpm-1Lv2 is one day behind that of 25rpm-1Lv1. However, these observations are very subtle, and the mean cell specific growth rate from day 0 to 7 remains similar between the two runs, with 0.46 $cell.cell^{-1}.day^{-1}$ and 0.47 $cell.cell^{-1}.day^{-1}$ for runs 1 and 2, respectively (calculated using the mean of VCC/IVC for days 0 to 7).

Increasing the rocking rate to 42 rpm results in a significant increase in stationary phase VCC (with VCC of up to $9.19x10^6$ cells/mL, shown in Figure 7.8), along with

a 15% increase in the cell specific growth rate (from days 0 to 7) to 0.56 $days^{-1}$. A reduction in viability on day 1 of the 42rpm-1L culture can also be noted, showing a decrease in viability of 3.5% compared with day 0 of the culture which is quickly recovered by day 2. This is similar to the observation of Sorg et al. (2011), who operated a Lobed Taylor-Couette bioreactor (at 150 rpm) with an overall ε (defined as the viscous dissipation of turbulent kinetic energy) equivalent to that observed in the impeller zone of a stirred bioreactor (operating at 150 rpm). In this work, a small drop in cell viability of approximately 4% occurred on day 1 of the culture and was quickly recovered on day 2. It was suggested that this drop indicated a period of adaption of the cells to their hydrodynamic environment, with possible selective elimination of small subpopulations of the "weakest" cells (Sorg et al., 2011). However, it is still possible that this deviation represents a degree of batch-to-batch error. It is also worth stating that in the study, the Lobed Taylor-Couette bioreactor was considered to be more comparable to a rocked bag bioreactor, than that of stirred tanks, due to its mixing mechanism and bubble-free aeration (Sorg et al., 2011).

7.3.2 Protein productivity

Figure 7.9 shows the IgG_4 concentration present in samples obtained daily throughout the duration of the Cultibag RM cultures. The maximum recombinant protein concentration of 1.24 g/L was expressed by cells grown at 42rpm-1L, whilst those cultivated at 25rpm-1L in runs 1 and 2 obtained final day protein titres of 1.00 and 1.03 g/L, respectively. This is a reduction of 24% and 20% in IgG_4 titre, which clearly can be attributed to the 20% greater cellular growth achieved at the condition with the higher power input. Cell specific productively levels throughout the cultures, determined using the integral viable cell concentration, are noted in Table 7.4.

Table 7.4: Rocked Bag Bioreactor Cell Specific Productivity of IgG_4 (picograms per cell per day)

Bioreactor & Conditions	**IgG_4 ($pg.cell^{-1}.day^{-1}$)**
Wave 25 rpm Run 1	15.9
Wave 25 rpm Run 2	17.2
Wave 42 rpm	15.5

Cell specific productivity is 8% higher in 25rpm-1Lv2 (17.20 pg.cell^{-1}.day^{-1}) than in 25rpm-1Lv1 (15.90 pg.cell^{-1}.day^{-1}). This is offset by the 6.4% greater cumulative IVC 25rpm-1Lv1. Even though there are slight differences between the protein productivity and cellular growth in the reproducibility study, this would not be considered to be outside of batch-to-batch variation. In addition, given the difference of only 3% between final day titres of both runs at 25 rpm, this suggests that there were no significant changes (metabolic or otherwise) that would have impacted upon the overall protein production performance of the cells. Cell specific productivity at 42rpm-1L is slightly lower (at 15.5 pg.cell^{-1}.day^{-1}) than its counterparts conducted at 25 rpm, but within range of their values (within one standard deviation of the mean of the two runs at 25 rpm, to 2 significant figures).

7.3.3 Metabolite analysis

Although lactate is normally strongly produced during the exponential phase of cell growth, with net lactate consumption occurring during the stationary phase (Zagari et al., 2013); a correlation has also been observed between high lactate production and reduced oxidative metabolism within CHO-S cells (Zagari et al., 2013). Figure 7.10 shows the lactate concentration profiles during the Cultibag fed-batch cultures. Slight differences are noted in the lactate profile of both runs at 25 rpm (as seen in Figure 7.10), whereby lactate production temporarily stops on day 7 of 25rpm-1Lv2, and net production of lactate subsequently increases on day 12. This behaviour is opposite to what is observed at 25rpm-1Lv1, where net lactate production continues throughout the culture. The change regarding the lactate profile was more pronounced at 42 rpm, where the final day lactate concentration was 1.59 g/L, compared with the 3.92 and 3.20 g/L at 25 rpm for runs 1 and 2, respectively. This significant increase in net lactate consumption can be attributed to the augmented cellular growth within the culture at 42 rpm, resulting in an increase in demand for a carbon source. k_La studies conducted within the Cultibag (using the static gassing out method) indicate a k_La of 11 and 33 hr^{-1} at N = 25 and 42 rpm, respectively. Since the optical DOT probes are at the bottom of the bioreactor bag, these values should be a good representation of the oxygen transfer efficiency due to surface aeration mechanism of the Cultibag. The greater turbulence levels present in the fluid at 42rpm-1L led to a culture not requiring any base addition throughout the culture.

This is perhaps due to the enhanced CO_2 stripping at these conditions, allowing for the control of pH to be augmented. Although, the dissolved oxygen concentration throughout each culture was maintained at 30%, the enhanced oxygen transfer to the cells (throughout the volume of the fluid) at 42rpm-1L would result in a greater oxidative metabolism (coinciding with the net lactate consumption), which correlates with the work of Zagari et al. (2013). Furthermore, the improved mass transfer conditions present at the higher rpm could have impacted upon cellular access to nutrients (as a greater spatial spread of cells was noted, using the Vi-Cell, at 42rpm-1L compared with experiments conducted at 25 rpm), leading to the greater cellular growth observed at 42rpm-1L.

The mean cell diameter during the three cultures under investigation is shown in Figure 7.11, whilst Figure 7.12 shows the particle size distribution on the final day (day 14) of each of the Cultibag cultures. With mean cell diameters (at day 14) of 18.9 and 18.7 µm for runs 1 and 2, respectively, compared with the final day mean cell diameter of 17.0 µm at 42 rpm, there is a 10% reduction in cell size. Given the 1% difference between cell size measured in both cultures at 25 rpm, a difference of 10% can be regarded as significant. This correlates with the works on the CellReady and that of Al-Rubeai et al. (1995) and Godoy-Silva et al. (2009), which show that repetitive exposure to high levels of ε can lead to a reduction in cell size.

7.4 Rocked bag and stirred tank comparison

GS-CHO cells grown in the Cultibag and CellReady exhibited different cellular and metabolic responses to the two hydrodynamic environments. VCC is greater at the stationary phase of the stirred bioreactor compared to the rocked bag, whereas the lower cell density and slower growth rate in the Cultibag is compensated by a cell specific productivity that is over 70% higher than its stirred counterpart. This phenomenon has been observed before in hybridoma cell cultures in which growth was slowed by up to 50% (using thymidine, a DNA synthesis inhibitor that inhibited growth but not mAb production), resulting in a 50-130% increase in mAb production rate (Suzuki and Ollis, 1990). Previous works in the published literature have reported contradictory findings on the relationships between cell growth and cell specific productivity. Merten (1988) noted a negative relationship between growth

rate and cell specific productivity of hybridoma cell cultures. In this case, cell specific productivity (cell line 255) initiated at a relatively high rate at the start (lag phase) of a batch culture, proceeded to decrease during the exponential phase of cell growth and then increase during the stationary phase. This was stated to be a very general pattern, noted in many investigations. A different cell line (1663) maintained a constant cell specific productivity during the lag and exponential phase, followed by a reduction of this parameter during the death phase (Merten, 1988). Higher cell specific antibody production rates have been found to occur when hybridomas cells were arrested and maintained at the G1/S phases, in addition to cell specific productivity being greater in the death phase, compared to the exponential phase (Al-Rubeai and Emery, 1990). The latter relationship was thought to be due to the release of the intracellular monoclonal antibody into the medium during the death phase (Al-Rubeai and Emery, 1990). Thus, these differences in the relationship between cell growth and recombinant protein production is not surprising, due to differences in cell line and culture conditions. In addition, the growth rate represents the net effects of the cell cycle time and the rate of cell death, which implies that the specific productivity rate is affected by the factors that regulate the antibody production and secretion during the different stages of the cell cycle, in addition to the release of antibodies during cell death (Al-Rubeai et al., 1992). Given the heterogeneity of cell cultures with subpopulations of varying growth rates and productivities, the relationship between cell growth and productivity is further complicated (Al-Rubeai et al., 1992).

Figure 7.13 shows the cell specific productivity ($pg.cell^{-1}.day^{-1}$) of the IgG_4 recombinant protein for days 1 to 14 in cell cultures conducted in the CellReady at 200rpm-2.4L and the Sartorius Cultibag 25rpm-1L. The figure shows the distinct difference in productivity rates throughout each culture period. The CellReady shows an increase in cell specific productivity upon commencement of the exponential phase (from 0 to 9.1 $pg.cell^{-1}.day^{-1}$ between days 2 and 3) that remains relatively constant at an approximate value of 10 $pg.cell^{-1}.day^{-1}$ from day 3 to the end of the culture. With regards to the Cultibag, the cell specific productivity increases from day 1 to reach a maximum of 24.6 $pg.cell^{-1}.day^{-1}$ at day 8 (one day before the stationary phase began), then gradually decreases until the end of the culture to a value of 12.18 $pg.cell^{-1}.day^{-1}$. As mentioned previously, a slower or inhibited growth

rate, can lead to the increase in specific production rates of mammalian cell cultures (Al-Rubeai and Emery, 1990; Suzuki and Ollis, 1990), which may explain the increased productivity rates observed in the Cultibag.

7.5 Concluding remarks

Given the distinct shifts in metabolic behaviour and the changes in productivity and cellular growth observed in the CellReady at varying fluid flow conditions, it can be concluded that the fluid dynamics is likely to have an impact upon cell performance. Given the robustness of this GS-CHO cell line, the fluid dynamic stresses generated in the present study are not deleterious to the cells. However, the impact would be more pronounced for industrial cell lines with greater sensitivity to their environment, e.g. human T cells (Carswell and Papoutsakis, 2000), hybridoma cells (Petersen et al., 1988) as well as adherent cells grown on microcarriers (Gregoriades et al., 2000). The segregated regions of turbulence present throughout the bioreactor and identified using PIV, allows one to better understand the localised environmental conditions cells experience during the culture period. The range of turbulence and velocity levels measured at the different operating conditions, correlated with the different cellular metabolic responses, and the changes to cell physiology and recombinant protein productivity exhibited by the GS-CHO cells. They indicate that whilst the cells can physically adapt to the increased energy input to the culture (without hampering cell growth), there are differences regarding metabolic behaviour that can explain the reduction in protein production as turbulence levels are increased.

Unlike the CellReady, the Sartorius Cultibag does not induce a flow regime with a fixed structure. In this case, the fluid surface and shape is constantly changing throughout operation. So although cells are subjected to repetitive cycles of hydrodynamic stress, these are likely to be experienced at a greater frequency (over the course of half a rock at the very least), and with a much narrower range of energy dissipation rate levels. Given the mechanism of mixing, and the greater homogeneity regarding turbulence levels, oxygen transfer characteristics and mass transfer may have an impact on the cellular growth and metabolic characteristics when compared with cells grown in the CellReady. Differences in metabolic activity between cells

grown at 25 and 42 rpm in the Cultibag are not substantial, with only different lactate consumption during the stationary phase of cell growth. The latter observation can be correlated to the 20% higher VCC at the stationary phase of 42rpm-1L compared to its 25 rpm counterparts.

The differences in cellular response to increased levels of hydrodynamic stress within both the CellReady and Cultibag are distinct, with higher turbulence resulting in reduced cell specific IgG_4 production and augmented cellular growth densities in the CellReady and Cultibag, respectively. When comparing the cellular performance of both systems operating at their standard recommended conditions (including DOT = 30% and pH = 7 kept constant), the Cultibag results in: an approximate 49% reduction in stationary phase VCC; a 78% increase in IgG_4 cell specific productivity ($pg.cell^{-1}.day^{-1}$) and a 17% increase in IgG_4 titre.

The growth rates, metabolite concentration and cell specific productivity profiles obtained, show the distinct differences in cell culture behaviour engendered by both vessels. The implications for downstream processing should also be considered; with an extracellular protein, it may be auspicious to grow cells with a reduced cell density and augmented recombinant protein productivity for easier downstream separation of cells from the product. Whilst these differences may be cell line specific, its importance is significant for Quality by Design (QbD) approaches and need to be investigated further. This biological study, along with the fluid dynamic characterisation of these SUBs, has enabled an improved understanding of the impact of various hydrodynamic conditions upon cell culture performance. The next chapter will compare the pertinent hydrodynamic parameters quantified using PIV, between the single-use systems investigated. Novel strategies for scale translation and bioreactor cross-compatibility will be discussed.

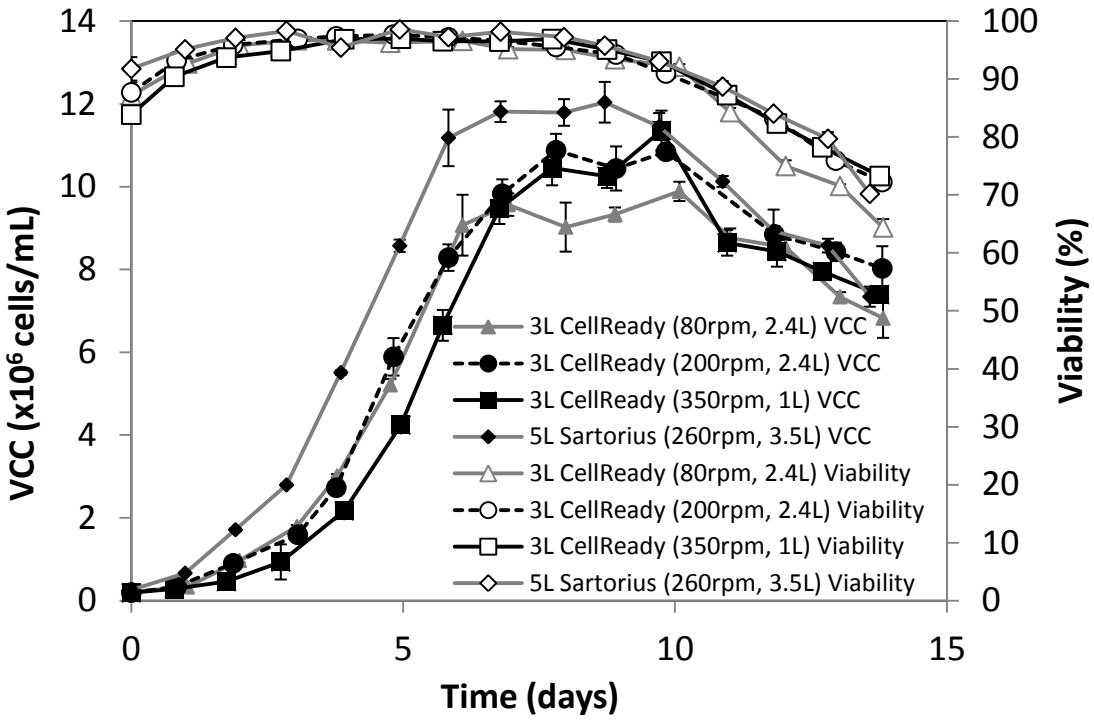

Figure 7.1: Viable cell count (x10^6 cells/mL) and viability (%) profiles for the CellReady fed-batch cell cultures conducted at 200rpm-2.4L, 350rpm-1L and 80rpm-2.4L conditions and the Sartorius BIOSTAT fed-batch cell culture conducted at 260rpm-3.5L.

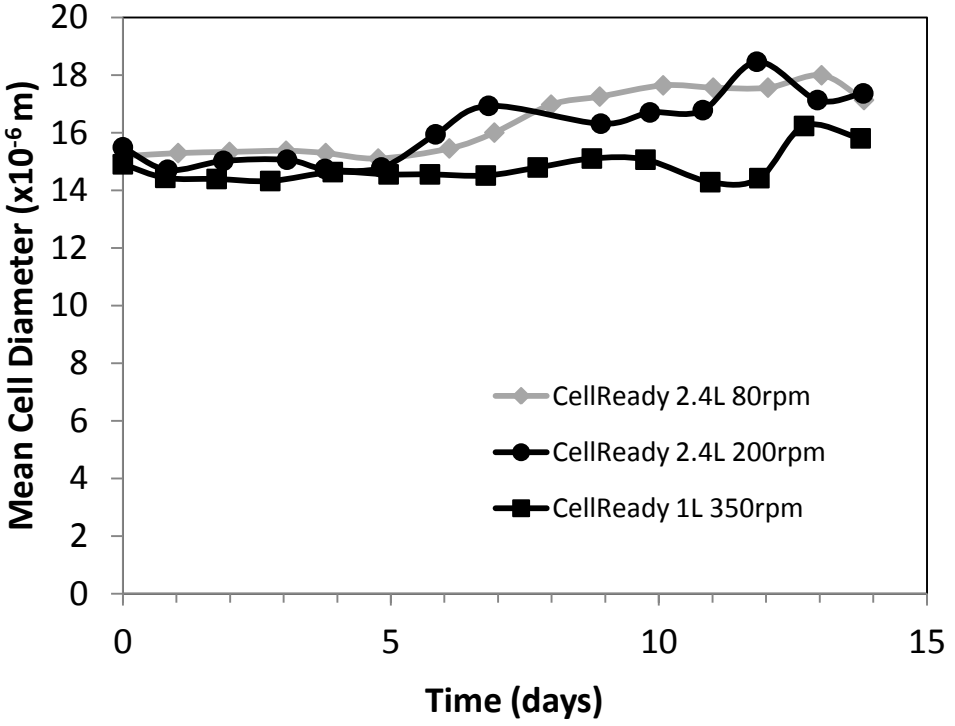

Figure 7.2: Mean cell diameter (µm) profile for the CellReady cell cultures conducted at 80rpm-2.4L, 200rpm-2.4L and 350rpm-1L conditions.

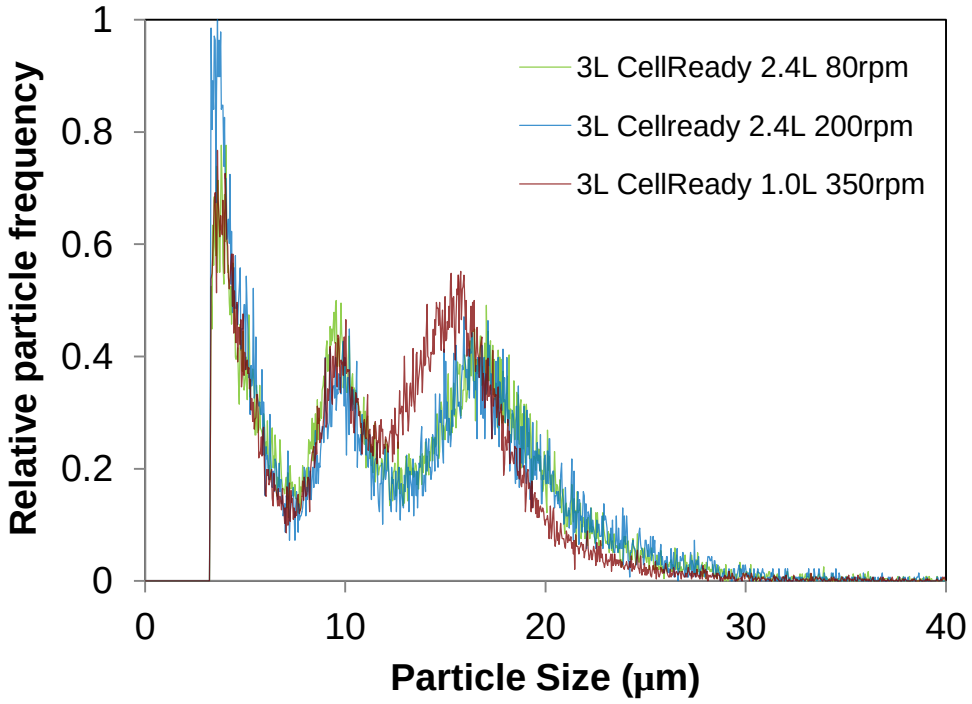

Figure 7.3: Particle size distribution, normalised to the maximum particle size frequency for the CellReady cell cultures conducted at 80rpm-2.4L, 200rpm-2.4L and 350rpm-1L conditions. Particle size distributions are taken from day 14 of each of the cell cultures.

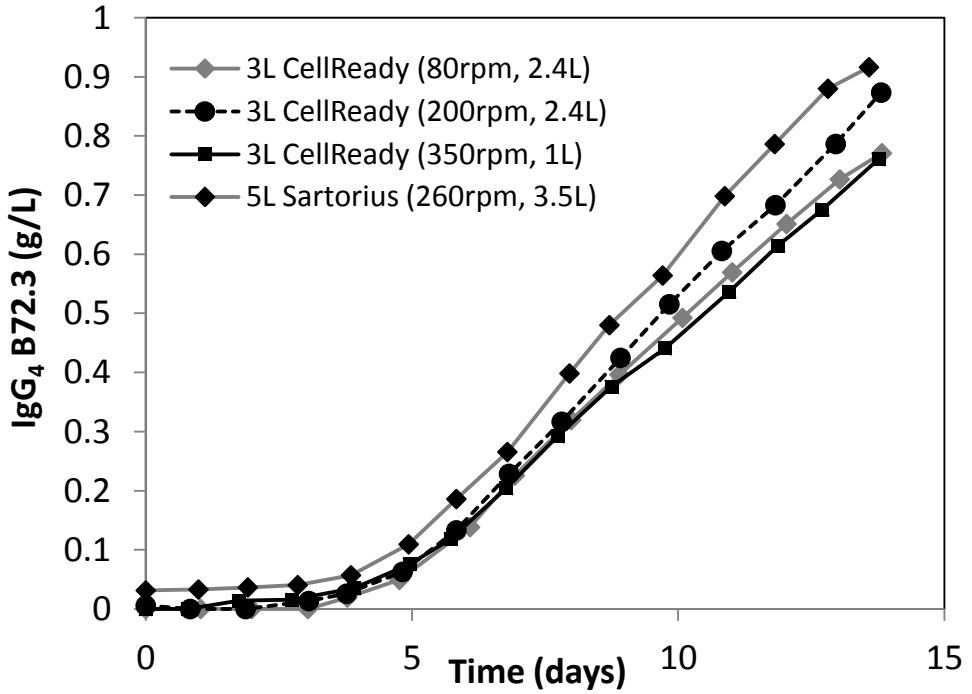

Figure 7.4: IgG_4 B72.3 (g/L) profile for the CellReady fed-batch cell cultures conducted at 200rpm-2.4L, 350rpm-1L and 80rpm-2.4L conditions and the Sartorius fed-batch cell culture conducted at 260rpm-3.5L.

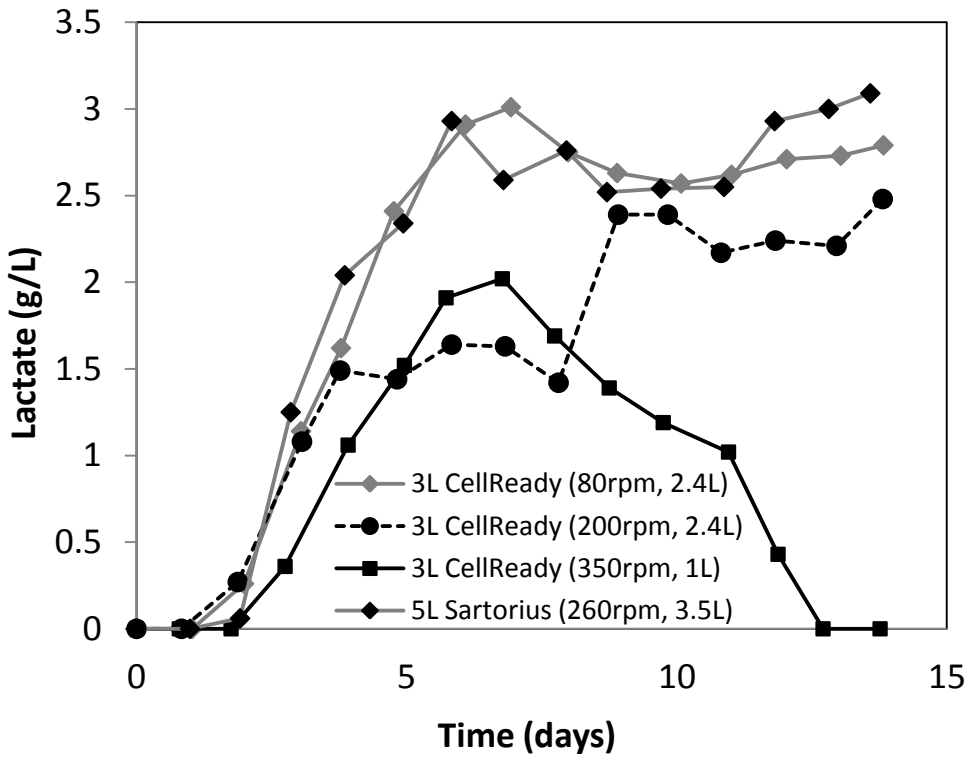

Figure 7.5: Lactate concentration (g/L) profile for the CellReady cell cultures conducted at 80rpm-2.4L, 200rpm-2.4L and 350rpm-1L conditions, as well as the 5L Sartorius BIOSTAT cell culture conducted at 260rpm-3.5L.

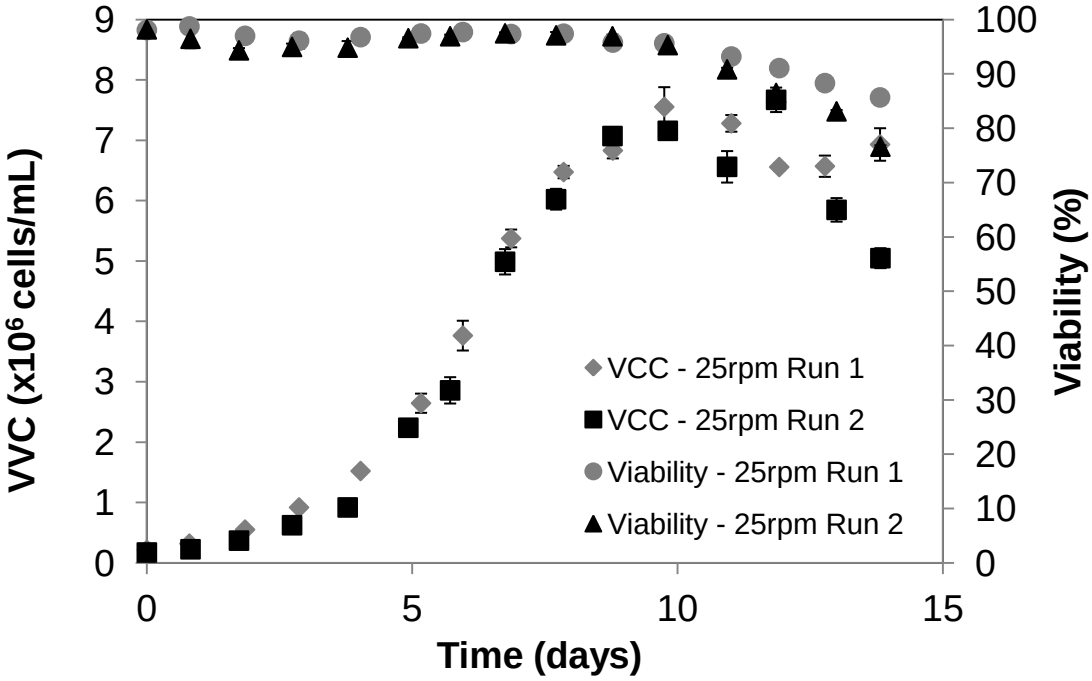

Figure 7.6: Viable cell count (x10^6 cells/mL) and viability (%) profiles for the Sartorius Cultibag cell cultures conducted at 25 rpm with 1.0 L working volume. The results for two cell cultures at 25 rpm and 1.0 L working volume are shown.

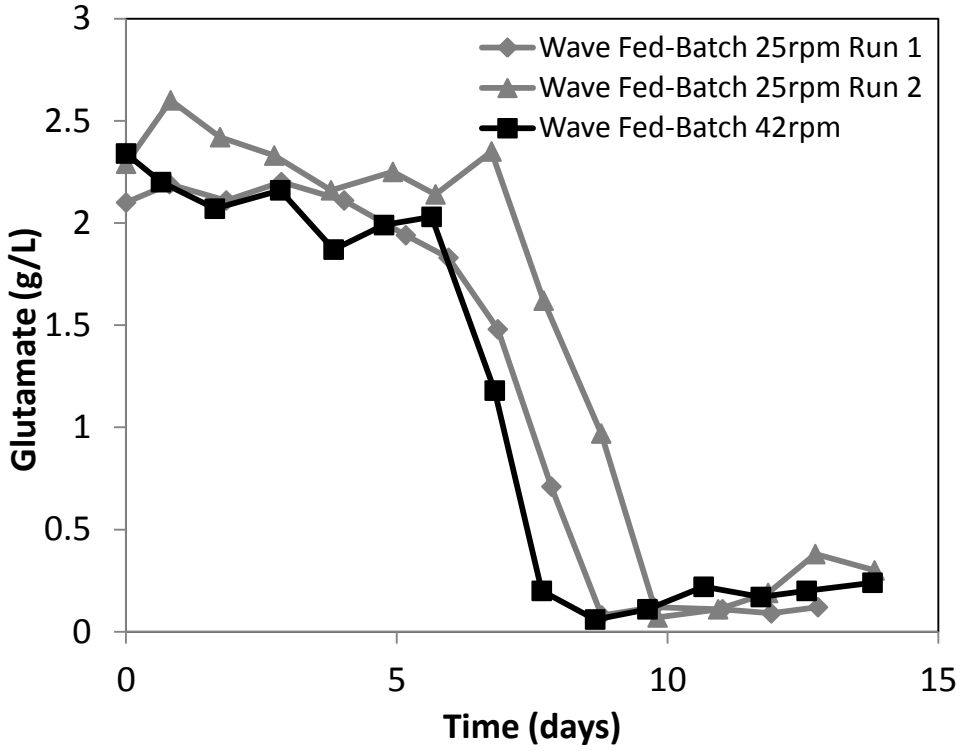

Figure 7.7: Glutamate concentration (g/L) profiles for Sartorius Cultibag cell cultures conducted at 25 rpm with 1.0 L working volume (profiles are shown for two repeat cultures at these conditions), and 42 rpm with 1.0 L working volume.

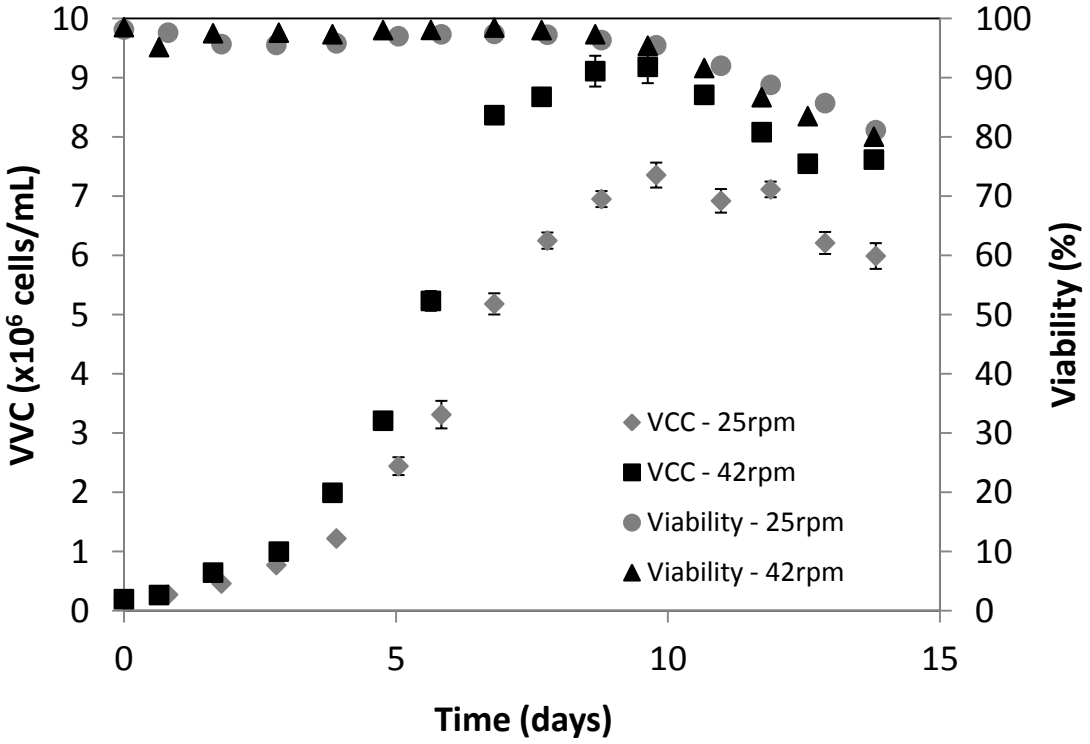

Figure 7.8: Viable cell count (x10^6 cells/mL) and viability (%) profiles for Sartorius Cultibag cell cultures conducted at 25 rpm with 1.0 L working volume (VCC and viability shown represent the average of two repeat cultures), and 42 rpm with 1.0 L working volume.

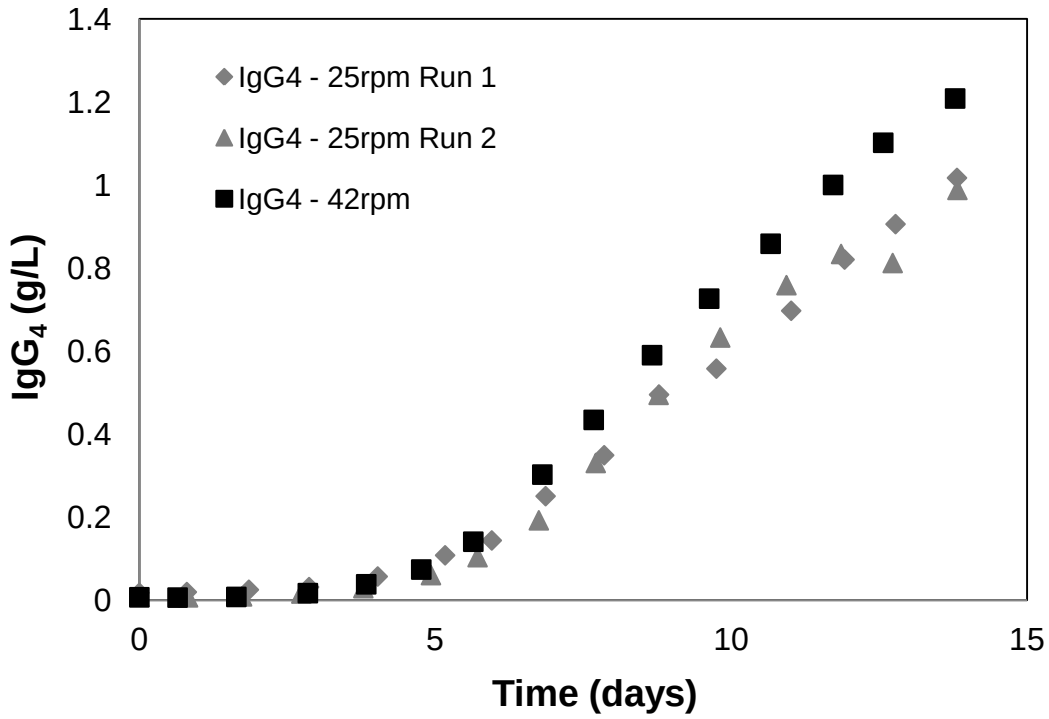

Figure 7.9: IgG_4 protein concentration (g/L) profiles for Sartorius Cultibag cell cultures conducted at 25 rpm with 1.0 L working volume (profiles are shown for two repeat cultures at these conditions), and 42 rpm with 1.0 L working volume.

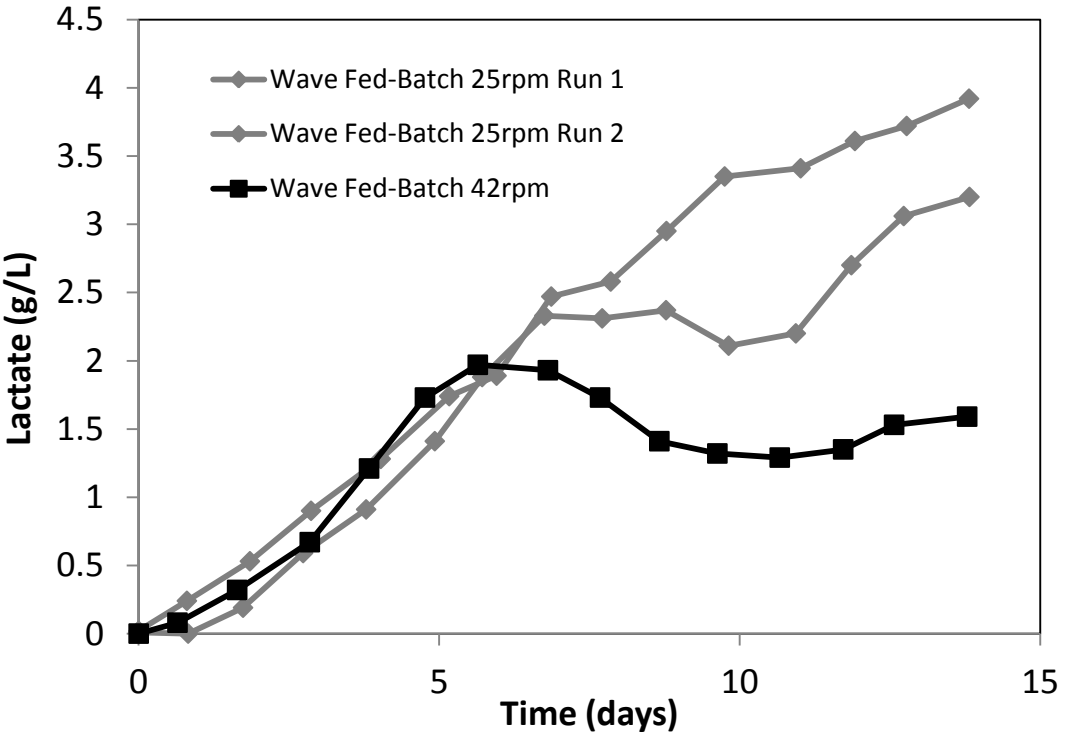

Figure 7.10: Lactate concentration (g/L) profiles for Sartorius Cultibag cell cultures conducted at 25 rpm with 1.0 L working volume (profiles are shown for two repeat cultures at these conditions), and 42 rpm with 1.0 L working volume.

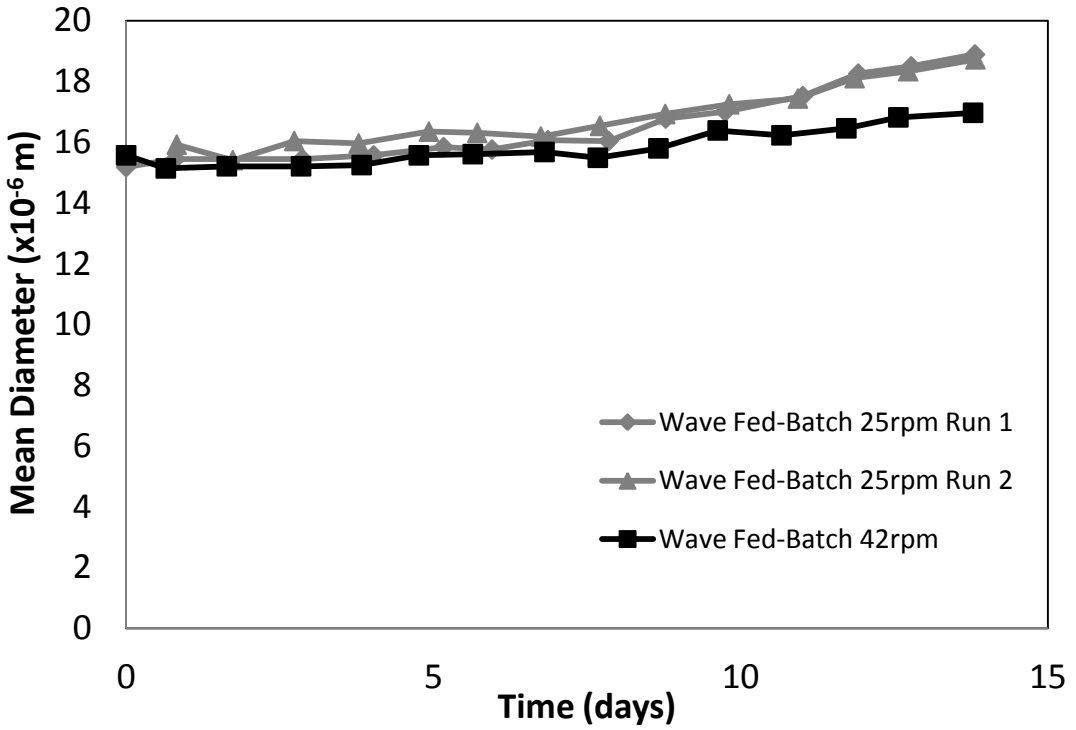

Figure 7.11: Mean cell diameter (x10^6m) profiles for Sartorius Cultibag cell cultures conducted at 25 rpm with 1.0 L working volume (profiles are shown for two repeat cultures at these conditions), and 42 rpm with 1.0 L working volume.

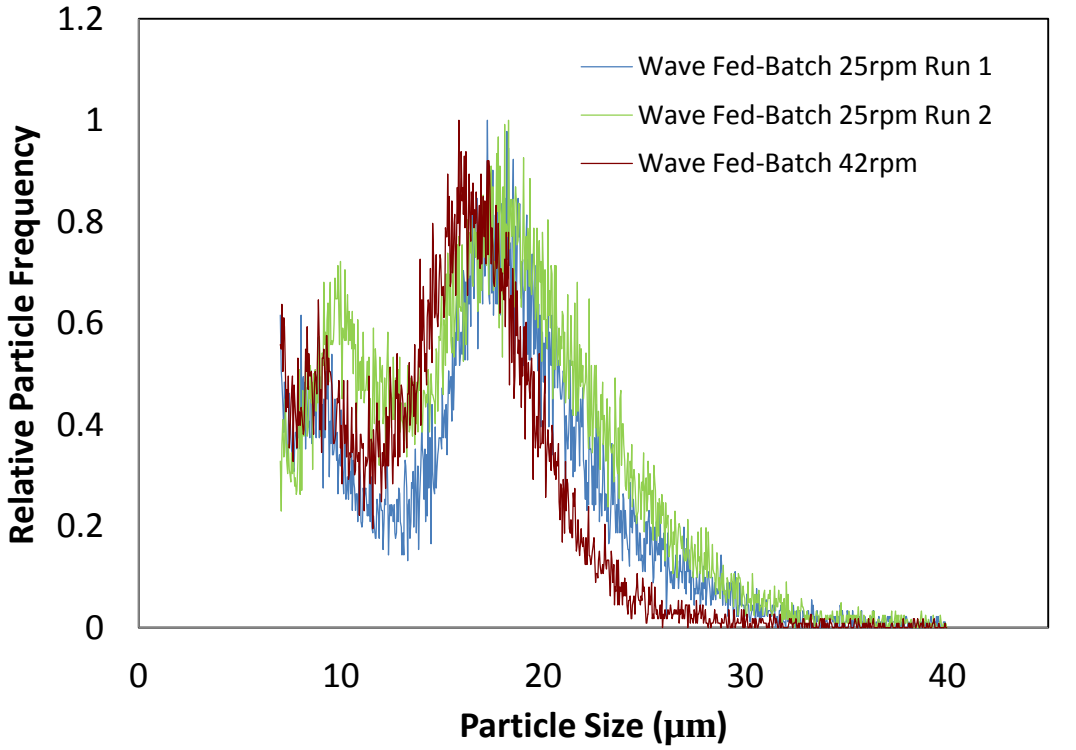

Figure 7.12: Particle size distribution, normalised to the maximum particle size frequency for Sartorius Cultibag cell cultures conducted at 25 rpm with 1.0 L working volume (profiles are shown for two repeat cultures at these conditions), and 42 rpm with 1.0 L working volume.

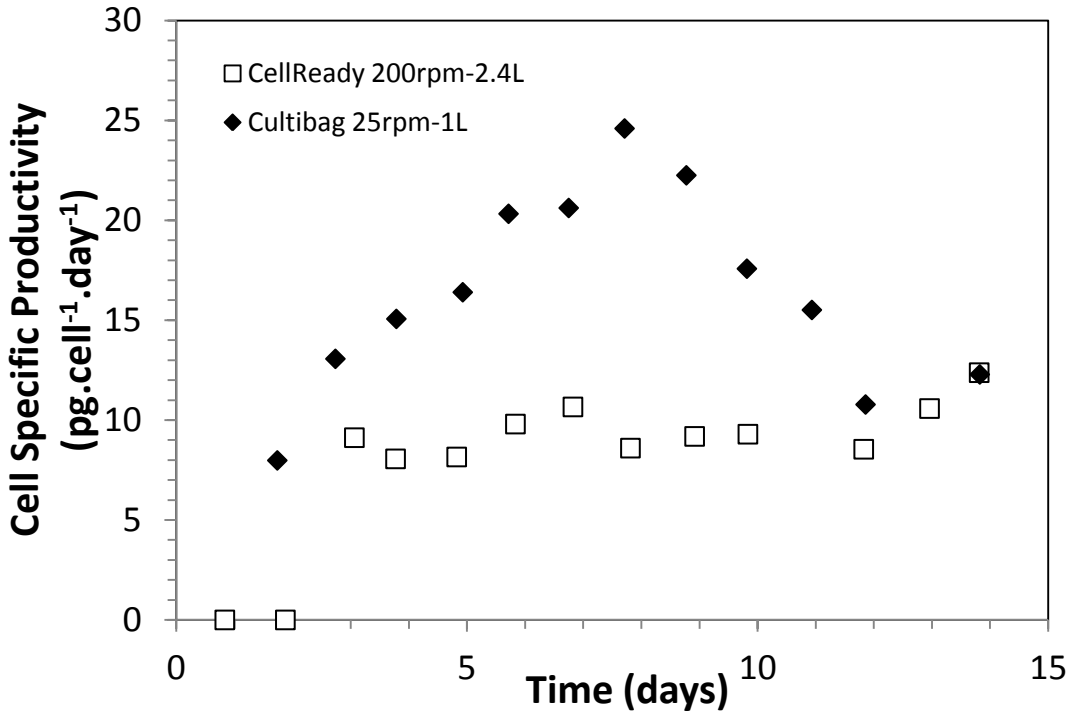

Figure 7.13: Cell specific productivity ($pg.cell^{-1}.day^{-1}$) of the IgG_4 recombinant protein for days 1 to 14 in cell cultures conducted in the CellReady at 200rpm-2.4L and the Sartorius Cultibag 25rpm-1L.

Chapter 8 Scale and Cross-Compatibility

8.1 Introduction

As previously mentioned in this thesis, typical scale-up parameters rely on physiochemical and geometric similarity (Zlokarnik, 2006), e.g. impeller tip speed, specific power input, Reynolds number, oxygen transfer coefficient, mixing time and flow time and length scales. However, given the interdependency of these various factors, it is important to identify the key parameters that have the strongest influence on protein productivity and cellular growth. Pertinent operating parameters such as oxygen transfer, mixing efficacy, mechanical stress can all be correlated to specific power input, although to varying degrees (Kaiser et al., 2011b). Mixing time in turbulent flow can be correlated to the specific power input using Equation 8.1. This would result in greater mixing times at higher scales (Nienow, 2006).

$$t_m \propto (P/V)^{-1/3} \qquad (8.1)$$

The power input into a bioreactor is a parameter that controls most of the performance characteristics of a vessel, in addition to the operating economics. For this reason, when comparing the performance of different bioreactors, specific power input is frequently used as the basis for comparison (Chisti, 1998).

Determining a parameter that can be universally utilised within bioreactors that exhibit disparate mixing regimes will be crucial in elucidating the impact of hydrodynamic conditions. Such a parameter could be the viscous dissipation of the turbulent kinetic energy (ε). The total power input represents the total sum of the energy dissipation rate throughout the volume of fluid. As previously stated, ε is intrinsic to any moving fluid; whilst being independent of the flow regime it accounts for both extensional components of 3-dimensional flow and shear (Godoy-Silva et al., 2009b). Although the specific mechanisms by which metabolic behaviour may be affected by hydrodynamic forces is unclear, the accurate quantification of this parameter for a number of mixing conditions may enable greater cross-compatibility between different types of bioreactors. In addition to the quantification of ε, the range of values measured throughout the bioreactor may also play an important role. For example, the chronic exposure to both high and low levels of ε within stirred tanks versus the more uniform distribution of ε within wave

induced bioreactors may engender a higher production of lactate in the latter condition (Sorg et al., 2011). ε is also used in the quantification of the Kolmogorov length scale; such knowledge being important when comparing the flow length scale with the size of suspended cells or microcarrier beads of anchored cells.

Thus far, ε has been determined using the direct evaluation (DE) method. PIV resolves to a scale several times larger than the Kolmogorov scale. So the following approaches have been proposed in an attempt to compensate for the limited resolution.

Dimensional Analysis

The dimensional analysis method was proposed by Wu and Patterson (1989) and determines the local energy dissipation rate from the turbulent kinetic energy based on a relationship postulated by Batchelor (1953):

$$\varepsilon_{DA} = A\frac{k^{3/2}}{\Lambda} \qquad (8.2)$$

k represents the turbulent kinetic energy, *A* is a constant of proportionality (typically taken to be 0.85) and $\Lambda = \left(\Lambda_i^2 + \Lambda_j^2 + \Lambda_k^2\right)^{1/2}$ is a "resultant" macroscale. The key assumptions regarding this relationship are that energy enters the turbulent flow at the largest integral length scales of motion (Λ) and is contained in the larger eddies, whilst this energy is transferred to smaller scales without loss by dissipation and in equilibrium. Λ values have been given in literature, however the assumption that this value is spatially constant throughout a stirred vessel, is obviously not the case (Gabriele et al., 2009). In addition, different values of the constant of proportionality (*A*) have been used by different groups.

Smagorinsky Analysis

The Smagorinsky Closure Method aims to compensate for the limited resolution of cameras when resolving flow length scales at the Kolmogorov scale. It achieves this using a low pass filter. The largest length scales where TKE is generated are strongly flow dependent (assuming dynamic equilibrium within turbulent flows); at the smallest scales (where the energy is dissipated), the structures are more universal. Large eddy simulation (LES) exploits this approach. A low pass filter is applied to the Navier Stokes equations (which are solved for the larger scales), whilst a model for the smaller scales is used to find the sub-grid scale (SGS) stress (Gabriele et al.,

2009). This reduces the computational expense when solving using commercial CFD software packages**.** Sheng et al. (2000) used the SGS models to calculate the contribution to the total energy dissipation rate below the resolution of their time-average PIV measurements. The most reliable closure model was found to be the eddy viscosity model proposed by Smagorinsky (1963), however, little difference was found between the various SGS closure models examined. Similar conclusions were made in experiments performed on small high throughput stirred reactors (Hall et al., 2005).

The energy dissipation rate can be calculated from the filtered gradients obtained from 2- D PIV using (Khan, 2005). Δ is the cut-off scale, or the filter width.

$$\varepsilon_{SGS} = (C_s\Delta)^2\left(4\overline{\left(\frac{\partial u_\iota^{'}}{\partial x_\iota}\right)^2} + 4\overline{\left(\frac{\partial u_J^{'}}{\partial x_J}\right)^2} + 2\overline{\left(\frac{\partial u_\iota^{'}}{\partial x_J}\right)^2} + 2\overline{\left(\frac{\partial u_J^{'}}{\partial x_\iota}\right)^2}\right)^{3/2} \qquad (8.3)$$

The constant *Cs* is the Smagorinsky constant, which is generally assumed in earlier works to vary from 0.17 to 0.21. Isotropic assumptions are used to compensate for the missing 3rd dimensional component (Gabriele et al., 2009).

8.2 Impeller Stream maximum energy dissipation rates

Correct measurement of the ε_{max} is of importance, given that bioreactors stirred by "low shear" impellers, may in fact have ε_{max} values greater than those found for Rushton turbines (Nienow, 2006). Again, given the resolution limitations, it should be considered that ε_{max} obtained through direct evaluation of the spatial fluctuating velocity gradients may be underestimated. This underestimation is particularly exacerbated at the higher ε_{max} that are measured, as more of the energy that is dissipated is not captured by the measurements taken. Previous work on the various energy dissipation rate calculation methods indicate that 20% of the total power is measured using the direct evaluation method, whilst the DA and SGS methods overestimate the total power input by a factor of 5 and 2, respectively (Gabriele et al., 2009). Thus, the Smagorinsky Closure Method appears to give the more realistic estimation of whole flow field and localised energy dissipation rates. Given the statement above, it is likely that the values calculated in this chapter will be an

overestimation of the actual value of ε. It should be noted that the comparison of works from different investigators utilising both methods show significant differences with regards to the $\varepsilon_{max}/\bar{\varepsilon}$ (Gabriele et al., 2009). This may be attributed to the varying geometric ratios of the vessels used.

Given that the maximum energy dissipation rate (ε_{max}) in a stirred tank would be located at the impeller jet stream, ε_{max} could possibly be correlated to the tip speed of the impeller, for different impeller types. Each impeller type will have a different overall power input (or power number) upon fully turbulent flow and different maximum energy dissipation rates (located near the impeller tip) (Nienow, 2006). Knowledge of the ε_{max} for various impellers and geometries can be useful for process development and scale-up procedures.

Figure 8.1 shows the $\varepsilon_{max,SGS}$ (as calculated using the Smagorinsky Closure Method) for both the CellReady and the UniVessel in relation to the impeller tip speed (U_{tip}). There appears to be similar $\varepsilon_{max,SGS}$ values measured between the two vessels, until a U_{tip} of approximately 1 ms^{-1} (and beyond), where the CellReady $\varepsilon_{max,SGS}$ becomes significantly greater than its double-impeller counterpart. Performing a power regression analysis on both curves result in equations 8.4 in relation to the CellReady and equation 8.5 with regards to the UniVessel, both of which are similar:

$$\varepsilon_{max,SGS} = 2.8{U_{tip}}^{3.1} \qquad (8.4)$$

$$\varepsilon_{max,SGS} = 2.3{U_{tip}}^{2.9} \qquad (8.5)$$

It has been proposed by Kresta and Brodkey (2003) that the ε_{max} can be estimated from:

$$\varepsilon_{max} = \frac{P}{\rho V_{swept}} \propto \frac{P_O \rho N^3 D^5}{\rho D^3} = P_O N^3 D^2 \qquad (8.6)$$

Where V_{swept} is the fluid volume swept by the impeller. In this work, when using $\varepsilon_{max}/P_O N^3 D^2$ as a scaling parameter, four different impellers with power numbers ranging from 0.3 to 6, differed by a factor of 2.

An estimation of $\varepsilon_{max}/N^3 D^2$ using the Smagorinsky SGS method, with respect to the Reynolds number, is shown for both the CellReady and UniVessel in Figure 8.2.

$\varepsilon_{max,SGS}/N^3D^2$ values were obtained from the impeller jet stream (fluid radial to the impeller) in both bioreactors. $\varepsilon_{max,SGS}/N^3D^2$ of approximately 7 and 4 were measured for the CellReady and UniVessel, respectively. This is lower than the ε/N^3D^2 of up to 11 measured using PIV by Micheletti et al. (2004) in a baffled stirred tank, housing a six bladed Rushton turbine (T = 100 mm, $H = T$, $B = T/10$, $D = T/3$ and N = 1082 rpm). The ε/N^3D^2 noted in Micheletti et al. (2004) was measured at z/H = 0.335, estimated using the dimensional method and with a spatial resolution of 0.1 mm. The resolution of 0.1 mm could be the reason for a higher ε/N^3D^2 measured in the impeller region, compared to the results noted for the SUBs. A difference of a factor less than 2 between both the CellReady and UniVessel, is within the deviation noted by Zhou and Kresta (1996). Calculated ε has been shown to be proportional to N^3, when vessel dimensional ratios (D/T and C_1) remain constant (Zhou and Kresta, 1996). The variation of geometric ratios appear to impact upon the maximum energy dissipation rates: with the ε_{max} increasing as D/T decreases, perhaps due to flow interactions with the vessel wall (Zhou and Kresta, 1996). More investigations into the maximum and mean energy dissipation rates, along with verified ε data within stirred tanks would need to be conducted, in order to postulate a relationship that can be used to estimate the ε_{max} within a stirred bioreactor.

Figure 8.3 shows the maximum and minimum energy dissipation rates in relation to varying Reynolds number in the CellReady. The minimum energy dissipation rate in the CellReady calculated using the Smagorinsky SGS method, is taken as the average of the region r/R = 0.484 to 0.673 and z/H = 0.224 to 0.252. The average of this region was selected given the small values that are measured in the bulk of the fluid, thus any variation will be significant in proportion to any value that is measured. The influence of the impeller speeds upon the measured energy dissipation rate is much more pronounced closer to the impeller blade that the bulk fluid. Given the commensurately small values in the bulk fluid, the increase in ε_{max} at higher Reynolds numbers would not have as large an impact on cells, in comparison with the variation measured in the impeller jet stream. The knowledge of, and the ability to scale based upon ε_{max}, would be important for processes including protein aggregation in crystallisers, in addition to the culturing of "shear

sensitive" cells. Therefore understanding its relationships with tank geometry and operating conditions is of importance.

8.3 Scale translation of rocked bag bioreactors

As stated previously, the mixing time within stirred tanks can be correlated to the power input per unit volume (*P*/*V*), to the power of -1/3 (Nienow, 2006).

$$t_m = C[(P/\rho V)(D/T)/T^2]^{-1/3} \qquad (8.7)$$

Although mixing time correlations within impeller agitated vessels have been studied extensively, only very few works aimed to compare mixing times between stirred and rocked bag bioreactors using the correlation stated. This is because there is significant disparity between the slopes of the power input effect, when using the same relationship in rocked bags (i.e. the exponent is not equal to -1/3) (Bowers, 2011). This is not surprising given that correlations such as Equation 8.7 (where *C* is a constant) were obtained within stirred vessels. Scale-up of a rocked bioreactor based on mixing times would result in a significantly higher power input into the system (*P*/*V* in a 200 L bag would need to be 30% greater than a 10 L bag), which would translate to a 60% greater rocking rate or 30% higher rocking angle at the 100 L scale compared to the 10 L scale (Bowers, 2011). Figure 8.4 shows the whole flow field ensemble-averaged energy dissipation rate (Smagorinsky SGS) within the Sartorius Cultibag Perspex mimic, at working volumes of 30, 40, 50 and 60% wv. In this work the whole flow field ensemble-averaged ($\bar{\varepsilon}_{SGS}$) is noted to increase by 59% from working volumes of 50% to 30%. Equation 8.8, obtained from the polynomial regression of the data points in Figure 8.4, could be used to determine the change in $\bar{\varepsilon}_{SGS}$ (and hence *P*/*V*) at varying fluid working volumes (wv):

$$\bar{\varepsilon}_{SGS} = -2 \times 10^{-5} wv^2 + 0.001 wv + 0.009 \qquad (8.8)$$

The working volume could be a useful parameter with which to maintain the equivalent power input conditions upon scale-up. Although the various geometries of rocked bags on the market and their impact on the $\bar{\varepsilon}_{SGS}$ need to be taken into account. Further understanding of the relationship between working volume and overall energy dissipation for the variety of rocked bags on the market is necessary for the utilisation of this parameter to aid in scale translation.

8.4 Flow & cell culture categorisation

Understanding the impact of flow conditions upon the cellular productivity, metabolic activity and physical characteristics is very important for both process understanding, scalability and optimisation. In addition, the characterisation of the whole flow field whereby either discrete counter-rotating flow structures can be observed (i.e. in the CellReady) or non-discrete "merging" flow regimes through interacting flow structures (as in the UniVessel) must be considered. Many aspects of cell culture conditions can vary, between different stirred systems. This can occur through differing levels of gas phase entrainment, temporal characteristics of flow structures (which may affect the frequency with which cells experience different shear stress levels) and the temperature gradients that can occur as a result. Therefore, characterising the fluid flow environment and scaling based on comparability in whole field/volume and localised turbulence levels, would be an improvement on the traditional approach of using whole volume approximations such as power input per unit volume and k_La.

Table 8.1 categorises the flow structure of each bioreactor studied in this work. This includes identification of discrete flow structures, repetitive exposure to high and low levels of ε and whole flow field turbulence ranges.

Table 8.1: ε range within CellReady, UniVessel, PBS and Cultibag

	Reynolds No.	**U_{tip} (ms^{-1})**	**ε_{SGS}/N^3D^2 range**	**ε_{SGS} (m^2s^{-3}) range**	**Discrete Flow Structures**	**η ($x10^6$ m)**
3L CellReady	21747	0.798	0.057-6.9	0.0122-1.48	YES	26.3-87.2
2L UniVessel	21808	1.13	1.3-3.7	1.12-3.22	YES	21.6-28.2
3L PBS	5667	N/A	N/A	0.02-0.11	NO	50.3-91.6
2L Cultibag	N/A	N/A	N/A	0.001-0.16	NO	45.9-161

As noted from Figure 8.2, the CellReady exhibits a greater $\varepsilon_{max,SGS}/N^3D^2$ (and $\varepsilon_{max,SGS}$ when tip speed > 1 ms^{-1}) than its UniVessel counterpart, whilst the UniVessel has the smaller *D*/*T* ratio (0.42), compared to the *D*/*T* = 0.56 of the CellReady. This is in slight contrast with the observation of (Zhou and Kresta, 1996) stated previously, where a reduced *D*/*T* results in an increase in ε_{max}. Zhou and Kresta (1996) concluded the increased interaction of impeller exit fluid with the vessel wall as a reason for the reduced ε_{max} (at the higher *D*/*T*). However, the conclusion presented by Zhou and Kresta (1996) may explain the reduced ε_{max} of the Univessel, whereby the primary circulatory loops generated by the impellers interact, resulting in "merging" flow regions.

Regions of high and low energy dissipation rates were not as discrete within the UniVessel (compared with that observed in the CellReady), due to the interacting impeller discharge flows in the dual-impeller system. The structured flow regime within the CellReady may be the reason behind the more consistent $\varepsilon_{max,SGS}$ values in the region of 6.7-7.1 (between *N* = 200 and 350 rpm). $\varepsilon_{max,SGS}$ within the UniVessel shows a slightly wider range ($\varepsilon_{max,SGS}$ between 3.6 and 4.9). The higher $\varepsilon_{max,SGS}$ values of 4.9 and 4.8 measured at *Re* = 13,630 and 16,356, respectively, that subsequently reduce to approximately 3.3 and 3.7 (at *Re* = 19,082 and 21,808, respectively) may be due to the reduced interaction between the two clockwise rotating loops pumped by the impellers at the lower Reynolds number. Turbulent flow within stirred reactors is considered to occur at Reynolds numbers of 10,000 and above (Sinnott, 2005). Thus the lower $\varepsilon_{max,SGS}$ values at the lower Re of around 10,000, could be attributed to the fact that turbulent flow was not fully established at those conditions.

Table 8.2 categorises the response of CHO cells to varying fluid flow characteristics (with the CellReady at 200rpm-2.4L being the basis for comparison). This is derived from observations made in this work, along with references to similar interpretations from investigators, including the response to repetitively high ε values, and high/low homogenous ε conditions.

Table 8.2: Categorisation of CHO cell response to ε

	Growth	Cell Specific Protein Productivity	Cell Diameter	Lactate Production
Repetitive High/Low ε	No change (Oh et al., 1989)	Reduced (Nienow et al., 2013)	Decrease (Godoy-Silva et al., 2009a)	Decreased
Homogenous Low ε	Reduced (Sorg et al., 2011)	Increased	Increase	Increased (Sorg et al., 2011)
Homogenous High ε	No change (Sorg et al., 2011)	No change	Decrease	Increased (Sorg et al., 2011)

When considering flow regimes with distinct regions of high and low turbulence levels during the culture of GS-CHO cells, it is important to note that the $\varepsilon_{max,SGS}$ values within stirred tanks (operated within "normal" impeller rate conditions), do not attain a level so as to directly physically damage the cells. As noted in Table 1.1 of Chapter 1 of this thesis, physical damage to suspended hybridoma cells was reported to occur at $7x10^6$ W/m^3. However, the increase in gas phase entrainment, combined with high dissipation rates in a localised zone can lead to increased levels of oxidative stress (Mckenna, 2009). Thus when scaling vessels that engender distinct regions of high and low ε (where a difference of two orders of magnitude can be noted), it may be beneficial to scale using the ε_{max}, whilst keeping the geometric ratios of the vessel constant. EMD Millipore have highlighted the power input per unit volume as their primary scaling parameter for their 3 L, 50 L and 200 L CellReady vessels, whilst adjusting the k_La where necessary through the gas flow rate. So through knowledge of the $\varepsilon_{max,SGS}/N^3D^2$ at the 3 L CellReady scale, one could match the $\varepsilon_{max,SGS}$ accordingly via the impeller rate (N), and maintain adequate k_La levels using the gas flow rate. Although its effectiveness would need to be determined through experimentation.

Moving to a flow regime with a narrower ε range, leads to a distinct change in CHO cell performance, with a significant increase in cell specific protein productivity. This coincides with a reduction in cell density (particularly at lower mean whole flow field ε_{SGS} values of approximately 0.001 m^{2}s^{-3}), thus resulting in similar overall titres compared with stirred tank bioreactors. Assuming that no change in product

quality (e.g. glycosylation) occurs between mixing vessels of e.g. the Sartorius Cultibag and Millipore CellReady, it is important to determine the importance of a reduced cell density for downstream clarification/purification purposes, in addition to optimising cell specific productivity and cell density. Therefore upon scale-up, maintaining either a homogenous or heterogeneous turbulent environment should be taken into account.

8.5 Concluding remarks

When considering bioreactor scaling and cross-compatibility procedures, understanding the varying fluid dynamics, along with their impact on the performance of the cells is highly important. The stark difference between the turbulence properties in the impeller zone and the bulk fluid of a single impeller stirred tank, such as the CellReady, is evident. As noted in Chapter 3 Figure 3.10, the influence of the impeller speed on both the axial and radial turbulence decreases further from the impeller jet stream (in the axial direction). Therefore, the maximum energy dissipation rate observed in the impeller region will have the most significant impact upon the overall power inputted to the fluid. So upon scale-up to a vessel with a similar geometry and impeller, given the knowledge of an approximate value for the normalised maximum energy dissipation rate $\left(\varepsilon_{max,}/N^3D^2\right)$, one can make an educated estimation at the approximate conditions that would generate the desired dimensional value of the maximum energy dissipation rate, and match them accordingly between the two scales.

When considering two very different flow types, understanding the biological impact of operating conditions, can help one to match growth characteristics between the varying systems. It appears that the cell density and size can be influenced by altering the flow conditions within mixing vessels. The ability of cells to better adapt to a more consistent environment may also allow them to maintain a stable level of cell specific protein productivity, upon a change in hydrodynamic conditions.

The data presented provides an improved comprehension of the whole flow field and localised flow characteristics within cell culture vessels. Values such as the ε_{max} can be a viable tool to utilise during scale-up and cross-compatibility between stirred systems, whilst its influence on more disparate mixing regimes is of importance.

Further investigations are indeed required in order to accurately correlate maximum and whole flow field ε values with stirred tank geometry (T/D ratio, impeller power number etc.) and operating conditions. The work presented has elucidated the flow fields of two widely used commercial stirred vessels, along with the change in hydrodynamics (flow structure, dimensionless velocities and turbulence etc.) engendered by the impeller speed. This should facilitate a more informed perspective from which to optimise the design of stirred bioreactors for the cell-type they are intended. The difference in velocity and turbulence between the more traditional stirred tanks and the novel pneumatic and rocked bag bioreactors is also of significance. This work provides an enhanced understanding of the flow conditions and their correlation to cell culture performance, thus enabling better translation of processes between differing mixing systems.

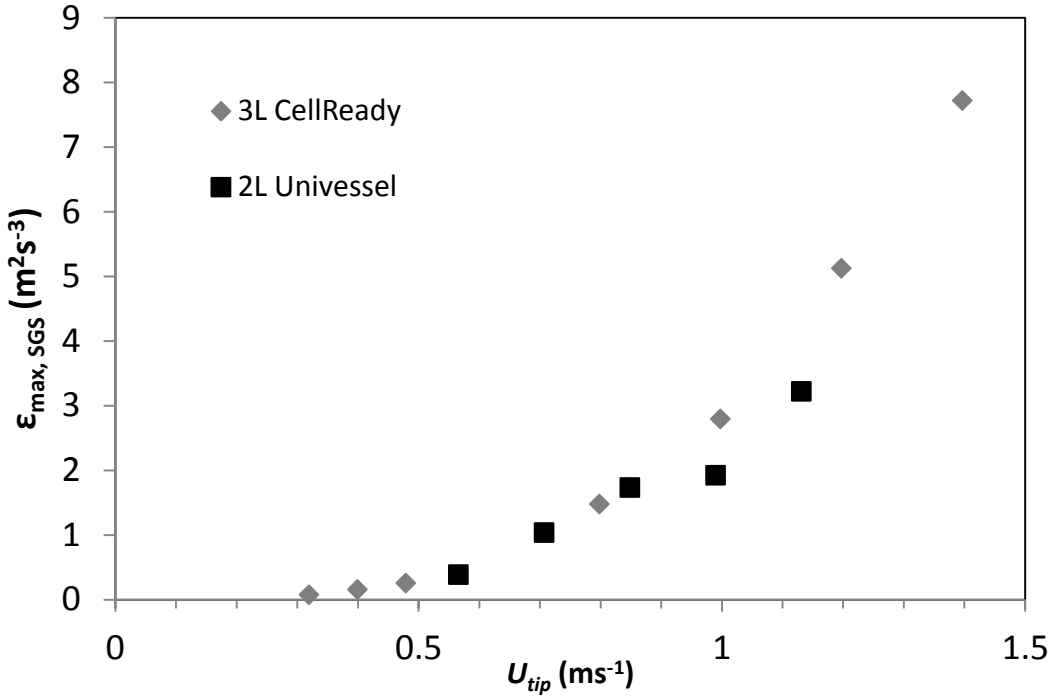

Figure 8.1: Plot of the maximum energy dissipation rate ($\varepsilon_{max,SGS}$) calculated using the Smagorinsky Closure sub-grid scale (SGS) method vs. impeller tip speed (U_{tip}). Maximum $\varepsilon_{max,SGS}$ is measured at the impeller jet stream. Values are shown for both the 3 L CellReady and 2 L UniVessel.

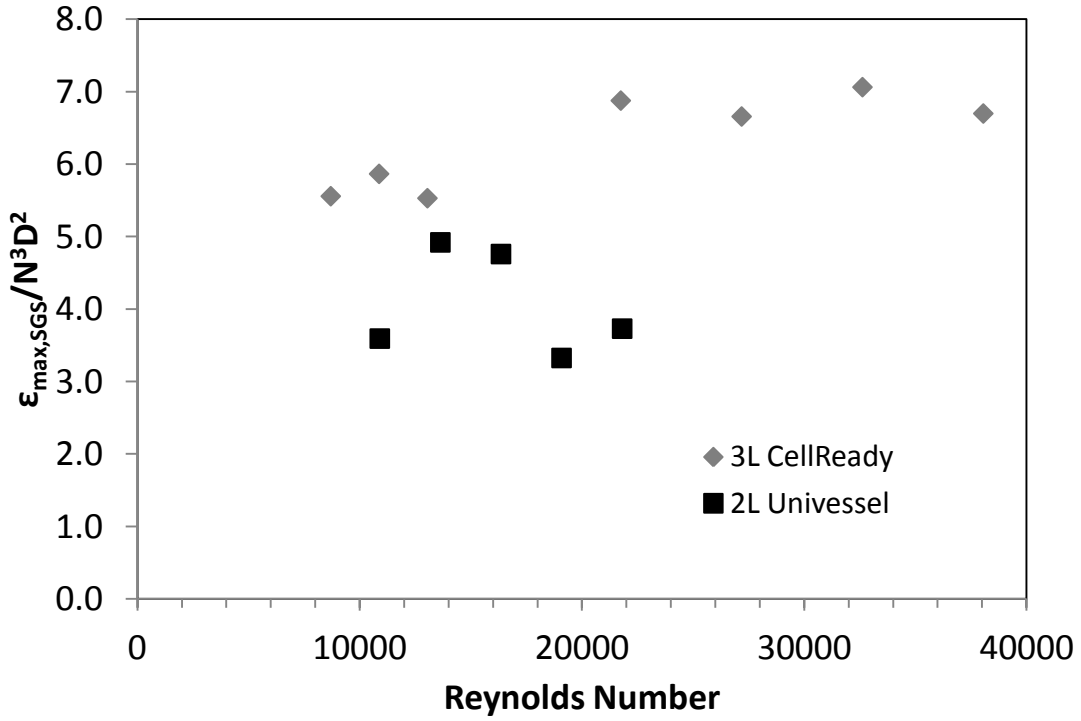

Figure 8.2: Plot of the dimensionless maximum energy dissipation rate ($\varepsilon_{max,SGS}/N^3D^2$) calculated using the Smagorinsky Closure sub-grid scale (SGS) method, from 2-D PIV data. Maximum $\varepsilon_{max,SGS}/N^3D^2$ is measured at the impeller jet stream. Values are shown for both the 3 L CellReady and 2 L UniVessel.

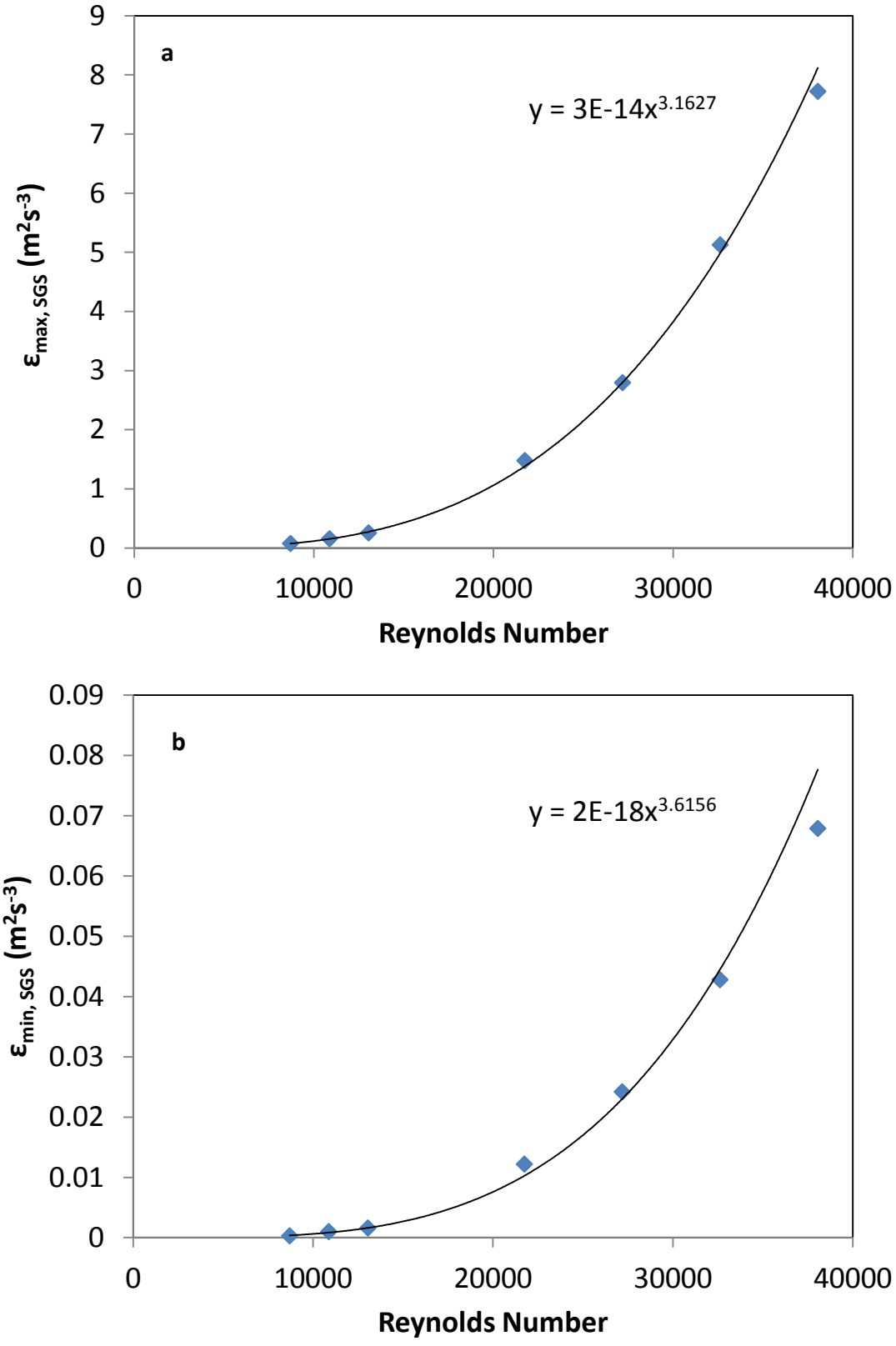

Figure 8.3: Plot of the a) maximum energy dissipation rate ($\varepsilon_{max,SGS}$) and b) minimum energy dissipation rate ($\varepsilon_{min,SGS}$) calculated using the Smagorinsky Closure sub-grid scale (SGS) method in the CellReady from 2-D PIV data.

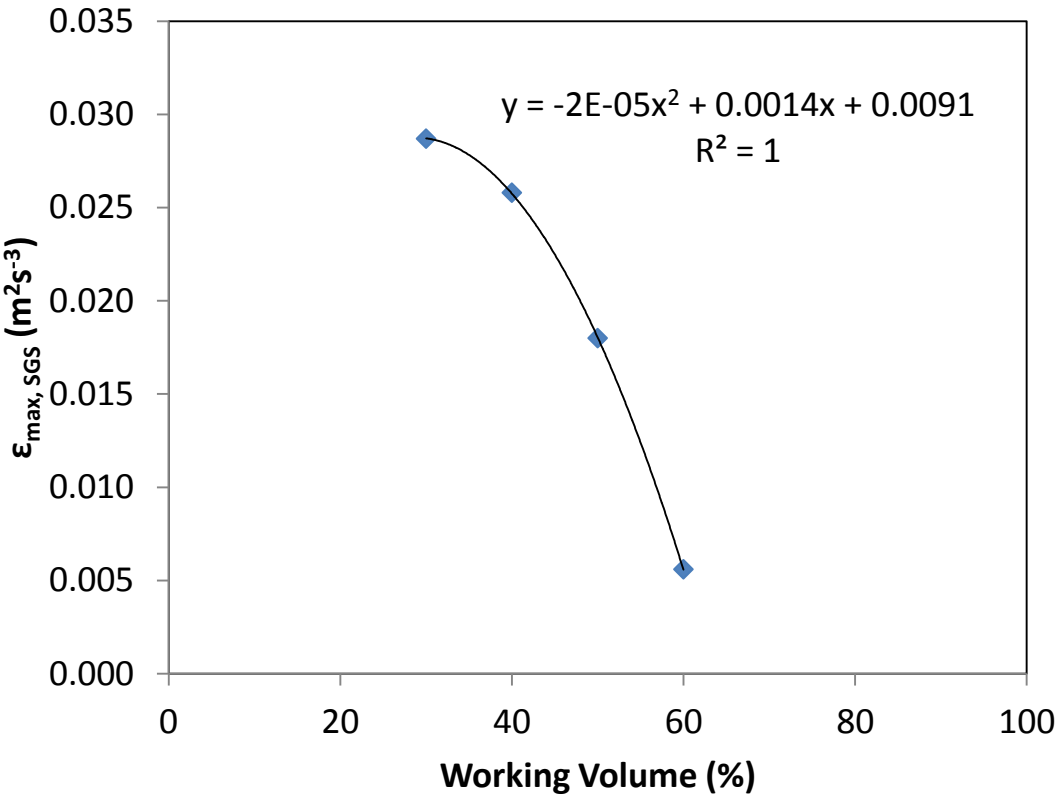

Figure 8.4: Mean energy dissipation rate ($\bar{\varepsilon}_{SGS}$) averaged throughout a full rock. Values shown are the mean ε values per pixel, for each of the four fluid working volumes investigated using PIV (V_L = 30, 40, 50 and 60% wv).

Chapter 9 Conclusions

9.1 The present contribution

The objectives of this research work were to characterise novel single-use bioreactors from a fluid dynamics engineering perspective. Using the knowledge gained to understand the impact of hydrodynamic conditions upon the cell culture performance of a mammalian cell line and to help inform on bioreactor scale translation.

Particle Image Velocimetry was used to measure the single-phase whole flow field 2-D velocity and turbulence characteristics within a range of single-use bioreactors. Single-phase flow was measured in order to limit laser light distortion caused by the presence of a gas phase. The study included stirred, rocked and pneumatically driven bioreactor systems. The Mobius® 3 L CellReady bioreactor is a commercially available bioreactor with a single marine scoping impeller, widely used in industry and academia for research and scale translation purposes. Measurements were acquired at a range of impeller rotation rates, and angular locations, to identify the impact of rpm on the fluid flow conditions. Laser and motor synchronisation enabled the acquisition of instantaneous, phase-resolved, and time-resolved velocity data, in order to determine the flow regime and a number of fluid dynamic parameters.

Double-impeller stirred tank systems have not been as extensively investigated (as their single-impeller counterparts) using laser-based methods, as they are typically employed at the larger scale (pilot and production scale) of processes. This study offered an opportunity to characterise the interacting flow structures developed between two impellers, typically found at the larger scale. The whole flow field instantaneous velocity conditions within the 2 L UniVessel® SU (a double-impeller, pitched segment blade stirred tank) was investigated using PIV. The influence of impeller speed, upon the flow structure and turbulence levels were studied, whilst both time and phase-resolved measurements were acquired to describe the time-averaged flow regime and angle-resolved flow development.

Pneumatically driven bioreactors are a novel method of inducing mixing for mammalian cell culture processes, due to their reduced footprint and mode of mixing. It is generally noted that pneumatic bioreactor systems engender a

comparatively lower shear environment when compared with traditional bioreactors (Thomasi et al., 2010). However, such assertions regarding the hydrodynamic environment require experimental characterisations, given that the fluid dynamics is dependent upon a number of aspects including bioreactor geometry, mixing mechanisms, bioreactor operational conditions, in addition to the rheological properties of the system (Thomasi et al., 2010). For this reason, the flow characteristics within PBS Biotech's® PBS 3 were studied using PIV at a range of air flow rates. Flow characteristics such as Reynolds stress, turbulent kinetic energy and energy dissipation rate were calculated.

Rocked bag based bioreactor systems represent a significant segment of single-use bioreactor technology used both in industry and academia. The novel bag shape and mixing method precludes the accurate estimation of flow conditions within this type of vessel using CFD, as such, limited work has been conducted to elucidate the fluid dynamics they engender. A custom-built Perspex mimic of the Sartorius BIOSTAT® 2 L Cultibag RM, along with a rocking platform mimic was designed and constructed to enable investigations using PIV. Whole field fluid flow characteristics were obtained at a number of phase-resolved rocking platform angular positions and fluid working volumes.

The impact of differing hydrodynamic conditions within the 3 L CellReady was investigated using the GS-CHO (Lonza, Slough, UK) cell line. Both the impeller rotation rate and fluid working volume were varied, whilst cell density, cell viability, protein productivity and metabolic activity were monitored and analysed. The hydrodynamic environment within the 2 L Cultibag RM was also studied by analysing the impact of rocking rate upon the GS-CHO mammalian cell culture. Again the cellular growth and metabolic activities were monitored. The differences in cellular performance between the two vessels were also analysed, in context with the measured hydrodynamic environment within both bioreactor systems.

9.2 Main findings of the investigations

An upward flow in the Mobius® 3 L CellReady induced by the impeller at a trajectory of approximately 26^{o} (with respect to the horizontal plane was present), compares well with the 25^{o} noted by Kaiser et al. (2011a). With the ejected fluid impinging on the wall, to then subsequently divide into two counter-rotating vortices

in the planes below and above the impeller. The two circulatory loops exhibit differing flow conditions, with higher velocities and turbulence present in the lower quarter of the bioreactor. Velocities of up to $0.25U_{tip}$ was observed from ensemble-averaged data in the impeller discharge stream of the CellReady, and the impeller jet stream velocities were dominated by the radial component of velocity. Given the greater impact of the radial velocity, turbulence within the bulk of the fluid were significantly lower. An impeller located further up the shaft, along with a design to create an enhanced axial component of velocity may enable improved mixing in the upper regions of the bioreactor. Reynolds stress values of up to 2.5 Pa at 350 rpm were measured in the CellReady. This is greater than the 0.4 Pa observed by Sorg et al. (2011) for a 3.5L BIOSTAT® B-DCU STR at N = 150 rpm (Re = 20,263), but well below the conditions (i.e. > 150Pa) noted by Godoy-Silva et al. (2009a) that resulted in a fatal response by CHO (GS) cells, and lower still than the shear stress (approximately 6 Pa) that induced a change in recombinant protein glycosylation profile (Godoy-Silva et al., 2009a). So although the cells would experience a distinct range of hydrodynamic conditions during cell culture, for distinct periods of time, they do not exceed thresholds reported to cause a fatal response, or a reduction in product quality.

The UniVessel impeller discharge zones were characterised by mean velocities of up to $0.35U_{tip}$. This value is comparable with the maximum velocities of $0.4U_{tip}$ in the discharge of a segment pitched blade impeller in a single-use UniVessel®, calculated using CFD (Kaiser et al., 2011b). The turbulence was observed to be greater for the axial component, with r.m.s. axial velocity values in the region of $0.13U_{tip}$, whilst r.m.s. radial velocities were noted to be $0.10U_{tip}$ in the same region. The angled PBT employed within the 2 L UniVessel and the proximity between the two impellers induce "merging" flow regimes, due to interacting flow structures that create high turbulence zones (with reduced velocity) encompassing a broader spatial scale than that of a single-impeller system with a similar impeller (Zhu et al., 2009). This allows for a more homogenous environment within the system, resulting in greater consistency when comparing turbulence at varying spatial locations and Re. The observations made within the UniVessel enable a greater understanding of a commonly used impeller configuration for large-scale operations.

Maximum velocities within the PBS 3 matched well with the known wheel speed at the measured aeration rate. The influence of the wheel speed on fluid velocity decreases further away from the wheel and its air cups. At 38 rpm, the fluid radial velocity can range from 0.027 to 0.104 ms^{-1} in the bulk fluid. The lower bulk fluid radial velocity of 0.027 ms^{-1} being 10.4% of the wheel speed. Similar to the peripheral velocities mentioned in Löffelholz et al. (2011) in both 10 L and 200 L PBS vessels, that were estimated using CFD to be approximately 10% of the wheel speed (20 rpm). The mixing mechanism and the lower stress and turbulence levels generated in the PBS, enhance the degree of uniformity (with respect to velocity and r.m.s. velocity) within the bioreactor. The consistency of hydrodynamic parameters in the fluid, is illustrated by the small range (0.005 to 0.03 ms^{-1}) of both the r.m.s. axial and r.m.s. radial velocities across the entire air flow range investigated. The turbulence spatial range is largest at 38 rpm, with r.m.s. axial velocity (u'_z) values between 0.016 and 0.033 ms^{-1} being measured in the bulk fluid. For this reason, the utilisation of traditional parameters for scaling across the PBS range is more feasible (compared to the more disparate environment of single-impeller stirred tanks). As the consistency (and hence scalability) regarding mixing time and oxygen transfer rates across the bioreactor volumes in the PBS series is enhanced (Kim et al., 2013).

Whole flow field averaged velocity values ($\bar{U}_{rz}$) within the Cultibag RM ranged from 0.03 to 0.11 ms^{-1} over the course of one rock. Decomposition of the velocity indicated that the radial component is by far the more dominant. R.m.s. axial velocity profiles show very little deviation away from u'_z = 0.02 ms^{-1} (at all the fill volumes investigated) at each platform position. Whilst r.m.s. radial velocity levels show the greater range, where at a rocking angle of $+8^o$ (descending) u'_r values of up to 0.11 ms^{-1} are noted, along with u'_r values as low as 0.012 ms^{-1} at other platform angles. Although the range of turbulence and velocity measured in the Cultibag are significant, the degree of spatial uniformity is greater, than that which typically exists within the fluid of a stirred tank.

An increase in both whole flow field averaged velocity and turbulence was observed as the working volume was decreased. The greater resistance to flow at the greater fill volumes and the greater speed with which the fluid reaches the other side of the bag (and the subsequent earlier fluid deceleration associated) could explain this. The range of velocity and r.m.s. velocity values measured throughout a single rock was

smallest at 60% wv, due to the reduced space available for the fluid to move. This may have implications for oxygen transfer due to the surface aeration mechanism. The augmented turbulence levels at the lower working volumes is also of importance to mass and oxygen transfer mechanisms, in addition to the power inputted to the system.

The narrow range of hydrodynamic properties in the Cultibag, when compared with stirred tanks (i.e. the CellReady), was confirmed by the results obtained in this work. Due to rocking motion, the temporal changes in hydrodynamic conditions, will also differ from other mixing regimes. From vector plot analysis of the data obtained, regions of flow entrainment or segregation are not visibly evident. Couple this with the much narrower range of flow conditions (in particular the energy dissipation rates) within the fluid, leads one to acknowledge the enhanced degree of consistency regarding the flow environment within the Cultibag compared with stirred tanks.

The range of turbulence and velocity levels measured at the different operating conditions, correlated with the different cellular growth and metabolic responses, and the changes to cell physiology and recombinant protein productivity exhibited by the GS-CHO cells. The studies indicate that whilst the cells can physically tolerate the increased energy inputted to the culture, there are differences regarding metabolic behaviour that can explain the reduction in protein production as turbulence levels are increased.

The differences in cellular response to increased levels of hydrodynamic stress within both the CellReady and Cultibag are distinct and affect cellular growth, metabolic activity, protein productivity and cell size distribution, with higher energy dissipation rates resulting in significantly lower mean cell diameters in both bioreactors, in addition to reduced IgG_4 and augmented cellular growth densities in the CellReady and Cultibag, respectively. The shift from lactate production to lactate consumption in the stationary phase of the CellReady at 350rpm-1L, was correlated to a 12% reduction in stationary phase IgG_4 productivity (when compared to the 200rpm-2.4L culture), whilst a Cultibag RM rocking rate increase of 25 to 42 rpm induced a 59% reduction of final day lactate (g/L), in addition to a maintaining the same cell specific protein productivity levels ($pg.cell^{-1}.day^{-1}$). When comparing the cellular performance of both systems operating at laboratory established standard

conditions (including DOT = 30% and pH = 7 kept constant), the Cultibag engenders an approximate 49% reduction in stationary phase VCC, a 78% increase in IgG_4 cell specific productivity ($pg.cell^{-1}.day^{-1}$) and a 17% increase in IgG_4 titre, indicating the effect of varying fluid dynamics, and the cellular response they engender.

The exponential relationship between ε and the impeller tip speed, remain similar at different spatial locations in the vessel. The difference between ε_{max} and $\bar{\varepsilon}$ will increase at higher power inputs. The SGS estimated $\varepsilon_{max,SGS}/N^3D^2$ for both the CellReady and UniVessel were within one order of magnitude of each other, with values of approximately 7 and 4, respectively, in the *Re* range investigated. This is within the deviation noted by Zhou and Kresta (1996) between a range of impeller types. The aforementioned study noted that geometric similarity between stirred tanks will serve to improve the equating of ε_{max}/N^3D^2 between different impeller types. The dimensional ε_{max} with respect to increasing U_{tip}, also showed a strong correlation. Although a slight deviation occurred at tip speeds of > 1 ms^{-1}, likely due to the flow interaction between the impeller discharge flows of the UniVessel impellers. Nevertheless, upon scale-up to a vessel with a similar geometry, given the knowledge of an approximate value for the normalised maximum energy dissipation rate (ε_{max}/N^3D^2), an estimate of the impeller rotation rate that would generate the desired maximum energy dissipation rate can be made. Using this method, the ε_{max} can remain constant upon scale-up.

The data presented greatly improves knowledge of the whole flow field and localised flow characteristics within cell culture vessels. Values such as the ε_{max} can be a viable tool to utilise during scale-up and cross-compatibility between stirred systems, whilst its influence on more disparate mixing regimes (including rocking motion, shaking and pneumatic mixing) is of importance. Further investigations are indeed required in order to accurately correlate maximum and whole flow field ε values with stirred tank geometry (*T*:*D* ratio, impeller power number etc.) and operating conditions. The work presented has elucidated the flow fields of two widely used commercial stirred vessels, a pneumatic and a rocked bag bioreactor, along with the change in hydrodynamics (flow structure, dimensionless velocities and turbulence etc.) engendered by the impeller, wheel and rocking speed. This should facilitate a more informed perspective from which to optimise the design of bioreactors, for a

given cell-type. In addition, the difference in hydrodynamic parameters such Reynolds stress and energy dissipation rate between the more traditional stirred tanks and the novel pneumatic and rocked bag bioreactors, can also be of significance during scale-up practices. This work provides an enhanced understanding of the localised and whole flow field conditions within commercially available single-use bioreactors and the varying cellular responses that they engender. Thus enabling the translation of processes between differing mixing vessels from a more informed position.

9.3 Recommendations for future work

The work presented in this thesis required a multidisciplinary approach to understanding the effects of fluid dynamics upon cell culture performance. Both engineering characterisation and biological studies must continue in order to fully understand the interactions between the two.

Particle Image Velocimetry is a useful tool to measure and characterise the flow conditions within mixing vessels. Though PIV has a number of limitations such as resolving flow length to the Kolmogorov scale. This would ultimately require higher capability camera systems and smaller particle sizes, however, the models used to compensate for this limitation can be improved. The 2-D dimensional aspect of the measurements taken is also a clear area for future work, given the necessary isotropic assumption when estimating the third component of velocity. Sharp et al. (2000) indicate a difference of up to 70% when comparing spatial velocity gradients based on 1-D measurements, to spatial velocity gradients based on 2-D velocity data (with the isotropic assumption used in both cases to estimate the missing components of velocity). This is indeed a significant difference, though one would expect that the 2-D measurements would be much closer to the actual 3-D estimations of spatial velocity gradient than its 1-D counterpart, given that it provides more measured information. Furthermore, with an impeller diameter and rotation rate of 50.8 mm and 100 rpm, respectively (used in the aforementioned study), equating to a tip speed of 0.096 ms^{-1}; the degree of isotropy may also be much greater at the higher tip speeds and *Re* numbers used in this thesis (Sharp et al., 2000). Though, measurement of all three dimensional components of velocity at significantly enhanced resolutions would be the ideal enhancement regarding hydrodynamic characterisation of fluid

flow regimes. The data that has been obtained using both 1-D and 2-D data, can indeed be used in order to further enhance the accuracy of CFD predictions, with the ultimate aim of producing accurate flow estimations for any flow regime without the need of using PIV for each scenario.

Performing PIV investigations in a two-phase system was not feasible within the stirred tanks in the present study. Studies have been able to use red fluorescent seeding particles combined with a camera fitted filter to only allow light scattered by the particles (greater than 545 nm) to be viewed on the acquired images (Zhu et al., 2009). More studies regarding the flow characteristics within a two-phase system would improve further the current understanding of the multi-phase flow dynamics, and assist the improvement of computer modelling and simulations.

Cell culture behaviour and performance is highly convoluted, given the varying cell lines available and their different responses to physical, nutritional and environmental stimuli. Further investigations are required to elucidate the role of parameters such as ε upon cellular behaviour, to progress from the typical measurements of cellular death thresholds in response to ε levels found in literature. The impact of cyclical environmental changes to which the cells are exposed (both in terms of absolute spatial variation in hydrodynamic parameters and temporal disparities), warrants further study: In order to understand whether extended exposure to a specific ε environment, or a transient exposure to such an environment, would elicit differing responses from the cells. Further work pertaining to the effect of hydrodynamics, upon gas phase parameters such as k_La and CO_2 would also provide greater understanding of cell culture performance.

Considering the significant variation of cell specific protein productivity at different stages of cellular growth between the CellReady and Cultibag, it is clear that much more effort needs to be placed in understanding the metabolic flux occurring during different environmental stress conditions, to further correlate cell culture performance to hydrodynamic conditions. The ability to control protein productivity and cell density, may be important to primary recovery and purification efforts i.e. it may be auspicious to have a greater or lower cell density whilst maintaining overall titres. Thus an improved understanding of cellular response to physical stimuli can

be used to further process optimisation at the upstream stage, in line with downstream requirements.

To conclude, this thesis has enabled an enhanced level of hydrodynamic characterisation using non-invasive laser technology within novel single-use bioreactor systems not yet attempted in previous studies. Quantification of the relative differences of turbulence and velocity levels throughout the whole flow field of a bioreactor provides a unique insight into the impact of bioreactor design on the mixing efficacy of vessels in the context of cell culture behaviour and performance. The next step is to further refine the accuracy of the measurements acquired, in particular regarding flow scales, energy dissipation rates and isotropic assumptions (as technological advances permit). Furthermore, a more comprehensive study into all aspects of cellular behaviour, including cell cycle, metabolic activity/flux, cell growth, cell size and protein productivity is required in order to fulfil Quality by Design principles, as well as enhance both productivity and scalability. With this understanding, a more informed approached can be used in the actual design of bioreactor systems, to ultimately optimise the efficiency of mammalian cell culture processes; one of the key components of the biopharmaceutical industry.

References

Abu-Reesh, I., Kargi, F., 1991. Biological responses of hybridoma cells to hydrodynamic shear in an agitated bioreactor. Enzyme Microb. Technol. 13, 913–9.

Ahn, W.S., Antoniewicz, M.R., 2011. Metabolic flux analysis of CHO cells at growth and non-growth phases using isotopic tracers and mass spectrometry. Metab. Eng. 13, 598–609.

Al-Rubeai, M., Emery, A.N., 1990. Mechanisms and kinetics of monoclonal antibody synthesis and secretion in synchronous and asynchronous hybridoma cell cultures. J. Biotechnol. 16, 67–85.

Al-Rubeai, M., Emery, A.N., Chalder, S., Jan, D.C., 1992. Specific monoclonal antibody productivity and the cell cycle-comparisons of batch, continuous and perfusion cultures. Cytotechnology 9, 85–97.

Al-Rubeai, M., Singh, R.P., Goldman, M.H., Emery, a N., 1995. Death mechanisms of animal cells in conditions of intensive agitation. Biotechnol. Bioeng. 45, 463–72.

Aubin, J., Le Sauze, N., Bertrand, J., Fletcher, D.., Xuereb, C., 2004. PIV measurements of flow in an aerated tank stirred by a down- and an up-pumping axial flow impeller. Exp. Therm. Fluid Sci. 28, 447–456.

Augenstein, D.C., Sinskey, A.J., Wang, D.I., 1971. Effect of shear on the death of two strains of mammalian tissue cells. Biotechnol. Bioeng. 13, 409–18.

Aunins, J.G., Woodson, B.A., Hale, T.K., Wang, D.I., 1989. Effects of paddle impeller geometry on power input and mass transfer in small-scale animal cell culture vessels. Biotechnol. Bioeng. 34, 1127–32.

Bakker, A., Myers, K.J., Ward, R.W., Lee, C.K., 1996. The Laminar and Turbulent Flow Pattern of a Pitched Blade Turbine. Trans IChemE 74, 485–491.

Baldi, S., Hann, D., Yianneskis, M., 2002. On the measurement of turbulence energy dissipation in stirred vessels with PIV techniques, in: Proceedings of the 11th International Symposium on Applied Laser Techniques in Fluid Mechanic, Lisbon. pp. 1–12.

Baldi, S., Yianneskis, M., 2004. On the quantification of energy dissipation in the impeller stream of a stirred vessel from fluctuating velocity gradient measurements. Chem. Eng. Sci. 59, 2659–2671.

Barbaroux, M., Sette, A., 2006. Properties of Materials Used in Single-Use Flexible Containers: Requirements and Analysis. Biopharm Int. 11.

Batchelor, G.K., 1953. The Theory of Homogenous Turbulence. Cambridge University Press, London.

Bittorf, K.J., Kresta, S.M., 2000. Active volume of mean circulation for stirred tanks agitated with axial impellers. Chem. Eng. Sci. 55, 1325–1335.

Boulton-Stone, J.M., Blake, J.R., 1993. Gas bubbles bursting at a free surface. J. Fluid Mech. 254, 437–466.

Bowers, J., 2011. Scale and Bioreactor Design Translation for Rocking Bag Bioreactors, in: Comprehensive Quality by Design in Pharmaceutical Development and Manufacture. AIChE.

Brecht, R., 2009. Disposable Bioreactors: Maturation into Pharmaceutical Glycoprotein Manufacturing. Adv. Biochem. Eng. Biotechnol. 115, 1–31.

Bryson, A.E., 1964. Film Notes for Waves in Fluids. National Committee for Fluid Mechanics Films.

Campbell, N., Reece, J., 2005. Biology, 7th ed. Benjamin-Cummings Pub Co, San Francisco.

Cappia, J.-M., Vachette, E., Langlois, C., Barbaroux, M., Hackel, H., 2014. Enhanced Assurance of Supply for Single-Use Bags. Sartorius Stedim Biotech.

Carswell, K.S., Papoutsakis, E.T., 2000. Culture of Human T Cells in Stirred Bioreactors for Cellular Immunotherapy Applications: Shear, Proliferation, and the IL-2 Receptor. Biotechnol. Bioeng. 68, 328–338.

Cherry, R.S., 1993. Animal cells in turbulent fluids: Details of the physical stimulus and the biological response. Biotechnol. Adv. 11, 279–299.

Chimica, I., Bonino, P.G.B., Pia, O., Converti, A., Zilli, M., Arni, S., Felice, R. Di, Borghi, M. Del, 1999. Estimation of viscosity of highly viscous fermentation media containing one or more solutes. Biochem. Eng. J. 4, 81–85.

Chisti, M.Y., Moo-Young, M., 1987. Airlift Reactors: Characteristics, Applications and Design Considerations. Chem. Eng. Commun. 60, 195–242.

Chisti, Y., 1998. Pneumatically agitated bioreactors in industrial and environmental bioprocessing: Hydrodynamics, hydraulics, and transport phenomena. Appl. Mech. Rev. 51, 33–112.

Clancy, L.J., 1975. Aerodynamics.

Clincke, M.F., Mölleryd, C., Zhang, Y., Lindskog, E., Walsh, K., Chotteau, V., 2013. Very high density of CHO cells in perfusion by ATF or TFF in WAVE bioreactor™. Part I. Effect of the cell density on the process. Biotechnol. Prog. 29, 754–67.

Dantec, 2010. Dynamic Studio v3.12 User Guide.

Deen, N., Hjertager, B., 2002. Particle image velocimetry measurements in an aerated stirred tank. Chem. Eng. Commun. 189, 1208–1221.

Devi, T.T., Kumar, B., 2013. Comparison of flow patterns of dual rushton and CD-6 impellers. Theor. Found. Chem. Eng. 47, 344–355.

Ducci, A., Yianneskis, M., 2005. Direct determination of energy dissipation in stirred vessels with two-point LDA. AIChE J. 51, 2133–2149.

Eibl, R., Eibl, D., 2006. Design and Use of the Wave Bioreactor for Plant Cell Culture. Plant Tissue Cult. Eng. 6, 203–227.

Eibl, R., Eibl, D., 2011. Single-Use Technology in Biopharmaceutical Manufacture. Wiley.

Eibl, R., Werner, S., Eibl, D., 2009. Bag Bioreactor Based on Wave-Induced Motion: Characteristics and Applications. Adv. Biochem. Eng. Biotechnol. 115, 55–87.

Fishwick, R.P., Winterbottom, J.M., Parker, D.J., Fan, X., Stitt, E.H., 2005. Hydrodynamic Measurements of Up- and Down-Pumping Pitched-Blade Turbines in Gassed, Agitated Vessels, Using Positron Emission Particle Tracking. Ind. Eng. Chem. Res. 44, 6371–6380.

Foulon, A., Trach, F., Pralong, A., Proctor, M., Lim, J., 2008. Using Disposables in an Antibody Production Process. Bioprocess Int. 3, 12–18.

Gabriele, A., Nienow, A.W., Simmons, M.J.H., 2009. Use of angle resolved PIV to estimate local specific energy dissipation rates for up- and down-pumping pitched blade agitators in a stirred tank. Chem. Eng. Sci. 64, 126–143.

Garcia-Briones, M.A., Chalmers, J.J., 1994. Flow Parameters Associated with Hydrodynamic Cell Injury. Biotechnol. Bioeng. 44, 1089–1098.

Godoy-Silva, R., Chalmers, J.J., Casnocha, S.A., Bass, L.A., Ma, N., 2009a. Physiological responses of CHO cells to repetitive hydrodynamic stress. Biotechnol. Bioeng. 103, 1103–17.

Godoy-Silva, R., Mollet, M., Chalmers, J.J., 2009b. Evaluation of the effect of chronic hydrodynamical stresses on cultures of suspensed CHO-6E6 cells. Biotechnol. Bioeng. 102, 1119–30.

Gregoriades, N., Clay, J., Ma, N., Koelling, K., Chalmers, J.J., 2000. Cell damage of microcarrier cultures as a function of local energy dissipation created by a rapid extensional flow. Biotechnol. Bioeng. 69, 171–82.

Hall, J.F., Barigou, M., Simmons, M.J.H., Stitt, E.H., 2005. Comparative study of different mixing strategies in small high throughput experimentation reactors. Chem. Eng. Sci. 60, 2355–2368.

Hill, D., Troolin, D., Walters, G., Lai, W., Sharp, K., 2008. Volumetric 3-component velocimetry (V3V) measurements of the turbulent flow in stirred tank reactors. 14th Int Symp Appl. Laser Tech. to Fluid Mech. 1–12.

Hinze, J.O., 1975. Turbulence, 2nd ed. McGraw-Hill, New York.

Hirt, C., Nichols, B., 1981. Volume of fluid (VOF) method for the dynamics of free boundaries1. J. Comput. Phys. 39, 201–225.

Hu, W., Berdugo, C., Chalmers, J.J., 2011. The potential of hydrodynamic damage to animal cells of industrial relevance: current understanding. Cytotechnology 63, 445–60.

Jenke, D., 2007. Evaluation of the Chemical Compatibility of Plastic Contact Materials and Pharmaceutical Products ; Safety Considerations Related to Extractables and Leachables. October 96, 2566–2581.

Joshi, J.B., Elias, C.B., Patole, M.S., 1996. Role of hydrodynamic shear in the cultivation of animal, plant and microbial cells. Chem. Eng. J. 62, 121–141.

Ju, L., Chase, G.G., 1992. Improved scale-up strategies of bioreactors. Bioprocess Eng. 8, 49–53.

Kaiser, S.C., Eibl, R., Eibl, D., 2011a. Engineering characteristics of a single-use stirred bioreactor at bench-scale: The Mobius CellReady 3L bioreactor as a case study. Eng. Life Sci. 11, 359–368.

Kaiser, S.C., Löffelholz, C., Werner, S., Eibl, D., 2011b. CFD for Characterizing Standard and Single-use Stirred Cell Culture Bioreactors, in: Computational Fluid Dynamics Technologies and Applications. pp. 97–122.

Khan, F.R., 2005. Investigation of turbulent flows and instabilities in a stirred vessel using particle image velocimetry. Loughborough University.

Khan, F.R., Rielly, C.D., Brown, D.A.R., 2006. Angle-resolved stereo-PIV measurements close to a down-pumping pitched-blade turbine. Chem. Eng. Sci. 61, 2799–2806.

Khopkar, A., Aubin, J., Rubio-Atoche, C., Xuereb, C., Le Sauze, N., Bertrand, J., Ranade, V. V., 2004. Flow Generated by Radial Flow Impellers: PIV Measurements and CFD Simulations. Int. J. Chem. React. Eng. 2, 1–17.

Kim, J.C., Seong, J.H., Lee, B., Hashimura, Y., Groux, D., Oh, D.J., 2013. Evaluation of a novel pneumatic bioreactor system for culture of recombinant Chinese hamster ovary cells. Biotechnol. Bioprocess Eng. 18, 801–807.

Koch, S., Cobb, H.D., Stuart, N.A., 2010. Notes on Gravity Waves – Operational Forecasting and Detection of Gravity Waves Weather and Forecasting [WWW Document]. NOAA.

Krampe, B., Al-Rubeai, M., 2010. Cell death in mammalian cell culture: molecular mechanisms and cell line engineering strategies. Cytotechnology 62, 175–88.

Kresta, S., 1998. Turbulence in Stirred Tanks: Anisotropic, Approximate, and Applied. Can. J. Chem. Eng. 76, 563–576.

Kresta, S.M., Brodkey, R.S., 2003. Turbulence in mixing applications, in: Paul, E.L., Atiemo-Obeng, V.A., Kresta, S.M. (Eds.), Handbook of Industrial Mixing: Science and Practice. Wiley-Interscience, New York, pp. 19–87.

Kretzmer, G., Schiigerl, K., 1991. Response of mammalian cells to shear stress. Appl. Microbiol. Biotechnol. 34, 613–616.

Krishnan, R., Chen, H., 2012. A Comprehensive Strategy to Evaluate Single-use Bioreactors for Pilot-scale Cell Culture Production. Am. Pharm. Rev. 15.

Kumaresan, T., Nere, N.K., Joshi, J.B., 2005. Effect of Internals on the Flow Pattern and Mixing in Stirred Tanks. Ind. Eng. Chem. Res. 44, 9951–9961.

Kunas, K.T., Papoutsakis, E.T., 1990. Damage mechanisms of suspended animal cells in agitated bioreactors with and without bubble entrainment. Biotechnol. Bioeng. 36, 476–83.

Landahl, M.T., Mollo-Christensen, E., 1992. Turbulence and Random Processes in Fluid Mechanics, 2nd ed. Cambridge University Press.

Lee, B., Fang, D., Croughan, M., Carrondo, M., Paik, S.-H., 2011. Characterization of novel pneumatic mixing for single-use bioreactor application., in: BMC Proceedings. BioMed Central Ltd, p. O12.

Li, J., Wong, C.L., Vijayasankaran, N., Hudson, T., Amanullah, A., 2012. Feeding lactate for CHO cell culture processes: Impact on culture metabolism and performance. Biotechnol. Bioeng. 109, 1173–86.

Lim, J.A.C., Sinclair, A., 2007. Process Economy of Disposable Manufacturing - Process Models to Minimise Upfront Costs. Am. Pharm. Rev. 10, 114–121.

Löffelholz, C., Husemann, U., Greller, G., Meusel, W., Kauling, J., Ay, P., Kraume, M., Eibl, R., Eibl, D., 2013. Bioengineering Parameters for Single-Use Bioreactors: Overview and Evaluation of Suitable Methods. Chemie Ing. Tech. 85, 40–56.

Löffelholz, C., Kaiser, S.C., Werner, S., Eibl, D., 2011. CFD as a Tool to Characterize Single-Use Bioreactors, in: Eibl, R., Eibl, D. (Eds.), Single-Use Technology in Biopharmaceutical Manufacture. Wiley, pp. 264–278.

Ma, N., Koelling, K.W., Chalmers, J.J., 2002. Fabrication and use of a transient contractional flow device to quantify the sensitivity of mammalian and insect cells to hydrodynamic forces. Biotechnol. Bioeng. 80, 428–37.

Martín, M., Montes, F.J., Galán, M.A., 2008. Bubbling process in stirred tank reactors I: Agitator effect on bubble size, formation and rising. Chem. Eng. Sci. 63, 3212–3222.

Mckenna, T., 2009. Oxidative stress on mammalian cell cultures during recombinant protein expression. Linkoping University Institute of Technology.

McQueen, A., Bailey, J.E., 1989. Influence of Serum Level, Cell Line, Flow Type and Viscosity on Flow-Induced Lysis of Suspended Mammalian Cells. Biotechnol. Lett. 11, 531–536.

Melling, A., 1997. Tracer particles and seeding for particle image velocimetry. Meas. Sci. Technol. 8, 1406–1416.

Merten, O.W., 1988. Batch production and growth kinetics of hybridomas. Cytotechnology 1, 113–21.

Meyers, J., Sagaut, P., 2006. On the model coefficients for the standard and the variational multi-scale Smagorinsky model. J. Fluid Mech. 569, 287–319.

Micheletti, M., Baldi, S., Yeoh, S.L., Ducci, A., Papadakis, G., Lee, K.C., Yianneskis, M., 2004. On spatial and temporal variations and estimates of energy dissipation in stirred reactors 82, 1188–1198.

Mikola, M., Seto, J., Amanullah, A., 2007. Evaluation of a novel Wave Bioreactor cellbag for aerobic yeast cultivation. Bioprocess Biosyst. Eng. 30, 231–41.

Mirro, R., Voll, K., 2009. Which Impeller Is Right for Your Cell Line? A Guide to Impeller Selection for Stirred-Tank Bioreactors. Bioprocess Int. 7.

Mishra, V.P., Joshi, J.B., 1994. Flow Generated by a Disc Turbine Part IV: Multiple Impellers. Chem. Eng. Res. Des. 72, 657–668.

Mollet, M., Godoy-Silva, R., Berdugo, C., Chalmers, J.J., 2007. Acute Hydrodynamic Forces and Apoptosis : A Complex Question. Biotechnol. Bioeng. 98, 772–788.

Mollet, M., Ma, N., Zhao, Y., Brodkey, R., Taticek, R., Chalmers, J.J., 2004. Bioprocess equipment: characterization of energy dissipation rate and its potential to damage cells. Biotechnol. Prog. 20, 1437–48.

Mulukutla, B.C., Khan, S., Lange, A., Hu, W.-S., 2010. Glucose metabolism in mammalian cell culture: new insights for tweaking vintage pathways. Trends Biotechnol. 28, 476–84.

Munson, B.R., Young, D.F., Okiishi, T., 2002. Fundamentals of Fluid Mechanics 4th Ed. John Wiley & Sons, Inc.

Nienow, A.W., 2006. Reactor engineering in large scale animal cell culture. Cytotechnology 50, 9–33.

Nienow, A.W., Scott, W.H., Hewitt, C.J., Thomas, C.R., Lewis, G., Amanullah, A., Kiss, R., Meier, S.J., 2013. Scale-down studies for assessing the impact of different stress parameters on growth and product quality during animal cell culture. Chem. Eng. Sci. Des. 91, 2265–2274.

Odeleye, A.O.O., Marsh, D.T.J., Osborne, M.D., Lye, G.J., Micheletti, M., 2014. On the fluid dynamics of a laboratory scale single-use stirred bioreactor. Chem. Eng. Sci. 111, 299–312.

Oh, S., Nienow, A., Alrubeai, M., Emery, A., 1989. The effects of agitation intensity with and without continuous sparging on the growth and antibody production of hybridoma cells. J. Biotechnol. 12, 45–62.

Oncül, A.A., Kalmbach, A., Genzel, Y., Reichl, U., Thévenin, D., 2010. Characterization of flow conditions in 2 L and 20 L wave bioreactors using computational fluid dynamics. Biotechnol. Prog. 26, 101–10.

Oosterhuis, N.M.G., Hudson, T., D'Avino, A., Zijlstra, G.M., Amanullah, A., 2011. Comprehensive Biotechnology Volume 2: Engineering Fundamentals of Biotechnology, Second. ed. Elsevier.

Pan, C., Min, J., Liu, X., Gao, Z., 2008. Investigation of Fluid Flow in a Dual Rushton Impeller Stirred Tank Using Particle Image Velocimetry. Chinese J. Chem. Eng. 16, 693–699.

Pavlou, A.K., Reichert, J.M., 2004. Recombinant protein therapeutics--success rates, market trends and values to 2010. Nat. Biotechnol. 22, 1513–9.

Petersen, J.F., McIntire, L. V., Papoutsakis, E.T., 1988. Shear sensitivity of culture hybridoma cells (CRL-8018) depends on mode of growth, culture age and metabolite concentration. J. Biotechnol. 7, 229–246.

Petersen, J.F., McIntire, L. V., Papoutsakis, E.T., 1990. Shear Sensitivity of hybridoma cells in batch, fed-batch, and continuous cultures. Biotechnol. Prog. 6, 114–120.

Plion, P., Costes, J., Couderc, J.P., 1985. Study by Laser Doppler Anemometry of the Flow Induced by a Propeller in a Stirred Tank - Influence of Baffles, in: 5th European Conference on Mixing. Wurzburg, Germany, pp. 341–353.

Raffel, M., Willert, C., Wereley, S., 2007. Particle image velocimetry: a practical guide, Current science. Springer Verlag.

Rao, G., Moreira, A., Brorson, K., 2009. Disposable bioprocessing: the future has arrived. Biotechnol. Bioeng. 102, 348–56.

Reichert, J.M., Rosensweig, C.J., Faden, L.B., Dewitz, M.C., 2005. Monoclonal antibody successes in the clinic. Nat. Biotechnol. 23, 1073–8.

Rushton, J.H., Costich, E.W., Everett, H.J., 1950. Power Characteristics of Mixing Impellers. Chem. Eng. Prog. 46, 395–404.

Rutherford, K., Lee, K.C., Mahmoudi, S.M.S., Yianneskis, M., 1996. Hydrodynamic characteristics of dual Rushton impeller stirred vessels. AIChE J. 42, 332–346.

Sardeing, R., Aubin, J., Xuereb, C., 2004. GAS – LIQUID MASS TRANSFER A Comparison of Down- and Up-pumping Axial Flow Impellers with Radial Impellers. Chem. Eng. Res. Des. 82, 1589–1596.

Schaefer, M., Hofken, M., Durst, F., 1997. Detailed LDV Measurements for Visualization of the Flow Field Within a Stirred-Tank Reactor Equipped with a Rushton Turbine. Chem. Eng. Sci. Des. 75, 729–736.

Schaefer, M., Yianneskis, M., Wachter, P., Durst, F., 1998. Trailing Vortices around a 45 Degree Pitched-Blade impeller. AIChE J. 44, 1233–1246.

Schmid, G., Huber, F., Kerschbaumer, R., 1992. Adaptation of hybridoma cells to hydrodynamic stress under continuous culture conditions, in: Spier, R.E., Griffiths, J.B., Macdonald, C. (Eds.), Animal Cell Technology: Developments, Processes and Products. Butterworth-Heinemann, Oxford, pp. 203–205.

Scott, W.H., Thomas, C.R., Hewitt, C.J., Lewis, G., Meier, S.J., Amanullah, A., Kiss, R., Nienow, A.W., 2012. Scale-down studies for assessing the impact of different stress parameters on growth and product quality during mammalian cell culture, in: 14th European Conference On Mixing. pp. 10–13.

Sengupta, N., Rose, S.T., Morgan, J.A., 2011. Metabolic flux analysis of CHO cell metabolism in the late non-growth phase. Biotechnol. Bioeng. 108, 82–92.

Sharp, K. V, Kim, K.C., Adrian, R., 2000. Dissipation Estimation Around a Rushton Turbine Using Particle Image Velocimetry, Laser Techniques Applied to Fluid Mechanics.

Sharp, K. V., Adrian, R.J., 2001. PIV study of small-scale flow structure around a Rushton turbine. AIChE J. 47, 766–778.

Sheng, J., Meng, H., Fox, R.O., 2000. A large eddy PIV method for turbulence dissipation rate estimation. Chem. Eng. Sci. 55, 4423–4434.

Sidoli, F.R., Mantalaris, A., Asprey, S.P., 2004. Modelling of Mammalian cells and cell culture processes. Cytotechnology 44, 27–46.

Sieblist, C., Jenzsch, M., Pohlscheidt, M., 2013. Influence of pluronic F68 on oxygen mass transfer. Biotechnol. Prog. 29, 1278–88.

Sinclair, A., Leveen, L., Monge, M., Lim, J., Cox, S., 2008. The Environmental Impact of Disposable Technologies. Biopharm Int. 1–9.

Sinnott, R.K., 2005. Coulson and Richardson's Chemical Engineering Volume 6, 4th ed, Coulson and Richardson's Chemical Engineering. Butterworth-Heinemann.

Smagorinsky, J., 1963. General circulation experiments with the primitive equations. Mon. Weather Rev. 91, 99–164.

Smales, C.M., James, D.C., 2005. Therapeutic Proteins: Methods and Protocols. Humana Press Inc., Totowa, New Jersey.

Sorg, R., Tanzeglock, T., Soos, M., Morbidelli, M., Périlleux, A., Solacroup, T., Broly, H., 2011. Minimizing hydrodynamic stress in mammalian cell culture through the lobed Taylor-Couette bioreactor. Biotechnol. J. 6, 1504–15.

Suzuki, E., Ollis, D.F., 1990. Enhanced antibody production at slowed growth rates: experimental demonstration and a simple structured model. Biotechnol. Prog. 6, 231–6.

Tanzeglock, T., Soos, M., Stephanopoulos, G., Morbidelli, M., 2009. Induction of mammalian cell death by simple shear and extensional flows. Biotechnol. Bioeng. 104, 360–70.

Terrier, B., Courtois, D., Henault, N., Cuvier, A., Bastin, M., Aknin, A., Dubreuil, J., Petiard, V., 2006. Two new disposable bioreactors for plant cell culture: The wave and undertow bioreactor and the slug bubble bioreactor. Biotechnol. Bioeng. 96, 914–923.

Thomas, C.R., Al-Rubeai, M., Zhang, Z., 1994. Prediction of mechanical damage to animal cells in turbulence. Cytotechnology 15, 329–35.

Thomasi, S.S., Cerri, M.O., Badino, A.C., 2010. Average shear rate in three pneumatic bioreactors. Bioprocess Biosyst. Eng. 33, 979–88.

Van Der Molen, K., Van Maanen, H.R.E., 1978. Laser-Doppler Measurements of the Turbulent Flow in Stirred Vessels to Establish Scaling Rules. Chem. Eng. Sci. 33, 1161–1168.

Varley, J., Birch, J., 1999. Reactor design for large scale suspension animal cell culture. Cytotechnology 29, 177–205.

Venkat, R. V, 1995. Study of Hydrodynamics due to Turbulent Mixing in Animal Cell Microcarrier Bioreactors. The Ohio State University.

Wave GE Healthcare Life Sciences URL www.gelifesciences.com/webapp/wcs/stores/servlet/catalog/en/GELifeSciences-UK/brands/wave

Weber, A., Husemann, U., Chaussin, S., Adams, T., Wilde, D. De, Gerighausen, S., Greller, G., Fenge, C., 2013. Development and Qualification of a Scalable, Disposable Bioreactor for GMP-Compliant Cell Culture. Bioprocess Int. 6–17.

Wernersson, E.S., Tragardh, C., 1998. Scaling of turbulence characteristics in a turbine-agitated tank in relation to agitation rate. Chem. Eng. J. 70, 37–45.

Wernersson, E.S., Tragardh, C., 1999. Scale-up of Rushton turbine-agitated tanks. Chem. Eng. Sci. 54, 4245–4256.

Wu, H., Patterson, G.K., 1989. Laser-Doppler Measurements of Turbulence-Flow Parameters in a Stirred Mixer. Chem. Eng. Sci. 44, 2207–2221.

Zagari, F., Jordan, M., Stettler, M., Broly, H., Wurm, F.M., 2013. Lactate metabolism shift in CHO cell culture: the role of mitochondrial oxidative activity. N. Biotechnol. 30, 238–45.

Zhang, Z., Al-Rubeai, M., Thomas, C.R., 1993. Estimation of disruption of animal cells by turbulent capillary flow. Biotechnol. Bioeng. 42, 987–93.

Zhou, G., Kresta, S.M., 1996. Impact of Tank Geometry on the Maximum Turbulence Energy Dissipation Rate for Impellers. AIChE J. 42, 2476–2490.

Zhu, H., Nienow, A.W., Bujalski, W., Simmons, M.J.H., 2009. Mixing studies in a model aerated bioreactor equipped with an up- or a down-pumping "Elephant Ear" agitator: Power, hold-up and aerated flow field measurements. Chem. Eng. Res. Des. 87, 307–317.

Zlokarnik, M., 2006. Scale-Up in Chemical Engineering, Second, Completely Revised and Extended Edition. Wiley-VCH, Weinheim.